SOLID OXIDE FUEL CELL CATHODE INFILTRATE PARTICLE SIZE CONTROL AND OXYGEN SURFACE EXCHANGE RESISTANCE DETERMINATION

By

Theodore E. Burye

A THESIS

Submitted to
Michigan State University
in partial fulfillment of the requirements
for the degree of

Chemical Engineering – Doctor of Philosophy

2015

ABSTRACT

SOLID OXIDE FUEL CELL CATHODE INFILTRATE PARTICLE SIZE CONTROL AND OXYGEN SURFACE EXCHANGE REISTANCE DETERMINATION

By

Theodore E. Burye

Over the past decade, nano-sized Mixed Ionic Electronic Conducting (MIEC) – micro-sized Ionic Conducting (IC) composite cathodes produced by the infiltration method have received much attention in the literature [1-9] due to their low polarization resistance (R_P) at intermediate (500-700°C) operating temperatures. Small infiltrated MIEC oxide nano-particle size and low intrinsic MIEC oxygen surface exchange resistance (R_s) have been two critical factors allowing these Nano-Micro-Composite Cathodes (NMCCs) to achieve high performance and/or low temperature operation. Unfortunately, previous studies have not found a reliable method to control or reduce infiltrated nano-particle size. In addition, controversy exists on the best MIEC infiltrate composition because: 1) R_s measurements on infiltrated MIEC particles are presently unavailable in the literature, and 2) bulk and thin film R_s measurements on nominally identical MIEC compositions often vary by up to 3 orders of magnitude [10].

Here, two processing techniques, precursor nitrate solution desiccation and ceria oxide pre-infiltration, were developed to systematically produce a reduction in the average La_{0.6}Sr_{0.4}Co_{0.8}Fe_{0.2}O_{3- δ} (LSCF) infiltrated nano-particle size from 50 nm to 22 nm. This particle size reduction reduced the SOFC operating temperature, (defined as the temperature where R_P =0.1 Ω cm²) from 650°C to 540°C. In addition, R_s values for infiltrated MIEC particles were determined for the first time through finite element

modeling calculations on 3D Focused Ion Beam-Scanning Electron Microscope (FIB-SEM) reconstructions of electrochemically characterized infiltrated electrodes.

ACKNOWLEDGEMENTS

This work was supported by National Science Foundation (NSF) Award No. CBET-1254453 and a Michigan State University faculty startup grant to Dr. Jason D. Nicholas. Microscopy work was conducted at the Michigan State Composites Center, which is supported by the NSF Major Instrumentation Program and Michigan State University. Profilometry work was conducted at the W.M. Keck Microfabrication Facility supported by the W.M. Keck Foundation and Michigan State University.

I would also like to thank my committee members for their support in my academic studies and research. First, I would like thank my advisor, Dr. Jason D. Nicholas, who has helped me numerous times throughout my studies and helped me understand Material Science. Next, I would like to thank Dr. Lunt, who has provided a vast amount of diffraction knowledge which helped me characterize my samples. My understanding of impedance characterization has been greatly improved by Dr. Barton, and Dr. Duxbury has also provided a valuable critical external perspective.

I would also like to thank previous and current group members for their support and guidance through my doctoral program. Dr. Qing Yang, Lin Wang, Andrew Flegler, Peter Su, Vasiliy Sharikov-Bass, Tridip Das, Eric Straley, Hongjie Tang, and Yuxi Ma all contributed to my work and provided me with helpful insights into my research and useful discussions. Finally, I would like to thank my family for supporting me through my time in the Ph.D program.

TABLE OF CONTENTS

LIST OF TABLES	ix
LIST OF FIGURES	X
KEY TO ABBREVIATIONS	xvii
CHAPTER 1: Thesis Motivation and Overview	1
1.1 The World Energy Problem	
1.2 Solid Oxide Fuel Cells as a Solution to the World Energy Problem	1
1.3 Solid Oxide Fuel Cell Knowledge Gaps	3
1.4 Thesis Overview	3
1.5 Summary	4
CHAPTER 2: Literature Review	5
2.1 Solid Oxide Fuel Cell Overview	5
2.1.1 Solid Oxide Fuel Cell Operating Principles	6
2.1.2 Traditional and Nano-Micro-Composite Cathodes	
2.1.3 Thin Film Cathodes.	
2.2 Planar Solid Oxide Fuel Cell Geometric Arrangements	12
2.3 Commonly Used Solid Oxide Fuel Cell Materials	
2.3.1 Ionic Conductors	
2.3.2 Electronic Conductors	14
2.3.3 Mixed Ionic Electronic Conductors	14
2.4 Composite Solid Oxide Fuel Cell Cathode Geometries	15
2.4.1 Electronic Conducting Scaffolds	
2.4.2 Mixed Ionic Electronic Conducting Scaffolds	16
2.4.3 Ionic Conducting Scaffolds	
2.5 Models Identifying the Parameters Controlling Nano-Micro-Composite Cathodo	e
Performance	18
2.5.1 The Surface Resistance Model	18
2.5.2 The Simple Infiltration Microstructure Polarization Loss Estimation Model	. 19
2.6 Infiltrate Particle Size is Difficult to Control According to the Literature	22
2.6.1 Fabrication Techniques that Reduce Particle Size	
2.6.2 Fabrication Techniques that Have No Impact on Particle Size Reduction	
2.7 Literature Oxygen Surface Exchange Resistance Measurement Techniques	
2.7.1 Oxygen Surface Exchange Resistance from Thin Film Electrochemical	
Impedance Spectroscopy	26
2.7.3 Oxygen Surface Resistance from Chemical Rate Constant Measurements	
2.8 Large Uncertainties Exist in the R_s Value of Even the Most Common Mixed Ion	
Electronic Conducting Materials	
2.9 Summary	

CHAPTER 3: Experimental Methods	35
3.1 Symmetrical Cathode Fabrication Processes	
3.1.1 Cathode-Electrolyte-Cathode Symmetric Cell Production	
3.1.2 Cathode Fabrication	
3.1.3 Mixed Ionic and Electronic Conducting Precursor Solution Fabrication and	
Cathode Infiltration	
3.1.4 Mixed Ionic and Electronic Conducting Oxide Phase Purity Analysis	
3.1.5 Current Collector Application	
3.2 Characterization Techniques	
3.2.1 Electrochemical Impedance Spectroscopy	
3.2.2 Scanning Electron Microscopy	
3.2.3 Solid Oxide Fuel Cell Nano-Particle Coarsening Rate	
3.2.4 X-ray Diffraction	
3.2.5 Williamson-Hall Particle Size Determination from X-ray Diffraction	
3.2.6 ThermoGravimetric Analysis	
3.2.7 Profilometry	
3.2.8 Focused Ion Beam-Scanning Electron Microscopy 2D Serial Sectioning	
3.3 Finite Element Modeling of Cathode Microstructure and Performance	
3.3.1 Motivation for Using Finite Element Modeling	
3.3.2 Finite Element Modeling Performance Calculation Overview	
3.3.3 Focused Ion Beam-Scanning Electron Microscopy Sample Preparation 3.3.4 Cathode Microstructure 3D Reconstruction	
3.3.5 3D Cathode Reconstruction Volume Meshing	
3.3.6 Infiltrated Solid Oxide Fuel Cell Cathode Finite Element Modeling to Pred	
Polarization Resistance	
5.4 Summary	30
CHAPTER 4: The Impact of Precursor Nitrate Solution Desiccation on Infiltrated	
$La_{0.6}Sr_{0.4}Co_{0.8}Fe_{0.2}O_{3-\delta} Cathodes.$	
4.1 Introduction	
4.2 Experimental Methods	61
4.2.1 Cathode-Electrolyte-Cathode Symmetric Cell Production	
4.2.2 Symmetric Cell Impedance Measurements	63
4.2.3 X-ray Diffraction Measurements	64
4.2.4 Scanning Electron Microscopy Measurements	65
4.2.5 Nano-Micro-Composite Cathode Performance Modeling	65
4.3 Results	67
4.3.1: Desiccant Impacts on Infiltrate Particle Size	
4.3.2: Desiccant Impacts on Infiltrate Phase Purity	
4.3.3: Desiceant Impacts on Cathode Electrochemical Performance	
4.4 Summary	
T.T Dullillal y	/ 0
	, 1
CHAPTER 5: The Impact of Surfactants on Desiccated La _{0.6} Sr _{0.4} Co _{0.8} Fe _{0.2} O _{3-δ} Infiltr	
Solid Oxide Fuel Cell Cathodes	
5.1 Introduction	79

5.2 Experimental Methods	79
5.2.1 Cathode-Electrolyte-Cathode Symmetric Cell Production	
5.2.2 Symmetric Cell Impedance Measurements	
5.2.3 X-ray Diffraction Measurements	81
5.2.4 Scanning Electron Microscopy Measurements	81
5.2.5 Nano-Micro-Composite Cathode Performance Modeling	81
5.2.6 Williamson-Hall Particle Size and Strain Calculations	
5.3 Results	82
5.3.1: Desiccant and Solution Additive Impacts on Infiltrate Particle Size	82
5.3.2: Desiccant and Solution Additive Impacts on Infiltrate Phase Purity	94
5.3.3 Impurity Impacts on LSCF Nano-Particle Coarsening Behavior	102
5.3.4 Desiccant and Solution Additive Impacts on Performance and Stability	105
5.4 Summary	110
CHAPTER 6: The Impact of Nano-Ceria Pre-Infiltration on La _{0.6} Sr _{0.4} Co _{0.8} Fe _{0.2} O _{3-δ}	
Infiltrated Solid Oxide Fuel Cell Cathodes.	111
6.1 Introduction	
6.2 Experimental Methods	
6.2.1 Cathode-Electrolyte-Cathode Symmetric Cell Production	
6.2.2 Symmetrical Cell Impedance, X-ray Diffraction, and Scanning Electron	111
Microscopy Measurements	114
6.2.3 ThermoGravimetric Analysis Measurements	
6.2.4 Nano-Micro-Composite Cathode Performance Modeling	
6.3 Results.	
6.3.1 Pre-Infiltration and Solution Additive Impacts on Infiltrate Particle Size	
6.3.2 Pre-Infiltration and Solution Additive Impact on Infiltrate Phase Purity	
6.3.3 Pre-Infiltration and Solution Additive Impact on Precursor Solution	100
Decomposition Behavior	134
6.3.4 Pre-Infiltration and Solution Additive Impacts on Performance and Stabil	
CID 1 2 2 2 2 2 2 2 2 2 2 2 2 2 2 2 2 2 2	•
6.4 Summary	
G S = ======== ,	105
CHAPTER 7: The Impact of Precursor Solution Desiccation and Nano-Ceria Pre-	1 4 1
Infiltration on $La_{0.6}Sr_{0.4}Co_{1-x}Fe_xO_{3-\delta}$ ($0 \le x \le 1$) Infiltrated Cathodes	
7.1 Introduction	
7.2 Experimental Methods	
7.2.1 Cathode-Electrolyte-Cathode Symmetric Cell Production	141
7.2.2 Symmetrical Cell Impedance, X-ray Diffraction, and Scanning Electron	1.40
Microscopy Measurements	
7.2.3 Nano-Micro-Composite Cathode Performance Modeling	
7.3 Results	
7.3.1 Pre-Infiltration, Desiccation and Infiltrated Composition Impacts on Infil	
Particle Size and Performance	
7.3.2 Pre-Infiltration, Desiccation and Infiltrated Composition Impacts on Infil	
Phase Purity	
7.4 Summary	151

CHAPTER 8: Determination of Infiltrated Mixed Ionic and Electronic Conducting N	√ano-
Particle Oxygen Surface Exchange Material Properties through Finite Element Mode	eling
of 3D Reconstructed Microstructures	153
8.1 Introduction	153
8.2 Experimental Methods	154
8.2.1 Cathode-Electrolyte-Cathode-Symmetric Cell Production	154
8.2.2 Electrochemical Impedance Spectroscopy Measurements	154
8.2.3 Nano-Micro-Composite Cathode Finite Element Modeling of 3D	
Reconstructions	154
8.3 Results	155
8.3.1 A Comparison of Finite Element Modeling Mixed Ionic Electronic Condu	icting
Materials Intrinsic Oxygen Surface Exchange Material Properties	155
8.3.2 Identifying the Materials Property Combinations Causing the Surface	
Resistance Limit and the Simple Infiltration Microstructure Polarization Loss	
Estimation Model to Breakdown	158
8.4 Summary	161
CHAPTER 9: Dissertation Conclusions	162
CITAL TER 7. Dissertation Conclusions	102
A PREMINICES	1.5
APPENDICES	165
Appendix 1: Simple Infiltrated Microstructure Polarization Loss Estimation	1.00
(SIMPLE) Model Derivation	
Appendix 2: Focused Ion Beam – Scanning Electron Microscopy (FIB-SEM) 3D	
Reconstruction and Modeling Instructions	195
BIBLIOGRAPHY	210

LIST OF TABLES

Table 1:	Desiccated TXD LSCF-GDC NMCC Cathodes	1
Table 2:	Desiccated PND, TXD and CAD LSCF-GDC NMCC Cathodes	33
Table 3:	Pre-Infiltrated PND, TXD and CAD LSCF-GDC NMCC Cathodes	6

LIST OF FIGURES

Figure 1.1: Gravimetric and Volumetric Energy Densities for Electricity Generating Devices
Figure 2.1: Traditional LSM-YSZ YSZ YSZ-Ni SOFC Component Overpotential Comparison
Figure 2.2: Traditional SOFC Cathode and Anode Chemical Reactions6
Figure 2.3: Current-Voltage and Power Density Curves for SOFC Devices
Figure 2.4: Traditional SOFC Cell Efficiency
Figure 2.5: Representative Micro-Composite Cathode Microstructure10
Figure 2.6: Representative Nano-Micro-Composite Cathode Microstructure with Connected MIEC Nano-Particles
Figure 2.7: SOFC SIMPLE Model Approximated Geometry
Figure 2.8: Infiltrated MIEC Nano-Particle Size for SSC, LSCF, and LSFC23
Figure 2.9: SOFC LSCF R _s Measurement using Electrochemical Impedance Spectroscopy
Figure 2.10: Typical Nano-Micro-Composite Cathode Equivalent Circuit Model28
Figure 2.11: Oxygen Concentration and Thermodynamic Factor Values for LSF, LSFC, LSCF, LSC, SSC and BSCF in Air Reported in Literature Studies
Figure 2.12: k _{chem} and k _o Values Reported in Literature for the Cathode MIEC Materials LSF, LSFC, LSCF, LSC, SSC, and BSCF
Figure 2.13: R _s , Values Reported in Literature for Cathode MIEC Materials LSF, LSFC, LSCF, LSC, SSC, and BSCF
Figure 3.1: Uniaxial Press Device
Figure 3.2: Screen Printer Device
Figure 3.3: Representative X-ray Diffraction Data for Phase Pure LSCF Oxide

Figure 3.4: Nano-Micro-Composite Cathode Electrochemical Impedance Measurement Device
Figure 3.5: Scanning Electron Microscopy Component Schematic
Figure 3.6: X-ray Diffraction Component Schematic
Figure 3.7: Thermo-Gravimetric Analysis Schematic
Figure 3.8: Profilometer Schematic
Figure 3.9: Epoxy Coated Porous GDC Scaffold on a Dense GDC Electrolyte Oriented Inside the FIB-SEM
Figure 3.10: FIB-SEM Cathode Backscatter Image used for 3D Reconstruction54
Figure 3.11: FIB-SEM 3D Reconstruction for Cathode and Electrolyte55
Figure 3.12: FIB-SEM 3D Reconstruction Volume Mesh of Cathode and Electrolyte
Figure 3.13: FIB-SEM 3D Reconstruction Electrochemical Potential Gradient58
Figure 4.1: Scanning Electron Microscope Fracture Surface Image
Figure 4.2: Scanning Electron Micrographs for Desiccated LSCF Nano-Particles Produced by using Triton X-100
Figure 4.3: Bar-Graph of Desiccated Average LSCF Infiltrate Particle Sizes from Scanning Electron Microscopy Images
Figure 4.4: XRD Scans of LSCF Nano-Particles Produced by Firing Desiccated Precursor Nitrate Solutions
Figure 4.5: Desiccated LSCF-GDC NMCC R _P EIS Nyquist Plot
Figure 4.6: Desiccated LSCF-GDC NMCC R _P Arrhenius Plots
Figure 4.7: Arrhenius R _P Plot for Desiccated LSCF-GDC NMCCs Tested under Different Atmospheres
Figure 4.8: Arrhenius Ohmic Resistivity Plots for LSCF-GDC NMCCs Tested in Air76
Figure 5.1: Scanning Electron Micrographs of Desiccated LSCF Nano-Particles Produced by using Different Triton X-100 Solution Volumes

Figure 5.2: Scanning Electron Micrographs of Desiccated LSCF Nano-Particles Produced using Different Solution Additives
Figure 5.3: Scanning Electron Micrographs of Desiccated LSCF Nano-Particles Produced using Different Solution Additives
Figure 5.4: Desiccated Williamson-Hall Raw Data Plot for PND LSCF, TXD LSCF and CAD LSCF Nano Particles
Figure 5.5: Strain Plots for Desiccated PND LSCF, TXD LSCF and CAD LSCF Nano-Particles
Figure 5.6: Bar-Graph of Average Desiccated LSCF Infiltrate Particle Size Produced using Different Solution Additives
Figure 5.7: Raw Impedance Data Plots of Desiccated LSCF-GDC NMCCs Produce using Citric Acid and Triton X-100
Figure 5.8: LSCF-GDC R _P Arrhenius Plots for Desiccated NMCCs Produced using Different Solution Additives
Figure 5.9: Arrhenius Ohmic Resistivity Plots for Desiccated LSCF-GDC NMCCs Tested in Air and produced using Different Solution Additives
Figure 5.10: XRD Scans of Desiccated LSCF Nano-Particles Produced using Different Solution Additives
Figure 5.11: XRD Scans for CaCl2-Desiccated PND LSCF Fired between 80°C and 800°C95
Figure 5.12: XRD Scans for Dry Air-Desiccated TXD LSCF Fired between 80°C and 800°C96
Figure 5.13: XRD Scans for CaSO ₄ -Desiccated TXD LSCF Fired between 80°C and 800°C
Figure 5.14: XRD Scans for CaCl ₂ -Desiccated TXD LSCF Fired between 80°C and 800°C98
Figure 5.15: XRD Scans for Dry Air-Desiccated CAD LSCF Fired between 80°C and 800°C99
Figure 5.16: XRD Scans for CaSO ₄ -Desiccated CAD LSCF Fired between 80°C and 800°C

Figure 5.17: XRD Scans for $CaCl_2$ -Desiccated CAD LSCF Fired between $80^{\circ}C$ and $800^{\circ}C$
Figure 5.18: Williamson-Hall Raw Data Plots for Coarsened Undesiccated TXD LSCF Nano-Particle Sizes Produced at 600°C, 700°C and 800°C
Figure 5.19: Strain Plots for Coarsened Undesiccated TXD LSCF Nano-Particle Sizes Produced at 600°C, 700°C and 800°C
Figure 5.20: Coarsened Undesiccated TXD LSCF Average Nano-Particle Sizes Produced at 600°C, 700°C and 800°C
Figure 5.21: LSCF-GDC 500 hour R _P hour Plot for NMCCs Produced using Desiccation and Different Solution Additives
Figure 5.22: Desiccated Scanning Electron Micrographs for CAD and TXD LSCF-GDC Symmetric Cells Tested for 500 hrs
Figure 5.23: Raw Impedance Data Plots of Desiccated LSCF-GDC NMCCs Produced using Different Solution Additives
Figure 6.1: Pre-Infiltrated Cathode Nano-Particle Fabrication Diagram113
Figure 6.2: Scanning Electron Micrographs for Pre-Infiltrated TXD LSCF Nano-Particles Produced using Different Solution Molarities
Figure 6.3: Scanning Electron Micrographs for Pre-Infiltrated LSCF Nano-Particles Produced using Different Solution Volumes
Figure 6.4: Scanning Electron Micrographs for Pre-Infiltrated LSCF Nano-Particles Produced using Different Solution Additives
Figure 6.5: Williamson-Hall Raw Data Plots Pre-Infiltrated for PND LSCF, TXD LSCF and CAD LSCF Nano-Particles
Figure 6.6: Strain Plots Pre-Infiltrated for PND LSCF, TXD LSCF and CAD LSCF Nano-Particles
Figure 6.7: Williamson-Hall Raw Data Plots for Pre-Infiltrated Nano-GDC Particle Sizes in TXD LSCF and CAD LSCF Infiltrated Cells
Figure 6.8: Strain Plots for Pre-Infiltrated Nano-GDC Particles in TXD LSCF and CAD LSCF Infiltrated Cells
Figure 6.9: Bar-Graph of Average LSCF Infiltrate Particle Size Produced using Pre- Infiltration and Different Solution Additives

Figure 6.10: Bar-Graph of Average Nano-GDC Infiltrate Particle Size Produced using Pre-Infiltration and Different Solution Additives
Figure 6.11: Raw Impedance Data Plots of Pre-Infiltrated LSCF-GDC NMCCs Produced using Citric Acid and Triton X-100
Figure 6.12: LSCF-GDC R _P Arrhenius Plots for NMCCs Produced using Pre-Infiltration and Different Solution Additives
Figure 6.13: Arrhenius Ohmic Resistivity Plots for Pre-Infiltrated LSCF -GDC NMCCs Tested in Air using Different Solution Additives
Figure 6.14: XRD Scans for Pre-Infiltrated LSCF and GDC Nano-Particles with Different Solution Additives
Figure 6.15: XRD Scans for 7.4 vol% Pre-Infiltrated PND LSCF Fired between 80°C and 800°C
Figure 6.16: XRD Scans for 7.4 vol% Pre-Infiltrated TXD LSCF Fired between 80°C and 800°C
Figure 6.17: XRD Scans for 7.4 vol% Pre-Infiltrated CAD LSCF Fired between 80°C and 800°C
Figure 6.18: Pre-Infiltrated TGA Plot using Different Solution Additives between 25°C and 850°C
Figure 6.19: LSCF-GDC 500 hour R _P hour Plot for NMCCs Produced using Pre- Infiltration and Different Solution Additives
Figure 6.20: Pre-Infiltrated Scanning Electron Micrographs for CAD and TXD LSCF-GDC Symmetric Cells Tested for 500 hrs
Figure 6.21: Raw Impedance Data Plots of Pre-Infiltrated LSCF-GDC NMCCs Produced using Different Solution Additives
Figure 7.1: Raw Impedance Data Plots of Desiccated and Pre-Infiltrated $La_{0.6}Sr_{0.4}Co_xFe_{1-x}O_{3-\delta}$ ($0 \le x \le 1$) using Citric Acid
Figure 7.2: Desiccated or Pre-Infiltrated $La_{0.6}Sr_{0.4}Co_xFe_{1-x}O_{3-\delta}$ ($0 \le x \le 1$) R_P Arrhenius Plots for NMCCs Produced using Citric Acid145
Figure 7.3: Desiccated or Pre-Infiltrated La _{0.6} Sr _{0.4} Co _x Fe _{1-x} O _{3-δ} (0≤x≤1) Nano-Particle Sizes Produced using Citric Acid

Figure 7.4: La _{0.6} Sr _{0.4} Co _x Fe _{1-x} O _{3-δ} Nano-Particle Sizes Determined from Scanning Electron Microscopy Images
Figure 7.5: Arrhenius Ohmic Resistivity Plots for Desiccated or Pre-Infiltrated $La_{0.6}Sr_{0.4}Co_xFe_{1-x}O_{3-\delta}$ ($0 \le x \le 1$) NMCCs Produced using Citric Acid and Tested in Air
Figure 7.6: XRD Scans for $CaCl_2$ -Desiccated $La_{0.6}Sr_{0.4}Co_xFe_{1-x}O_{3-\delta}$ ($0 \le x \le 1$) Produced using Citric Acid
Figure 7.7: XRD Scans for 7.4 vol% Pre-Infiltrated $La_{0.6}Sr_{0.4}Co_xFe_{1-x}O_{3-\delta}$ ($0 \le x \le 1$) Produced using Citric Acid
Figure 8.1: R _s , k _{chem} and k _o values Reported in Literature and Calculated using FIB-SEM FEM 3D Reconstructions for the Cathode MIEC Materials LSF, LSFC, LSCF, LSC and SSC
Figure 8.2: R_s , k_{chem} and k_o Values Calculated using the FIB-SEM FEM 3D Reconstruction for Cathode MIEC Materials LSF, LSFC, LSCF, LSC and SSC158
Figure 8.3: Calculated R _P Values from the FIB-SEM FEM 3D Microstructure, SIMPLE Model and Surface Resistance Model Determined for Different R _{ct} / Scaffold GDC Conductivity Ratio Values
Figure 9.1: Infiltrated Cell Comparison from Different Infiltration Groups163
Figure A1.1: An Idealized Representation of a Symmetric SOFC Cathode Cell167
Figure A1.2: Oxygen Transport Proof
Figure A1.3: Electrode Polarization Resistance Proof
Figure A1.4: Repeat Unit with Numbered Interfaces Across with Current Flow178
Figure A1.5: Solving for Laplace's Equation
Figure A1.6: Determining I_1
Figure A1.7: Determining I_2
Figure A1.8: Determining I_3
Figure A1.9: Determining I_4
Figure A1.10: Applying the 1 st Boundary Condition Locally

Figure A1.11: Applying the 2^{nd} Boundary Condition to Solve for C_2	188
Figure A1.12: Applying the 1^{st} Boundary Condition Across the Entire Cathode to Solve for C_1	190
Figure A1.13: Solving for the Cathode Polarization Resistance	192
Figure A1.14: Altering the TFV Equation	193
Figure A2.1: Representative 2D FIB-SEM Serial Section Stacked Images used for 3 Reconstruction	
Figure A2.2: 3-Matic Imported 3D Microstructure	196
Figure A2.3: 3-Matic Cathode and Electrolyte Merged Microstructures	198
Figure A2.4: COMSOL Volume Mesh Import Screen	200
Figure A2.5: GDC Conductivity Assigned to Cathode and Electrolyte Microstructur Volume Mesh	
Figure A2.6: Scaled R _s Surface Impedance Assigned to the Cathode Surface Layer Mesh	203
Figure A2.7: 0V Reference Potential Applied to the Electrolyte Surface Layer Mesh	204
Figure A2.8: FIB-SEM 3D Reconstruction Electrochemical Potential Gradient	205
Figure A2.9: FIB-SEM 3D Reconstruction Electrochemical Potential Gradient Mult Plot	
Figure A2.10: Cutplane used to Integrate Current Density Across Electrolyte Surfac Mesh	
Figure A2.11: COMSOL Integration Area Calculation	209

KEY TO ABBREVIATIONS

BSCF=Barium Strontium Cobalt Iron Oxide (Ba_{0.5}Sr_{0.5}Co_{0.8}Fe_{0.2}O_{3-δ})

CAD=Citric Acid Derived

DC=Direct Current

EIS=Alternating Current Electrochemical Impedance Spectroscopy

EISA=Evaporation Induced Self Assembly

FIB=Focused Ion Beam

FEM=Finite Element Modeling

GBCO=Gadolinium Barium Cobalt Oxide (GdBaCo₂O_{5+δ})

GDC=Gadolinia Doped Ceria Oxide (Gd_{0.1}Ce_{0.9}O_{1.95})

IC=Ionic Conducting

 k_{chem} =Chemical Rate Constant into the Lattice

 k_o =Chemical Rate Constant through the Bulk

 L_C =Characteristic Thickness

LNO=Lanthanum Nickel Oxide (La₂NiO₄)

LSC=Lanthanum Strontium Cobalt Oxide (La_{0.6}Sr_{0.4}CoO_{3-δ})

LSCF=Lanthanum Strontium Cobalt Iron Oxide (La_{0.6}Sr_{0.4}Co_{0.8}Fe_{0.2}O_{3-δ})

LSCF55=Lanthanum Strontium Cobalt Iron Oxide (La_{0.5}Sr_{0.5}Co_{0.8}Fe_{0.2}O_{3-δ})

LSF=Lanthanum Strontium Iron Oxide (La_{0.6}Sr_{0.4}FeO_{3-δ})

LSFC=Lanthanum Strontium Iron Cobalt Oxide (La_{0.6}Sr_{0.4}Co_{0.2}Fe_{0.8}O_{3-δ})

LSGM=Lanthanum Strontium Gallium Magnesium ((La,Sr)(Ga,Mg)O₃)

LSM=Lanthanum Strontium Manganese Oxide (La_{0.6}Sr_{0.4}MnO_{3-δ})

MIEC=Mixed Ionic Electronic Conducting

MCC=Micro-Composite Cathode

NMCC=Nano-Micro-Composite Cathode

OCV=Open Circuit Voltage

PND=Pure Nitrate Derived

 R_P =Cathode Polarization Resistance

 R_s =Oxygen Surface Exchange Resistance

SDC=Samaria Doped Ceria Oxide (Sm_{0.2}Ce_{0.8}O_{1.9})

SEM=Scanning Electron Microscopy

SIMPLE=Simple Infiltrated Microstructure Polarization Loss Estimation

SOFC=Solid Oxide Fuel Cell

SR=Surface Resistance

SSC=Samarium Strontium Cobalt Oxide (Sm_{0.5}Sr_{0.5}CoO_{3-δ})

SSCF=Samarium Strontium Cobalt Iron Oxide (Sm_{0.5}Sr_{0.5}Co_{0.8}Fe_{0.2}O_{3-δ})

TEC=Thermal Expansion Coefficient

TGA=Thermo-Gravimetric Analysis

TPB=Triple Phase Boundary

TXD=Triton X-100 Derived

XRD=X-ray Diffraction

YSB=Yttria Stabilized Bismuth (Y_{0.25}Bi_{0.75}O_{1.5})

YSZ=8 mol% Yttria Stabilized Zirconia ((Y₂O_{3)0.08}(ZrO₂)_{0.92})

CHAPTER 1: Thesis Motivation and Overview

1.1 The World Energy Problem

According to the U.S. Census Bureau, the world population in 2012 was approximately 7 billion people and is projected to continue to increase by approximately 6.5 million people each month on average [11]. According to the Energy Information Administration, world energy consumption for fossil fuels has increased from 354 quadrillion BTUs in 1990 to 505 quadrillion BTUs in 2008 and is projected to increase to 770 quadrillion BTUs by 2035 [12]. This increasing world energy demand stimulates the need for the development of alternative energy sources and/or improved energy conversion devices, such as Solid Oxide Fuel Cells (SOFCs).

1.2 Solid Oxide Fuel Cells as a Solution to the World Energy Problem

As demonstrated in Figure 1.1 [13-15], SOFCs have some of the highest gravimetric and volumetric power densities of any electricity generating technology. SOFCs also have the ability to operate on a variety of fuel types (hydrogen, ethanol, biofuel, gasoline, natural gas, syngas, landfill gas, jet-fuel, etc.) [15, 16]. These benefits provide SOFCs with the capability to both reduce the environmental impacts of today's hydrocarbon based economy while simultaneously developing the infrastructure for a CO₂-neutral economy utilizing biofuels, solar fuels or hydrogen. SOFCs can also be used for: 1) chemical separation, 2) chemical sensing, and 3) energy storage when operated in reverse as Solid Oxide Electrolysis Cells [17-19].

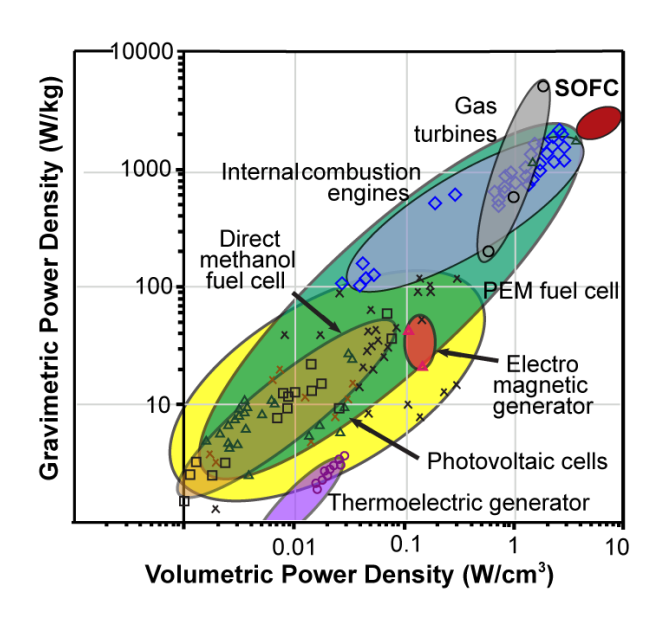


Figure 1.1: Gravimetric and Volumetric Energy Densities for Electricity Generating Devices. Modified from [13-15].

SOFCs demonstrate high electrical conversion efficiencies greater than traditional electricity generating technologies. For example, typical coal-fired electricity generating plants have demonstrated electrical efficiencies around 46% [20] compared to 60% for SOFCs [21, 22]. When both heat and electricity are valued, coal-fired power plants have demonstrated efficiencies near 60% [20], compared to 90% for SOFCs [23, 24]. SOFC efficiencies are also size independent, (a feature not shared by many chemical to electrical conversion devices such as gas turbines), which allows SOFCs to range from 1 Watt to multi-Megawatt [25, 26].

Commercial SOFC devices using traditional macro-porous cathodes typically operate at temperatures above 750°C. However, in the past two decades Nano-Micro-Composite Cathodes (NMCCs) have been shown to increase cathode performance (i.e. lower the polarization resistance, R_P) and/or reduce the SOFC operating temperature compared to traditional Micro-Composite cathodes. In addition, many studies have sought to experimentally improve [5, 27, 28] and/or mathematically model NMCC

performance [5, 29]. Unfortunately, two knowledge gaps are currently preventing additional NMCC performance improvements.

1.3 Solid Oxide Fuel Cell Knowledge Gaps

The first knowledge gap is the inability to control the size of infiltrated Mixed Ionic and Electron Conducting (MIEC) nano-particles [5, 7, 30]. Small MIEC nano-particle diameters allow for increased oxygen exchange into the cathode microstructure due to an increased MIEC surface area to volume ratio. Unfortunately, most infiltrated NMCCs exhibit average particle sizes around 40 nm or greater [5, 7, 30], and previous literature studies have not identified a reliable method to further reduce infiltrated MIEC particle sizes.

The second knowledge gap is an inability to accurately determine intrinsic NMCC MIEC oxygen surface exchange resistance (R_s) values. Previous literature studies have only determined R_s values on thin film and bulk MIEC materials and the surface structure and/or stress state of MIEC infiltrate could be very different. Further, the magnitude of the R_s value reported in these thin film and bulk studies can vary by as much as 3 orders of magnitude for the same material composition [10]. An accurate set of MIEC infiltrate R_s numbers are needed to determine the best MIEC infiltrate material and to perform cathode microstructural optimization (such as that done in Song *et al.* [31]).

1.4 Thesis Overview

This thesis will address these two knowledge gaps. Specifically, Chapter 2 will delve into a literature review of SOFC devices and explore the status of research today. Chapter 3 will address the experimental methods and characterization techniques used to conduct the experiments in this thesis. Chapters 4-7 will illustrate two methods,

desiccation (aka precursor nitrate solution desiccation) and pre-infiltration (aka ceria oxide pre-infiltration), that were developed to systematically control infiltrated MIEC nano-particle size. The effect of organic solution additives and MIEC composition are also explored in these chapters to examine their effect on desiccated and pre-infiltrated particle sizes. Chapter 8 will show infiltrated MIEC R_s determinations made by performing Finite Element Modeling (FEM) on Focused Ion Beam–Scanning Electron Microscopy (FIB-SEM) 3D reconstructed SOFC cathodes. Lastly, Chapter 9 will provide a set of overall conclusions and restate the advances this work has provided to the scientific community.

1.5 Summary

In summary, SOFCs are a promising alternative energy conversion technology because they: 1) have one of the highest gravimetric and volumetric power densities of any electricity generating technology, and 2) have the capability to both reduce environmental impacts of today's hydrocarbon based economy while also one day serving as the infrastructure for a CO_2 -neutral economy utilizing biofuels, solar fuels or hydrogen. Commercialization of this technology is held back by poor performance at low operating temperatures, especially on the cathode side. NMCCs help improve the performance at low operating temperatures but additional performance increases are being restrained by: 1) a lack of control of infiltrate nano-particle size, and 2) a lack of accurate infiltrated MIEC R_s values. The work presented in this thesis advances SOFC technology by addressing these two knowledge gaps.

CHAPTER 2: Literature Review

2.1 Solid Oxide Fuel Cell Overview

Even though SOFC performance improvements have occurred through the use of NMCCs [1, 5] there still exists the need to control infiltrated MIEC nano-particle size and understand the R_s values of infiltrated MIEC materials. As pointed out in Section 1.3 addressing these two limitations will greatly improve SOFC devices by allowing the operating temperature to be lowered, which in turn will limit the performance degradation caused by nano-particle size coarsening.

As shown in Figure 2.1 [32], the cathode is the most resistive component of a traditional LSM-YSZ|YSZ|YSZ-Ni SOFC device (the resistance can be calculated from the slope of each curve and clearly the cathode has the greatest resistance at low and

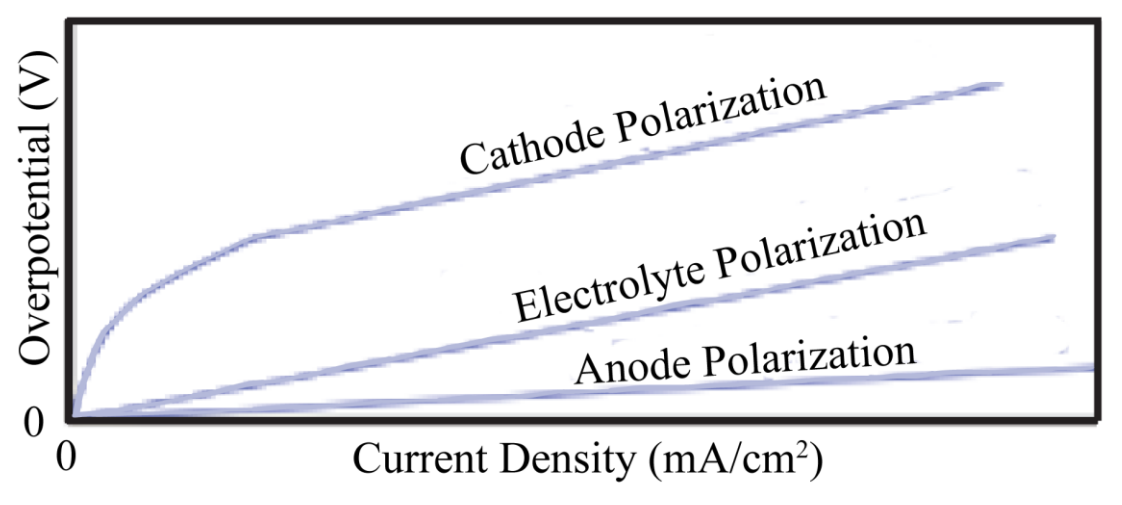


Figure 2.1: Traditional LSM-YSZ/YSZ/YSZ-Ni SOFC Component Overpotential Comparison. Resistance values depicted as the slope of each Polarization curve [32].

moderate currents). The greatest source of resistance in the cathode comes from limitations in oxygen incorporation into the MIEC lattice structure [5, 33]; hence the need for smaller MIEC nano-particles. Further, reliable measurements of the intrinsic oxygen surface exchange resistance process, R_s , of the MIEC infiltrate are needed to

accurately select the best MIEC material to infiltrate, and for SOFC microstructure optimization [31]. This chapter will provide an overview of SOFC operating principles and discuss how infiltrate particle size and infiltrate R_s values play a role in determining SOFC performance.

2.1.1 Solid Oxide Fuel Cell Operating Principles

Figure 2.2 [34] shows the three components of an SOFC, which are the: 1) cathode, 2) electrolyte, and 3) anode. Figure 2.2 also demonstrates the chemical reactions and/or the transport of charged species that take place in each component [34]. The cell shown in Figure 2.2 yielded the performance curves shown in Figure 2.1. At the cathode, oxygen gas is first incorporated into oxygen vacancies located in the MIEC lattice structure and then transported to the anode through the electrolyte. At the anode, the fuel (hydrogen, methane, etc.) rips oxygen out of the anode MIEC crystal structure to form oxygen vacancies, water and electrons.

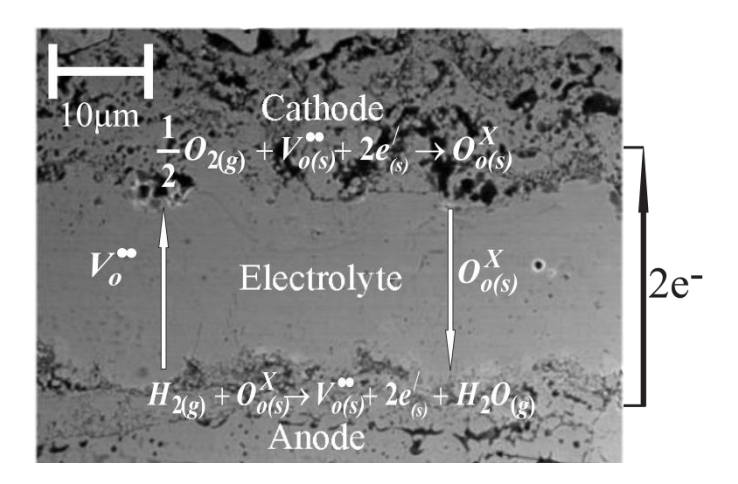


Figure 2.2: Traditional SOFC Cathode and Anode Chemical Reactions. Modified from [34].

The resulting gradient in oxygen vacancies and electrons across the cell drives the flux of these species. An external circuit conducts the electrons (thus creating electricity)

from anode to cathode. The electrolyte acts as a gas barrier and prevents fuel cross-over to the cathode or gaseous O_2 transport to the anode. Operational SOFCs have a thermodynamically determined open circuit voltage (OCV) (which is ~1.2 V at SOFC operating temperatures) [35] and generate power through the flow of electrons shown in Figure 2.2. Note that to balance the reaction, for a given number of electrons to flow through an external circuit, half that number of oxygen vacancies must flow across the electrolyte. Therefore, high rates of oxygen ion transport are critical for the development of high power SOFCs.

Figure 2.3 shows that the SOFC operating voltage (V) can be plotted against the operating current (I) to form an I-V plot, and the power can also be plotted against current to form a power density plot. Both of these plots are useful to help characterize SOFC performance.

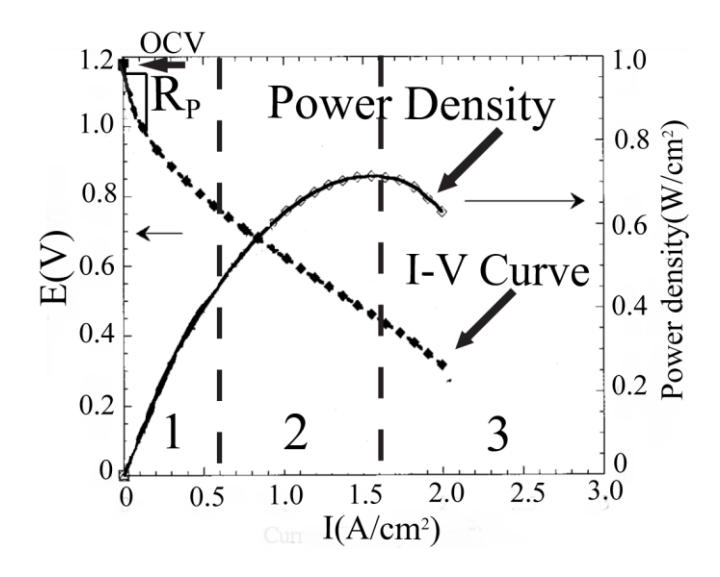


Figure 2.3: Current-Voltage and Power Density Curves for SOFC Devices. Region 1 is below 0.6 A/cm², Region 2 is between 1.6 and 0.6 A/cm² and Region 3 is above 1.6 A/cm² [35].

Figure 2.3 [35] shows the current-voltage (I-V) curve and power density curve for a typical SOFC which provides an idea of how SOFCs operate. The slope of the I-V curve is the sum of all three resistances (cathode, electrolyte and anode). Region 1 is where the electrical losses are dominated by oxygen incorporation into or removal from the cathode or anode lattice structure, respectively. Region 2 is where electrical losses are dominated by ohmic losses (resistances originating from the electrolyte and electrode), and Region 3 is where R_P losses occur due to the current density being so large that the SOFC consumes more oxygen than can diffuse through the pores in the cathode microstructure or hydrogen than can diffuse through the pores in the anode microstructure; a condition referred to as gas-phase polarization. The slope in Region 1 is the sum of the cathode and anode polarization resistances. However, in common SOFCs, this slope reduces to the cathode polarization resistance, R_P , because the cathode performance is so much worse than the anode performance. Hence, Region 1 is where NMCC infiltrate nano-particle size control and an understanding of cathode MIEC R_s values will have the largest impact.

Figure 2.4 shows that SOFCs are not operated at their maximum power densities because as the output power density increases, the cell efficiency decreases [36]. Instead, SOFCs are operated at current densities to the left of the maximum power density value [36]. The cell efficiency is calculated by dividing the cell power by the enthalpy of combustion of the fuel [36].

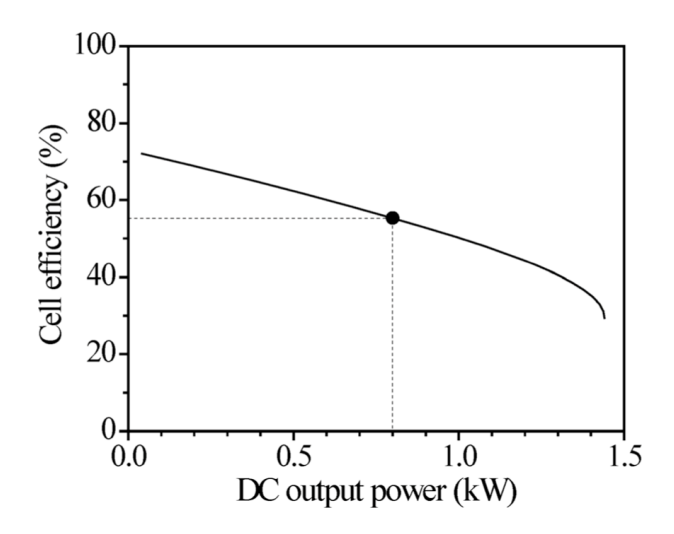


Figure 2.4: **Traditional SOFC Cell Efficiency**. Cell efficiency decreases as power output increases. [36].

One possible approach to lower the cathode R_P and increase SOFC performance is to fabricate NMCCs. A lower R_P value will decrease the initial slope of the I-V curve which also results in an increase in the maximum power obtainable at a given efficiency.

2.1.2 Traditional and Nano-Micro-Composite Cathodes

NMCCs are a type of SOFC cathode that combine materials with low R_s values (MIEC materials) and materials with high ionic conductivity, such as $Gd_{0.1}Ce_{0.9}O_{1.95}$ (GDC) [7] or Y_2O_3 -ZrO₂ (YSZ) [16]. NMCCs are produced by first infiltrating metal nitrate solutions into porous ionic conducting (IC) scaffolds, and then firing the gelled solutions at elevated temperatures to form MIEC oxide nano-particles upon decomposition of the nitrate solutions [5]. The techniques used to fabricate MIEC nanoparticles are described in more detail in Chapters 3-7. Both traditional Micro-Composite Cathodes and NMCCs have interconnected particles which allow electronic and ionic transport, but only NMCCs have nano-scale MIEC particles which allow for increased oxygen incorporation into the MIEC lattice due to an increase in MIEC surface area (shown in Figures 2.5 [37] and 2.6 [7]). Traditional Micro-Composite Cathodes have

MIEC and IC particles sizes that are tens of micrometers in size while NMCCs have particles that are tens of nanometers in size. This small MIEC particle size causes increased catalytic activity [38] resulting in lower cathode operating temperatures (defined here as the cathode operating temperature where R_P values equal $0.1\Omega*cm^2$ [1, 5, 9]).

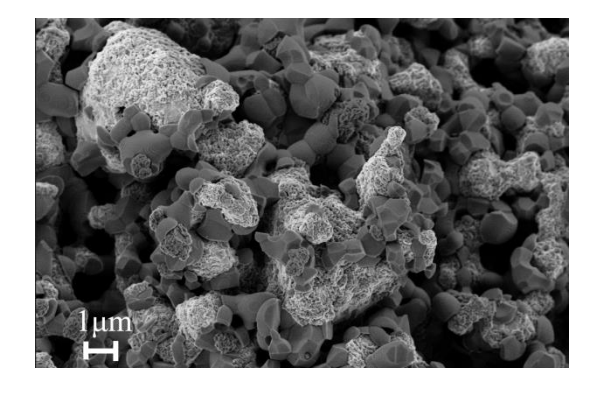


Figure 2.5: Representative Micro-Composite Cathode Microstructure. White components are ionic conducting material is the black component is MIEC material. [37].

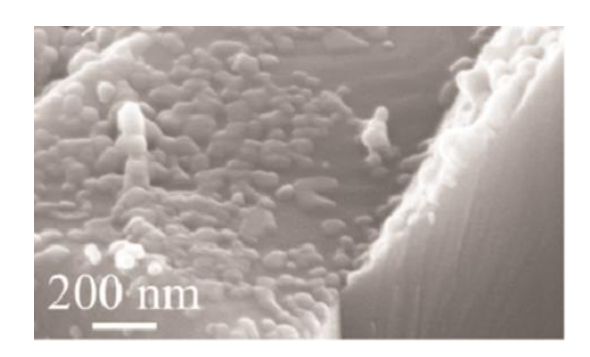


Figure 2.6: Representative Nano-Micro-Composite Cathode Microstructure with Connected MIEC Nano-Particles. Nano-particles are MIEC materials that have been infiltrated [7].

By lowering the operating temperature of NMCCs, MIEC particle coarsening can also be limited. Particle coarsening reduces SOFC performance by decreasing the number of active surface sites for oxygen incorporation into the MIEC lattice structure by decreasing the MIEC surface area to volume ratio. In a NMCC, the low R_S values of the

MIEC infiltrate particles (which facilitates oxygen surface exchange), the high characteristic thickness (L_C) of the MIEC infiltrate particles (which ensures that the oxygen exchange reaction takes place over the entire MIEC infiltrate particle surface), and the high MIEC infiltrate surface area (which provides many locations for the oxygen surface exchange reaction), work together with a high IC scaffold (which facilitates oxygen transport to the electrolyte), and a high MIEC electronic conductivity (which facilitates electron transport to the current collectors) to produce cathodes reported to reach polarization resistances of $0.1 \,\Omega \text{cm}^2$ at temperatures as low as 550°C [1].

2.1.3 Thin Film Cathodes

Thin film SOFC electrodes are another area of research. These electrodes can be used as part of SOFCs or as model electrodes to better understand or measure SOFC material properties. Thin film electrodes are typically dense, single phase, substrate supported films, with thicknesses less than 100 nm. Thin film electrodes can be fabricated through many different approaches such as radio frequency sputtering, DC sputtering, vacuum plasma spraying, pulsed laser deposition [39-45], etc.

Using thin films, material properties such as R_s and the bulk oxygen conductivity can be measured, which has been shown numerous times in the literature using both cathode and anode materials [46-52]. Compared to traditional porous electrodes, the geometry of a thin film is less complex since only a single, dense layer on top of a substrate is present. This allows for easily known surface and cross-sectional areas and hence easy conversion of a measured resistance into area-corrected intrinsic materials properties [53, 54]. For this reason many authors have performed MIEC R_s measurements using thin film micro-electrodes [47, 53, 54]. These thin film R_s

measurements are often performed using the Electrochemical Impedance Spectroscopy (EIS) characterization technique. However, since thin film measurements may not accurately describe the R_s of infiltrated MIEC particles, (due to differences in surface structure, stress states, etc.) further analysis of infiltrated MIEC R_s values is needed. Unfortunately, no studies containing this information have ever been reported in the literature.

2.2 Planar Solid Oxide Fuel Cell Geometric Arrangements

Three different types of SOFCs are described in the literature: 1) cathode supported, 2) anode supported, and 3) electrolyte supported SOFCs. The mechanically supporting layer is typically the thickest (and typically the first to be fabricated).

In cathode supported cells the cathode layer thickness is typically several hundred microns thick, while the anode and electrolyte layers are typically much thinner (\sim 20 nanometers to 100 microns) [55]. Typically cathode supported cells are not used for SOFC devices because increasing the thickness of the cathode layer will not increase the performance of the SOFC due to the active area of the cathode being set to less than \sim 50 microns by the typical MIEC infiltrate R_s and ionic conductivity of the scaffold materials [51].

Anode supported cells have anodes that are much thicker than either the cathode or electrolyte. Like cathode supported cells, these cells have the advantage of using a thinner electrolyte, which minimizes ohmic resistance performance losses [56]. In these cells, the cathode is typically fabricated after the anode and electrolyte, which prevents the cathode materials from seeing the higher fabrication temperatures used in processing the anode and electrolyte. This promotes less coarsening of the cathode MIEC nano-

particles [57, 58] than cathode supported cells. Anode supported SOFCs are typically used for commercial SOFC devices because the anode R_s value is typically much lower (an order of magnitude or lore lower) than cathode R_s values [59, 60] due to increased oxygen exchange in the anode material compared to the cathode material. This means that the electrochemically active region in the anode is larger than the cathode. Since the optimal electrochemically active region is much larger than the cathode, the anode is often made the mechanical support.

Electrolyte supported SOFCs have electrolytes as the thickest component, which are typically hundreds of microns thick [5, 7] as opposed to the cathode or anode electrodes which are thinner [56]. In these cells the electrolyte is typically fabricated first, with the result that any cathode and/or anode nano-particles present do not coarsen significantly in response to a high electrolytic firing temperature. Since the electrolyte is the thickest component it also will have increased ohmic resistance performance losses, preventing their use in commercial SOFCs. However, electrolyte supported SOFCs are often used in laboratory experiments when electrode performance, not total SPFC performance is of interest [5, 7, 61].

2.3 Commonly Used Solid Oxide Fuel Cell Materials

Chapter 1 pointed out that one key knowledge gap was a lack of understanding of the infiltrated MIEC R_s values for the cathode. In fact, because of this knowledge gap, the SOFC community has no clear consensus on which material makes the best MIEC cathode infiltrate (cathode microstructural effects make it difficult to judge MIEC performance from the cathode R_P). Since this thesis focuses on improving the cathode

performance, the following sections discuss the various MIEC and IC materials found in literature and their roles in improving NMCC performance.

2.3.1 Ionic Conductors

For the electrolyte there currently exist a number of materials used to promote bulk oxygen transport from the cathode to the anode, including: 1) Bi₂V_{0.9}Cu_{0.1}O_{5.35} (BICVOX) [62], 2) Ce_{0.9}Gd_{0.1}O_{1.95} (GDC) [7], 3) La_{0.9}Sr_{0.1}Ga_{0.8}Mg_{0.2}O_{2.85} (LSGM) [63], 4) Sc₂O₃-ZrO₂ (ScSZ) [64], and 5) (ZrO₂)_{0.9}(Y₂O₃)_{0.1} (YSZ) [65]. Due to its combination of high ionic conductivity and chemical compatibility with most MIEC materials, doped ceria is commonly used as an ionic conductor in SOFC cathodes [66].

2.3.2 Electronic Conductors

Typically a layer is applied on top of the electrode, named the current collection layer. This high electronic conductivity layer promotes a uniform flow of electrons across the entire electrode surface. Commonly used current collector materials include: La_{0.6}Sr_{0.4}TiO_{3-x} (LST) [67, 68], and La_{0.8}Sr_{0.2}MnO_{3-x} (LSM) [5].

2.3.3 Mixed Ionic Electronic Conductors

Section 2.1.1 showed that oxygen in an SOFC is exchanged from the gas phase into the oxygen vacancies in the MIEC lattice structure in the cathode, and is then transported through the electrolyte to the anode. Currently a number of different MIEC materials have been used as cathodes or infiltrated into cathode microstructures to promote oxygen incorporation. The most commonly used MIEC materials include: La_{0.6}Sr_{0.4}FeO_{3-x} (LSF), La_{0.6}Sr_{0.4}Co_{0.2}Fe_{0.8}O_{3-x} (LSFC), La_{0.6}Sr_{0.4}Co_{0.8}Fe_{0.2}O_{3-x} (LSCF), La_{0.6}Sr_{0.4}CoO_{3-x} (LSC), Ba_{0.5}Sr_{0.5}Co_{0.8}Fe_{0.2}O_{3-x} (BSCF), and Sm_{0.5}Sr_{0.5}CoO_{3-x} (SSC) [54].

2.4 Composite Solid Oxide Fuel Cell Cathode Geometries

Section 2.2 discussed that there are a number of SOFC geometries. However, there are also a number of cathode geometries as well. The following are different cathode geometries that exist in literature which utilize different MIEC and ionic conducting materials. The cathode scaffold (into which the infiltrate precursor solutions are infiltrated and to which the MIEC particles cling) can be manufactured from either: 1) electronic conducting materials (such as La_{0.6}Sr_{0.4}MnO_{3-δ}) infiltrated with an ionic conducting material, 2) ionic conducting materials (such as Yttria Stabilized Zirconia) infiltrated with electronic conducting or mixed-conducting materials (which all have >99% of the conductivity resulting from the transfer of electronic, not ionic, species), or 3) mixed-conducting materials (such as La_{0.6}Sr_{0.4}Co_{0.8}Fe_{0.2}O_{3-δ}) and infiltrated with electronic, ionic or mixed-conducting materials.

A composite cathode allows for the combination of multiple materials that each do something well, so the entire cathode can benefit from both materials. As shown in Figure 2.2, electrons, oxygen vacancies, and oxygen gas must all be transported to support the cathode reaction. For instance, in the composite cathode of Figure 2.6, the MIEC material nano-particles transports electrons and incorporates oxygen gas into the MIEC lattice structure, while the GDC ionic conducting scaffold material transports the oxygen vacancies through the scaffold.

2.4.1 Electronic Conducting Scaffolds

Cathodes fabricated using an electronic conducting scaffold typically utilize LSM screen printed onto an ionic conducting electrolyte pellet (such as YSZ) and fired to form a porous electrode [69-71]. Ionic materials are then typically infiltrated into the porous

electrode to form nano-particles on the electronic conducting surface [69-71]. An advantage of an electronic conducting scaffold is that it facilitates oxygen incorporation into the ionic conductor at the triple-phase-boundary where the gas, electronic conductor and ionic conductors all meet, and has a high electronic conductivity. The infiltration of electronic or mixed-conducting nano-particles into the electronic scaffold is typically not performed because, as discussed in Section 2.3, both materials have low ionic conductivity [72] and hence no path would exist in the cathode for ionic conduction from the cathode to the electrolyte. Another disadvantages of using electronic conducting scaffolds is that there is the problem of thermal expansion mismatch between the electronic conducting scaffold and the electrolyte material, which, if different enough, cause cracks to form and damage cell performance [28]. Since the scaffold material has a low R_s value and high electronic conductivity, but a low ionic conductivity, these reasons make electronic conducting scaffolds a poor choice to use for the SOFC cathode geometry.

2.4.2 Mixed Ionic Electronic Conducting Scaffolds

Cathodes with MIEC conducting scaffolds are typically made by screen printing an MIEC layer onto an ionic conducting electrolyte and firing the cell to form a porous MIEC electrode [73, 74]. An electronic conducting, ionic conducting or mixed-conducting material is then infiltrated onto the mixed-conducting scaffold surface. MIEC scaffolds have the advantage of high electronic conductivity, low R_s values, but unfortunately have an ionic conductivity much lower than IC scaffolds such as GDC [66, 72].

There are two disadvantages to using a mixed-ionic electronic conducting scaffold geometry. The first is that there can be a thermal expansion mismatch between the MIEC scaffold and the IC electrolyte material, which, if large enough, can cause cracks to form and reduce the cell performance. MIEC thermal expansion coefficients (for temperatures between 30-1000°C) are between ~17.5*10⁻⁶ K⁻¹ (LSFC) [72], and ~25*10⁻⁶ K⁻¹ (LSC) [72], while the thermal expansion coefficient of IC scaffold materials (for temperatures between 30-1000°C) are between ~10*10⁻⁶ K⁻¹ (GDC) [75] and ~13*10⁻⁶ K⁻¹ (GDC). The second disadvantage is that the oxygen ion diffusion through all of today's MIEC materials is much lower than traditional IC materials such as YSZ or GDC. This means that IC materials must be infiltrated into the MIEC scaffold to transport oxygen to the electrolyte. Unfortunately this reduces the MIEC surface area available for oxygen exchange.

2.4.3 Ionic Conducting Scaffolds

Cathodes IC scaffolds are typically made by screen printing an ionic conducting layer onto an ionic conducting electrolyte and firing the cell to form a porous IC electrode [5, 61]. An electronic conducting (such as La_{0.6}Sr_{0.4}MnO_{3-δ}) [76] or mixed-conducting (such as La_{0.6}Sr_{0.4}Co_{0.8}Fe_{0.2}O_{3-δ} or Sm_{0.5}Sr_{0.5}CoO_{3-δ}) [5, 61] material are then typically infiltrated into the ionic conducting scaffold structure. The advantage of infiltrating an MIEC into an IC scaffold is that the oxygen incorporation reaction into the lattice structure is spread over the entire MIEC surface and not just limited to the triple phase boundary [7]. Another advantage to using an ionic conducting scaffold is that there is no thermal expansion mismatch between the scaffold and electrolyte (assuming

the same IC material is used for both) [28]. Hence MIEC infiltrated IC scaffolds were examined in this these.

2.5 Models Identifying the Parameters Controlling Nano-Micro-Composite Cathode Performance

Since oxygen surface exchange into the cathode typically limits overall performance [5, 77], being able to reduce infiltrate oxide nano-particle size is very important to ultimately achieve lower R_P values at lower operating temperatures. In addition, being able to model the impact that different parameters (such as R_s values, infiltrate nano-particle size, the scaffold ionic conductivity, the cathode thickness, the cathode porosity, etc.) have on cathode performance is also important. Two of the most widely used MIEC on IC NMCC performance models in the literature are the Surface Resistance (SR) model [5, 7, 61], and Simple Infiltration Microstructure Polarization Loss Estimation (SIMPLE) model, [5, 7, 61, 78]. Both models quantify the performance increases possible by varying infiltrated nano-particle size and infiltrate MIEC R_s values, but the SIMPLE model also partially accounts for IC scaffold effects.

2.5.1 The Surface Resistance Model

The Surface Resistance (SR) model predicts the SOFC cathode performance using the equation:

$$R_P = \frac{R_s A_G}{A_{lnf}} \tag{1}$$

where R_P is the polarization resistance of the cathode, R_s is the intrinsic MIEC oxygen surface exchange resistance, A_G is the geometric area(i.e. footprint) of the cathode, and A_{Inf} is the surface area of the MIEC infiltrate particles [7]. The SR model ignores any

resistance caused by the ionic conducting scaffold, assuming instead that the R_P is just linearly related to the MIEC R_S and the MIEC surface area in a specific unit of cathode. Oftentimes this is a good assumption because: 1) the R_S for oxygen incorporation into the IC scaffold is typically much higher than the R_S of the MIEC material (meaning that oxygen exchange directly into the IC scaffold is limited), and 2) the resistance associated with bulk transport through the IC scaffold is typically low. That said, as the operating temperature increases, the SR model deviates more from the experimental results because the IC ionic transport resistance starts to become a larger contributor to the R_P value. Due to the fact that only the oxygen surface resistance is accounted for, literature studies have shown that this model is typically not as effective as the SIMPLE Model at accurately predicting cathode performance values [7].

2.5.2 The Simple Infiltration Microstructure Polarization Loss Estimation Model

The SIMPLE model takes into account both the surface resistance of oxygen incorporation into the MIEC lattice and the bulk resistance of oxygen transport to the electrolyte material. The SIMPLE Model is also "simple" in that it is an analytical expression that can be evaluated quickly (in contrast to the more rigorous finite element modeling methods), and can typically predict the R_P values of cathodes made from today's best performing materials to within 33% of experimentally measured values [7].

Figure 2.7 [7] depicts the approximated SOFC NMCC microstructure geometry used to predict the overall R_P value of NMCCs using the SIMPLE model. The actual

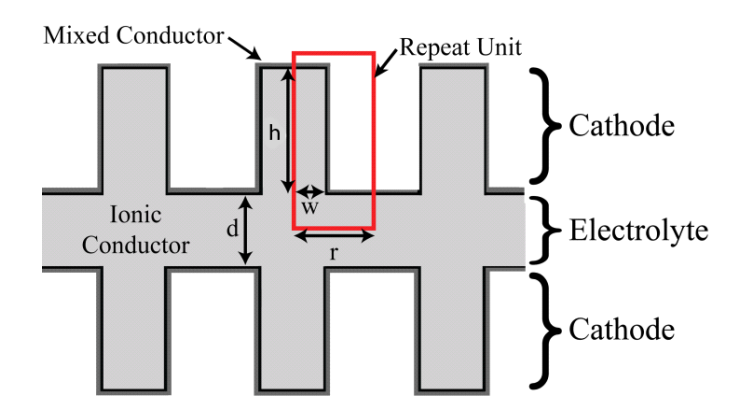


Figure 2.7: SOFC SIMPLE Model Approximated Geometry. SIMPLE model approximated geometry is for a symmetrical cell that contains two cathodes in this example [7].

microstructure of a NMCC is complex, but here it is modeled as a symmetrical NMCC with repeating unit cell columns. Symmetrical cells are NMCCs that have both scaffold microstructures fabricated as if they were cathodes on each side of a mechanicallysupporting electrolyte. The benefit of experimentally testing symmetrical cells, instead of a whole SOFC, is that the individual open-circuit electrode performance values, such as each cathode, can be obtained by dividing the total measured electrode response by 2. In the SIMPLE model, the cathode thickness is L, the column within the unit cell is w, the unit cell width is r, and the electrolyte thickness is d, as labeled in Figure 2.7. The SIMPLE mode assumes that the surface of each IC column is heavily coated with an MIEC electrocatalyst infiltrate which has an R_s value associated with the MIEC material's ability to incorporate oxygen into its lattice structure. Having the MIEC heavily infiltrated onto the surface of the electrode also promotes electronic contact within the current collector, helping ensure that all the MIEC particles are electrochemically active. This, coupled with the high electronic conductivity of the MIEC infiltrate and the low current (i.e. open-circuit) conditions, also place each infiltrate particle surface (i.e. every MIEC-gas interface) at the same electrochemical

potential. The SIMPLE model is derived from the Tanner, Fung, and Virkar (TFV) model for Micro-Composite Cathodes. The difference is that the SIMPLE mode correctly accounts for the surface area ratio between the MIEC and the IC; which is close to 1, and can therefore be ignored in a nano-composite cathode but often greater than 2 in a NMCC. The SIMPLE model does this by mathematically spreading the R_s value across the entire IC scaffold [33]. By using microstructural parameters from Figure 2.7 (such as cathode thickness, MIEC infiltrate nano-particle size, IC scaffold ionic conductivity, etc.), and intrinsic material properties (MIEC infiltrate R_s and IC scaffold ionic conductivity), the SIMPLE model provides an estimate of the NMCC R_p value using the equation:

$$R_{p}(T) = \frac{r\left[\frac{R_{s}(T)A_{sc}}{A_{lnf}}\right]}{\left[\frac{1+\beta(T)}{1+\beta(T)\exp\left(\frac{-2h}{\alpha(T)}\right)}\right]r(1-p)\exp\left(\frac{-h}{\alpha(T)}\right) + \left[\frac{1+\beta(T)\exp\left(\frac{-h}{\alpha(T)}\right)}{1+\beta(T)\exp\left(\frac{-2h}{\alpha(T)}\right)}\right]\alpha(T)\left[1-\exp\left(\frac{-h}{\alpha(T)}\right)\right] + pr}$$
[2]

where:

$$\alpha(T) = \sqrt{\sigma_{O^{2-}}(T)r(1-p)\left[\frac{R_s(T)A_{Sc}}{A_{Inf}}\right]},$$
 [3]

$$\beta(T) = \frac{\sigma_{o^{2-}}(T) \left[\frac{R_s(T) A_{Sc}}{A_{Inf}} \right] - \alpha(T)}{\sigma_{o^{2-}}(T) \left[\frac{R_s(T) A_{Sc}}{A_{Inf}} \right] + \alpha(T)}$$
[4]

 R_s is the effective oxygen surface exchange resistance, A_{Sc} is the surface area of the IC scaffold, A_{Inf} is the surface area of the infiltrated MIEC material, r is the repeat unit

thickness, h is the height of the repeating unit cell, σ_{o2} is the IC scaffold oxygen conductivity, and p is the non-infiltrated scaffold porosity. The SIMPLE Model has been compared to experimental data from NMCCs with varying MIEC infiltrate loading levels [7, 8], cathode thicknesses [7] and MIEC materials [5]. In all cases the results to date indicate that the SIMPLE Model is capable of accurately predicting R_P values for the NMCC microstructures and materials combinations used today to within an order of magnitude. A complete derivation of the SIMPLE model is included in Appendix 1 of this thesis.

As shown in Equations 1-4, both the SR limit and the SIMPLE model indicate that the cathode R_P drops (i.e. cathode performance increases) as the MIEC surface area (A_{inf}) increases and the R_s value decreases. Unfortunately, as discussed in the next section, experimental methods to increase A_{inf} by reducing MIEC nano-particle size and precisely determined infiltrated R_s values are presently lacking in the literature.

2.6 Infiltrate Particle Size is Difficult to Control According to the Literature

Figure 2.8 shows nano-particle sizes for a number of literature studies using SSC, LSCF, and LSFC [5, 7-9, 30]. Each set of literature studies for a given material was processed in exactly the same manner, yet reported a large range in average nano-particle size. The SSC nano-particles were produced using a 10°C/min firing ramp rate, an 800°C firing temperature, a 1 hr hold time at 800°C, a 12.0 vol% MIEC loading level, and a 0.5 molar precursor solution. The LSCF and LSFC nano-particles were produced using a 5°C/min firing ramp rate, an 800°C firing temperature, a 1-2 hr hold time at 800°C, a 12.0 vol% MIEC loading level, and a ~0.5 molar precursor solution. The

different literature studies also used different solution additives such as Triton X, Citric Acid, or a lack of solution additives (i.e. Pure Nitrate). As shown in Figure 2.8, there appears to be a lack of control in infiltrated nano-particle size for particles 40 nm and larger, and an inability to produce MIEC infiltrate particles with average sizes less than 40 nm, which may be partly the result of different solution additives used in the literature studies. That being said, some studies have reported MIEC particle sizes less than 15 nm [79, 80], but the process variables necessary to achieve this have not been clearly identified or understood.

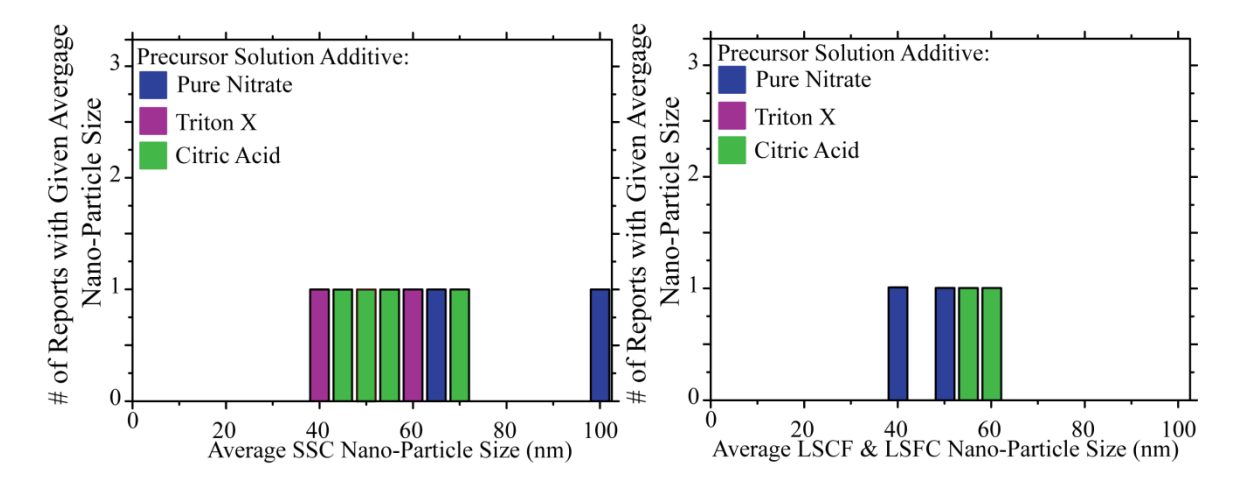


Figure 2.8: Infiltrated MIEC Nano-Particle Size for SSC, LSCF, and LSFC. Colors indicate which solution additives were used in each literature study for easy comparison [5], [7-9], [30].

The following sections will discuss in greater detail the different fabrication techniques used in the literature to reduce MIEC infiltrate particle size and improve performance.

2.6.1 Fabrication Techniques that Reduce Particle Size

The addition of an additive to the precursor solution has been shown in literature to reduce infiltrate particle size and improve performance. Solution additives (Surfactants, Chelating agent, etc.) are typically used to prevent the precipitation of

individual nitrate cations from the precursor solution [5, 7]. However, Nicholas *et al.* [5] have shown SSC nano-particle size also is reduced when using Triton X-100 as compared to not using a solution additive. Nicholas *et al.* [5] have also shown that not all solution additives reduce nano-particle size. For example, SSC made with Citric Acid had similar nano-particle size when compared to not using a solution additive. The mechanism behind these nano-particle size reductions using solution additives may be described by the synthesis method Evaporation-Induced Self-Assembly (EISA). The EISA synthesis method has been documented in multiple literature studies and has been shown to result in the reduction of nano-particle sizes [81-86]. EISA was initially used to create micro and meso-porous silica nano-particles which were ordered [87]. The EISA method takes advantage of the fact that solution additives generate templates (such as micelles for surfactants) as the solution there are in becomes evaporated [88]. Thermal decomposition is then used to remove the additive template and to form continuous nano-oxide particles with a high level of porosity [89].

Alternatively, increasing the heating rate of the thermal decomposition of the precursor solutions has been shown in literature [1] to decrease the average size of MIEC oxide particles formed. Zhao *et al.* [1] also showed that the performance of their SOFC cells increased as a result of reduced infiltrate nano-particle size as a result of the increased heating rate.

Overall, the connection between solution additives, the water content in the gelled precursor solutions, and infiltrate MIEC nano-particle oxide sizes suggested by the literature [79, 80] matches other studies using different material compositions demonstrating that 1) the EISA method with organic solution additives is capable of

controlling the nano-particle size, geometry, and template arrangement produced from thermally decomposition gels [85, 89], and 2) that the water content in precursor gels can have a large effect on the oxide nano-particle size resulting from this process [84, 90].

2.6.2 Fabrication Techniques that Have No Impact on Particle Size Reduction

The amount of MIEC precursor solution infiltrated into a porous IC scaffold can easily be adjusted by increasing or decreasing the volume of each infiltration. Literature studies have shown that increasing or decreasing the volume of MIEC precursor solution has little to no effect on the average MIEC infiltrate particle size and the resulting cathode performance [5, 7]. The molarity of the MIEC precursor solution infiltrated into the porous IC scaffold can also be changed by increasing or decreasing the amount of water used in the solution. Literature studies have also shown that the precursor solution molarity has little to no effect on the average MIEC oxide nano-particle size and the resulting cathode performance [5].

Therefore, the first objective of this thesis is to investigate how and why several processing variables can be used to reduce MIEC infiltrate particle sizes. The second objective of this thesis is to obtain MIEC infiltrate R_s values for the first time. As background, the next part of Chapter 2 will discuss common approaches used to measure R_s values for different infiltrate MIEC materials.

2.7 Literature Oxygen Surface Exchange Resistance Measurement Techniques

As discussed at the end of Section 2.5.2, measuring the R_s values for various MIEC materials is crucial for gauging whether a material will be a good choice when used in NMCCs. A smaller R_s value indicates that the material has a lower resistance for

exchanging oxygen into its lattice structure and would therefore lower overall SOFC resistance and/or SOFC operating temperatures if it were employed in a NMCC. The following measurement techniques are typically used to determine R_s values found in the literature: 1) thin film EIS measurements, 2) R_s conversions from k_o measurements, and 3) R_s conversions from k_{chem} measurements. R_s values determined through these three techniques can then be input into the active models such as the SR and SIMPLE models to predict NMCC performance.

2.7.1 Oxygen Surface Exchange Resistance from Thin Film Electrochemical Impedance Spectroscopy

The R_s value is often measured in literature using the EIS characterization technique [47, 54]. In this method a thin film (described in Section 2.1.3) of a MIEC material is typically deposited onto a substrate (such as YSZ or GDC), and an AC signal is passed through the thin film at various frequencies (typically between 10^5 and 10^{-1} Hz). This process is repeated over a wide range of temperatures to understand how the R_s value of each MIEC material varies as a function of temperature. R_s values are typically extracted from electrochemical impedance spectroscopy using Nyquist plots produced by plotting the real (x-axis) and imaginary (y-axis) components of each frequency impedance data point. As shown in Figure 2.9, multiple arcs may be present in an impedance spectra, but once the arc related to MIEC oxygen surface exchange is identified, the distance between the two x-axis intercepts multiplied by the electrode area can be used to extract the R_s value [47].

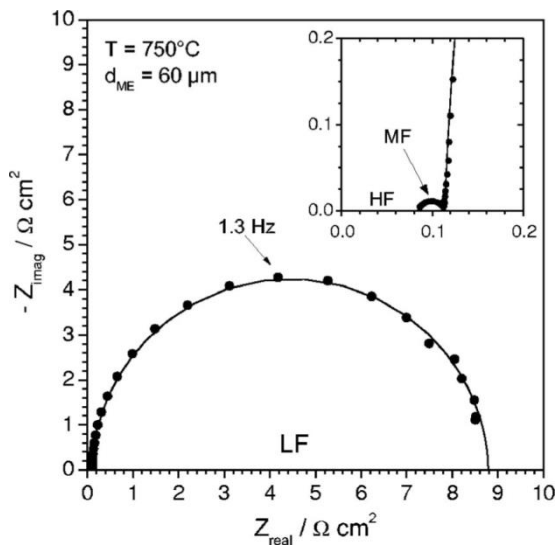


Figure 2.9: **SOFC LSCF** R_s Measurement using Electrochemical Impedance Spectroscopy. The Electrochemical Impedance plot is depicted as a Nyquist plot in this example [47].

Oftentimes, identification and fitting of the AC arc corresponding to oxygen surface exchange is facilitated by equivalent circuit modeling [59, 91-94]. Figure 2.10 [59, 91-94] shows an equivalent circuit commonly used in the literature to describe the physical processes involved in a NMCC. Figure 2.10 shows three resistive processes: 1) resistance through the bulk (R_b) , 2) resistance through an interfacial layer between the MIEC and the IC scaffold (R_i) , and 3) the oxygen surface exchange resistance in the MIEC material (R_s) . Because they occur across interfaces the R_i and R_s processes also have capacitance values. Each process is assumed to be independent of each other, which is why the R_b , R_i , and R_s RC elements are shown in series in Figure 2.10.

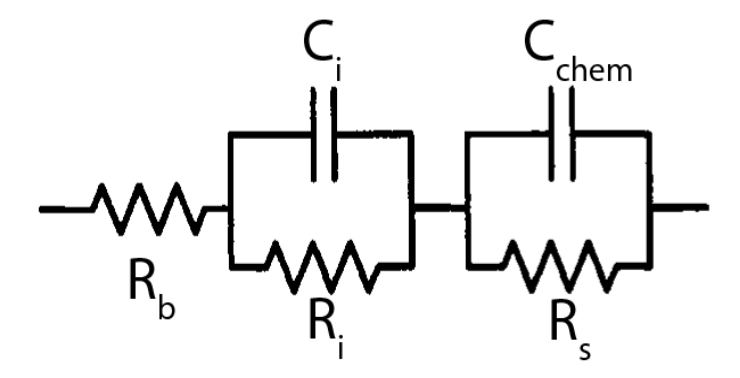


Figure 2.10: Typical Nano-Micro-Composite Cathode Equivalent Circuit Model. This example depicts three resistive processes in series, where two resistive processes have capacitance elements [59], [91-94]

The equivalent circuit has been used to determine R_s values in Figure 2.10 [59, 91-94] and can be depicted mathematically described by:

$$Z = R_b + \left\lceil \frac{R_i}{1 + j\omega R_i C_i} \right\rceil + \left\lceil \frac{R_s}{1 + j\omega R_s C_{chem}} \right\rceil$$
 [5]

where Z is the total calculated impedance ("AC resistance"), R_b is the resistance for the electrolyte, R_i is the resistance for either the ionic bulk transport through the IC scaffold or the interfacial resistance between the IC scaffold and the MIEC lattice, R_s is the resistance for oxygen surface exchange into the MIEC lattice structure, C_i is the capacitance for the ionic bulk transport through the IC scaffold or the interfacial capacitance between the IC scaffold and the MIEC lattice, C_{chem} is capacitance for the oxygen surface exchange into the MIEC lattice structure, ω is the frequency, and j is the imaginary component of the equation. Fitting the equivalent circuit model to experimentally determined EIS results allows for the different resistance values to be determined. In the literature, fitting the equivalent circuit is typically accomplished by

adjusting the R_b , R_i , and R_s values (and the capacitance values too) in Equation 5 so the resulting impedance arcs match the experimental data.

2.7.3 Oxygen Surface Resistance from Chemical Rate Constant Measurements

 R_s values can be converted from chemical rate constant values, (k_o or k_{chem}) found in the literature. The difference between k_o and k_{chem} is that k_o is only dependent on the diffusion of oxygen vacancy species through the material, while k_{chem} is dependent on the combined ambipolar diffusion of oxygen vacancies and electrons through the material. The relationship between R_s and k_o is described as:

$$R_S = \frac{k_b T}{4e^2 k_o C_o} \tag{6}$$

where k_b is the Boltzmann constant, T is temperature (K), e is the elementary charge, C_o is the concentration of oxygen in the MIEC lattice structure, and k_o is the chemical rate constant through the bulk [10]. If the k_{chem} value is provided in literature, then k_o can be determined from k_{chem} and k_o can be determined using Equation 5. The relationship between k_{chem} and k_o is described as:

$$k_{chem} = k_o \gamma$$
 [7]

where γ is the thermodynamic factor (which is determined by dividing the derivative of the natural log oxygen partial pressure of the equilibrium gas by the derivative of the natural log of the oxide concentration in the MIEC material) [95].

Figure 2.11 shows the literature-reported concentration of oxygen in the MIEC lattice structure [50, 54, 95-98] as a function of temperature for the MIEC materials LSF, LSFC, LSCF, LSC, SSC and BSCF. All these materials increase the amount of oxygen in the MIEC lattice structure as the temperature increases except for SSC, which stays constant. (The fact that SSC has constant oxygen concentrations with respect to temperature may indicate that this material is operating in the extrinsic regime). Figure 2.11 also shows the thermodynamic factor, γ , for the different cathode MIEC materials as a function of temperature [48, 95, 97-99]. These C_o and γ values were all used in Equations 6 and 7 to calculate R_s from k_{chem} , and k_o .

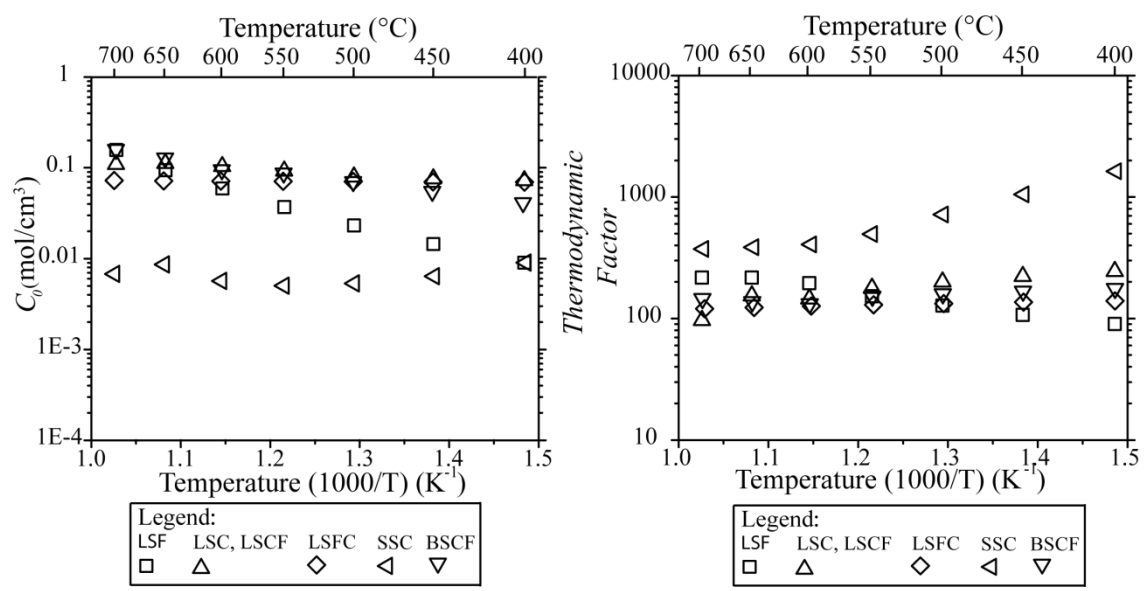


Figure 2.11: Oxygen Concentration and Thermodynamic Factor Values for LSF, LSFC, LSCF, LSC, SSC and BSCF in Air Reported in Literature Studies. The oxygen concentration values [50], [54], [95-98] are shown on the left and the thermodynamic factor values are shown on the right [48], [95], [97-99].

Due to literature sources typically only reporting k_{chem} or k_o values, C_o and γ values from multiple literature studies were used to convert k_{chem} or k_o values into R_s values. This may not be completely legitimate since differences in sample preparation, surface structure, grain size, stress state, etc. could lead to different k, C_o and γ values between samples with the same composition. The uncertainty introduced by the need to

mix study results produces an additional incentive to directly measure the R_s values of MIEC infiltrate particles.

Figure 2.12 shows both k_{chem} and k_o values for some typical MIEC materials found in literature [48-51, 54, 95-102]. These values were determined from EIS

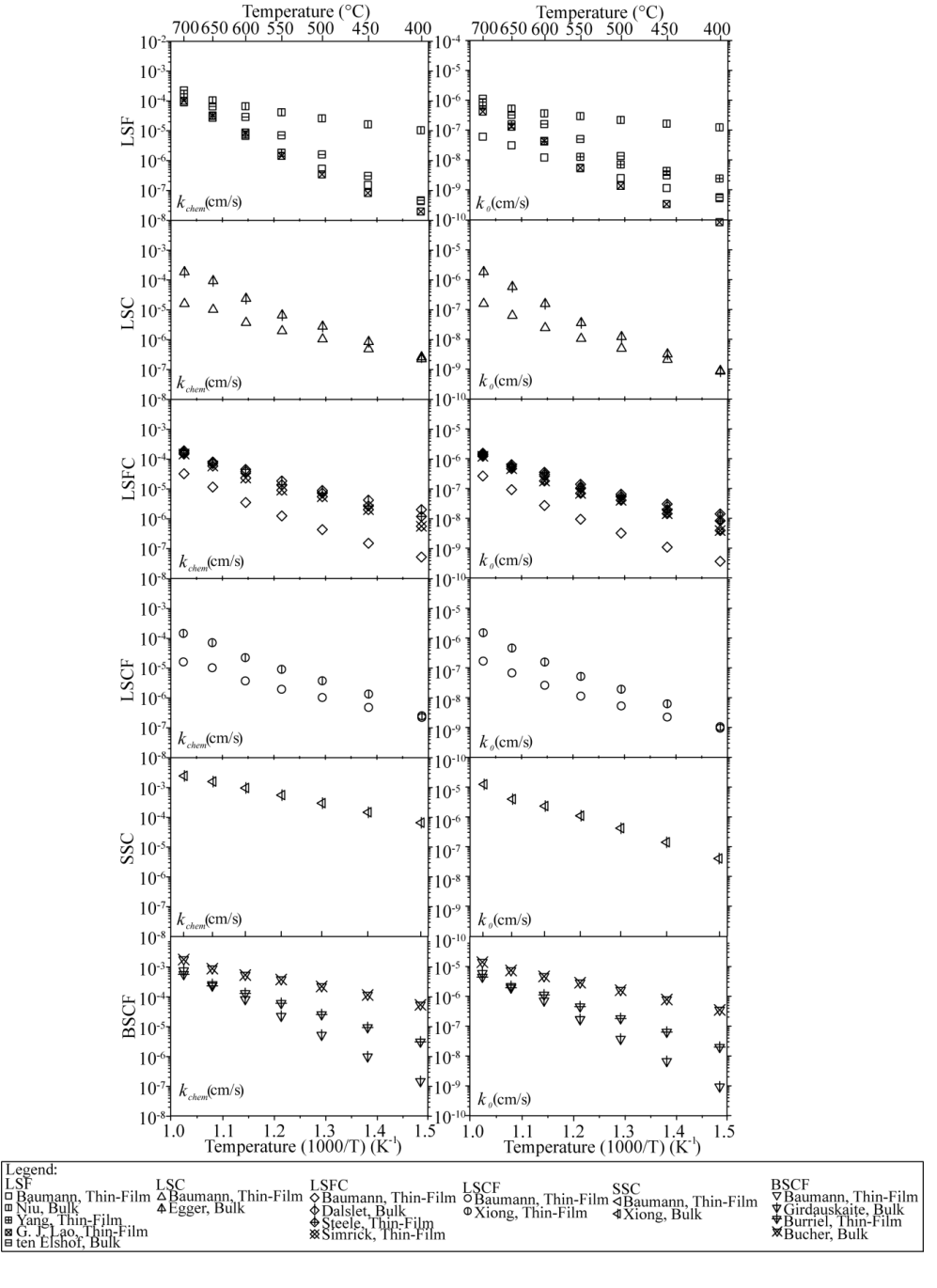


Figure 2.12: k_{chem} and k_o Values Reported in Literature for the Cathode MIEC Materials LSF, LSFC, LSCF, LSC, SSC, and BSCF. Literature study authors are listed in the legend [48-51], [54], [95-102].

measurements or were converted using Equations 6 and/or 7. The values shown in Figure 2.12 vary in magnitude between reports within a single material, for unknown reasons, which also promotes large variations in the R_s value.

2.8 Large Uncertainties Exist in the R_s Value of Even the Most Common Mixed Ionic Electronic Conducting Materials

Figure 2.13 shows R_s values for several common MIEC materials (with a lower R_s value promoting more oxygen incorporation) [10, 48-51, 54, 95-97, 99-102]. The values shown in Figure 2.13 were determined using: 1) EIS, 2) R_s conversion from k_o values, or 3) R_s conversion from k_{chem} values. As shown in Figure 2.13, some MIEC materials have reported R_s values that range by as much as 3 orders in magnitude. This inconsistency in R_s values within the same material composition demonstrates the need to understand where infiltrated MIEC R_s values lie in comparison to the bulk and thin film R_s literature values in Figure 2.13. R_s values determined from EIS measurements were from Baumann (LSF, LSFC, LSCF, LSC, SSC, and BSCF), Niu (LSF), Egger (LSC), and Xiong (LSCF). R_s values converted from k_{chem} or k_o values were from Yang (LSF), G.J. La O' (LSF), ten Elshof (LSF), Dalslet (LSFC), Steele (LSFC), Simrick (LSFC), Yeh (SSC), Girdauskaite (BSCF), Burriel (BSCF), and Bucher (BSCF)

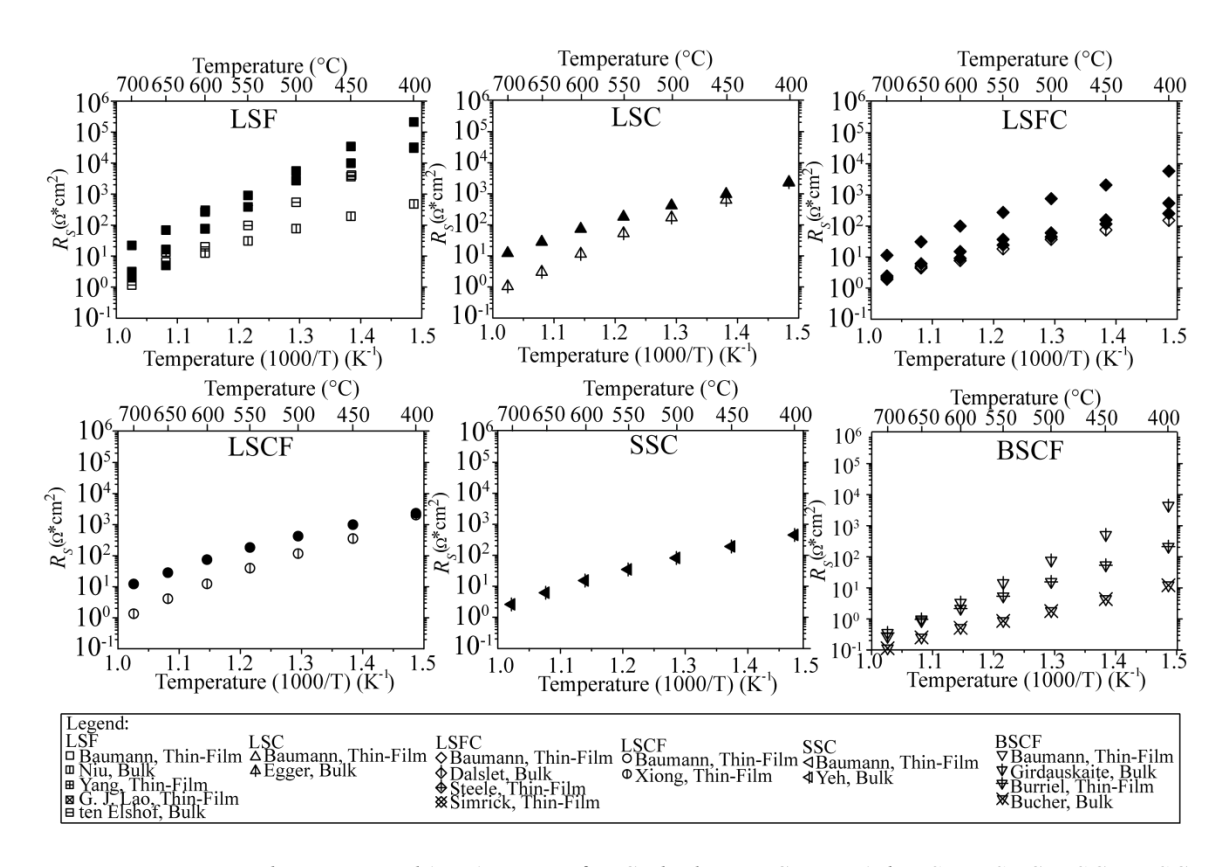


Figure 2.13: R_s, Values Reported in Literature for Cathode MIEC Materials LSF, LSFC, LSCF, LSC, SSC, and BSCF. Literature study authors are listed in the legend[10], [48-51], [54], [95-97], [99-102].

2.9 Summary

In summary, previous literature studies have shown that SOFCs have had their performance improved through the use of NMCCs. Cathode, electrolyte and anode supported SOFCs are have been used previously in literature. The NMCC itself can also use different combinations of ionic conducting, electronic conducting, or mixed-conducting scaffolds and infiltrate materials. Despite the performance advances in SOFCs made possible through the use of NMCCs, there exist two knowledge gaps that previous literature studies have not adequately addressed: 1) controlling NMCC infiltrate MIEC nano-particle size, and 2) accurately determining the R_s values for MIEC infiltrate materials. The first knowledge gap (lack of infiltrate particle size control) needs to be filled to increase cathode performance at operating lower temperatures. The second

knowledge gap (accurate determination of infiltrate MIEC R_s values) need to be filled to improve cathode performance at lower operating temperatures, and provide the scientific community useful knowledge which MIEC material is the best to use.

CHAPTER 3: Experimental Methods

3.1 Symmetrical Cathode Fabrication Processes

Since SOFC electrode performance and not entire SOFC performance was the objective of this thesis, for the reasons described in Section 2.2, electrolyte supported cells were used here to explore the impact of processing conditions on NMCC performance and infiltrate particle size. Although specific sample fabrication details can be found in later chapters, this section provides an overview of the NMCC fabrication process.

3.1.1 Cathode-Electrolyte-Cathode Symmetric Cell Production

Dense SOFC electrolytes can be fabricated through a number of approaches including dry pressing and firing [103, 104], chemical vapor deposition [105, 106], electrochemical vapor deposition [107, 108], spray pyrolysis [109, 110], pulsed laser deposition [111, 112], 6) sputtering [113, 114], etc. Here, electrolyte-supported cells were prepared first by pressing GDC powder in a steel die using a uniaxial press, shown in Figure 3.1 [115], to form a porous cylindrical pellet. The resulting porous pellet was sintered at temperatures close to 1450°C and then cooled to room temperature to produce pellets with relative densities >95%. Lastly, the top and bottom of these cylindrical pellets were sanded flat and parallel, first using 240 grit SiC sandpaper and then 600 grit SiC to obtain final thickness values ranging from 430 to 480 μm, which promotes a uniform electrode thickness.



Figure 3.1: Uniaxial Press Device. Uniaxial press used to produce green strength electrolyte samples [115].

3.1.2 Cathode Fabrication

The cathode scaffold was fabricated using the screen printing technique. Porous well-necked GDC IC scaffolds were produced on both sides of the electrolyte cell. To achieve this, GDC powder was coarsened prior to being mixed with an electronic vehicle to form a GDC ink. Three layers of GDC ink were then screen printed, using a screen printer shown in Figure 3.2 [116], onto each side of the dense GDC pellet. Before the next ink layer was applied, each ink layer was allowed to flow across the pellet surface, and then was placed in a bake oven to extract the electronic vehicle solvent and increase the green strength (i.e. mechanical strength prior to sintering). After screen printing, the samples were then sintered and cooled to room temperature. Sintered IC scaffold thickness and roughness measurements were made with a profilometer.



Figure 3.2: Screen Printer Device. The screen printer is used to fabricate the porous cathode microstructure [116].

3.1.3 Mixed Ionic and Electronic Conducting Precursor Solution Fabrication and Cathode Infiltration

MIEC lanthanum strontium cobalt iron oxide (La_{0.6}Sr_{0.4}Co_{0.8}Fe_{0.2}O_{3-x}, LSCF) metal nitrate precursor solutions were prepared by dissolving lanthanum nitrate, strontium nitrate, cobalt nitrate and iron nitrate in distilled water, with or without a solution additive (such as Triton X-100 or Citric Acid). These LSCF precursor solutions were infiltrated into symmetrical cells fabricated using both the desiccation and pre-infiltration techniques (mentioned in Section 2.6.3). GDC precursor solutions, used in the pre-infiltration technique, were prepared by dissolving gadolinium nitrate and cerium nitrate. GDC precursor solutions were only used with the pre-infiltration technique.

After being infiltrated these solution were allowed to soak into the scaffold for 5 minutes and gelled at 80°C in a drying oven for 10 minutes. Desiccated cells were then sealed inside a desiccator with chemical desiccant, and then thermally decomposed after

being desiccated. The two step infiltrate-gel-fire technique omits the desiccation step, and thermally decomposes the precursor solutions after being infiltrated and dried in the oven at 80°C.

3.1.4 Mixed Ionic and Electronic Conducting Oxide Phase Purity Analysis

After the MIEC precursor solution was thermally decomposed, the phase purity of the resulting MIEC oxide powder was characterized using XRD. Precursor solutions were placed onto an alumina slide, gelled and then thermally decomposed. The resulting oxide powder was placed onto a low X-ray background fused silica slide and characterized using XRD to determine the resulting oxide powder phase purity.

The purpose of analyzing the LSCF oxide powder outside the scaffold was that XRD characterization of the LSCF powder inside the GDC scaffold was much more difficult due to XRD peak overlap between the LSCF and GDC [117, 118]. The phase purity of the resulting LSCF oxide powder was assumed to be the same inside the scaffold as outside the scaffold, since the processing conditions were the same using both fabrication techniques. A representative phase pure XRD scan for LSCF is shown in Figure 3.3.

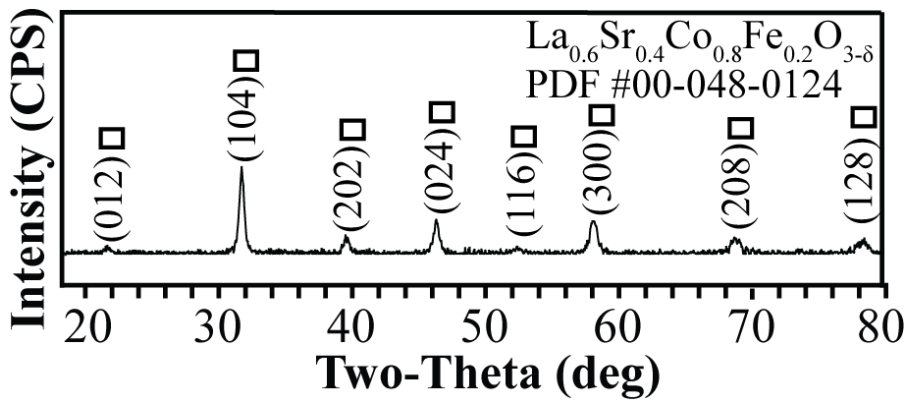


Figure 3.3: Representative X-ray Diffraction Data for Phase Pure LSCF Oxide Powder. The PDF file was obtained from the JADE XRD computer program for LSCF.

3.1.5 Current Collector Application

After complete NMCC fabrication, current collector layers were applied to symmetrical cathodes by screen printing bilayer LSM – Au layers onto the surface of each NMCC. The LSM ink was prepared by mixing LSM powders with a polymer formulation to form an ink with a 34% solids loading. A single layer of LSM ink was then screen printed onto each NMCC cathode, and the samples were sintered and allowed to cool to room temperature. Finally Au paste was screen printed in an open grid pattern across the surface of each LSM current collector.

3.2 Characterization Techniques

3.2.1 Electrochemical Impedance Spectroscopy

Here, EIS measurements were used to measure cathode performance (i.e. cathode R_P) at open circuit as a function of temperature using the setup schematic shown in Figure 3.4 [10]. EIS measurements were evaluated in both air, 20%O₂-80%He, and 20%O₂-80%N₂. EIS measurements using the two-point technique were taken every 50°C between 400°C and 700°C. An unbiased AC signal, at frequencies typically between 1 MHz and 0.1 Hz [1, 5, 61, 119], was applied to the sample to collect impedance measurements. 4-point EIS measurements are performed in literature, but were not performed for this thesis because lead and contact resistances for the EIS measurement are minimal compared to the cathode R_P [5, 61]. Samples were allowed to thermally equilibrate before each EIS measurement was collected.

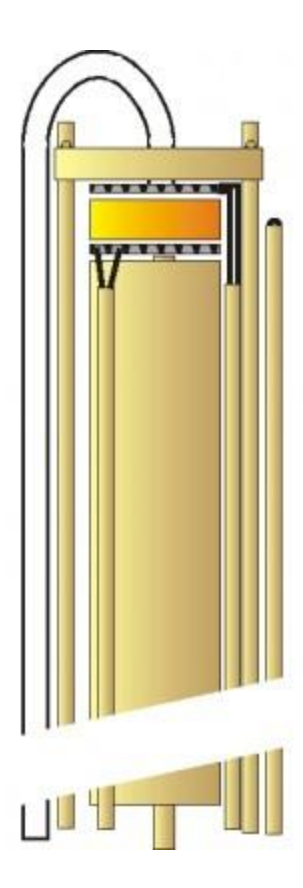


Figure 3.4: Nano-Micro-Composite Cathode

Electrochemical Impedance Measurement Device. The
depicted measurement device uses a 2-point measurement
technique instead of the 4-point technique [10].

Cathode R_P values were extracted by measuring the distance between the high and low frequency x-axis intercepts on Nyquist plots, which had been multiplied by the geometric cathode area and divided by two (since each symmetric cell has two cathodes). Ohmic resistivity (ρ_{Ohmic}) values for each cell were determined by combining the measured distance between the origin and the high frequency x-intercept on the Nyquist plot (R_{Ohmic}), the geometric cathode area (A), and the measured electrolyte thicknesses (l) using the definition of resistance:

$$\rho_{Ohmic} = \frac{R_{Ohmic}A}{l}$$
 [8]

3.2.2 Scanning Electron Microscopy

Figure 3.5 [120] shows a diagram of the SEM characterization technique which can be used to determine whether different fabrication techniques impact nano-particle size. The SEM characterization technique was also useful for evaluating the morphology and overall size of powders and bulk samples. Inside a SEM electrons are generated,

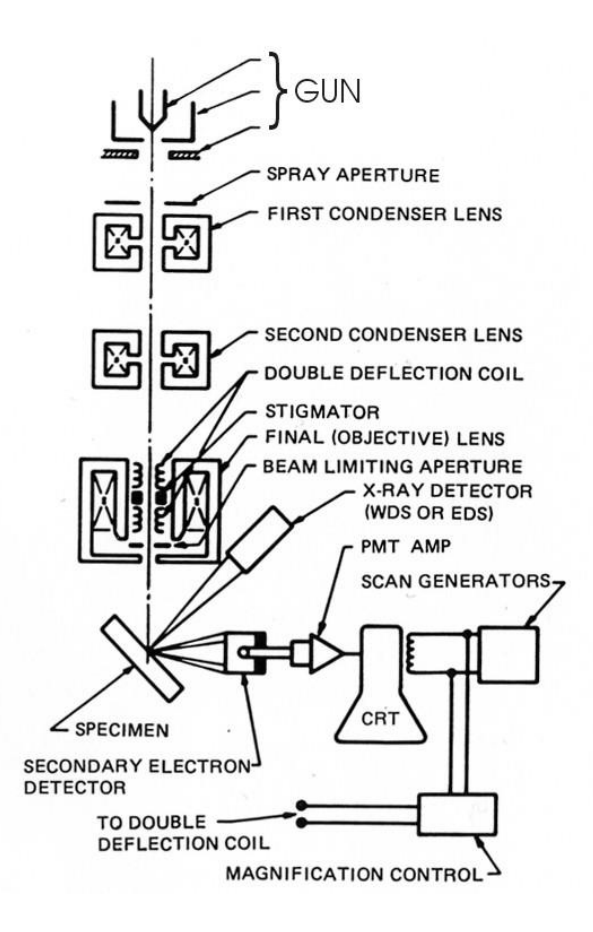


Figure 3.5: Scanning Electron Microscopy Component Schematic. The schematic depicts the Scanning Electron Microscopy components from the electron producing component to the individual detectors [120].

focused using condenser lenses, and directed onto the sample. These high velocity electrons interact with the sample and generate different signals which are: secondary electrons, backscatter electrons, diffracted backscatter electrons, etc. and are measured by various detectors. The secondary electrons and backscatter electrons are typically used in literature [1, 3, 5, 7, 9] for image processing and were used to characterize nano-particle

sizes and the cathode microstructure in this thesis. The SEM characterization technique has been used in many different literature studies to determine MIEC and IC particle sizes [1, 5, 7, 61].

3.2.3 Solid Oxide Fuel Cell Nano-Particle Coarsening Rate

At the elevated temperatures at which SOFCs operate, an opportunity for MIEC nano-particle size growth via diffusion exists. Further, during the thermal decomposition of MIEC precursor solutions the precursor oxides that form also have an opportunity to coarsen in order to reduce the nano-particle surface area. Here nano-particles coarsening were characterized through either SEM images or through the Williamson-Hall method using X-ray diffraction (XRD). Specifically, various precursor solutions were first thermally decomposed at the same starting conditions (such as molarity, solution composition, solution infiltration volume, heating rate, dwell time, etc.), and the resulting oxide powders were characterized to determine the average particle size using SEM or the XRD Williamson-Hall method. After being characterized, the same oxide powders were again heated at an elevated temperature, cooled and characterized (using SEM or XRD Williamson-Hall) a second time to determine how much the average oxide particle size increased (if at all).

3.2.4 X-ray Diffraction

The XRD characterization technique was used to identify the crystal structure of the different powders. In this technique, X-rays are generated from a metal target by hitting the target with electrons generated from a sealed tungsten filament, shown in Figure 3.6 [121]. When the electrons hit the target they eject electrons from the target K or L shells, which are then filled by electrons in the shell above the lost electron (L or M

shells, respectively). The process of transferring electrons from an upper shell to a lower shell releases energy in the form of an X-ray. The most common X-rays are the K_{alpha} (from the K shell) and K_{beta} (from the L shell). X-rays are generated in all directions

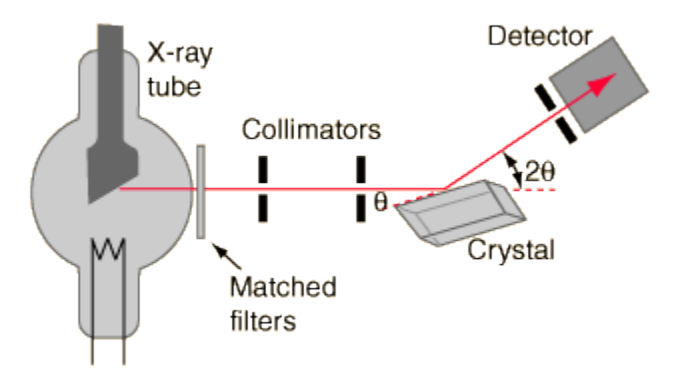


Figure 3.6: **X-ray Diffraction Component Schematic**. Components depict filtered x-rays impacting sample crystal [121].

around the target, but a filter is applied in the direction of the sample to generate a monochromatic, or nearly monochromatic, X-ray beam. The X-ray beam hits the crystal or powder sample and diffracts, according to Bragg's Law:

$$n * \lambda = 2 * d * \sin\theta$$
 [9]

where n is an integer, λ is the X-ray wavelength (nm), d is the lattice plane spacing (nm), and θ is the angle between the incident and scattered X-rays off the crystal or powder sample, before being measured in an X-ray detector.

3.2.5 Williamson-Hall Particle Size Determination from X-ray Diffraction

Nano-particle size characterization was not simply limited to the SEM characterization technique. Infiltrated MIEC oxide nano-particle sizes were calculated via the Williamson-Hall method [122] for powders fabricated inside and outside a porous

IC scaffold. The Williamson-Hall method was applied to XRD spectrum taken of the MIEC powder, assuming that peak broadening was caused by the instrument, particle size, and nano-particle strain. The full-width half-max (FWHM) values for at least two peaks were utilized to obtain average particle size and strain. These XRD peak were carefully selected so only peaks corresponding to a single miller index are used; (i.e. in order to prevent peak broadening caused by additional diffraction from additional lattice planes). Peak broadening contributions for the instrument were removed by: 1) measuring the peak breadth (β) (breadth of each peak was calculated using the FWHM values measured with the JADE computer program) for a number of particle sizes, and 2) subtracting the instrument β value from the total β value. The y-axis linear intercept value from the plot of $\beta*Cos(\theta)$ vs $4*Sin(\theta)$ was then used to calculate the infiltrate MIEC nano-particle size, using the following equation:

$$\frac{K * \lambda}{intercept} = D$$
 [10]

where D is the average infiltrate MIEC nano-particle size (nm), K is shape factor (typical value of 0.9) and λ is the X-ray wavelength (0.154 nm for Cu K_{α} X-rays). The particle strain was determined directly from the slope of the linear trend line determined from $\beta \text{Cos}(\theta)$ vs $4\text{Sin}(\theta)$.

3.2.6 ThermoGravimetric Analysis

The ThermoGravimetric Analysis (TGA) technique was also used to elucidate precursor solution decomposition processes. A TGA device, such as that shown in Figure 3.7 [123], was used to measure mass changes during sample heating for a small sample (usually between 25 and 50 mg) placed inside a platinum or alumina pan. As the

sample was heated, decomposition products were released until only oxide powder remained, with the mass loss caused by sample decomposition measured by the TGA. Here, experiments were conducted in flowing nitrogen to determine the waters of hydration for each nitrate, and in air for precursor solution decomposition measurements.



Figure 3.7: **Thermo-Gravimetric Analysis Schematic**. The depicted Thermo-Gravimetric Analysis uses a hanging scale to measure mass changes. [123].

3.2.7 Profilometry

Characterization of the cathode thickness was necessary to accurately determine the precursor solution volumes required for infiltration [33]. The profilometry characterization technique, shown in Figure 3.8 [124], allows for careful measurement of both the cathode thickness and surface roughness. The profilometer used a needle that was lowered and moved across the surface of the cathode. The needle was attached to a spring and as the needle was raised and lowered, due to height changes in the cathode, and the profilometer calculates cathode thickness values according to Hooke's Law.

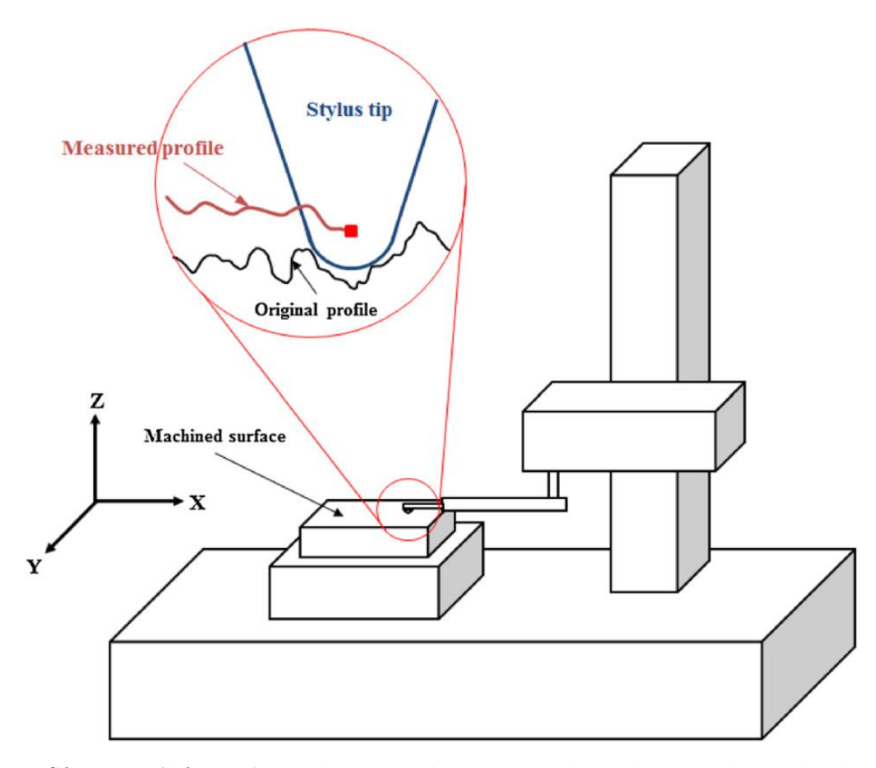


Figure 3.8: **Profilometer Schematic**. The zoomed image of the stylus tip shows the difference in the measured and original surface profile. [124].

3.2.8 Focused Ion Beam-Scanning Electron Microscopy 2D Serial Sectioning

NMCC microstructure 2D serial sectioning was performed using Focused Ion Beam-Scanning Electron Microscopy (FIB-SEM). The 2D microstructural images were obtained using a scanning electron microscope (Auriga Dual Column Focused Ion Beam-Scanning Electron Microscope) operated with an electron beam voltage of 20 kV, an 120 um aperture, a 40 second scan speed, a 5.0 mm working distance, and a 10,000x magnification. The FIB-SEM x-y spatial resolution was 1 nm and the z spacing between each 2D section was 20 nm [125]. The FIB was operated with a beam voltage of 2 kV and a 5.0 mm working distance. The FIB beam current used to initially clear around the desired target image area was 16 nA, while the beam current used to collect 2D serial section images was reduced to 4 nA. The reduction in beam current allowed for more

detailed image to be obtained for image processing. A detailed outline of FIB-SEM sample preparation and analysis technique is presented in Appendix 2.

3.3 Finite Element Modeling of Cathode Microstructure and Performance

3.3.1 Motivation for Using Finite Element Modeling

In addition to experimentally determined EIS measured and SIMPLE Model predicted R_P measurements, Finite Element Modeling (FEM) was used to predict R_P values on imported cathode 3D microstructures taken from FIB-SEM images. Here, the R_S values used in FEM R_P calculations were adjusted until the FEM R_P value matched the EIS measured R_P values. In this manner, MIEC infiltrate R_S values were obtained for the first time. Determination of R_S values from FIB-SEM images is not a common technique found in the literature because sample preparation is a lengthy process, and construction of 3D models used in the FEM calculations are not a trivial task.

Since only R_s values for thin film microstructures and bulk samples currently exist as a guide to select which MIEC cathode materials provided improved performance FEM allows for a much more accurate determination of infiltrated MIEC R_s values in NMCCs.

The assumptions used to determine R_s from R_P via FEM were that the 1) gasphase concentration polarization resistance was minimal, 2) the interfacial resistances were minimal, 3) the electronic resistance losses in the oxygen surface exchange layer were minimal, and 4) the ionic conductivity in the MIEC infiltrate was minimal due to the layer being 50 nm or less in thickness. These assumptions were valid for the following reasons. First, post-infiltration porosity measurements for all cells in this thesis were 20 vol% or greater (Post-infiltration porosity measurements were determined by

subtracting infiltration volume % values from FIB-SEM porosity measurements on noninfiltrated cathode microstructures [33]). The fact that volume %'s greater than 18% are typically sufficient for percolation [7] suggests that the pore network in the reconstructed cathodes was percolated (and therefore gas-phase concentration polarization resistance was low). In addition, experimental tests performed in 20%O₂-80%He and 20%O₂- $80\% N_2$ have shown similar R_P results in air, which also indicates that gas-phase concentration polarization resistance is low [126]. Second, XRD scans taken on NMCCs only detect impurity phase fractions which are greater than 5% of the main peak, which indicates that any possible interfacial resistance from these oxide phases would be minimal. Literature studies have shown phase pure LSCF and GDC to be free of reaction products [5]. Third, electronic resistance losses were minimal because infiltrated MIEC nano-particles in the cathode microstructure have been shown to be interconnected at infiltration loading levels of 12 vol%, which was the case for all experimentally determined results in this thesis [5]. EIS ohmic offset NMCC values also indicate an absence of electronic losses in the open-circuit R_P measurements taken here. Fourth, the characteristic thickness (ratio of the diffusion coefficient to the oxygen surface exchange coefficient) of LSCF has been measured to be greater than ~100 µm [51], indicating that the 50 nm or smaller infiltrate particles here were electrochemically active over their entire surface and their performance was dominated by their surface resistance.

3.3.2 Finite Element Modeling Performance Calculation Overview

FEM open-circuit R_P modeling work was performed using the same set of microstructurally independent assumptions covered in Appendix 1 up to Equation A1.1. Like the SIMPLE model, this FEM open-circuit R_P modeling did not require the use of

the Buttler-Volmer equation to solve the current density flux across the electrolyte because both models predict open circuit R_P values. As done previously in the literature [127], the first step in deriving the FEM open-circuit potential was to assume that diffusion-limited oxygen vacancy flux density through the IC scaffold was controlled by dilute thermodynamics and therefore amenable to modeling via the Nernst-Planck equation:

$$\sum_{i} J = \sum_{i} - z_{i} \mu_{i} F c_{i} \nabla \varphi - D_{i} \nabla c_{i} + c_{i} \nu$$
 [11]

where J is the atomic flux, \sum_i is the sum of all the species charge carrier, z is the charge, μ is the mobility, F is the Faraday constant, φ is the electrical potential, D is the diffusivity of species, c is the concentration, v is the convective velocity, is i was the index number. The Nernst-Planck equation was then simplified by first assuming that the IC scaffold in the electrode and electrolyte had a constant composition (a common assumption used in the SOFC modeling community [33]). This assumption was reasonable because: 1) the current densities seen in SOFC cathodes near operation are relatively low, and 2) the oxygen partial pressure inside the cathode pore was constant (which leads to low concentration polarization). This first assumption allowed the second term of the Nernst-Planck equation to be removed and reduced the equation to the following form:

$$\sum_{i} J = \sum_{i} - z_{i} \mu_{i} F c_{i} \nabla \varphi + c_{i} \nu$$
 [12]

The second assumption was that no convection in the cathode or electrolyte materials existed. This was a reasonable assumption since the MIEC material, cathode microstructure, and electrolyte had been made of solid oxide materials which would lack convection. This assumption allowed the third term in the Nernst-Planck equation to be removed and reduced the equation to the following form:

$$\sum_{i} J = \sum_{i} - z_{i} \mu_{i} F c_{i} \nabla \varphi$$
 [13]

Using these assumptions and the fact that GDC was a pure ionic conducting material (at least in air) [128] allowed the atomic flux in the IC material to be reduced to the following form:

$$J = -2\mu_{V_{\ddot{o}}} F c_{v_{\ddot{o}}} \nabla \varphi \tag{14}$$

where z was replaced with 2 because each oxygen ion has a 2^+ oxidation state, the mobility was the mobility of oxygen vacancies (μ_{V_0}) , F was Faradays constant, and the concentration was the oxygen vacancy concentration (c_{v_0}) . In order to solve for the steady state cathode R_P the gradient of each side of Equation 14 was taken and the fact that at steady state $\nabla J=0$ was applied to yield Laplace's Equation:

$$\nabla^2 \varphi = 0 \tag{15}$$

Hence in this special, open-circuit situation for a NMCC with an IC scaffold, FEM programs such as ABAQUS or in this case COMSOL (capable of solving Laplace's equation) could be used to determine the potential distribution within the ionic conducting scaffold. Since the MIEC material was limited by the oxygen exchange across the surface, (i.e. since they were well below the characteristic thickness there was no electrical potential drop across the bulk of each MIEC particle, only across its surface) the MIEC nano-particles were modeled as a thin surface resistance layer across the cathode microstructure. The surface resistance for this MIEC layer was applied to the ionic conducting scaffold as a surface material property.

The final assumption was that an extremely small interfacial resistance between the MIEC surface impedance layer and the IC GDC cathode microstructure existed. This last assumption was realistic because Baumann *et al.* [47] have shown the interfacial resistance to be at least 2 orders of magnitude lower than the surface impedance resistance for MIEC-IC material combinations at SOFC operating temperatures. The assumptions up to this point are shown in the Appendix 1 derivation up to Equation A1.1.

The potential distribution, discussed in Equation A1.1, was then solved for within the GDC. After the potential distribution through the GDC had been determined by using COMSOL to solve Equation 15, the R_P value was determined by dividing the potential difference, V (i.e. φ in Equation A1.1), across the reconstructed volume by the total oxygen vacancy current density flowing through the reconstructed volume (A/I) (a derivation showing how $\frac{\sigma}{r} \int_0^r \frac{d\varphi(x,y)}{dy} |_{y=0} dx$, from Equation A1.1, can be determined from I/A can be found in Appendix 1, Figure A1.3) and subtracting out the ohmic resistance for the reconstructed electrolyte (i.e. $\frac{d}{2\sigma}$ in Equation A1.1). The potential difference was

defined as the difference between the 1V applied to the MIEC surface impedance layer and the 0V applied to the bottom of the electrolyte using the equation:

$$R_P = \left(\frac{\varphi}{I} * A\right) - \left(\frac{d}{2*\sigma_{IC}}\right)$$
 [16]

where R_P is the polarization resistance, φ is the applied reference potential to the MIEC surface, I is the integrated current across the electrolyte, A is the electrolyte area integrated across to obtain the current, t is the electrolyte thickness contained in the reconstructed volume, and σ_{IC} is the IC of the electrolyte and scaffold materials.

3.3.3 Focused Ion Beam-Scanning Electron Microscopy Sample Preparation

Samples for FIB-SEM analysis were prepared first by screen printing a porous GDC scaffolds on top of a dense, sanded electrolyte pellets. Samples were then epoxy infiltrated to improve pore-scaffold contrast in later FIB-SEM measurements. Epoxy resin and hardener (EpoThin, Buehler) previously mixed in a 5:1.95 mass ratio and stirred for ~5 minutes, were then placed inside a chamber where a vacuum was applied to remove bubbles from the epoxy (the vacuum was -20 inches Hg). While maintain the vacuum the epoxy was poured around the sample until the sample was submerged in epoxy. The vacuum was maintained for at least 5 minutes to remove gas bubbles, and allowed the epoxy to soak into the scaffold pores. The vacuum was then released and the epoxy was allowed to harden around the sample over 12 hrs. After the epoxy hardened the sample was cut to expose the scaffold surface, and was sanded using 1200 grit sandpaper which produced a mirror smooth surface. The sanded sample was bonded to an aluminum sample holder and had ~2 nm of tungsten sputtered on its surface.

Figure 3.9 shows the epoxy coated sample oriented in the FIB-SEM [129]. The sample was placed at a 54⁰ angle so it was perpendicular with the FIB. The FIB was used to remove a section of material in front of the desired observation surface and the SEM was aligned to image the observation surface. After each serial section, the FIB was used to remove 20 nm off the observation surface (in the direction of the arrow on Figure A2.1) and the SEM was used to take a 2D image of the newly exposed surface, shown in Figure 2.10 where black areas represent pores and the grey areas are electrode scaffold material. This process was repeated to create a set of 2D serial section images.

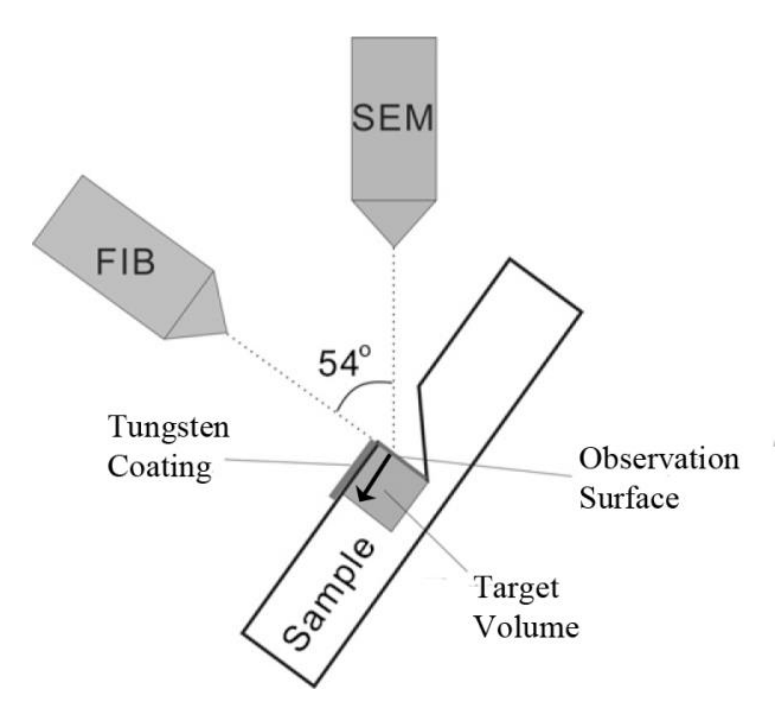


Figure 3.9: Epoxy Coated Porous GDC Scaffold on a Dense GDC Electrolyte Oriented Inside the FIB-SEM. The FIB is used to make serial sections in the direction of the arrow while the SEM images each newly exposed sample surface [129].

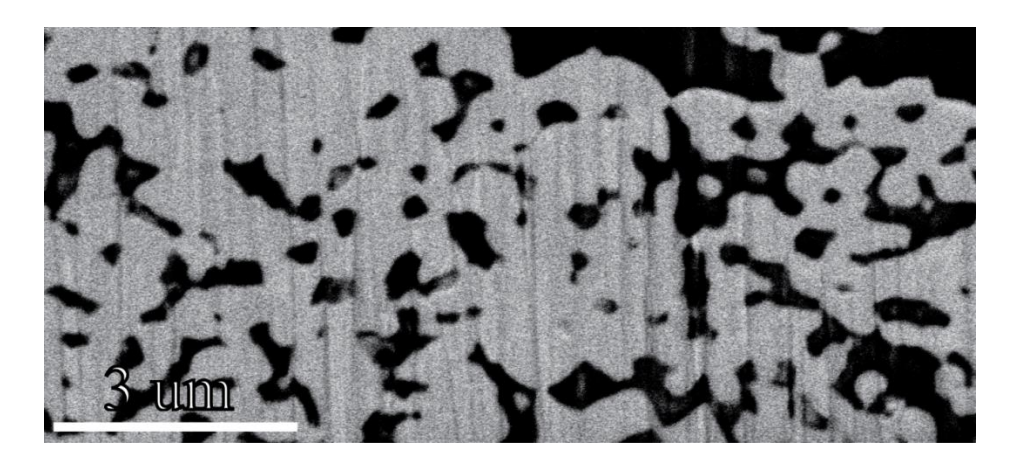


Figure 3.10: **FIB-SEM Cathode Backscatter Image used for 3D Reconstruction**. The depicted black areas are pores while the depicted lighter regions are scaffold material.

3.3.4 Cathode Microstructure 3D Reconstruction

These 2D serial section images were then recombined using a program called MIMICS [130] to create a 3D reconstruction of the cathode and electrolyte microstructure. A step-by-step discussion of how 3D reconstructions were created is shown in Appendix 2. For the work in this thesis, 205 serial section images were imported into the MIMICS program, and a threshold was applied to tell MIMICS what grey-scale values were IC scaffold and what gray-scale values were pores. From these images a 3D reconstruction was created for the cathode and electrolyte microstructures.

Figure 3.11 shows a 3D reconstruction created in MIMICS of the cathode and electrolyte, done separately. The 3D reconstruction can be generated using an optimum, high, medium, or low number of triangles. A larger number of triangles improves the accuracy of the final measurement but increases the calculation time required for 3D volume meshing and the R_P calculation. For this thesis, due to the sample size being large (in the millions of triangles), a medium density of triangles was used.

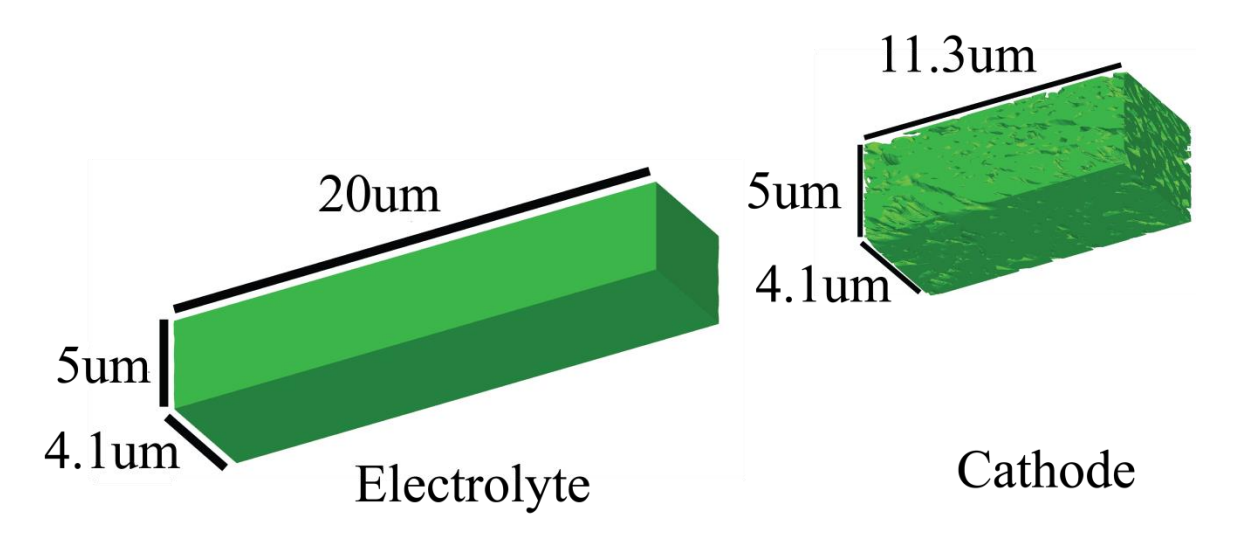


Figure 3.11: FIB-SEM 3D Reconstruction for Cathode and Electrolyte. The electrolyte is shown on the left and the cathode is shown on the right. Both parts were reconstructed in the MIMICS computer program separately.

3.3.5 3D Cathode Reconstruction Volume Meshing

Once a 3D representation of the electrolyte and cathode was created in MIMICS, the cathode and electrolyte were merged together and volume meshed using the 3-Matic computer program before being FEM modeled with the COMSOL computer program. The dense electrolyte layer was added to each cathode to facilitate summation of the current flowing across the cathode. Step-by-step instructions for how to merge the 3D reconstructions and volume mesh the entire sample are shown in Appendix 2. Figure 3.12 shows the volume mesh of the combined cathode and electrolyte microstructures produced using 3-Matic. This volume mesh was then exported to COMSOL for performance calculations.

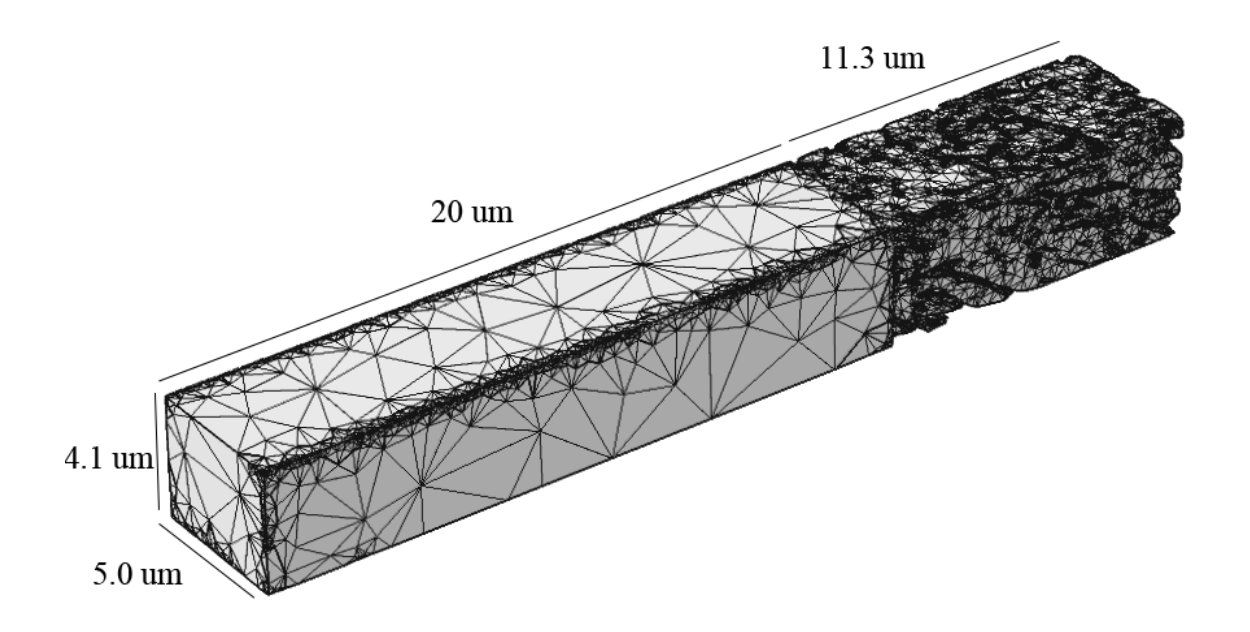


Figure 3.12: **FIB-SEM 3D Reconstruction Volume Mesh of Cathode and Electrolyte**. The electrolyte and cathode reconstructions from Figure 3.11 were merged and volume meshed using the 3-Matic computer program.

3.3.6 Infiltrated Solid Oxide Fuel Cell Cathode Finite Element Modeling to Predict Polarization Resistance

Figure 3.13 shows the electrochemical potential lines modeled in COMSOL using the 3-Matic assembled volume mesh shown in Figure 3.12. Inside COMSOL an oxygen exchange surface resistance layer was applied to the surface layer of the volume mesh around the electrode to represent the contribution from the infiltrated MIEC oxide nanoparticles to account for the non-flat nature of the MIEC infiltrate hemisphere. The boundary condition used by COMSOL for the applied surface resistance layer to the IC scaffold is described:

$$\boldsymbol{n}.\boldsymbol{J} = \frac{1}{R_{surf}}(V - \varphi)$$
 [17]

where n is the normal vector, J is the electric current density vector, R_{surf} is the surface resistance of the infiltrated MIEC material (defined in Equation 18), V is the potential through the IC GDC scaffold material, and φ is the 1V reference potential applied to the porous IC scaffold surface.

The oxygen exchange surface resistance value was scaled by multiplying the intrinsic R_s value by the surface area ratio between the total cathode surface area and the infiltrated nano-particle surface area on the cathode using the equation:

$$R_{surf} = \frac{R_s A_{Sc}}{A_{inf}}$$
 [18]

where R_{surf} is the R_s value spread over the surface of the IC scaffold, A_{Sc} is the surface area of the IC scaffold, and A_{inf} is the surface area of the infiltrate. The GDC conductivity was then assigned to the entire electrolyte and cathode IC scaffold volume mesh. Finally, a 1V bias was applied to the entire cathode microstructure surface (all four sides and the top) and a 0V bias was applied to the bottom of the electrolyte microstructure surface to simulate an electrochemical potential through the microstructure. Applying a potential to the edges of the microstructure is unphysical because in real life the edges of the reconstructed microstructure would be connected to other GDC particles in the next repeating unit and would not be covered by MIEC infiltrate. However, in large enough reconstructions these incorrect edge polarizations would not be expected to significantly contribute to the overall cathode results (as discussed in Chapter 8, reconstructions of various sizes all yielded identical R_P values, indicating these edge effects could be safely ignored). The COMSOL FEM program was

used to solve Laplace's equation (Equation 15) to calculate the electrochemical potential lines shown in Figure 3.12. The current generated from the electrochemical potential lines located at the 0V surface were then integrated (the I term in Equation 16) to determine R_P values at different operating temperatures.

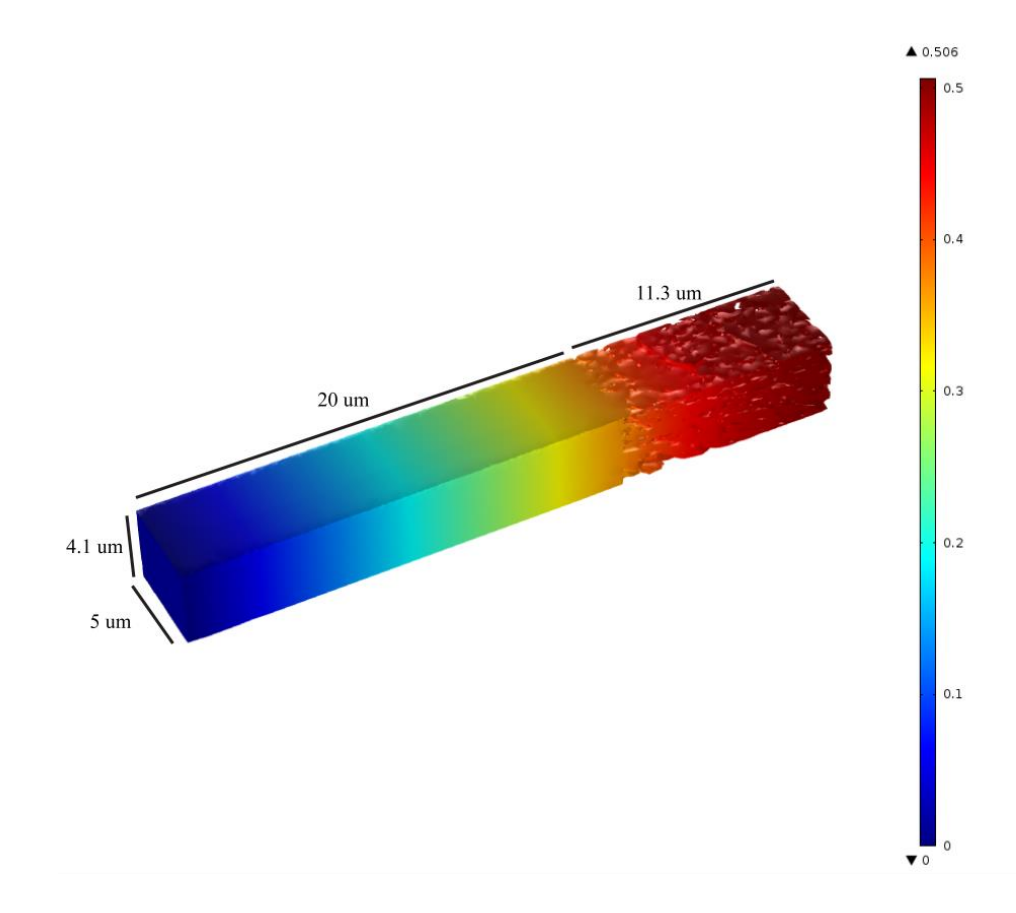


Figure 3.13: **FIB-SEM 3D Reconstruction Electrochemical Potential Gradient**. The electrochemical potential gradient was generated using the COMSOL computer program.

3.4 Summary

In summary, various processing and characterization techniques were used to analyze SOFC devices and better understand the underlying processes. The insights from these experimental techniques are discussed in the following chapters. The next chapters evaluate the effects desiccation and nano-ceria pre-infiltration have on infiltrated MIEC nano-particle size, MIEC oxide phase purity, and ultimately SOFC symmetrical cell

performance. In addition, different solution additives and infiltrated MIEC compositions will be used with desiccation and pre-infiltration to evaluate if infiltrated MIEC nanoparticle size can be controlled other parameters as well. The characterization techniques outlined in this chapter are used in the following chapters to evaluate the underlying processes that control MIEC nano-particle size, MIEC oxide phase purity and SOFC performance.

CHAPTER 4: The Impact of Precursor Nitrate Solution Desiccation on Infiltrated $La_{0.6}Sr_{0.4}Co_{0.8}Fe_{0.2}O_{3-\delta}$ Cathodes

4.1 Introduction

This chapter evaluates the desiccation fabrication approach as a means to systematically reduce infiltrated MIEC nano-particle size, and subsequently improve NMCC performance. Processing techniques, such as how desiccation was performed, will be discussed in detail in addition to the characterization techniques used. This chapter is intended to initially demonstrate that desiccation reduces nano-particle size. An in-depth analysis of what promotes this particle size reduction will be presented in Chapter 5. As mentioned in Section 2.1.2, NMCCs are typically produced by the dissolution of MIEC precursor nitrates in water, the infiltration of these nitrate solutions into porous IC scaffolds, and the thermal decomposition of the nitrates into MIEC oxide nanoparticles that cling to the IC scaffold.

Unfortunately, it has been difficult to control the size of MIEC nanoparticles obtained via the infiltration method. For instance, a survey of recent literature indicates that $Sm_{0.5}Sr_{0.5}CoO_{3-\delta}$ (SSC) – ceria NMCCs produced by infiltration, a 10° C/min heating ramp, and firing at 800° C for 1 hour after each infiltration step had average particle sizes ranging from 40 to 100 nm [5, 7, 30]. Similarly, LSCF – ceria NMCCs produced by infiltration, a 10° C/min heating ramp, and firing at 800° C for 1 hour after each infiltration step had average particle sizes ranging from 50 to 60 nm [7]. Lastly, LSFC – ceria NMCCs produced by infiltration, a 10° C/min heating ramp, and firing at 800° C for 2 hours after each infiltration step had average LSFC particle sizes ranging from 38 to 80 nm [8, 9]. Since past studies have shown that average SSC or LSCF infiltrate particle

sizes remain constant with successive infiltration and firing steps [7], the cause of these large average particle size variations remains a mystery.

This chapter shows that the chemical and physical desiccation of LSCF precursor nitrate solutions infiltrated into porous GDC scaffolds, prior to thermal decomposition, can be used to control the average LSCF infiltrate particle size.

4.2 Experimental Methods

4.2.1 Cathode-Electrolyte-Cathode Symmetric Cell Production

Cathode-supporting electrolytes were prepared in the following manner. First, 0.8 grams of GDC powder were pressed to 63 MPa in a steel die with a 19 mm diameter bore. According to manufacturer specifications, this ultra-high surface area powder (Rhodia; Cranbury, NJ, USA) had an agglomerate d₅₀ size of 240 nm, a specific surface area of 25.2 m²/g, and an average particle size of ~32 nm. The pressed porous pellets were heated to 1475°C at 3°C/min, held at 1475°C for ~10 hours, and then cooled to room temperature at a nominal cooling rate of 3°C/min to produce discs with relative densities >95%. These discs were sanded flat and parallel with SiC sandpaper until they achieved thicknesses ranging from 432 to 457 μm.

Porous, well-necked GDC IC scaffolds were then produced on both sides of these electrolyte pellets. To achieve this, some of the aforementioned Rhodia GDC powder was coarsened at 800°C for 4 hours and then mixed with a polymer (Heraeus; West Conshohocken, PA, USA) to form a GDC ink with a 34% solids loading. Three layers of GDC ink were then screen printed onto each side of the dense GDC electrolyte pellet using a patterned 80 mesh stainless steel screen with a circular 0.5 cm² open area. Before the next ink layer was applied, each ink layer was allowed to flow for 5 minutes and then

was placed in a bake oven at 120°C for 5 minutes to extract the electronic vehicle solvent and increase the green strength. After screen printing, the samples were heated to 400°C at 3°C/min, held at 400°C for one hour, heated to 600°C at 3°C/min, held at 600°C for one hour, heated to 1100°C at 5°C/min, held at 1100°C for 3 hours, and then cooled to room temperature at a nominal cooling rate of 10°C/min. Sintered IC scaffold thickness and roughness measurements were then made with a Dektak 3 profilometer (Bruker; Tucson, AZ, USA).

1.50 molar MIEC precursor solutions were infiltrated into these IC scaffolds, desiccated, and fired to coat the IC scaffold surface with MIEC oxide nanoparticles. As done in past studies [7], the infiltrated LSCF metal nitrate precursor solutions were prepared by dissolving 99.999% pure $La(NO_3)_3*6.3 H_2O$, 99.9965 % pure $Sr(NO_3)_2$, 99.999% pure $Co(NO_3)_2*5.67 H_2O$, and 99.999% pure $Fe(NO_3)_3*9.42 H_2O$ (Alfa Aesar; Ward Hill, MA, USA) in distilled water containing 3 wt% of pre-dissolved Triton-X 100 (weight Triton X-100/weight nitrate), (These precise nitrate water of hydration contents were determined prior to nitrate weighing by measuring the mass loss that occurred inside a Q500 thermogravimetric analyzer (TA Instruments; New Castle, DE, USA) with heating under nitrogen up to 850°C). These solutions were then pipetted into the porous GDC cathode scaffolds, allowed to soak into the scaffold for 5 minutes, and heated in an 80°C drying oven for 10 min before being desiccated. Based on previous desiccation kinetics studies [131], samples desiccated with dry air were desiccated for 30 minutes, samples desiccated with CaSO₄ were desiccated for 56 hours, and samples desiccated with CaCl₂ were desiccated for 8-10 hours. After each desiccation, the samples were heated to 700°C at 10°C/min, held at 700°C for one hour, and then cooled to room temperature at a nominal cooling rate of 20°C/min. This infiltrate-fire process was repeated 3 times to achieve the desired MIEC loading level of 12.0 vol%.

Lastly, symmetric cells were prepared for electrical measurements by screen printing bilayer $(La_{0.8}Sr_{0.2})_{0.98}MnO_{3-\delta}$ (LSM) – Au current collectors onto the surface of each NMCC. The LSM ink was prepared by mixing LSM powders (Praxair Specialty Ceramics; Woodinville, WA, USA) that had a d_{50} agglomerate size of 1.1 μ m, a specific surface area of 3.00 m²/g, and an average particle size of ~300 nm with V-737 electronic vehicle to form an ink with a 34% solids loading. A single layer of LSM ink was then screen printed onto each NMCC using a 290 mesh stainless steel screen with a circular 0.5 cm² open area. The samples were then heated to 700°C at 10°C/min, held at 700°C for 1 hour, and then cooled to room temperature at a nominal cooling rate of 20°C/min. Heraeus C5756 fritted Au paste was then screen printed in an open grid pattern across the surface of each LSM current collector using a patterned 290 mesh stainless steel screen.

4.2.2 Symmetric Cell Impedance Measurements

NMCC performance as a function of temperature was evaluated in air, 20%O₂-80%He, or 20%O₂-80%N₂ under open circuit conditions using EIS. Measurements in air were performed in a static atmosphere, while controlled atmosphere experiments in 20%O₂-80%He and 20%O₂-80%N2 were performed with a 100 mL/min flow rate. Two-point EIS measurements were taken every 50 degrees between 400 and 700°C using an IM6 impedance analyzer (Zahner Elektrik GmbH; Kronach, Germany). At each temperature, a 100 mV AC amplitude was used to collect impedance measurements between 100 kHz to 0.1 Hz. All samples were allowed to equilibrate for a minimum of 30 minutes before an EIS spectrum was collected. Cathode polarization resistances were

extracted by measuring the distance between x-axis intercepts on Nyquist plots that had been multiplied by the geometric cathode area (0.5 cm^2) and divided by two (since each symmetric cell had two cathodes). Ohmic resistivity (ρ_{Ohmic}) values for each cell were determined by combining the measured distance between the origin and the high frequency x-intercept on a Nyquist plot (R_{Ohmic}) , the 0.5 cm² geometric cathode area (A), and the measured electrolyte thicknesses (I) using the definition of resistance:

$$\rho_{Ohmic} = \frac{R_{Ohmic}A}{l}$$
 [19]

4.2.3 X-ray Diffraction Measurements

MIEC infiltrate phase purity was evaluated using XRD. XRD analyses were conducted from $20^{\circ} \le 2\theta \le 80^{\circ}$ with a 0.040° step, a 1.00 second scan speed, and a copper filament using a Miniflex II (Rigaku Americas Corporation; The Woodlands, TX, USA) operated at 30kV and 15 mA. Due to overlap of the 33.0° LSCF and 33.0° GDC peak, the 47.3° LSCF peak and the 47.4° GDC peak, the 69.2° LSCF peak and the 69.3° GDC peak, and the 78.6° LSCF peak and the 78.9° GDC peak [117, 118], LSCF XRD analyses were conducted on precursor nitrate solutions fired both inside a GDC scaffold and outside a GDC scaffold on an alumina plate.

4.2.4 Scanning Electron Microscopy Measurements

NMCC microstructure was evaluated after EIS testing using a Auriga Dual Column Focused Ion Beam-Scanning Electron Microscope (FIB-SEM) (Carl Zeiss Microscopy GmbH; Jena, Germany) operated with a beam voltage of 20 kV, a 30 µm aperture, a 40 second scan speed, a 1.4 mm working distance, and magnifications between 100,000 and 300,000 times. SEM samples were prepared by fracturing symmetric cells in half, bonding the remnants to an aluminum vertical sample holder, and sputtering 2.0 nm of tungsten on the surface.

Figure 4.1 [61] shows the infiltrate particle fracture surface measurements that were performed at the electrolyte-cathode interface. Particle size measurements were conducted using the Heyne linear intercept method [132], 3 micrographs per sample, and at least 35 intercepts per micrograph.

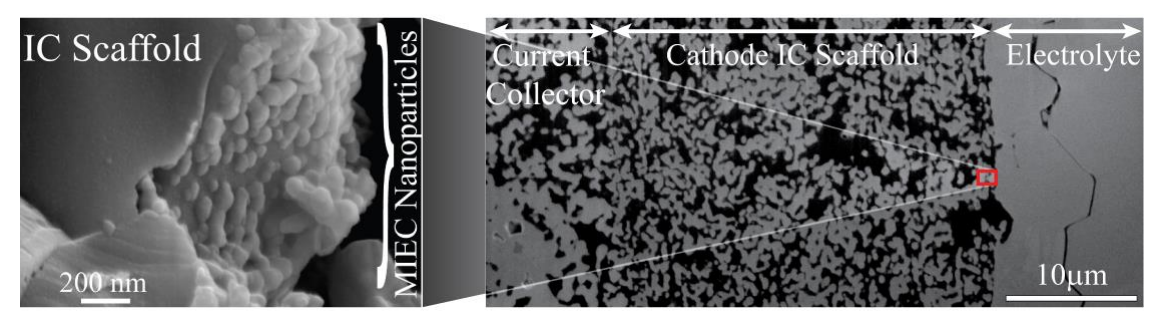


Figure 4.1: Scanning Electron Microscope Fracture Surface Image. The depicted parts are an undesiccated LSCF-GDC NMCC (left), and a FIB-SEM Serial Section Showing the Microstructure of a LSM Current Collector, a GDC Scaffold, and a GDC Electrolyte (right) [61].

4.2.5 Nano-Micro-Composite Cathode Performance Modeling

NMCC performance was modeled using the SIMPLE model [5, 7, 8]. As discussed [7], the SIMPLE model accounts for NMCC resistances associated with oxygen exchange across the MIEC infiltrate surface and oxygen transport through a microstructurally idealized IC scaffold. As such, it predicts the lowest-possible NMCC

 R_P , since additional sources of resistance (electronic transport losses through the MIEC infiltrate, IC tortuosity induced resistances, gas concentration polarization resistances, etc.) are ignored. The model is "simple" in that it only relies on intrinsic materials properties and easily-measured microstructural properties. These materials properties include the intrinsic area specific resistance for oxygen surface exchange into the MIEC (R_s) and the bulk oxygen vacancy conductivity of the IC scaffold $(\sigma_{V_{O,Sc}^{\bullet\bullet}})$. These microstructural parameters include the IC scaffold surface area (A_{Sc}) , the MIEC infiltrate surface area (A_{Inf}) , the cathode thickness (h), the IC scaffold column repeat unit width (r), and the scaffold porosity (p). The model is also "simple" in that R_P is expressed in terms of an analytical expression:

$$R_{P} = \frac{r\left(\frac{R_{S}A_{S_{C}}}{A_{Inf}}\right)}{\left(\frac{1+\beta}{1+\beta exp\left(\frac{-2h}{\alpha}\right)}\right)r(1-p)exp\left(\frac{-h}{\alpha}\right) + \frac{\left(1+\beta exp\left(\frac{-h}{\alpha}\right)\right)}{\left(1+\beta exp\left(\frac{-2h}{\alpha}\right)\right)}\alpha\left(1-exp\left(\frac{-h}{\alpha}\right)\right) + pr}$$
[20]

where:

$$\alpha = \sqrt{\sigma_{V_{O,Sc}} r (1-p) \frac{R_S A_{Sc}}{A_{Inf}}}$$
 [21]

and:

$$\beta = \frac{\sigma_{V_{O,Sc}^{\bullet \bullet} R_{S}A_{Sc}}^{\bullet \bullet} - \alpha}{\sigma_{V_{O,Sc}^{\bullet} R_{Inf}}^{\bullet \bullet} + \alpha}$$
 [22]

that can be quickly solved within a spreadsheet or via an online calculator, as done ondemand for a variety of user-selected NMCC materials and geometries at https://www.egr.msu.edu/nicholasgroup/simple.php. Here, the procedures described in the literature [7] were used to combine the SEM measurements, previous GDC IC scaffold measurements [7], literature LSCF R_S measurements [51], and literature GDC $\sigma_{V_{O,Sc}}$ measurements [7] to produce SIMPLE model NMCC R_P predictions. NMCC performance was also modeled using the surface resistance (SR) model that assumed oxygen surface exchange was the only source of NMCC resistance [5, 7, 8]. Based on the definition of area specific resistance this model predicts R_P using the following equation:

$$R_P = R_S A_G / A_{Inf} ag{23}$$

where A_G is the geometric (i.e. footprint) area of the cathode and the other symbols have their previously defined meanings.

4.3 Results

4.3.1: Desiccant Impacts on Infiltrate Particle Size

Both the SIMPLE model and the SR Limit indicate that NMCC performance is influenced by infiltrate oxide nano-particle size. The results in this chapter will demonstrate that precursor gel desiccation systematically reduces infiltrated LSCF oxide nano-particle size.

Figure 4.2 [131, 133] shows a series of representative scanning electron micrographs indicating that the chemical or physical desiccation of precursor nitrate solutions results in the reduction of the <u>average</u> size of infiltrated LSCF particles produced by firing precursor nitrate solutions at 700°C. In fact, precursor nitrate solutions that were infiltrated, air-dried, and subsequently fired at 700°C produced 48 +/- 15 nm diameter LSCF nano-particles while those infiltrated, desiccated with CaCl₂, and subsequently fired at 700°C, produced 22 +/- 5 nm diameter LSCF nano-particles.

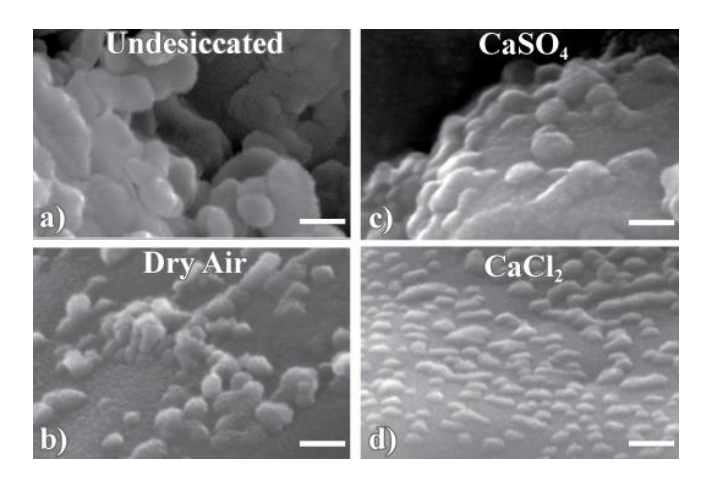


Figure 4.2: Scanning Electron Micrographs for Desiccated LSCF Nano-Particles Produced by using Triton X-100. LSCF oxide particles were produced inside GDC Scaffolds at 700°C. Note: Desiccants are Listed in Order of Increasing Effectiveness. [131,133] Each scale bar is 50 microns in width.

Figure 4.3 [131, 133] shows the impact of desiccation and firing temperature on the average LSCF particle size. As indicated in the literature, calcium chloride was the strongest chemical desiccant, followed by calcium sulfate, and finally treatment in dry air [131, 133]. Desiccant strength ranking is based on each chemical desiccant's thermodynamic driving force to lower the water partial pressure in the infiltrated precursor solution. At each firing temperature, increased amounts of precursor nitrate solution desiccation produced smaller LSCF particles. For each desiccant, increased firing temperature resulted in larger LSCF particles. Given the high number of particles counted (>100 in each case) and the high resolution of the SEM, the error bars mainly represent the actual infiltrate particle size distribution within each NMCC.

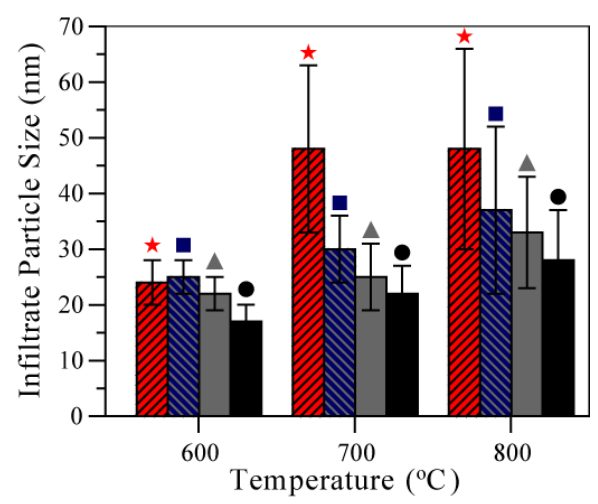


Figure 4.3: Bar-Graph of Desiccated Average LSCF Infiltrate Particle Sizes from Scanning Electron Microscopy Images. \star =Undesiccated, \blacksquare =Dry Air, \blacktriangle =CaSO₄, and \bullet =CaCl₂. Desiccants are listed in order of increasing effectiveness. [131,133] Error bars are +/- a standard deviation calculated using the SEM-measured particle size distribution.

4.3.2: Desiccant Impacts on Infiltrate Phase Purity

Figure 4.4 [117, 118, 134-137] shows that LSCF infiltrate phase purity remained constant with desiccation and firing at 700°C. Although intense signals from the large volume of GDC scaffold particles in the Figure 4.4a NMCCs XRD scans made the LSCF and impurity phase peaks difficult to resolve, those peaks were well resolved in the Figure 4.4b XRD scans taken on loose LSCF powders produced outside a GDC scaffold. Regardless of the precursor nitrate solution desiccation conditions, LSCF was the dominant infiltrate phase; making up ~85% of the infiltrate material based on peak intensity ratios. Similar phase purity has been observed in other LSCF-GDC cathodes reported in the literature [7, 138, 139]. Although generally similar to the phase purity observed after firing at 700°C, LSCF-GDC NMCCs fired at 600°C (not shown) had a larger percentage of impurity phases, while those fired at 800°C had a smaller percentage of impurity phases (not shown). NMCCs fired at 700°C were chosen for their combination of high LSCF infiltrate phase purity and small LSCF infiltrate particle size. It is important to note that the identity and phase fraction of each impurity phase shown

in Figure 4.4 remained essentially constant as the precursor nitrate solution desiccation conditions were varied.

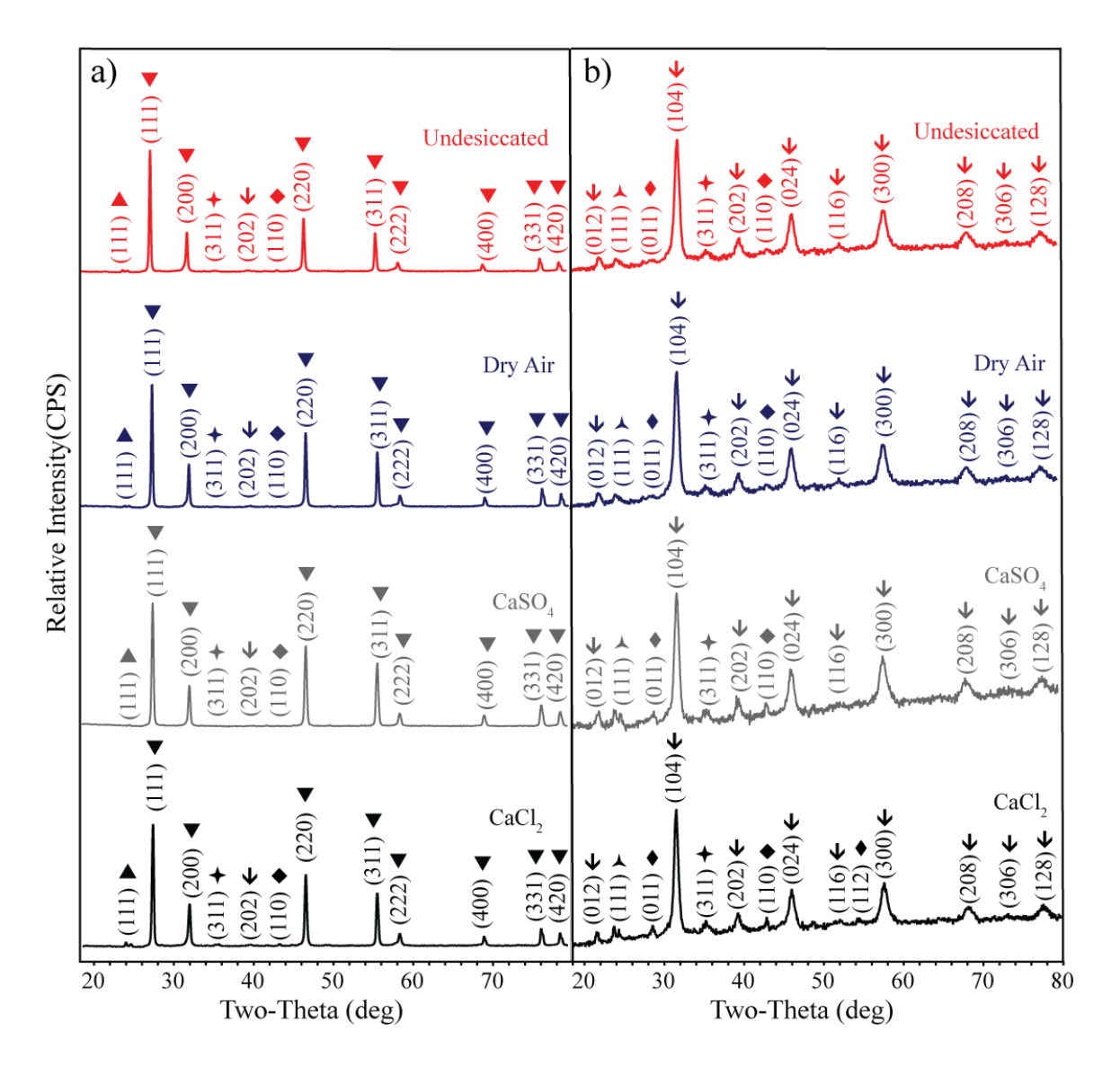


Figure 4.4: XRD Scans of LSCF Nano-Particles Produced by Firing Desiccated Precursor Nitrate Solutions. Solutions were fired at 700°C: a) outside a porous GDC scaffold, and b) inside a porous GDC scaffold. $\blacktriangledown = Ce_{0.9}Gd_{0.1}O_{1.95}$ (JCPDS # 01-075-0161) [118]. $\blacktriangledown = La_{0.6}Sr_{0.4}Co_{0.8}Fe_{0.2}O_3$ (JCPDS # 00-048-0124) [117], $\bigstar = CoCo_2O_4$ (JCPDS # 01-080-1537) [134], $\bigstar = La_2O_3$ (JCPDS # 00-040-1279) [135], $\bigstar = La(Co_{0.42}Fe_{0.58}O_3)$ (JCPDS # 01-074-9369) [136], $\bigstar = La_2O_3$ (JCPDS # 01-071-4953) [137].

4.3.3: Desiccant Impacts on Cathode Electrochemical PerformanceTable 1: **Desiccated TXD LSCF-GDC NMCC Cathodes**. Processing parameters are also shown.

Desiccant Type	LSCF Loading Level (Vol %)	Cathode Thickness (µm)	Scaffold RMS Surface Roughness (µm)	Electrolyte Thickness (µm)	LSCF Diameter (nm)	Total LSCF Surface Area (cm²)	Total GDC Surface Area (cm²)	LSCF Infiltrate Hemispherical Footprint Area/GDC Surface Area (%)	Air-LSCF Surface Area/GDC Surface Area (%)
Undesiccated	12.0	35.2	4.39	457	46	275	146	95	188
Undesiccated	12.0	36.1	4.05	457	46	282	150	95	188
Dry Air	12.0	32.1	4.11	432	30	385	133	145	289
Dry Air	12.0	35.8	3.91	432	30	429	148	145	290
CaSO ₄	12.0	34.9	3.67	432	25	503	145	173	347
CaSO ₄	12.0	36.7	4.64	432	25	529	152	173	348
CaCl ₂	12.0	36.6	4.28	432	22	599	152	197	394
CaCl ₂	12.0	36.2	4.36	432	22	592	150	197	395

Note, desiccants are listed in order of increasing effectiveness [118, 120]. All samples in this table were produced by infiltrating 1.50 M LSCF precursor solution into GDC scaffolds with a geometric area of 0.50 cm², an initial porosity of 32%, and a scaffold column width of 120 nm. See the experimental methods section for additional details.

Figure 4.5 [131, 133] shows EIS data for the LSCF-GDC symmetric cells listed in Table 1. EIS measurements taken using both 50 mV and 100 mV AC amplitudes produced similar results, indicating that these EIS results represent open-circuit behavior. The observed EIS curve shapes were similar to those observed previously for LSCF-GDC NMCCs [6, 7, 9]. As shown in Table 1 [131, 133], the only significant, systematic difference between these cells was the LSCF infiltrate particle size. This suggests that the systematic reduction in polarization resistance with desiccation shown in Figure 4.5 resulted from the reduction in LSCF infiltrate particle size.

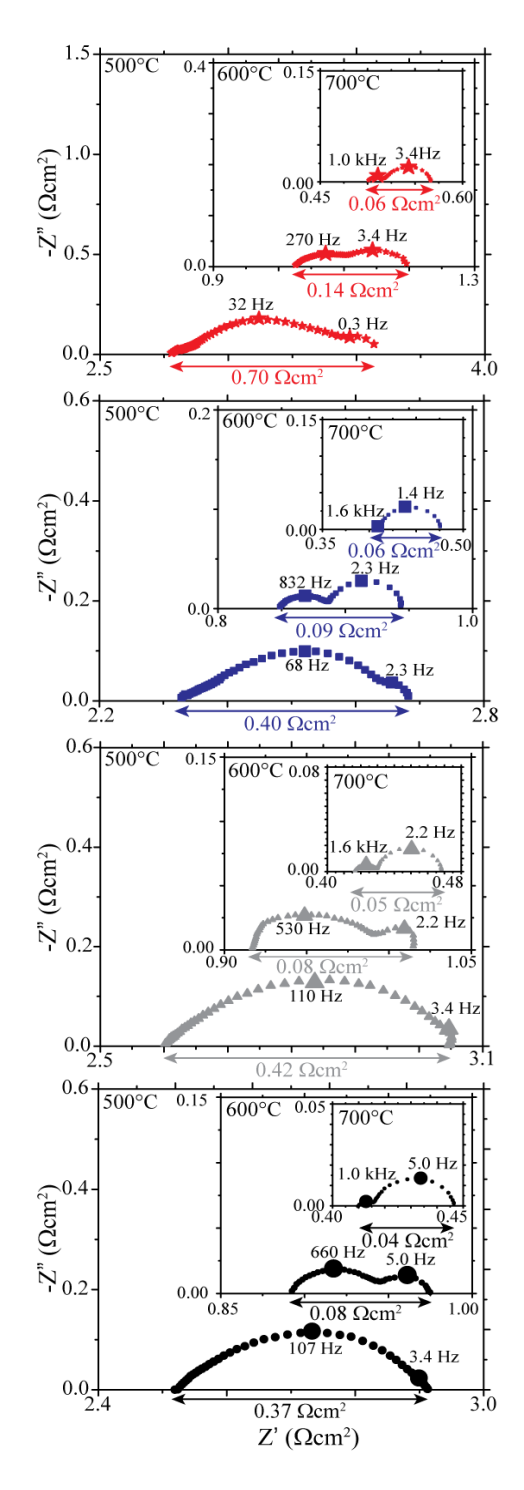


Figure 4.5: Desiccated LSCF-GDC NMCC R_P EIS Nyquist Plot. \star =Undesiccated, \bullet =Dry Air, \blacktriangle =CaSO₄, and \bullet =CaCl₂. Desiccants are listed in order of increasing effectiveness [131,133].

Figure 4.6 (derived from the EIS measurements including those in Figure 4.5) shows that increased amounts of precursor nitrate solution desiccation led to improved SOFC NMCC performance across the full 400-700°C range. Further, the cathode operating temperature (defined here as the temperature at which R_P =0.1 Ω cm², after Steele and Heinzel [16]) decreased from 640°C for an undesiccated LSCF-GDC NMCC to 575°C for a CaCl₂-desiccated LSCF-GDC NMCC. The 1.0-1.1 eV 400-600°C R_P activation energies displayed in Figure 4.6 are similar to the 1.1 eV 400-600°C R_P activation energy for LSCF reported in literature [51]. This suggests that poor oxygen exchange into the LSCF infiltrate particles was the dominant source of NMCC resistance between 400 and 600°C. The 0.56 eV 650-700°C R_P activation energy displayed in Figure 4.6 is identical to the 0.56 eV R_P activation energy for GDC reported [7].

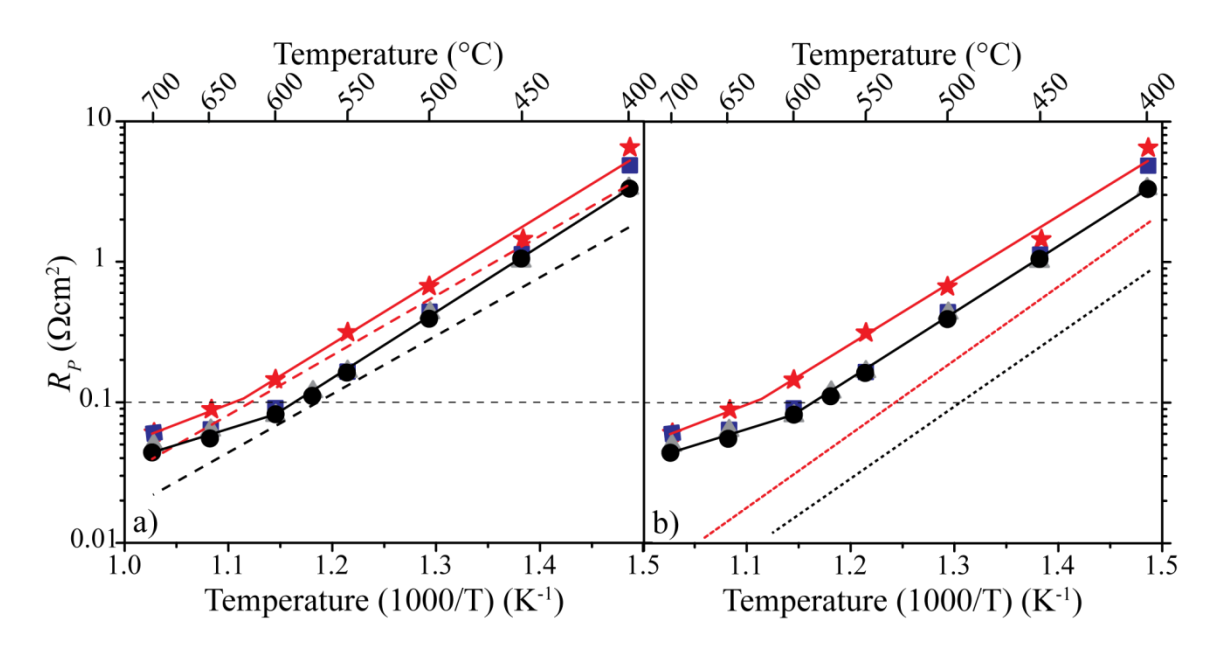


Figure 4.6: **Desiccated LSCF-GDC NMCC** R_P **Arrhenius Plots**. Plots produced by Desiccated Firing Precursor Nitrate Solutions at 700°C. R_P predictions for the undesiccated (top, red) and $CaCl_2$ -desiccated (bottom, black) NMCCs are compared to the a) SIMPLE model, and b) SR model. \neq =Undesiccated, \equiv Dry Air, \triangleq =CaSO₄, and \bullet =CaCl₂. The solid inclined lines are a guide to the eye linking the experimental data. The dashed horizontal line is the 0.1 Ω cm² performance target.

This suggests that poor ionic conduction through the GDC scaffold was the dominant source of NMCC resistance between 650 and 700°C.

Figure 4.6a also shows SIMPLE model [5, 7, 8] predictions for the undesiccated and CaCl₂-desiccated LSCF-GDC NMCCs. These predictions were made using the average SEM-measured particle sizes shown in Figure 4.3, the intrinsic LSCF oxygen surface exchange resistance [51], the GDC oxygen ion conductivity [7], and the NMCC microstructural properties listed in Table 1. Given the microstructural simplicity of the SIMPLE model, it is perhaps unsurprising that the model predictions were not an exact fit to the experimentally measured data. However, it is interesting to note that the factor of two 400-600°C R_P difference predicted by the SIMPLE model when changing the average LSCF infiltrate particle size from 48 nm (the size observed for the undesiccated samples) to 22 nm (the size observed for the CaCl₂-desiccated samples) is similar to the measured 400-600°C R_P difference between the CaCl₂-desiccated and undesiccated samples.

Figure 4.6b shows SR model [5, 7, 8] predictions for the undesiccated and CaCl₂-desiccated LSCF-GDC NMCCs. Like the SIMPLE model, the SR model predicted a factor of two 400-600°C R_P difference when changing the average LSCF infiltrate particle size from 48 nm (the size observed for the undesiccated samples) to 22 nm (the size observed for the CaCl₂-desiccated samples). This difference is close to the experimentally measured 400-600°C R_P difference between the undesiccated and CaCl₂-desiccated NMCCs, suggesting that the observed R_P reductions were solely the result of desiccation-induced infiltrate particle size reductions.

Figure 4.7 shows the performance of identical undesiccated NMCC's tested in air, 20%O₂-80%He, and 20%O₂-80%N₂. If gas concentration polarization were a significant source of resistance, the 3.5 times higher diffusivity of oxygen in a 20%O₂-80%He

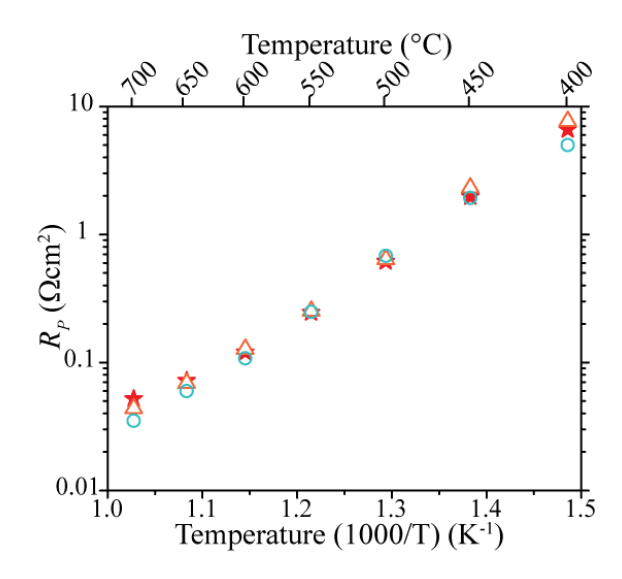


Figure 4.7: Arrhenius R_P Plot for Desiccated LSCF-GDC NMCCs Tested under Different Atmospheres. Air (\star), 20%O₂-80%He (\circlearrowleft), and 20%O₂-80%N₂ (\vartriangle).

mixture compared to that in air or a $20\%\,O2-80\%\,N_2$ mixture would be expected to lead a significantly lower R_P , as has been the case for other SOFC cathodes [126]. However, the essentially identical Figure 4.7 R_P values at $400-600^{\circ}$ C indicate that concentration polarization resistance was not a major source of resistance in undesiccated NMCCs in this temperature range. Therefore, the desiccation-induced R_P performance improvements shown in Figure 4.6 were not the result of a reduction in concentration polarization resistance. Temperature measurements were not conducted in pure O_2 because an oxygen partial pressure greater than air will improve the oxygen diffusion through the cathode microstructure, but also lower the oxygen vacancy concentration in

the MIEC material [95]. All three gas mixtures listed in Figure 4.7 contain approximately the same O_2 concentration where only the O_2 diffusivity was altered.

Figure 4.8 [7] shows that 400-700°C ohmic resistivity of all the NMCCs tested in air. Identical results (not shown) were also observed for the undesiccated NMCCs tested in 20%O₂-80%He and 20%O₂-80%N₂ [7] demonstrated that electronic transfer losses within infiltrated electrodes increase both the polarization resistance and the ohmic resistivity. The good agreement with the ohmic resistivity of each cell and that of pure

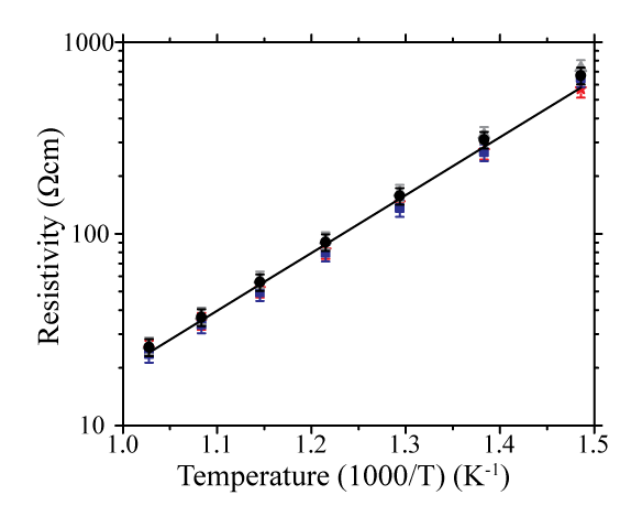


Figure 4.8: Arrhenius Ohmic Resistivity Plots for LSCF-GDC NMCCs Tested in Air. Samples produced by firing desiccated precursor nitrate solutions at 700°C. \star =Undesiccated, \blacksquare =Dry Air, \blacktriangle =CaSO₄, and \bullet =CaCl₂. The inclined solid line is the resistivity of pure GDC from the literature [7].

GDC [7] in Figure 4.8 indicates that oxygen ion transport through the electrolyte was the only source of ohmic resistance and that electronic losses within the current collectors or through the network of MIEC nano-particles were insignificant in magnitude. This indicates that the desiccation-induced R_P performance increases shown in Figure 4.6 were not the result of a reduction in electronic resistance. The fact that the Table 1 LSCF infiltrate hemispherical footprint area to GDC surface area ratios were much greater than

the 44% needed to ensure percolation between randomly deposited non-overlapping circles on a 2D plane [140] also supports this interpretation.

The previously mentioned constancy of the infiltrate phase compositions and fractions with desiccation in Figure 4.4 suggests that the desiccation-induced R_P performance increases shown in Figure 4.6 were not related to changes in LSCF phase purity. Additional studies performed on phase pure LSCF infiltrate showing similar desiccation-induced R_P and infiltrate particle size behavior [61] confirm this.

Taken together, the data in Figures 4.2-4.8 suggest that precursor nitrate solution desiccation led to a reduction in average LSCF infiltrate particle size that, in turn, lead to improved NMCC electrochemical performance. Although not previously recognized as a method to tailor infiltrate particle size, desiccation may be the reason why Bansal and Wise [79] were able to use an unconventional, 15 hour, 300°C precursor nitrate solution pre-heating treatment to produce 15 nm SSC particles, while other studies not employing a precursor nitrate solution pre-heating treatment [5, 7, 30] but using an identical maximum firing temperature of 800°C for 1 hour produced SSC particles larger than 40 nm in diameter. In addition, as mentioned in Section 2.6.1, EISA may be the mechanism which controls the desiccation process to reduce nano-particle size when using Triton X-100. By desiccating the precursor solution prior to thermal decomposition this chapter has shown that desiccation can be a useful tool for tailoring SOFC infiltrate particle size and infiltrated electrode electrochemical performance. Future chapters determine if desiccation has a similar effect on other infiltrate solution compositions, and provide a clearer understanding how desiccation alters infiltrate particle size.

4.4 Summary

This chapter represents the first time that chemical desiccants have been shown to impact the size of infiltrated SOFC nano-particles. For infiltrated LSCF in particular, precursor nitrate solution desiccation and firing at 700° C lowered the average LSCF particle size from 48 to 22 nm. However, desiccation did not alter the infiltrate phase purity, the NMCC concentration polarization resistance, or the NMCC electronic resistance. These results, coupled with mathematical R_P predictions made using the observed infiltrate particle sizes, indicate that the observed 65° C drop in cathode operating temperature was solely the result of desiccation-induced infiltrate particle size reductions. The precursor nitrate solution desiccation technique explored in this chapter may be useful for tailoring the size of nano-particles used as catalysts, fuel cells, and other applications.

CHAPTER 5: The Impact of Surfactants on Desiccated La $_{0.6}$ Sr $_{0.4}$ Co $_{0.8}$ Fe $_{0.2}$ O $_{3-\delta}$ Infiltrated Solid Oxide Fuel Cell Cathodes

5.1 Introduction

Many studies have used organic solution additives (surfactants, such as Triton X-100, and chelating agents, such as Citric Acid, etc.) [5, 7] to alter MIEC precursor solution behavior. Chapter 4 introduced precursor gel desiccation and showed that the desiccation of Triton X-100 containing LSCF precursor nitrate solutions was capable of controlling the average LSCF oxide infiltrate nano-particle size. The objective of this chapter was to examine the effect desiccation has on infiltrate solution nano-particle sizes containing different organic solution additives. A deeper evaluation of the desiccation processes is also conducted.

5.2 Experimental Methods

5.2.1 Cathode-Electrolyte-Cathode Symmetric Cell Production

Symmetrical infiltrated cathode-electrolyte cell fabrication was performed in the same manner as in Section 4.2.1. Specifically, GDC IC scaffolds were screen printed and sintered the same way as in Section 4.2.1. Infiltrated 1.50 molar Triton X-100 derived (TXD), 0.50 molar Citric Acid derived (CAD) LSCF, and 1.50 molar Pure nitrate derived (PND) precursor solutions were infiltrated into sintered GDC IC scaffolds, desiccated, and fired in the same manner as Section 4.2.1. Infiltrated TXD LSCF precursor solutions were prepared in the same manner as Section 4.2.1 and PND LSCF precursor solutions are the same as TXD LSCF solutions without the addition of a solution additive. Infiltrated CAD LSCF precursor solutions were fabricated by first

dissolving 99.999% pure La(NO₃)₃*6.3 H₂O, 99.9965 % pure Sr(NO₃)₂, 99.999% pure Co(NO₃)₂*5.67 H₂O, and 99.999% pure Fe(NO₃)₃*9.42 H₂O (Alfa Aesar; Ward Hill, MA, USA) in distilled water containing 0.75 mol Citric Acid/mol metal nitrates. (These precise nitrate water of hydration contents were determined prior to nitrate weighing by measuring the mass loss that occurred inside a Q500 thermogravimetric analyzer (TA Instruments; New Castle, DE, USA) with heating under nitrogen up to 850°C). These different molar solutions were then allowed to soak into the porous GDC scaffolds and gelled in a similar manner as Section 4.2.1. Desiccation times were based on previous desiccation kinetics literature studies [131]. PND LSCF, CAD LSCF, and TXD LSCF infiltrated cells were all heated to 700°C at 10°C/min, held at 700°C for one hour, and then cooled to room temperature at a nominal cooling rate of 20°C/min after being desiccated. This infiltrate-gel-desiccate-fire routine was repeated up to 6 times to achieve the desired MIEC loading level of 12.0 vol%. Lastly (LSM) – Au current collectors were screen printed onto the surface of each NMCC.

5.2.2 Symmetric Cell Impedance Measurements

Just like in Section 4.3.3 NMCC performance as a function of temperature was evaluated in air, 20%O₂-80%He, or 20%O₂-80%N₂ under open circuit conditions using EIS. Measurements in ambient air were performed in a static atmosphere, while controlled atmosphere experiments in 20%O₂-80%He and 20%O₂-80%N2 were performed with a 100 mL/min flow rate. Since each atmosphere contained 20% O₂ the only difference was the diffusivity of O₂ in those mixtures. EIS measurements were taken in the same manner as Section 4.2.2.

5.2.3 X-ray Diffraction Measurements

MIEC infiltrate phase purity was evaluated using XRD in the same manner as was described in Section 4.2.3.

5.2.4 Scanning Electron Microscopy Measurements

NMCC microstructure was evaluated after EIS testing using an Auriga Dual Column Focused Ion Beam-Scanning Electron Microscope (FIB-SEM) (Carl Zeiss Microscopy GmbH; Jena, Germany) in the same manner as was described in Section 4.2.4.

5.2.5 Nano-Micro-Composite Cathode Performance Modeling

The NMCC performance was modeled using the SIMPLE model [5, 7, 8] and was performed in the same manner as was described in Section 4.2.5.

5.2.6 Williamson-Hall Particle Size and Strain Calculations

LSCF nano-particle sizes were calculated via the XRD Williamson-Hall method [122] for powders fabricated outside a GDC scaffold. The full-width half-max (FWHM) values for the LSCF peaks located at ~22.7°, ~40.7°, and ~46.9° (2-Theta) were used for TXD LSCF and CAD LSCF precursor solutions, but PND LSCF precursor solutions calculated particle sizes using peaks only at ~22° and ~40.7° due to the PND LSCF solutions being amorphous even at firing temperatures above 600° C. The Lorentzian profile shape function using a parabolic background was used to determine the FWHM values using JADE 9. The breadth (β) of each peak was calculated using the FWHM values. The linear intercept values from plots of β *Cos(theta) vs 4*Sin(theta) were then used to calculate nano-particle size and strain values in the same manner described in Section

3.2.4. All other peaks had multiple planes that contribute to peak broadening and therefore could not be used to determine particle size from XRD peak broadening.

5.3 Results

5.3.1: Desiccant and Solution Additive Impacts on Infiltrate Particle Size

Table 2 shows the processing parameters used when fabricating symmetrical PND, TXD, or CAD LSCF NMCCs. Since the precursor solutions used different molarities, (0.5M and 1.5M), the infiltrate MIEC particle size was evaluated to see if it was influenced by precursor solution molarity. As shown in Table 2 nano-particle size, at least for PND and TXD LSCF precursor solutions were not altered by the solution molarity. Due to precursor nitrate solubility's it was not possible to make a 1.5 molar CAD LSCF precursor solution. Similarly the precursor solution infiltration volume was found to not influence the infiltrated oxide nano-particle size. These results indicate that it was legitimate to compare particle sizes between the 1.5 molar PND 1.5 molar TXD, and 0.5 molar CAD LSCF solutions.

Figure 5.1 [131, 133] shows that the infiltrated nano-particle size using PND LSCF and TXD LSCF did not change when using different solution molarities.

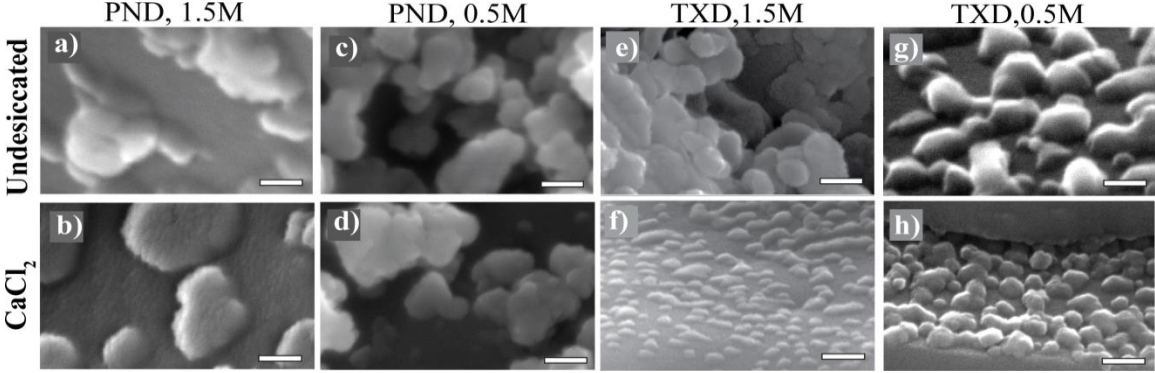


Figure 5.1: Scanning Electron Micrographs of Desiccated LSCF Nano-Particles Produced by using Different Triton X-100 Solution Volumes. 1.5 molar PND LSCF using a) undesiccated and b) desiccated precursor solutions, and 0.50 molar TXD LSCF c) undesiccated and d) desiccated precursor solutions inside GDC scaffolds at 700°C. Note, desiccants are listed in order of increasing effectiveness [131,133]. Each scale bar is 50 microns in width.

Table 2: Desiccated PND, TXD and CAD LSCF-GDC NMCC Cathodes. Processing parameters are also shown.

Surfactant	Desiccant Type	Firing Temperature (°C)	LSCF Loading Level (%)	Number of LSCF Infiltrations	LSCF Nitrate Solution Molarity	Cathode Thickness (µm)	Scaffold RMS Surface Roughness (µm)	Volume of Solution per Infiltration (µL)	Cathode Geometric Area (cm²)	Cathode Porosity (%)	Scaffold Column Width (nm)	LSCF Diameter (nm)	Total LSCF Surface Area (cm²)	Total GDC Surface Area (cm²)	LSCF Surface Area/GDC Surface Area (%)
PND	Undesiccated	700	12.0	3	1.5	35.7	4.00	2.78	0.5	32	120	65	198	148	134
PND	Undesiccated	700	12.0	3	1.5	36.3	4.05	2.82	0.5	32	120	65	202	151	134
PND	Undesiccated	700	12.0	6	0.5	35.4	3.50	4.13	0.5	32	120	62	206	147	140
PND	Undesiccated	700	12.0	6	0.5	36.4	3.41	4.25	0.5	32	120	62	212	151	140
PND	Dry Air	700	12.0	3	1.5	34.3	3.50	2.67	0.5	32	120	73	170	142	120
PND	Dry Air	700	12.0	3	1.5	35.2	3.90	2.74	0.5	32	120	73	174	146	120
PND	$CaSO_4$	700	12.0	3	1.5	36.3	4.30	2.82	0.5	32	120	72	182	151	121
PND	$CaSO_4$	700	12.0	3	1.5	36.0	4.42	2.80	0.5	32	120	72	180	149	121
PND	CaCl ₂	700	12.0	3	1.5	35.2	4.61	2.74	0.5	32	120	71	179	146	123
PND	CaCl ₂	700	12.0	3	1.5	35.7	4.04	2.78	0.5	32	120	71	182	148	123
PND	CaCl ₂	700	12.0	6	0.5	34.8	4.10	4.06	0.5	32	120	70	179	144	124
PND	CaCl ₂	700	12.0	6	0.5	35.8	3.95	4.18	0.5	32	120	70	185	148	125
CAD	Undesiccated	700	12.0	6	0.5	34.2	3.74	3.98	0.5	32	120	50	246	142	173
CAD	Undesiccated	700	12.0	6	0.5	34.5	3.54	4.02	0.5	32	120	50	249	143	174
CAD	Dry Air	700	12.0	6	0.5	26.7	3.84	3.11	0.5	32	120	43	224	111	202
CAD	Dry Air	700	12.0	6	0.5	31.8	4.67 8	3.70	0.5	32	120	43	266	132	202
CAD	$CaSO_4$	700	12.0	6	0.5	27.7	4.62	3.23	0.5	32	120	42	237	115	207
CAD	$CaSO_4$	700	12.0	6	0.5	29.5	4.35	3.44	0.5	32	120	42	253	122	207
CAD	CaCl ₂	700	12.0	6	0.5	32.1	3.50	3.74	0.5	32	120	41	282	133	212
CAD	CaCl ₂	700	12.0	6	0.5	34.1	3.55	3.97	0.5	32	120	41	300	141	213
TXD	Undesiccated	700	12.0	3	1.5	35.2	4.39	2.74	0.5	32	120	48	275	146	188
TXD	Undesiccated	700	12.0	3	1.5	36.1	4.05	2.81	0.5	32	120	48	282	150	188
TXD	Undesiccated	700	12.0	3	0.5	36.0	3.50	8.40	0.5	32	120	49	254	149	170
TXD	Undesiccated	700	12.0	9	0.5	36.3	3.41	2.82	0.5	32	120	51	256	151	170
TXD	Dry Air	700	12.0	3	1.5	32.1	4.11	2.50	0.5	32	120	30	385	133	289
TXD	Dry Air	700	12.0	3	1.5	35.8	3.91	2.78	0.5	32	120	30	429	148	290
TXD	$CaSO_4$	700	12.0	3	1.5	34.9	3.67	2.71	0.5	32	120	25	503	145	347
TXD	$CaSO_4$	700	12.0	3	1.5	36.7	4.64	2.85	0.5	32	120	25	529	152	348
TXD	$CaCl_2$	700	12.0	3	1.5	36.6	4.28	2.84	0.5	32	120	22	599	152	394
TXD	$CaCl_2$	700	12.0	3	1.5	36.2	4.36	2.81	0.5	32	120	22	592	150	395
TXD	CaCl ₂	700	12.0	3	0.5	35.2	4.30	8.20	0.5	32	120	23	551	146	377
TXD	CaCl ₂	700	12.0	9	0.5	36.6	4.21	2.85	0.5	32	120	23	575	152	378

Figure 5.2 [131, 133] shows SEM images of undesiccated and CaCl₂-desiccated symmetrical cells infiltrated with 0.50 molar TXD LSCF precursor solutions using different infiltration solution volumes. Figure 5.2 shows that the infiltration solution volume did not impact the average infiltrated oxide nano-particle size.

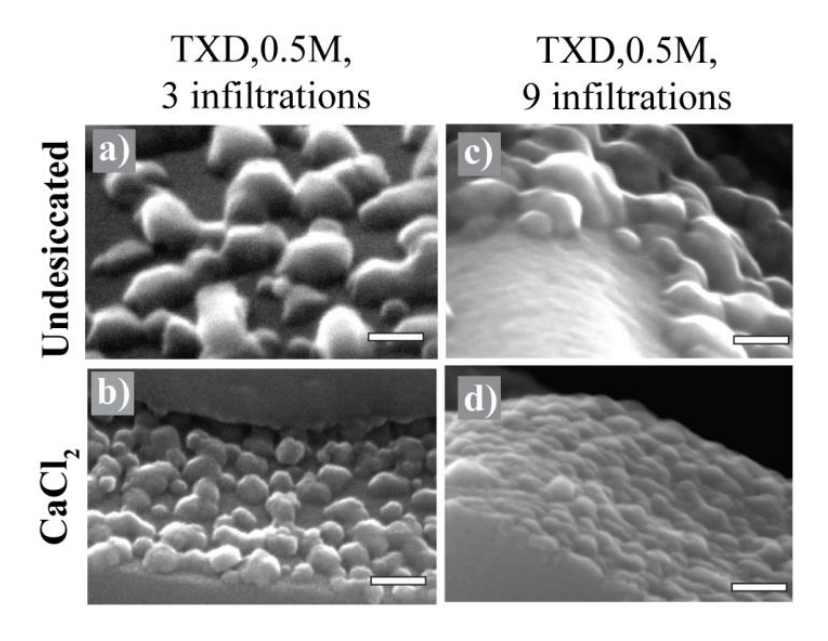


Figure 5.2: Scanning Electron Micrographs of Desiccated LSCF Nano-Particles Produced using Different Solution Additives. Samples used a) undesiccated 3 infiltrations, b) desiccated 3 infiltrations, c) undesiccated 9 infiltrations and d) desiccated 9 infiltrations, precursor solutions inside GDC scaffolds at 700°C. Note, desiccants are listed in order of increasing effectiveness [131,133]. Each scale bar is 50 microns in width.

Figure 5.3 [131, 133] shows that desiccation reduced the nano-particle size of TXD LSCF and CAD LSCF, but not the PND LSCF nano-particle size. SEM images of these infiltrated NMCCs show that both TXD and CAD nano-particles decreased their average size as the strength of the desiccant increased, while PND infiltrated oxide nano-particle sizes remained constant with increasing desiccant strength. Specifically, the TXD average infiltrated oxide nano-particle sizes were reduced from 50 nm to 22 nm, the CAD average infiltrated oxide nano-particle sizes were reduced from 48 nm to 41 nm and

the PND infiltrated oxide average nano-particle sizes remained constant with increasing chemical or physical desiccation strength at around 70 nm in diameter on average.

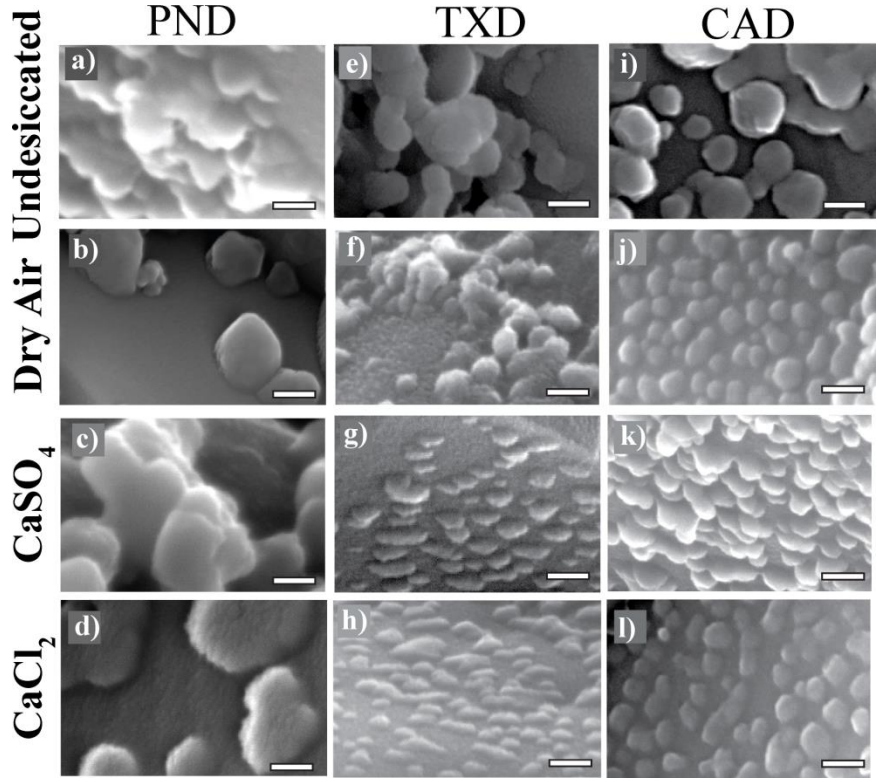


Figure 5.3: Scanning Electron Micrographs of Desiccated LSCF Nano-Particles Produced using Different Solution Additives. Pure nitrate-containing precursor nitrate solutions (a-d), 1.50 molar Triton X-containing precursor nitrate solutions (e-h) and 0.50 molar Citric Acid-containing precursor solutions (i-l) inside GDC scaffolds at 700°C. Note, desiccants are listed in order of increasing effectiveness [131,133]. Each scale bar is 50 microns in width.

Figure 5.4 shows the raw data used to calculate the XRD Williamson-Hall particle sizes and strains for the LSCF particles resulting from PND, TXD and CAD LSCF precursor solutions fired at 600°C, 700°C and 800°C outside a GDC scaffold. Due to the amorphous nature of the 600 and 700°C fired PND LSCF (as mentioned above) Williamson-Hall particle sizes could only be determined at the 800°C firing temperature. Further, particle sizes for the 800°C PND LSCF were calculated using only two peaks (instead of the standard 3) due to the amorphous nature of the powder. In all cases, a

linear relation between $\beta Cos(\theta)$ and $4Sin(\theta)$ indicating that the Williamson-Hall technique could be applied to determine size and strain.

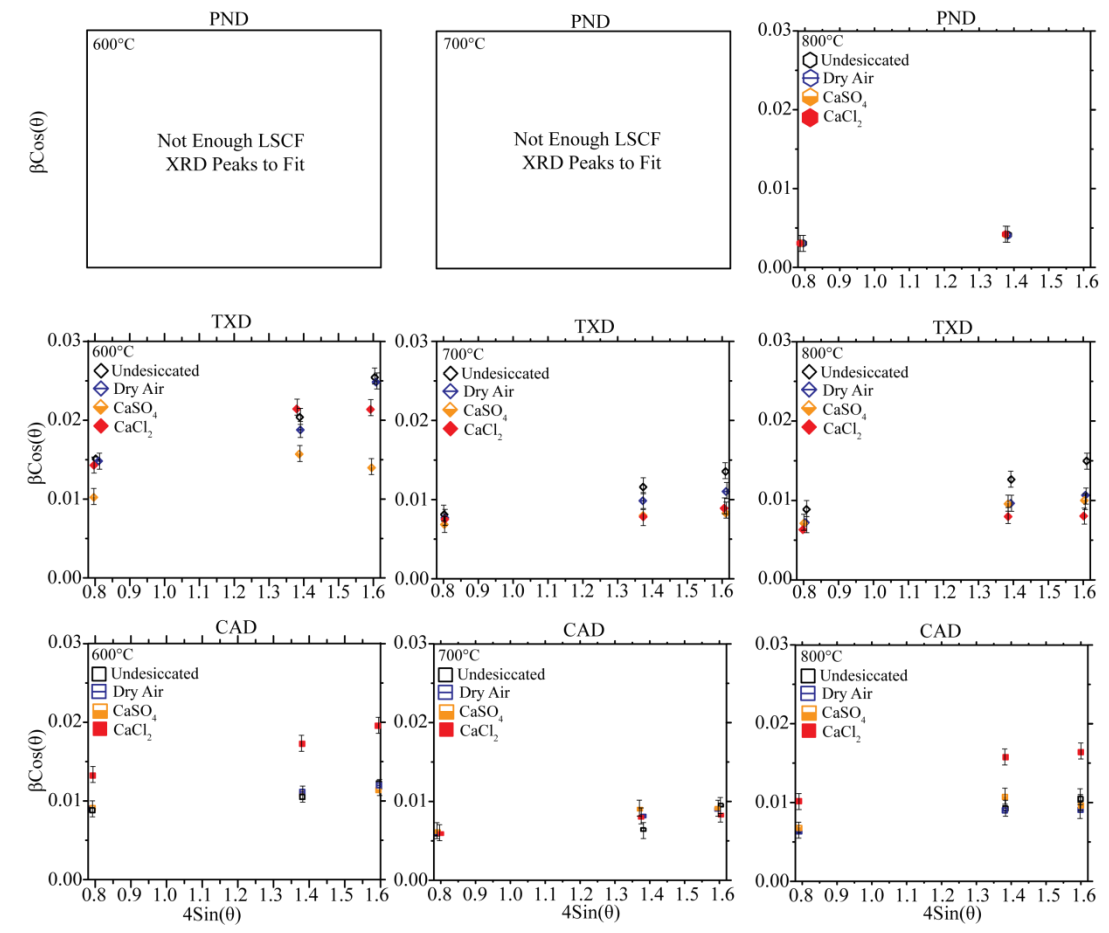


Figure 5.4: Desiccated Williamson-Hall Raw Data Plot for PND LSCF, TXD LSCF and CAD LSCF Nano Particles. Data was collected from XRD scans from samples fired at 600°C, 700°C and 800°C.

Figure 5.5 shows the XRD Williamson-Hall calculated strain % determined from Figure 5.4 for the desiccated LSCF nano powders outside a GDC scaffold using PND, TXD and CAD solution additives. Strain was calculated directly from the slope of each data set in Figure 5.4 using the error bars to calculate the standard deviation values shown in Figure 5.5.

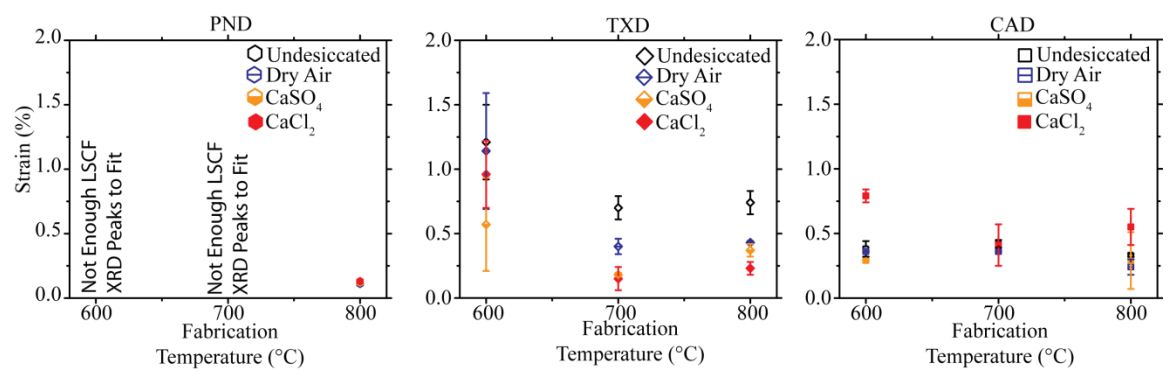


Figure 5.5: Strain Plots for Desiccated PND LSCF, TXD LSCF and CAD LSCF Nano-Particles. Strain was calculated using undesiccated, dry air, CaSO₄, and CaCl₂ desiccants fired at 600°C, 700°C and 800°C for 1 hr.

Overall, the strain for PND LSCF nano-particles, for all desiccation strengths, was much lower than CAD and TXD LSCF strain values, and was consistently similar in magnitude. Since the PND LSCF nano-particles also did not change size with desiccation strength it also makes sense the desiccation would not impact the PND LSCF nano-particle strain either. The TXD and CAD LSCF nano-particles showed similar trends where the strain was greatest at 600°C, was then reduced at 700°C, and stayed relatively constant at 800°C. The strain magnitude for TXD LSCF nano-particles at 600°C did show some overlap shown by the error bars. Overall the effect of desiccation on strain for TXD LSCF and CAD LSCF nano-particles is not conclusive.

Figure 5.6 [131, 133] shows the average oxide nano-particle sizes for PND, TXD and CAD LSCF using various desiccant strengths when fired at 600°C, 700°C or 800°C for 1 hr. Using the techniques described in Section 4.2.4 the particle sizes were calculated directly from the SEM images shown in Figure 5.3, and standard deviation values were also calculated from the same SEM images. In Figure 5.6 the SEM calculated particle sizes are displayed as opaque colored bars in the foreground. XRD Williamson-Hall calculated particle sizes from LSCF powders were also shown in transparent colors and were calculated from the raw XRD Williamson-Hall data in Figure

5.4. XRD particle sizes were unable to be calculated for the PND LSCF powders fabricated at 600°C and 700°C due to the powders being amorphous. In contrast, both TXD and CAD LSCF oxide nano-particle sizes were reduced when using desiccation, at least when fabricated above 600°C. Figure 5.6 shows that PND LSCF nano-particle sizes were not reduced with desiccation at 600°C, 700°C or 800°C, (the average nano-particle size is depicted in Figure 5.6 as a solid horizontal black line to show that the average nano-particle size for each fabrication temperature) was within the standard deviation for each temperature, and thus was not influenced by desiccation. The black horizontal bar in the 600°C TXD and CAD LSCF data indicates that desiccation had no effect on the particle size of TXD and CAD LSCF fired to 600°C.

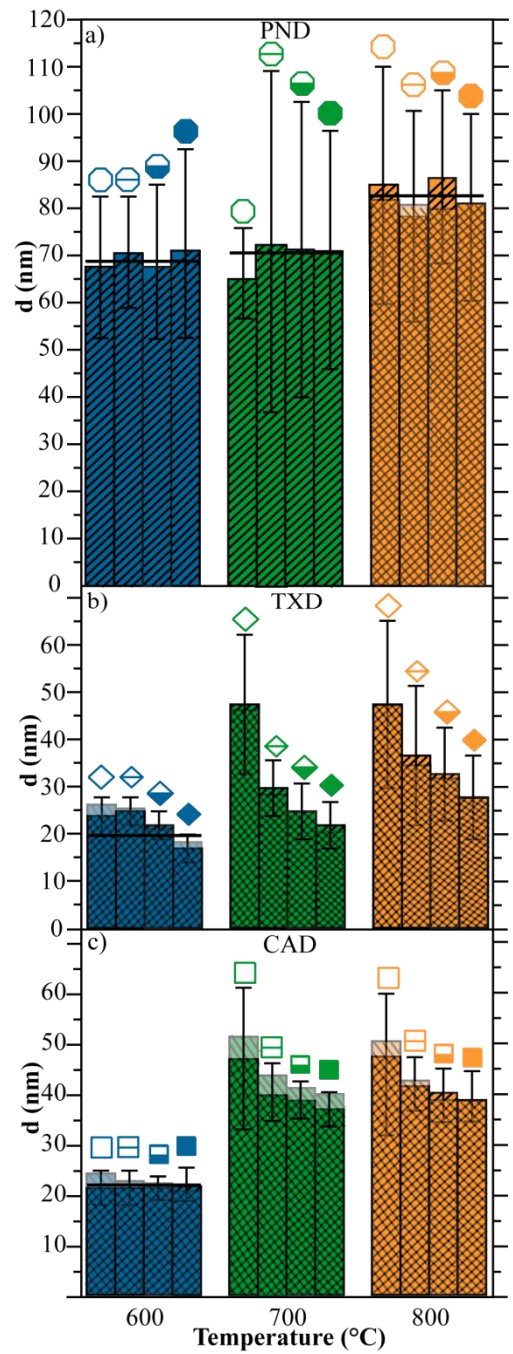


Figure 5.6: Bar-Graph of Average Desiccated LSCF Infiltrate Particle Size Produced using Different Solution Additives. Samples were: a) 1.50 molar pure nitrate-containing, (b) 0.50 molar Citric Acid-containing and c) 1.50 molar Triton X-containing precursor nitrate solutions at various temperatures. PND: \bigcirc = Undesiccated, \bigcirc = Dry Air, \bigcirc = CaSO₄, and \bigcirc = CaCl₂ CAD: \square = Undesiccated, \bigcirc = Dry Air, \bigcirc = CaSO₄ and \bigcirc = CaCl₂ and TXD: \bigcirc = Undesiccated, \bigcirc = Dry Air, \bigcirc = CaSO₄ and \bigcirc = CaCl₂. Particle size data collected from SEM images are shown with 100% opacity and are striped pointing to the left, while particle size data collected using the Williamson-Hall method are shown with 50% opacity and are striped pointing to the right. Desiccants are listed in order of increasing effectiveness [131,133]. Error bars are +/- a standard deviation calculated using the SEM-measured particle size distribution.

Figure 5.7 [131, 133] shows the raw EIS data for the desiccated CAD LSCF (left) and TXD LSCF (right) symmetrical cells at 500°C, 600°C and 700°C operating temperatures. The outermost nested impedance data was taken at an operating temperature of 500°C while the innermost nested impedance data was taken at an operating temperature of 700°C. PND LSCF raw data was collected for both the undesiccated and CaCl₂-desiccated cases, but showed no change in performance when desiccated. On the other hand, both the CAD and TXD LSCF raw EIS data show that the cathode resistance decreases with both increasing temperature and increasing desiccation strength.

Figure 5.8 shows the R_P data for desiccated PND, CAD and TXD LSCF symmetrical cells determined from the raw EIS data of Figure 5.7. Consistent with the collected particle size trends, the R_P data for CAD and TXD LSCF were both reduced with increasing desiccation strength, while PND did not change R_P with desiccation. Desiccation lowered the operating temperature (the temperature at which a R_P value of 0.1 Ω cm² is achieved) from 650°C to 570°C with TXD, and from 700°C to 650°C with CAD. In Figure 5.8 SIMPLE model R_P predictions are also included for the undesiccated and CaCl₂-desiccated cases using LSCF nano-particle sizes from Figure 5.1. For TXD and CAD LSCF, the SIMPLE model predictions show similar R_P reductions compared to the experimental results suggesting that nano-particle size reduction causes the measured performance gains. The SIMPLE model predictions also do not show any change in R_P for PND LSCF which makes sense since Figure 5.1 shows no change in particle size. The SIMPLE model in all cases predicts lower R_P values than the experimental results because (as mentioned in Section 2.5.2) the SIMPLE model does not take into account

tortuosity effects in the scaffold microstructure which can provide an additional source of resistance.

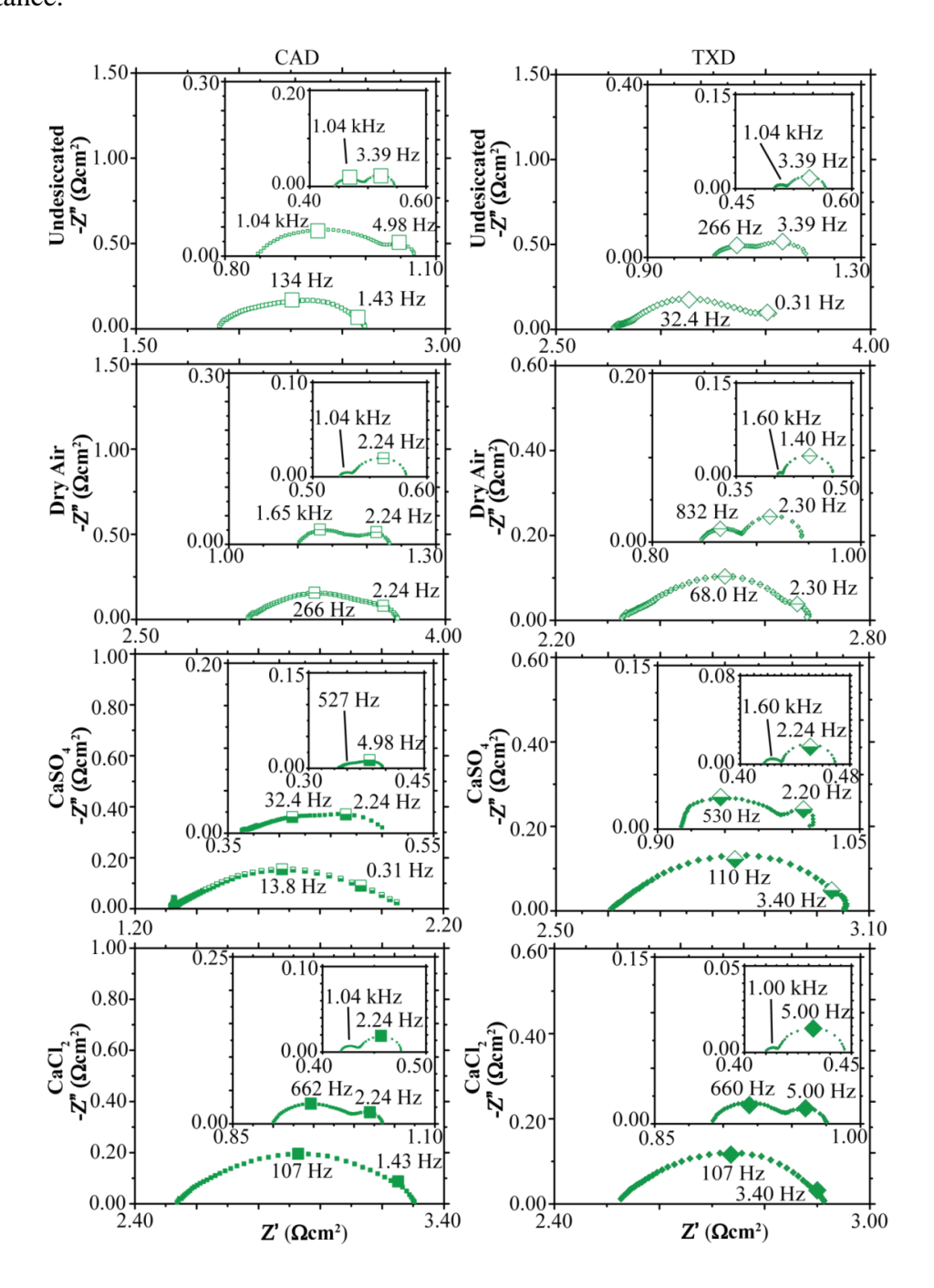


Figure 5.7: Raw Impedance Data Plots of Desiccated LSCF-GDC NMCCs Produce using Citric Acid and Triton X-100. Samples are: 0.50 molar CAD LSCF (left) and 1.50 molar TXD LSCF (right) precursor nitrate solutions fired at 700°C. The outermost data was taken at 500°C, the nested data was taken at 600°C and the double nested data was taken at 700°C. CAD: \Box =Undesiccated, \Box =Dry Air, \Box =CaSO₄, and \blacksquare =CaCl₂ TXD: \diamondsuit =Undesiccated, \Longrightarrow =Dry Air, \Longrightarrow =CaSO₄ and \clubsuit =CaCl₂. Desiccants are listed in order of increasing effectiveness [131,133].

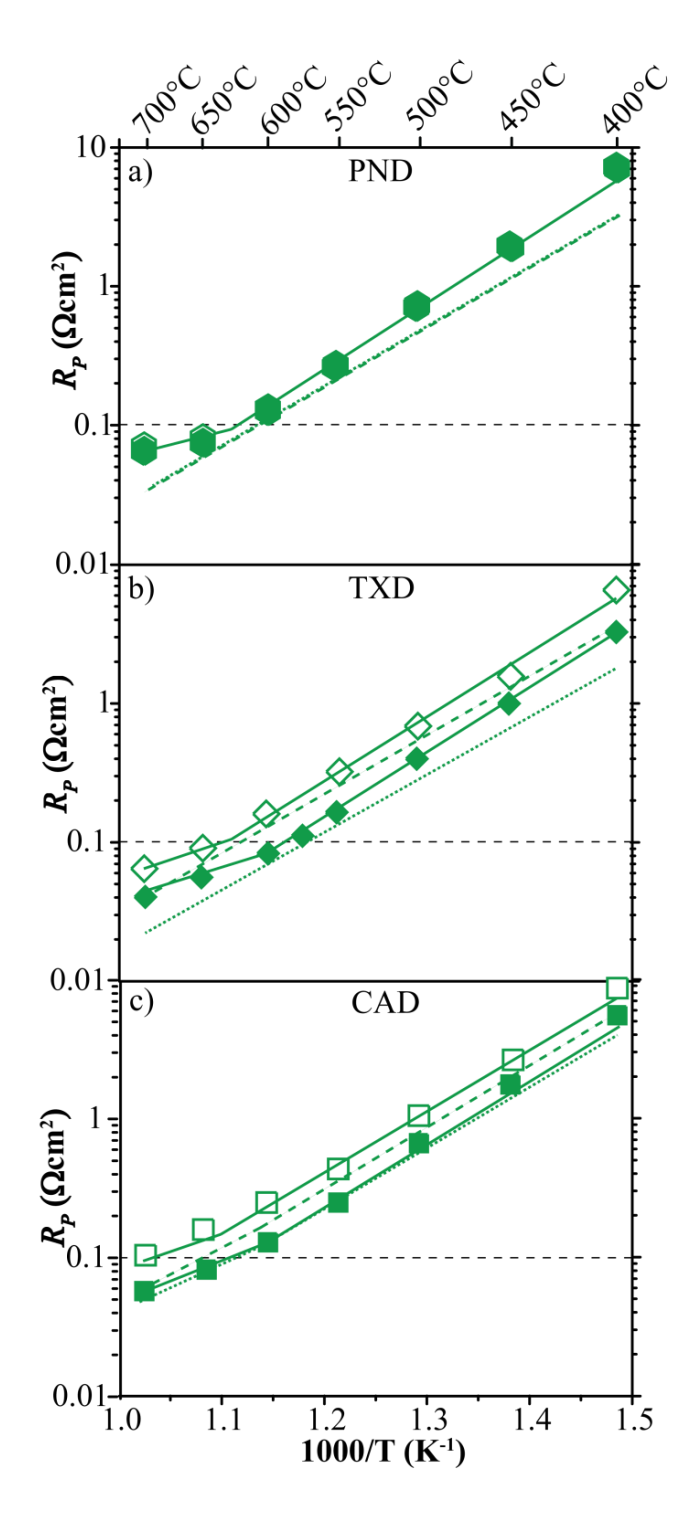


Figure 5.8: LSCF-GDC R_P Arrhenius Plots for Desiccated NMCCs Produced using Different Solution Additives. Samples are: a) 1.50 molar PND LSCF, b) 0.50 molar CAD LSCF, and c) 1.50 molar TXD LSCF precursor nitrate solutions fired at 700°C for 1 hour. PND: \square =Undesiccated, \square =CaCl2, CAD: \square =Undesiccated, \square =CaCl2 and TXD: \square =Undesiccated and \square =CaCl2. The solid inclined lines are a guide to the eye linking the experimental data. The dashed inclined lines are SIMPLE model predictions for the undesiccated and CaCl2 cases. The dashed horizontal line is the 0.1 Ω cm² performance target.

Figure 5.9 [7] shows the ohmic resistivity of the GDC IC scaffold at the different operating temperatures. All the ohmic resistivity data for PND, CAD and TXD LSCF symmetrical cells match the resistivity of pure GDC, which indicated that differences in performance shown in Figure 5.8 were not caused by electronic losses in the scaffold.

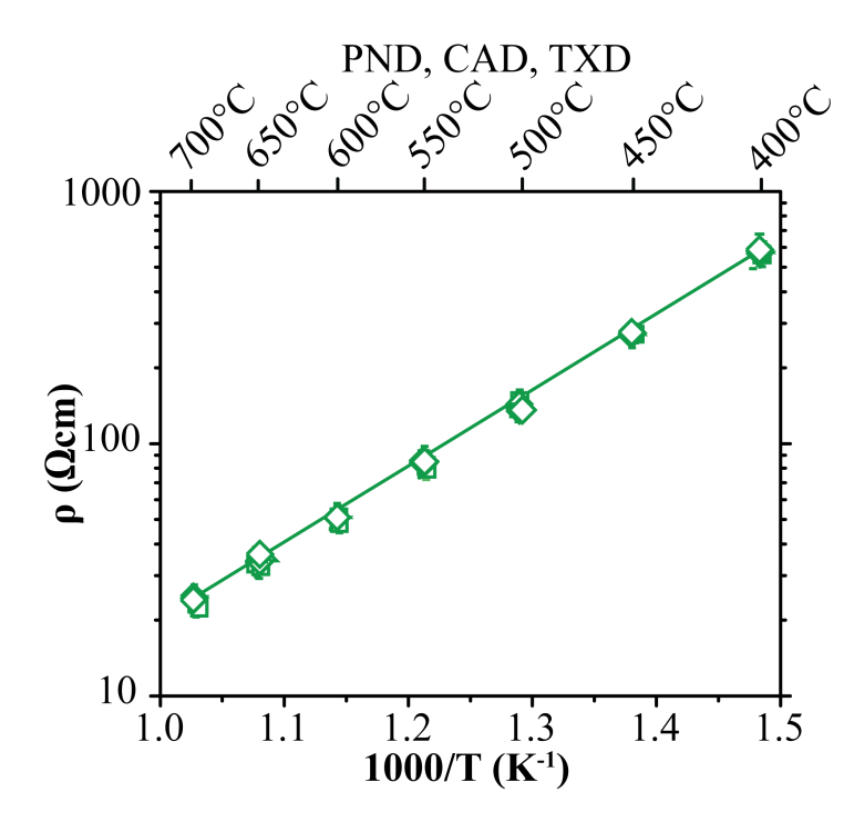


Figure 5.9: Arrhenius Ohmic Resistivity Plots for Desiccated LSCF-GDC NMCCs Tested in Air and produced using Different Solution Additives. Samples are fired at 700°C. PND: \Box = Undesiccated, \Box = Dry Air, \Box = CaSO4, \Box = CaCl2, CAD: \Box = Undesiccated, = Dry Air, = CaSO4, \Box = CaCl2 and TXD: \Box = Undesiccated, \Box = Dry Air, \Box = CaSO4 and \Box = CaCl2. The inclined solid line is the resistivity of pure GDC from literature [7].

5.3.2: Desiccant and Solution Additive Impacts on Infiltrate Phase Purity

Figure 5.10 shows ex-situ XRD data for PND, TXD and CAD LSCF oxide powders fired at 700°C for 1 hr using different desiccants. PND LSCF oxide powder XRD scans are shown on the left column, TXD LSCF oxide powder XRD scans are shown on the middle column, and CAD LSCF oxide powder XRD scans are shown on the right column. Each column, going from top to bottom, depicts XRD scans of each powder using increasingly stronger desiccants. Comparison of the measured XRD data with JCPDS reference spectrum [117, 134-137, 141, 142] indicates that LSCF was the dominant phase by volume in all cases. Within the leftmost column the phase impurity of the PND LSCF powder decreases with increasing desiccant strength, while the secondary phase impurity of the TXD LSCF and CAD LSCF powders remains relatively constant when using different desiccants. The fact that desiccant strength does not change the

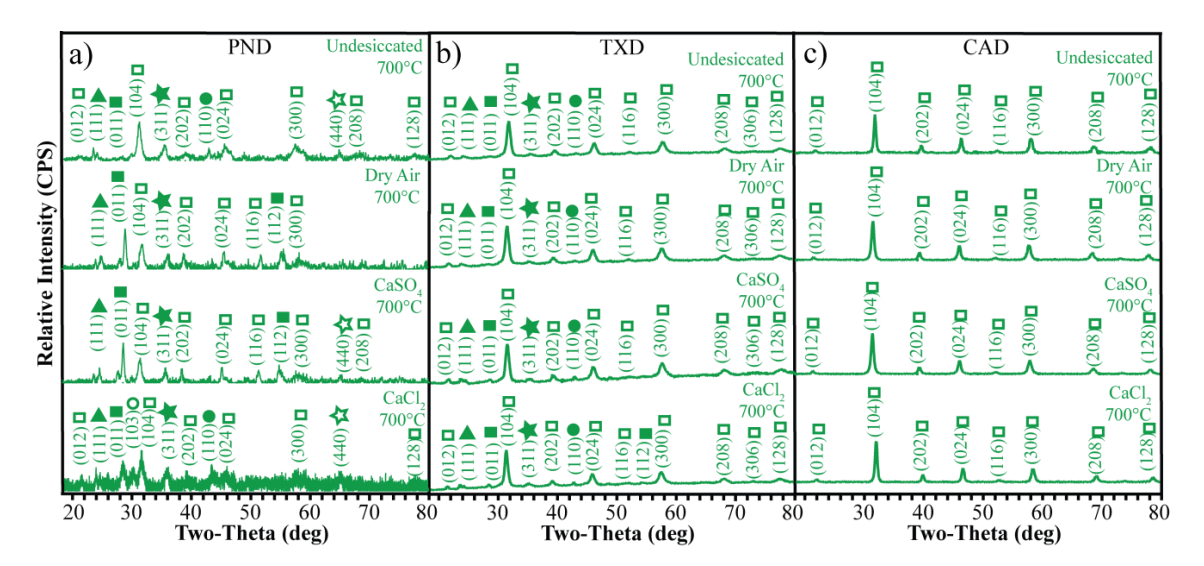


Figure 5.10: XRD Scans of Desiccated LSCF Nano-Particles Produced using Different Solution Additives. Samples are: a) 1.50 molar PND LSCF, b) 0.50 molar CAD LSCF, and c) 1.50 molar TXD LSCF nitrate solutions fired at 700°C. □= $La_{0.6}Sr_{0.4}Co_{0.8}Fe_{0.2}O_3$ (JCPDS # 00-048-0124) [117], $\not= Co_3O_4$ (JCPDS # 01-074-2120)[141], $\not= CoCo_2O_4$ (JCPDS # 01-080-1537)[134], $O=(La_{0.38}Sr_{0.62})_2FeO_4$ (JCPDS # 01-072-7576) [142], $O=(La_{0.38}Sr_{0.62})_2FeO_4$ (JCPDS # 01-072-7576) [142], $O=(La_{0.38}Sr_{0.62})_2FeO_4$ (JCPDS # 01-072-7576) [136], $O=(La_{0.38}Sr_{0.62})_2FeO_4$ (JCPDS # 01-074-9369) [136], $O=(La_{0.38}Sr_{0.62})_2FeO_4$ (JCPDS # 01-074-9369) [136], $O=(La_{0.38}Sr_{0.62})_2FeO_4$ (JCPDS # 01-074-953) [137].

secondary phase impurity fraction significantly for TXD and CAD LSCF powder suggests that LSCF phase purity changes were not responsible for the performance changes observed in Figure 5.8.

Figure 5.11 [117] shows undesiccated and CaCl₂-desiccated XRD data for PND LSCF precursor solutions fired at various temperatures between 80°C and 800°C. The phase purity of the undesiccated powder, compared to the CaCl₂-desiccated powder, did not improve and actually became worse at temperatures 600°C and above. The PND LSCF phase became dominant at fabrication temperatures of 700°C or greater.

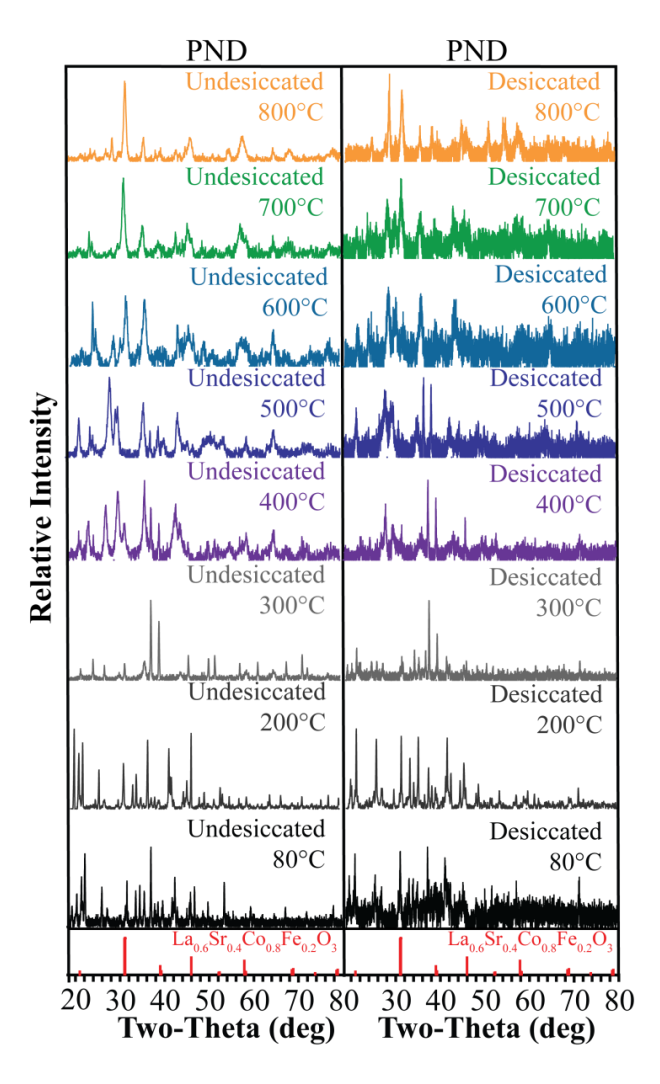


Figure 5.11: XRD Scans for CaCl₂-Desiccated PND LSCF Fired between 80° C and 800° C. $La_{0.6}Sr_{0.4}Co_{0.8}Fe_{0.2}O_{3-\delta}$ (PDF #00-048-0124) [117].

Figure 5.12 [117] shows undesiccated and dry air-desiccated XRD data for TXD LSCF precursor solutions fired at various temperatures between 80°C and 800°C. The phase purity of the undesiccated powder compared to the desiccated powder was improved at 600°C, 500°C, 400°C and 80°C, while 300°C and 200°C did not show any significant difference.

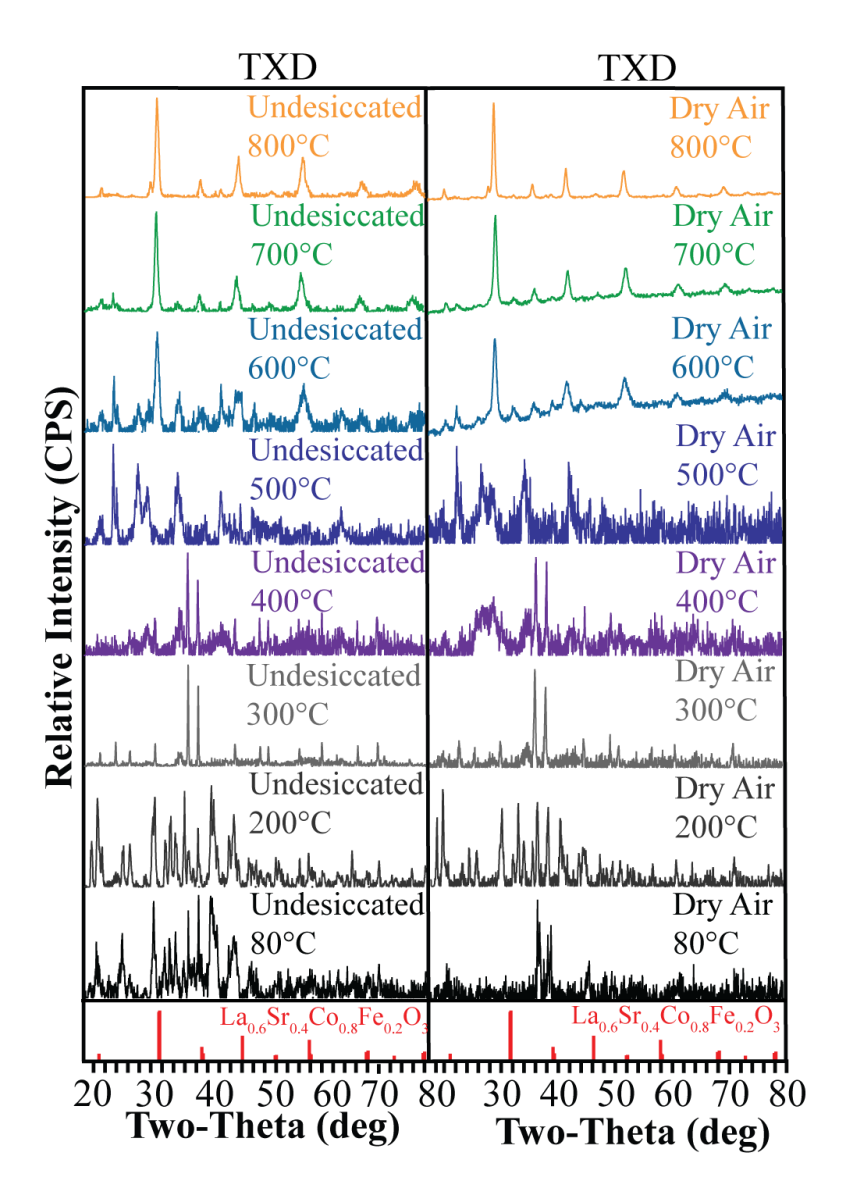


Figure 5.12: XRD Scans for Dry Air-Desiccated TXD LSCF Fired between 80°C and 800°C. $La_{0.6}Sr_{0.4}Co_{0.8}Fe_{0.2}O_{3-\delta}$ (PDF #00-048-0124) [117].

Figure 5.13 [117] shows undesiccated and CaSO₄-desiccated XRD data for TXD LSCF precursor solutions fired at various temperatures between 80°C and 800°C. The phase purity was similar to the previous plot (as far as the phases present and their relative percentage).

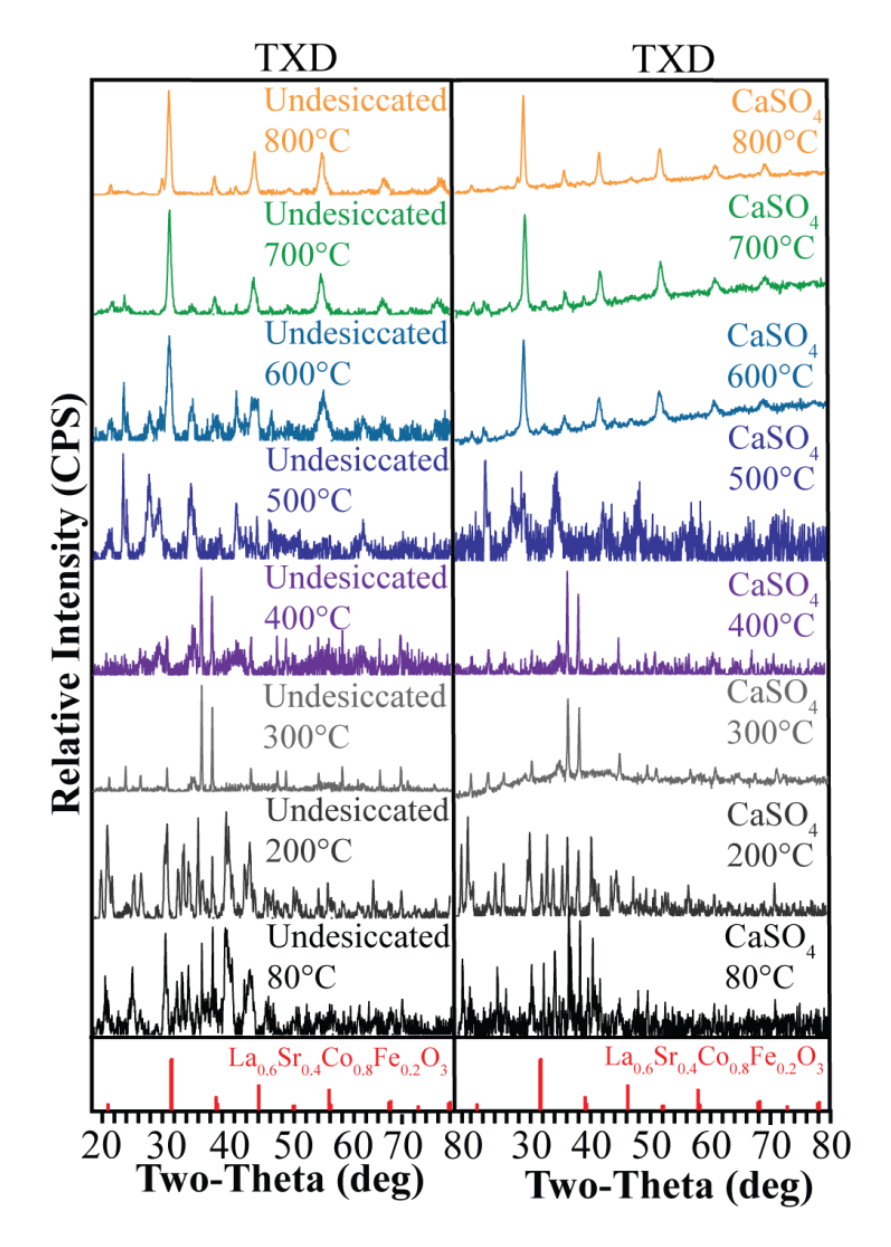


Figure 5.13: XRD Scans for CaSO₄-Desiccated TXD LSCF Fired between 80°C and 800°C. $La_{0.6}Sr_{0.4}Co_{0.8}Fe_{0.2}O_{3-\delta}$ (PDF #00-048-0124) [117].

Figure 5.14 [117] shows undesiccated and CaCl₂-desiccated XRD data for TXD LSCF precursor solutions fired at various temperatures between 80°C and 800°C and shows similar phase purity trends to those in Figure 5.13.

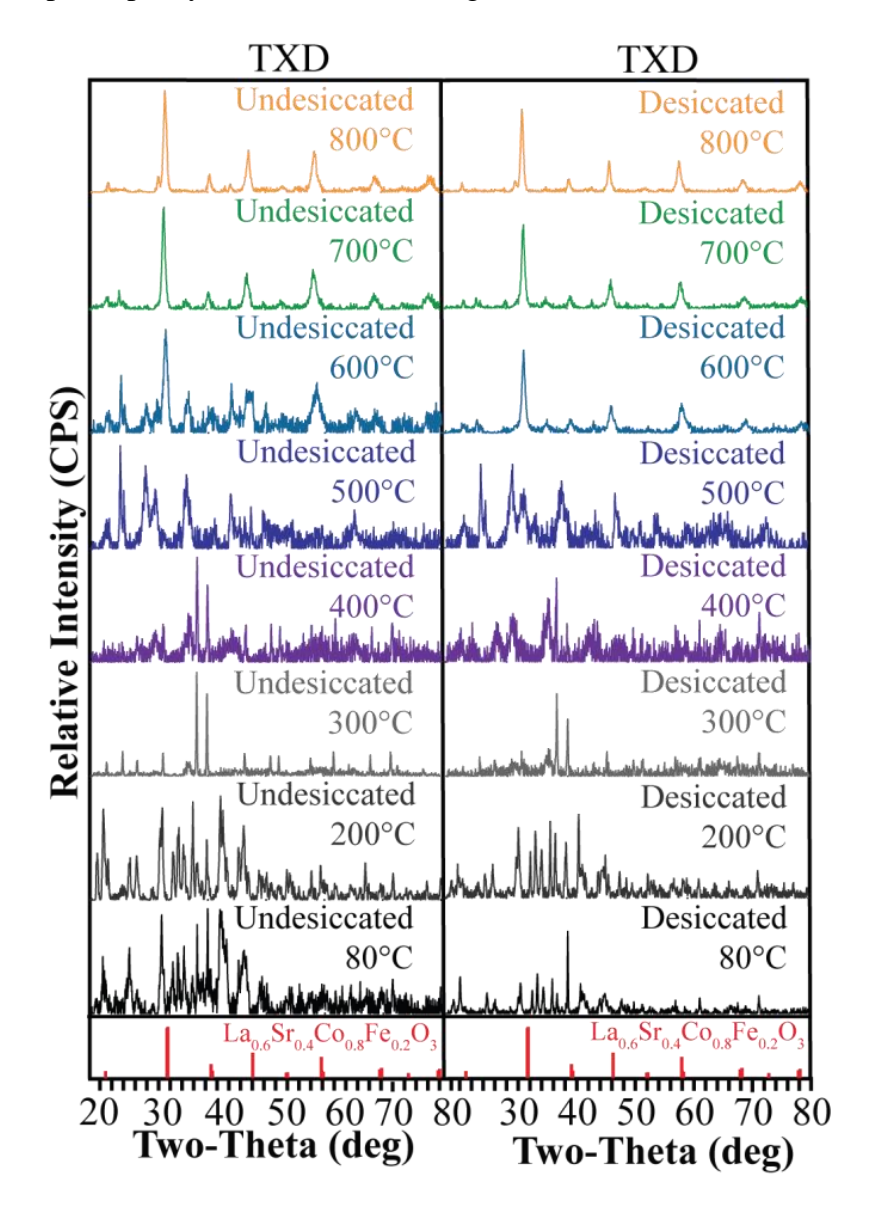


Figure 5.14: XRD Scans for CaCl₂-Desiccated TXD LSCF Fired between 80° C and 800° C. $La_{0.6}Sr_{0.4}Co_{0.8}Fe_{0.2}O_{3-\delta}$ (PDF #00-048-0124) [117].

Figure 5.15 [117] shows undesiccated and dry air-desiccated XRD data for CAD LSCF precursor solutions fired at various temperatures between 80°C and 800°C. The phase purity of the undesiccated powder compared to the desiccated powder was shown to change with dry air desiccation at 500°C and below. In all cases, phase pure LSCF was obtained at 600°C and above.

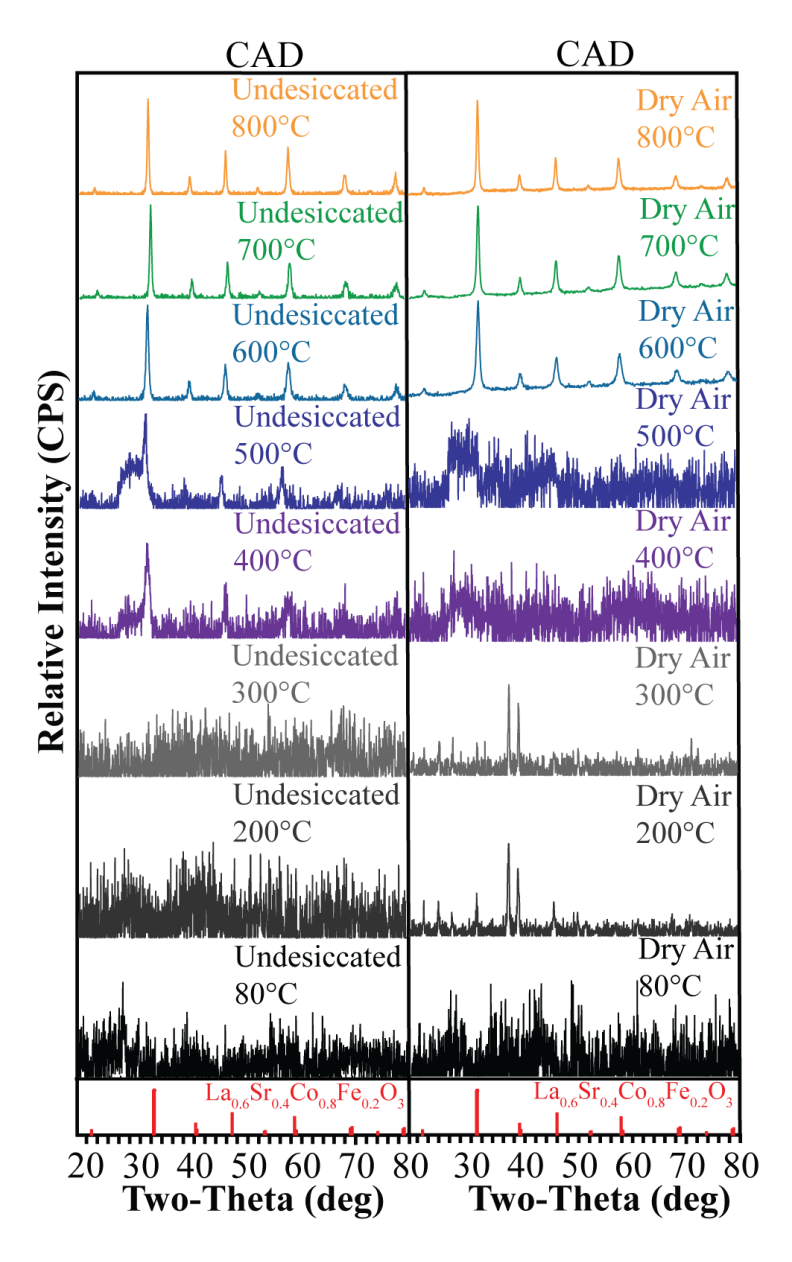


Figure 5.15: XRD Scans for Dry Air-Desiccated CAD LSCF Fired between 80°C and 800°C. $La_{0.6}Sr_{0.4}Co_{0.8}Fe_{0.2}O_{3-\delta}$ (PDF #00-048-0124) [117].

Figure 5.16 [117] shows undesiccated and CaSO₄-desiccated XRD data for CAD LSCF precursor solutions fired at various temperatures between 80°C and 800°C. The phase purity of the undesiccated powder compared to the desiccated powder was shown to be slightly different at 400°C and 500°C, but in all cases phase pure LSCF was obtained at 600°C and above.

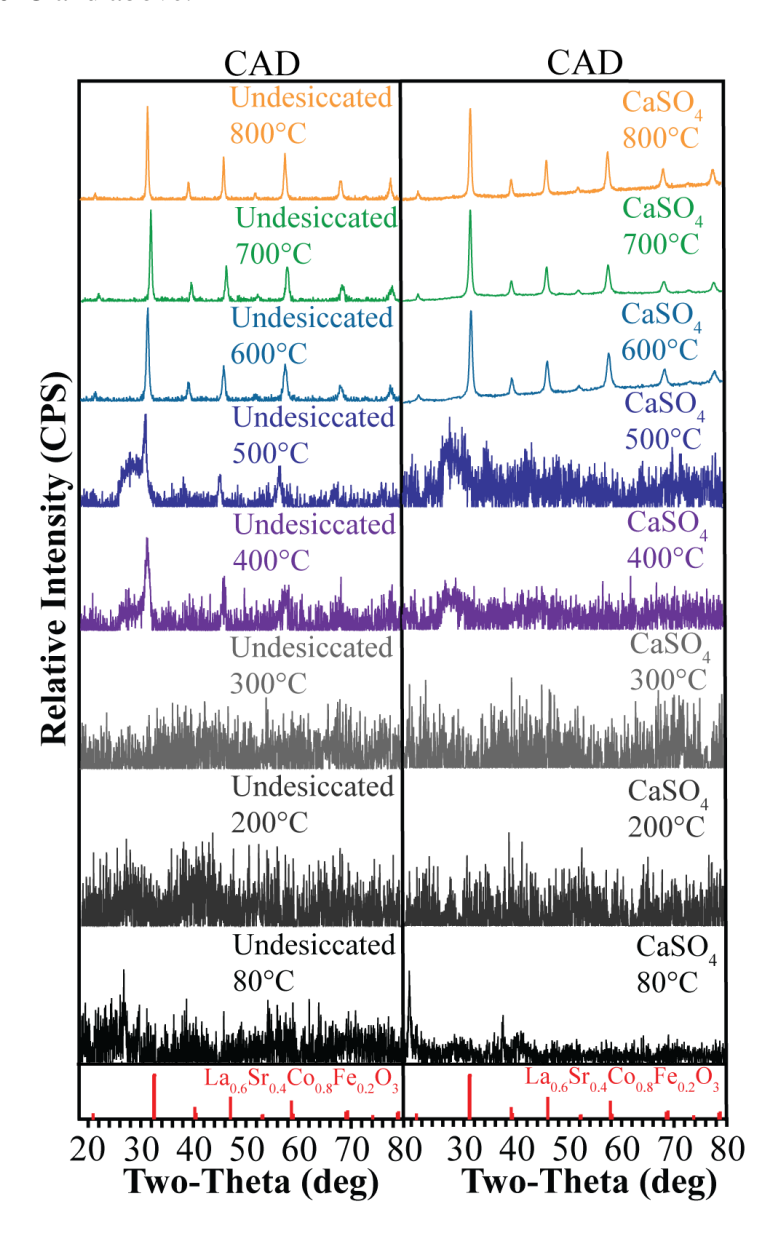


Figure 5.16: XRD Scans for CaSO₄-Desiccated CAD LSCF Fired between 80°C and 800°C. $La_{0.6}Sr_{0.4}Co_{0.8}Fe_{0.2}O_{3-\delta}$ (PDF #00-048-0124) [117].

Figure 5.17 [117] shows undesiccated and CaCl₂-desiccated XRD data for CAD LSCF precursor solutions fired at various temperatures between 80°C and 800°C. The phase purity of the undesiccated powder compared to the desiccated powder was different at processing temperatures below 600°C. According to Figures 5.15 through 5.17 CAD LSCF XRD phase purity was only affected at processing temperatures below 600°C, while retaining constant phase purity at temperatures 600°C and above. The reduction in impurity phases can possibly be attributed to reducing uncontrolled precipitation via cation-surfactant solution complexing.

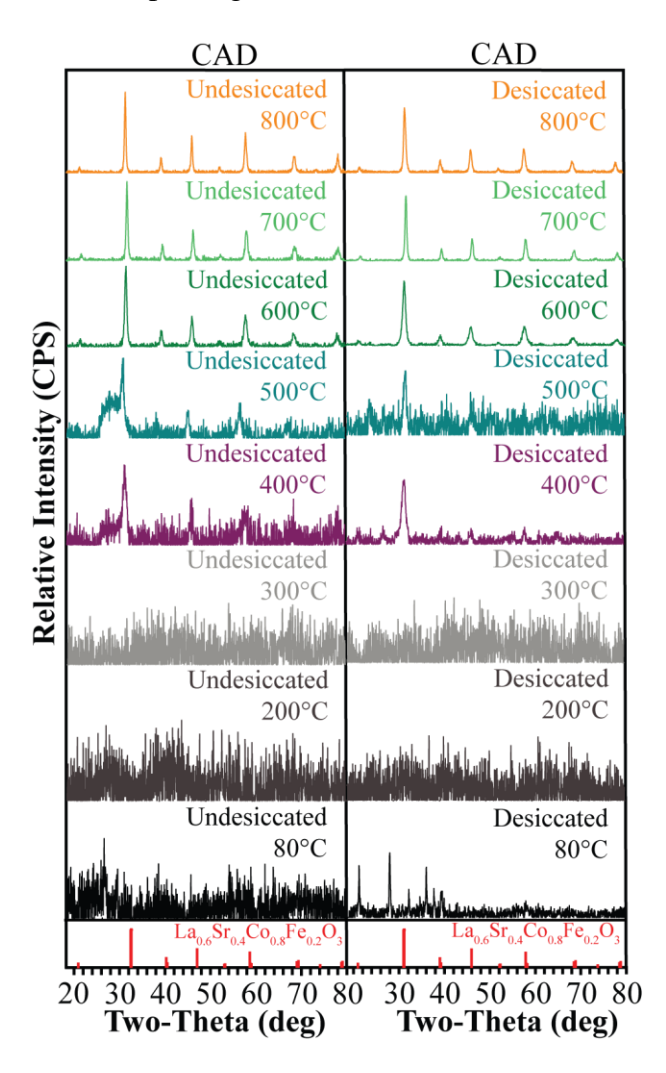


Figure 5.17: XRD Scans for CaCl₂-Desiccated CAD LSCF Fired between 80° C and 800° C. $La_{0.6}Sr_{0.4}Co_{0.8}Fe_{0.2}O_{3-\delta}$ (PDF #00-048-0124) [117].

Overall, Figures 5.12 through 5.14 indicate that the TXD LSCF XRD phase purity was only affected at fabrication temperatures below 700°C, and retained similar phase purity with desiccation at temperatures 700°C and above. The TXD LSCF XRD scans shown in Figure 5.12-5.14 possibly have a higher percentage of impurities compared to CAD LSCF XRD scans shown in Figure 5.15-5.17 because Triton X-100 only interacts with dissolved cations over a portion of its polymer chain, while Citric Acid can interact with the dissolved cations along its entire polymer chain which leads to an increased cation interaction to form phase pure LSCF. In addition, desiccation may lead to smaller nano-particle sizes by collapsing the Triton X-100 and Citric Acid polymer network chain to produce smaller decomposed solution volumes. These smaller solution volumes would be expected to reduce the diffusion distances the cations need to travel and hence increase phase purity.

While CAD and TXD LSCF XRD scans showed desiccation did not have an impact on the LSCF secondary phase purity at 700°C and above, desiccation did influence the secondary phase purity at processing temperatures below 700°C. This difference in phase purity at lower processing temperatures, when using desiccation, may influence low temperature impurity phase content and hence LSCF coarsening rates.

5.3.3 Impurity Impacts on LSCF Nano-Particle Coarsening Behavior

The impact impurity phases had on infiltrated MIEC particle size coarsening is the next area investigated in this chapter. Particle size reduction has been suggested to result in increased cell performance, which may be the result of coarsening caused by different oxide impurity phases shown in Figures 5.12-5.17.

Figure 5.18 shows the raw data used to calculate the XRD Williamson-Hall particle sizes for TXD LSCF precursor solutions. The 22^0 2-Theta, $\sim 40^0$ 2-Theta and $\sim 47^0$ 2-Theta peak positions were used to determine particle sizes. The linearity of the $\beta \text{Cos}(\theta)$ vs. $4 \text{Sin}(\theta)$ plots indicate that the Williamson-Hall method could accurately be used to extract LSCF size and strain values from this data.

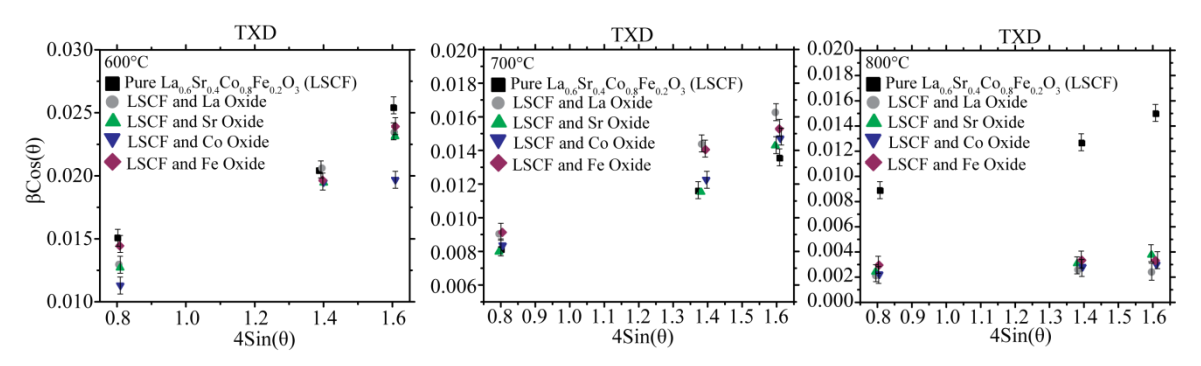


Figure 5.18: Williamson-Hall Raw Data Plots for Coarsened Undesiccated TXD LSCF Nano-Particle Sizes Produced at 600°C, 700°C and 800°C. Williamson-Hall data was obtain for LSCF nano-particles: a) without oxide additives, b) with La oxide added, c) with Sr oxide added, d) with Co oxide added, and e) with Fe oxide added.

Figure 5.19 shows the Williamson-Hall calculated strain % from Figure 5.18 for the TXD LSCF nano-powders combined with different impurity oxides. Strain was calculated directly from the slope of each data set in Figure 5.18. Desiccated TXD LSCF strain showed a reduction from 600°C to 700°C and then stayed relatively constant from 700°C to 800°C. When impurity phases were combined with LSCF, the resulting LSCF nano-particle strain decreased from 600°C to 800°C in almost a linear fashion. The strain data at 600°C did overlap when taking into account the error bars, which could suggest that strain for all cases was similar at 600°C and desiccation strength did not impact strain at that temperature. The only exception is phase pure LSCF, which decreased its strain from 600°C to 700°C and then remained relatively constant at 800°C, possibly due to its smaller particle size. The addition of iron oxide also reduced the LSCF nano-particle strain at 800°C but showed reduced particle size as well, which needs future

analysis. These impurity effects were only conducted on TXD LSCF and these trends may also occur with PND and CAD LSCF, but is not know at this time.

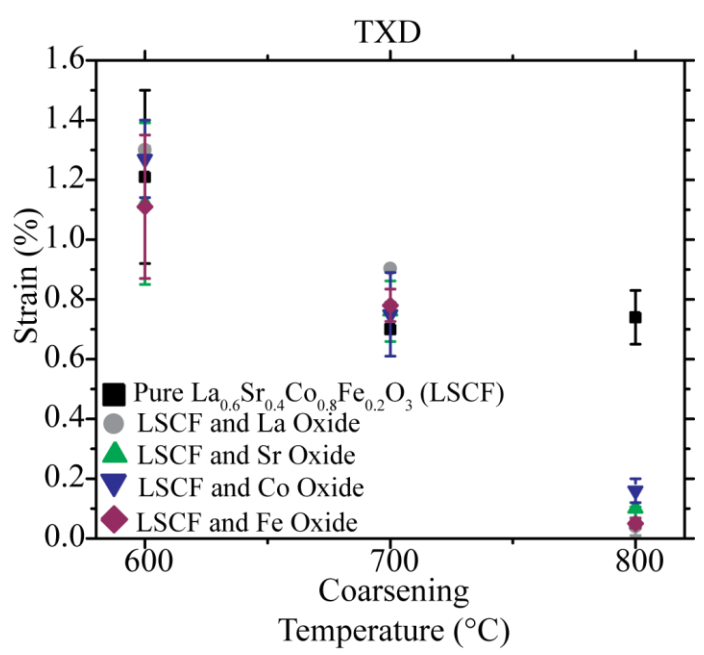


Figure 5.19: Strain Plots for Coarsened Undesiccated TXD LSCF Nano-Particle Sizes Produced at 600°C, 700°C and 800°C. Strain data was obtain for LSCF nano-particles: a) without oxide additives, b) with La oxide added, c) with Sr oxide added, d) with Co oxide added, and e) with Fe oxide added.

Figure 5.20 shows the average particles of TXD LSCF made from 1.50 molar precursor solutions that were first fired at 700°C for 1 hr, combined with various impurity oxides, and finally coarsened at 600°C, 700°C or 800°C for 1hr. The data shows that: 1) TXD LSCF nano-particle size coarsens with increasing processing temperature for all impurity oxides, and 2) TXD LSCF nano-particle size coarsening rates of were much larger with the addition of lanthanum oxide, cobalt oxide, or strontium oxide then that of phase pure TXD LSCF oxide nano-particles.

The effect of impurity phases on TXD LSCF nano-particle coarsening rates support the trends observed in the Figures 5.15-5.17 XRD data and the Figure 5.4 nano-particle size data. A possible explanation why desiccated CAD LSCF nano-particles are

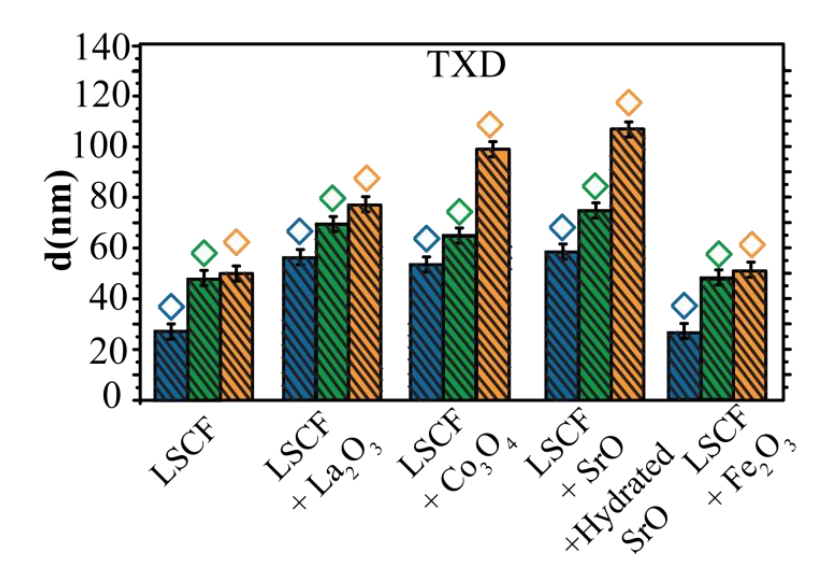


Figure 5.20: Coarsened Undesiccated TXD LSCF Average Nano-Particle Sizes Produced at 600°C, 700°C and 800°C. 600°C (blue, left), 700°C (green, middle) and 800°C (orange, right), each for 1 hour, with different oxide impurities. Particle size data collected using the Williamson-Hall method.

larger than TXD LSCF nano-particles could be due to the fact that different impurity phases (La₂O₃, Co₃O₄, etc.) that formed with different solution additives, in the process producing different LSCF particle sizes.

A second explanation for particle size reduction, when using precursor solution additives is EISA, which was discussed in Section 2.6.1. Both TXD and CAD LSCF nano-particles were reduced using desiccation, while PND LSCF nano-particles were not affected. After being evaporated (i.e. desiccated) both the Triton X-100 and Citric Acid solution additives could be forming into templates which produce, when thermally decomposed, reduced MIEC nano-particle sizes.

5.3.4 Desiccant and Solution Additive Impacts on Performance and Stability

Figure 5.21 shows 500 hr open-circuit R_P data for undesiccated PND LSCF, and desiccated TXD and CAD LSCF symmetrical cells all taken at an operating temperature of 540°C. The degradation rates for CAD and TXD LSCF are similar but PND LSCF

had a significantly higher degradation rate. All cells had a "break-in" period during the first 100 hrs and after that period the cells developed a lower, more constant degradation rate. SOFC durability and degradation stuides in literature have also observed this "break-in" period followed by a more constant degradation rate [143-145]. The degradation rates between 100-500 hrs were 9.8% /khr for PND LSCF, 1.7% /khr for TXD LSCF and 3.3% /khr for CAD LSCF. These degradation rates can also be related back to the phase purity. Both the CAD and TXD LSCF had either phase pure or nearly phase pure oxide powders and had the lower degradation rates, while the PND LSCF had much lower overall phase purity and had the largest degradation rate.

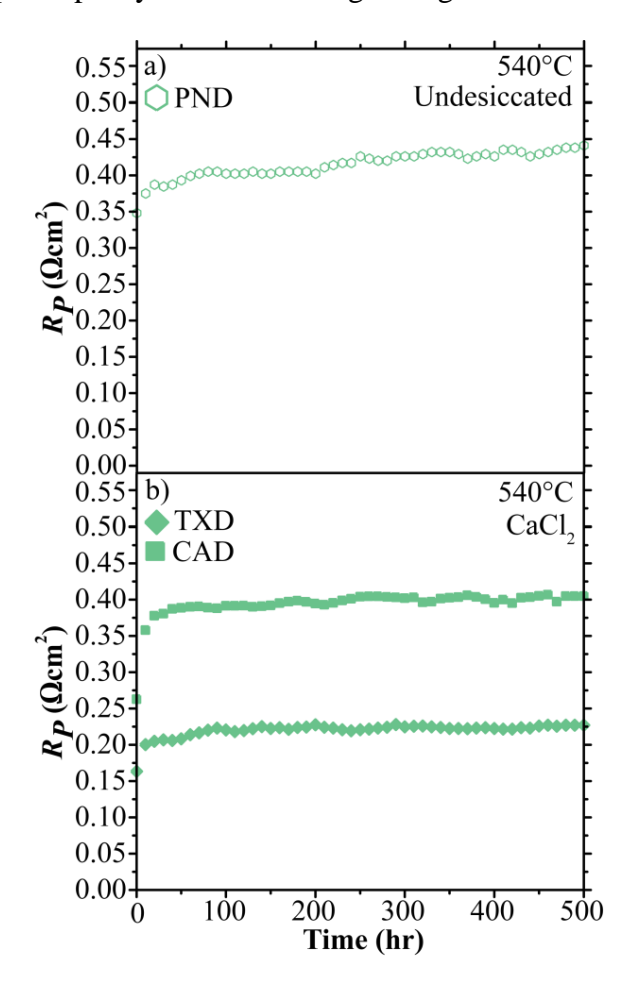


Figure 5.21: LSCF-GDC 500 hour R_P hour Plot for NMCCs Produced using Desiccation and Different Solution Additives. Samples are: a) 1.50 molar PND LSCF, \bullet b) CaCl₂ 0.50 molar CAD LSCF \bullet , and 1.50 molar TXD LSCF \bullet precursor nitrate solutions fired at 700°C for 1 hour.

Figure 5.22 shows SEM images of the CAD and TXD LSCF nano-particle sizes before and after 500 hr at 540°C. Even with 500 hrs at 540°C, the particle sizes remained constant and did not show any signs of coarsening. This can be related back to the low phase impurity fraction seen in the CAD and TXD LSCF XRD data. Unfortunately, SEM images of an aged PND LSCF cell were not obtained for this thesis due to the long time needed to perform an additional 500 hr PND LSCF test. Particle size coarsening could explain the increased R_P observed with the undesiccated PND LSCF. Particle sizes of ~ 100 nm would be needed to obtain the measured 500 hr R_P values (calculated using the SIMPLE model calculator), and this size of particles is within the standard deviation for 0 hr PND LSCF nano-particles shown in Figure 5.6. In contrast, the final 500 hr CAD and TXD LSCF nano-particle sizes required to obtain the observed 500 hr R_P values would need to be between 60-65 nm, which is much larger than the standard deviation shown in Figure 5.6 and the 500 hr CAD and TXD LSCF particles sizes shown in Figure 5.22. In addition, literature [146] shows that performance degradation, due to particle size coarsening, would show a different performance degradation trajectory than the one shown on Figure 5.21. This suggests that some mechanism other than MIEC particle size coarsening was responsible for the TXD and CAD LSCF degradation.

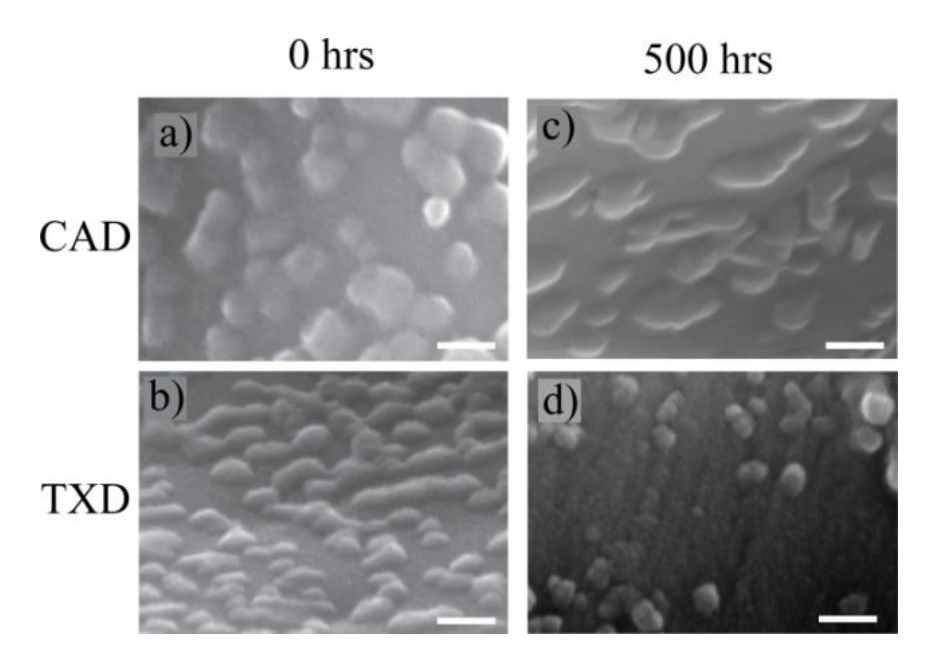


Figure 5.22: Desiccated Scanning Electron Micrographs for CAD and TXD LSCF-GDC Symmetric Cells Tested for 500 hrs. Samples held at 540°C were imaged using the SEM for 0.5 molar CAD LSCF symmetric cell after a) 0 hrs and c) 500 hrs, and CaCl₂-Desiccated 1.50 molar TXD LSCF symmetric cells tested at 540°C after b) 0 hrs and d) 500 hrs. Each scale bar is 50 microns in width.

Figure 5.23 shows the raw EIS data for Figure 5.21 taken at an operating temperature of 540° C over 500 hrs of aging. Consistent with Figure 5.22, the data shows that over time the R_P increased for PND, CAD and TXD LSCF NMCCs. However, Figure 5.23 also shows a significant increase in the ohmic offset with time. The increased ohmic offset, possibly caused by iron or cobalt doping the GDC over time, may help explain the performance degradation. However additional experiments beyond the scope of the present thesis are needed to investigate the operable degradation mechanisms.

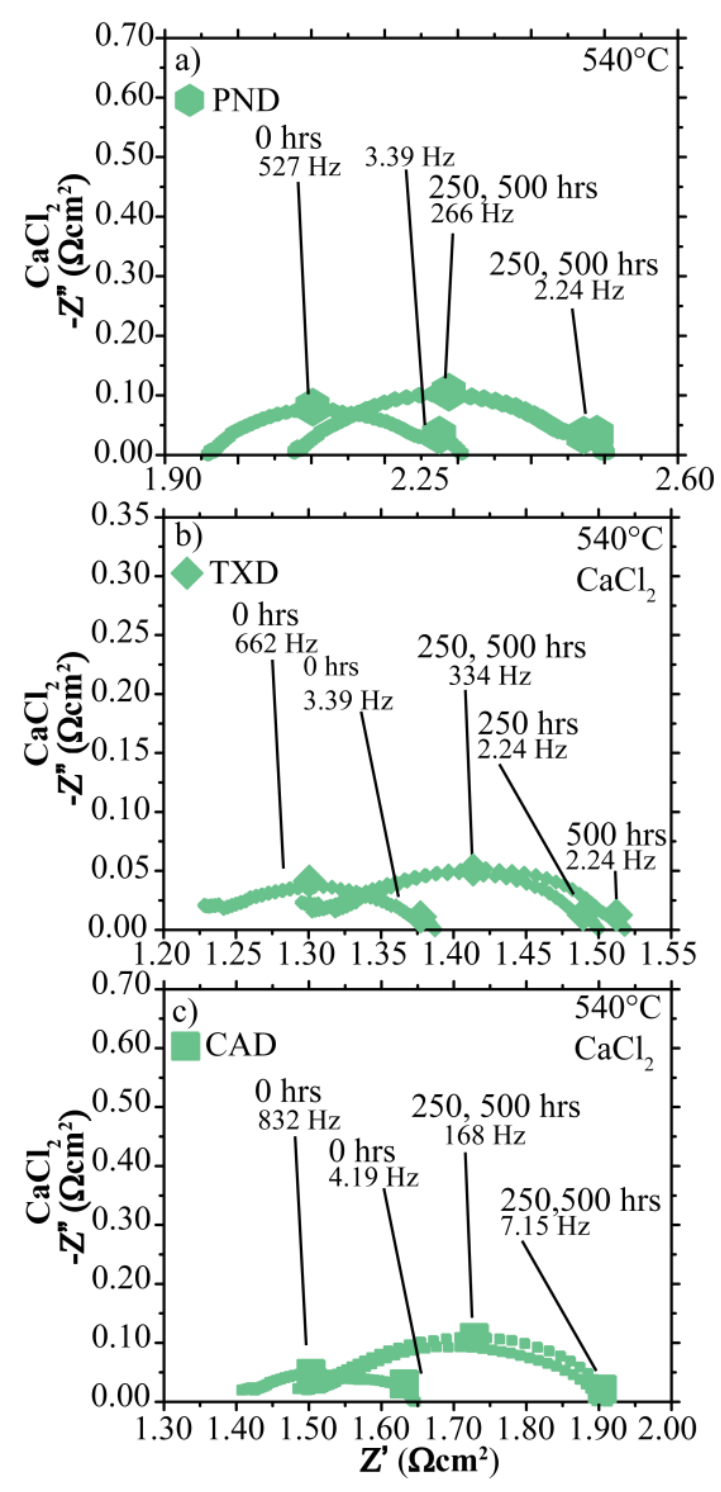


Figure 5.23: Raw Impedance Data Plots of Desiccated LSCF-GDC NMCCs Produced using Different Solution Additives. Samples are: a) 1.50 molar PND LSCF (\spadesuit), b) 0.50 molar CAD LSCF (\blacksquare) and c) TXD LSCF (\spadesuit) precursor nitrate solutions fired at 700°C. R_P LSCF-GDC NMCC's measurements were taken for 500 hours.

5.4 Summary

In summary, desiccation was shown to reduce infiltrated LSCF nano-particle size using different precursor solution additions, such as Triton X-100 and Citric Acid. In contrast, desiccation was shown to not have an effect on infiltrated LSCF nano-particle size when a precursor solution was not present, as with the PND case. The magnitude of nano-particle size reduction was dependent on the precursor solution additive choice, as average TXD LSCF nano-particles were reduced from 48 nm to 22 nm, while the average CAD LSCF nano-particles were reduced from 50 nm to 41 nm.

Performance was also shown to increase when using increasingly stronger desiccation, for both TXD and CAD LSCF symmetric cells. XRD data showed that the use of desiccation lowered the LSCF phase impurity fraction at temperatures below 700°C. Both Triton X-100 and Citric Acid may increase the LSCF infiltrate phase purity by reducing the amount of nitrate precursor precipitation via cation-surfactant solution complexing. The improved phase purity of CAD LSCF compared to TXD LSCF may result from the fact that only a portion of amphiphlic surfactants (such as TXD) interact with cations in the solution while chelating agents (such as CAD) deprotonate over their entire length and hence are typically better at preventing cation segregation during processing.

Finally, the LSCF oxide nano-particle coarsening rate was shown to increase when impurity oxide phases were present at aging temperatures of 600°C and above. At 540°C LSCF coarsening did not occur, but LSCF-GDC cell performance degraded by some other mechanism.

CHAPTER 6: The Impact of Nano-Ceria Pre-Infiltration on $La_{0.6}Sr_{0.4}Co_{0.8}Fe_{0.2}O_{3-\delta}$ Infiltrated Solid Oxide Fuel Cell Cathodes

6.1 Introduction

The previous two chapters evaluated the impact of desiccation and surfactant choice on infiltrated nano-particle size, NMCC performance, and NMCC performance stability. This chapter explains a second infiltration size variation technique: ceria oxide pre-infiltration. Pre-infiltration has been demonstrated in the literature to lower infiltrate oxide nano-particle size [27, 147-150]. However, these studies have not fully explored or explained the relationship between pre-infiltration and infiltrate particle size control. Therefore, the objective of this chapter was to: 1) characterize the effects ceria oxide pre-infiltration have on performance and LSCF nano-particle size, 2) investigate why pre-infiltration lowers nano-particle size, and 3) characterize the effects solution additives have on NMCC performance and LSCF nano-particle size when using pre-infiltration.

6.2 Experimental Methods

6.2.1 Cathode-Electrolyte-Cathode Symmetric Cell Production

Cathode-supporting electrolytes were prepared in the same manner as Section 4.2.1. Next, GDC IC scaffolds were then screen printed on both sides of these dense GDC electrolyte pellets. To achieve this, Rhodia GDC powder was coarsened at 800°C for 4 hours prior to being mixed with a polymer (Heraeus; West Conshohocken, PA) to form a GDC ink with a 34% solids loading. Three layers of GDC ink were screen printed onto each side of dense GDC pellets using a patterned 80 mesh stainless steel screen with a circular 0.5 cm² open area. Before the next ink layer was applied, each ink layer was

allowed to flow across the pellet surface for 5 minutes and then was placed in a bake oven at 120°C for 5 minutes to extract the electronic vehicle solvent and increase the green strength. After screen printing the GDC ink, the resulting scaffolds were heated to 400°C at 3°C/min, held at 400°C for one hour, heated to 600°C at 3°C/min, held at 600°C for one hour, heated to 1050°C at 5°C/min, held at 1050°C for 3 hours, and then returned to room temperature at a nominal cooling rate of 10°C/min. Sintered IC scaffold thickness and roughness measurements were then made with a Dektak 3 profilometer (Bruker; Tucson, AZ).

GDC precursor solutions were then infiltrated into the IC scaffolds, gelled, and fired at 700°C for 1 hr to coat the IC scaffold surface with nano-GDC oxide particles. GDC precursor solutions were prepared by dissolving 99.99% pure Ce(NO₃)₃*6.0 H₂O and 99.99 % pure Gd(NO₃)₃*4.0 H₂O (Alfa Aesar; Ward Hill, MA) in distilled water containing 3 wt% of pre-dissolved Triton-X 100 (weight Triton X-100/weight nitrate). (These precise nitrate water of hydration contents were determined prior to nitrate weighing by measuring the mass loss that occurred inside a Q500 thermogravimetric analyzer (TA Instruments; New Castle, DE) with heating under nitrogen up to 850°C.))

Next, LSCF precursor solutions were infiltrated into the nano-GDC coated micro-GDC scaffold. Specifically, TXD, CAD and PND LSCF precursor solutions were prepared and infiltrated in the same manner as Section 5.2.1. This infiltrate-gel-fire process was repeated twice for both the nano-GDC nanoparticles and LSCF nanoparticles to achieve both the desired nano-GDC loading levels between 0 vol% and 7.4 vol% and LSCF loading levels of 12.0 vol%. Lastly, symmetric cells were prepared for

electrical measurements by screen printing bilayer LSM –Au current collectors on each NMCC in the same manner described in Section 5.2.1.

Figure 6.1 visually demonstrates the nano-GDC pre-infiltration and LSCF infiltration processes described above. Figure 6.1a shows a bare micro sized GDC scaffold with no infiltrated nano-GDC or LSCF oxide nano-particles sintered onto the scaffold microstructure. Figure 6.1b shows how subsequent nano-GDC infiltration produced oxide particles sintered onto the bare micro sized GDC oxide scaffold. Finally, Figure 6.1c shows that LSCF infiltration produced nano-particles sintered onto both the bare micro sized GDC scaffold and nano-GDC oxide particles.

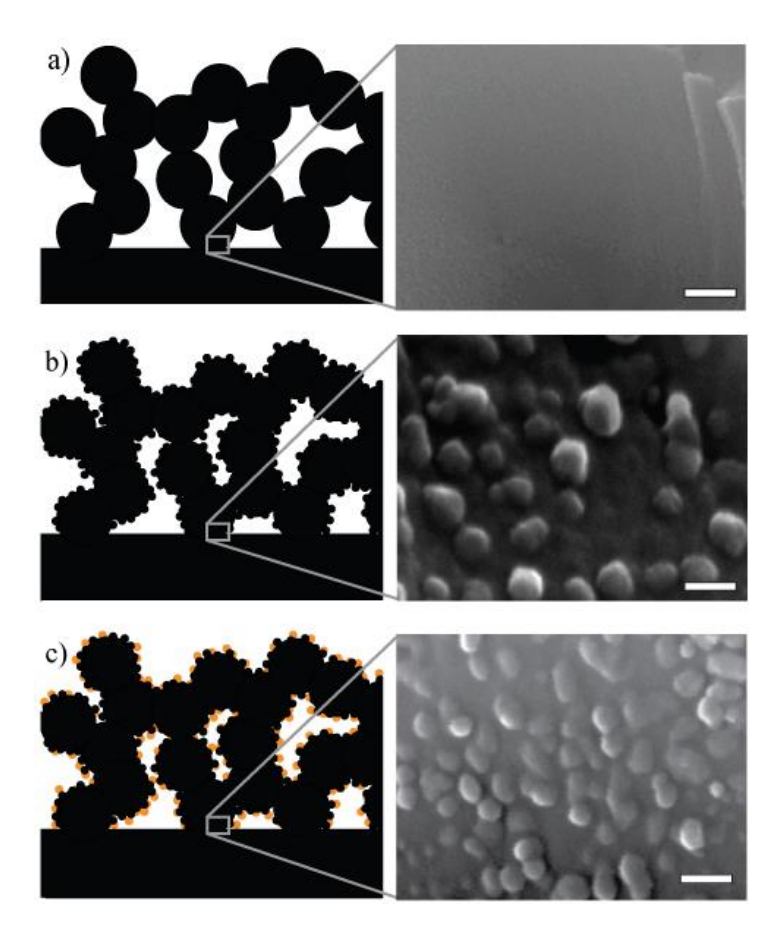


Figure 6.1: **Pre-Infiltrated Cathode Nano-Particle Fabrication Diagram**. (a) without pre-infiltration of nano-GDC or LSCF, (b) with pre-infiltrated nano-GDC particles and without LSCF and (c) pre-infiltrated nano-GDC particles (small black circles) and LSCF nano-particles (small orange circles). This schematic is not drawn to scale. SEM images are used to illustrate the diagram shown on the left for each stage in the infiltration process. Scale bars indicate a length of 50 nm.

6.2.2 Symmetrical Cell Impedance, X-ray Diffraction, and Scanning Electron Microscopy Measurements

NMCC symmetrical cells were characterized using EIS, XRD, and SEM in the same manner described in Section 5.2.2, 5.2.3, and 5.2.4 respectively. XRD Williamson-Hall particle size measurements were conducted in the same manner as Section 5.2.6 except that only two peaks (the $\sim 23^0$ and $\sim 40^0$ 2-Theta peaks) were used for particle size characterization. Williamson-Hall measurements were restricted to two LSCF XRD peaks because the addition of GDC (in the form of nano-GDC particles) resulted in peak broadening of the $\sim 47^0$ 2-Theta peak, excluding it from LSCF particle size analysis. Strain data was calculated from the slope of the raw data in the same manner as Section 5.2.6.

6.2.3 ThermoGravimetric Analysis Measurements

ThermoGravimetric Analysis (TGA) was performed by taking MIEC precursor solutions and evaluating their thermal decomposition behavior using a Q500 TGA (TA Instruments; New Castle, DE, USA) with a 0.01 mg mass resolution. Precursor solutions were gelled outside porous GDC scaffolds, placed in a platinum sample pan, and heated at 10°C/min in air up to 830°C with no hold time. For those samples containing nano-GDC, MIEC precursor solutions were infiltrated into loose GDC powders and then analyzed in the TGA.

6.2.4 Nano-Micro-Composite Cathode Performance Modeling

NMCC performance was modeled using the SIMPLE model [5, 7, 8] in the same manner as was described in Section 5.2.5.

6.3 Results

6.3.1 Pre-Infiltration and Solution Additive Impacts on Infiltrate Particle Size

Table 3 shows the processing parameters used when fabricating symmetrical, GDC pre-infiltrated cathodes using PND, TXD or CAD LSCF. Table 3 shows that TXD and CAD LSCF oxide nano-particles were reduced in size as the loading level of nano-GDC was increased to 7.4 vol%. Table 3 also shows that PND LSCF oxide nano-particle sizes were not affected by the addition of nano-GDC.

Both GDC pre-infiltration and desiccation showed no particle size reduction when using PND LSCF. The 700°C TXD LSCF nano-particle size reduction was the same for desiccation and ceria pre-infiltration, where both methods reduced the TXD LSCF nano-particles to ~22 nm. The 700°C CAD LSCF nano-particle reduction was, however, larger using ceria pre-infiltration than desiccation.

Figure 6.2 shows scanning electron microscopy images of ceria pre-infiltrated symmetric cells with 0.0 vol% and 7.4 vol% nano-GDC infiltrated with 1.50 molar and 0.50 molar PND and TXD LSCF precursor solutions. The particle sizes were not affected by molarity, as was seen in Section 5.3.1 for desiccated cells.

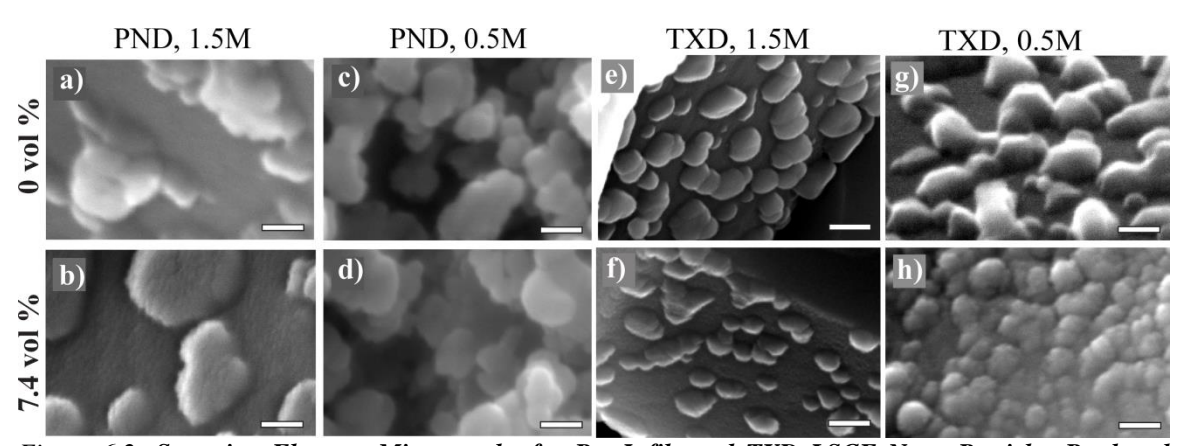


Figure 6.2: Scanning Electron Micrographs for Pre-Infiltrated TXD LSCF Nano-Particles Produced using Different Solution Molarities. 1.5 molar PND LSCF a) 0.0 vol% nano-GDC and b) 7.4 vol% nano-GDC precursor solutions, and 0.50 molar TXD LSCF c) 0.0 vol% nano-GDC and d) 7.4 vol% nano-GDC precursor solutions inside GDC scaffolds at 700°C. Each scale bar is 50 microns in width.

Table 3: Pre-Infiltrated PND, TXD and CAD LSCF-GDC NMCC Cathodes. Processing parameters also shown.

Surfactant	GDC Loading (%)	Firing Temperature (°C)	LSCF Loading Level (%)	Number of GDC Infiltrations	Number of LSCF Infiltrations	GDC/ LSCF Nitrate Solution Molarity	Cathode Thickness (µm)	Scaffold RMS Surface Roughness (µm)	Volume of Solution per Infiltration (µL)	Cathode Geometric Area (cm²)	Cathode Porosity (%)	Scaffold Column Width (nm)	LSCF& GDC Diameter (nm)	Total LSCF Surface Area (cm²)	Total GDC Surface Area (cm²)	LSCF Surface Area/GDC Surface Area (%)
PND	0.0	700	12.0	0	2	1.5/1.5	35.2	3.42	4.10	0.5	41	120	66	192	146	132
PND	0.0	700	12.0	0	2	1.5/1.5/	36.1	3.85	4.21	0.5	41	120	66	197	150	132
PND	0.0	700	12.0	0	6	1.5/0.5	35.5	4.01	4.14	0.5	41	120	62	206	147	140
PND	0.0	700	12.0	0	6	1.5/0.5	36.7	3.85	4.28	0.5	41	120	62	213	152	140
PND	5.0	700	12.0	2	2	1.5/1.5	34.2	4.10	3.99	0.5	41	120	72	171	142	121
PND	5.0	700	12.0	2	2	1.5/1.5	34.8	4.30	4.06	0.5	41	120	72	174	144	121
PND	6.4	700	12.0	2	2	1.5/1.5	35.5	3.95	4.14	0.5	41	120	77	166	147	113
PND	6.4	700	12.0	2	2	1.5/1.5	34.9	3.81	4.07	0.5	41	120	77	163	145	113
PND	7.4	700	12.0	2	2	1.5/1.5	36.7	3.75	4.28	0.5	41	120	77	172	152	113
PND	7.4	700	12.0	2	2	1.5/1.5	36.1	4.15	4.21	0.5	41	120	77	169	150	113
PND	7.4	700	12.0	2	6	1.5/0.5	36.5	4.05	4.26	0.5	41	120	70	188	151	124
PND	7.4	700	12.0	2	6	1.5/0.5	36.2	3.95	4.22	0.5	41	120	70	186	150	124
CAD	0.0	700	12.0	0	7	1.5/0.5	34.2	3.74	3.42	0.5	41	120	50	247	142	174
CAD	0.0	700	12.0	0	7	1.5/0.5	34.5	3.46	3.46	0.5	41	120	50	250	143	175
CAD	5.0	700	12.0	2	7	1.5/0.5	32.6	4.96	3.26	0.5	41	120	43	273	135	202
CAD	5.0	700	12.0	2	7	1.5/0.5	37.9	5.34	3.78	0.5	41	120	43	317	157	202
CAD	6.4	700	12.0	2	7	1.5/0.5	32.9	4.50	3.29	0.5	41	120	27	439	136	323
CAD	6.4	700	12.0	2	7	1.5/0.5	34.3	4.78	3.43	0.5	41	120	27	458	142	323
CAD	7.4	700	12.0	2	7	1.5/0.5	34.8	3.50	3.48	0.5	41	120	27	465	144	323
CAD	7.4	700	12.0	2	7	1.5/0.5	36.0	3.99	3.60	0.5	41	120	27	481	149	323
TXD	0.0	700	12.0	0	2	1.5/1.5	35.2	4.39	4.10	0.5	41	120	48	264	146	181
TXD	0.0	700	12.0	0	2	1.5/1.5	36.1	4.05	4.22	0.5	41	120	48	271	150	181
TXD	0.0	700	12.0	0	2	1.5/0.5	36.0	3.50	12.60	0.5	41	120	49	265	149	178
TXD	0.0	700	12.0	0	9	1.5/0.5	36.3	3.41	2.83	0.5	41	120	51	257	151	171
TXD	5.0	700	12.0	2	2	1.5/1.5	35.8	4.43	4.17	0.5	41	120	42	307	148	207
TXD	5.0	700	12.0	2	2	1.5/1.5	35.6	4.27	4.17	0.5	41	120	42	307	148	207
TXD	6.4	700	12.0	2	2	1.5/1.5	34.8	5.30	4.06	0.5	41	120	22	507	144	352
TXD	6.4	700	12.0	2	2	1.5/1.5	36.4	5.78	4.24	0.5	41	120	22	595	151	394
TXD	7.4	700	12.0	2	2	1.5/1.5	34.6	5.41	3.86	0.5	41	120	21	568	143	397
TXD	7.4	700	12.0	2	2	1.5/1.5	35.1	6.00	3.92	0.5	41	120	21	577	146	395
TXD	7.4	700	12.0	2	2	1.5/0.5	36.1	4.23	12.62	0.5	41	120	23	566	150	377
TXD	7.4	700	12.0	2	9	1.5/0.5	35.4	4.30	2.75	0.5	41	120	23	554	147	377

Figure 6.3 shows scanning electron microscopy images of pre-infiltrated symmetric cells with 0.0 vol% nano-GDC and 7.4 vol% nano-GDC infiltrated with 0.50 molar TXD LSCF precursor solutions using different infiltration volume amounts, as reported in Table 3. Similar to experiments on the desiccated cells in Section 5.3.1, the particle sizes of the ceria pre-infiltrated cells shown in Figure 6.3 were not impacted by the LSCF precursor solution infiltration volume.

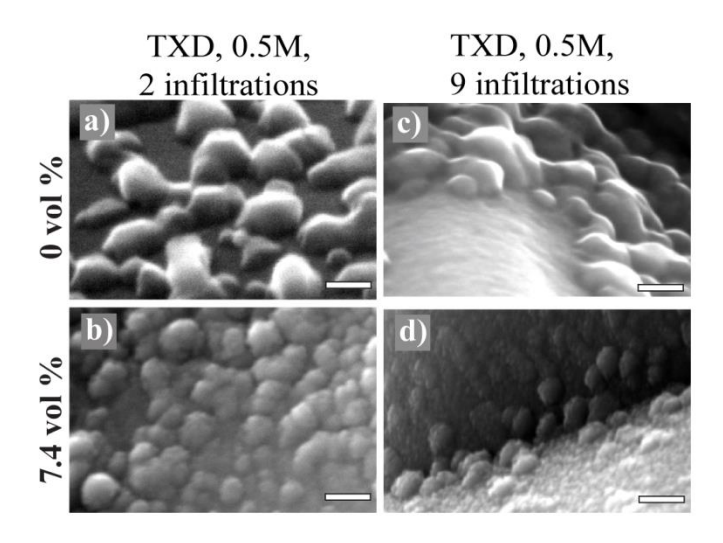


Figure 6.3: Scanning Electron Micrographs for Pre-Infiltrated LSCF Nano-Particles Produced using Different Solution Volumes. 1.50 molar TXD LSCF a) 0.0 vol% nano-GDC 2 infiltrations, b) 7.4 vol% nano-GDC 3 infiltrations, c) 0.0 vol% nano-GDC 9 infiltrations and d) 7.4 vol% nano-GDC 9 infiltrations, precursor solutions inside GDC scaffolds at 700°C. Each scale bar is 50 microns in width.

Figure 6.4 shows SEM images for PND, CAD and TXD LSCF nano-particles formed with increasing amounts of pre-infiltrated nano-GDC ranging from 0.0 vol% to 7.4 vol%. The SEM images show that both the CAD and TXD LSCF nano-particles decreased their average size once the amount of nano-GDC increased above 5.0 vol%, while PND LSCF nano-particle sizes remained constant with increasing nano-GDC loading levels. The TXD LSCF average nano-particle sizes were reduced from 48 nm to 22 nm, CAD LSCF average nano-particle sizes were reduced from 50 nm to 27 nm, and PND LSCF average nano-particle sizes remained constant at around 70 nm.

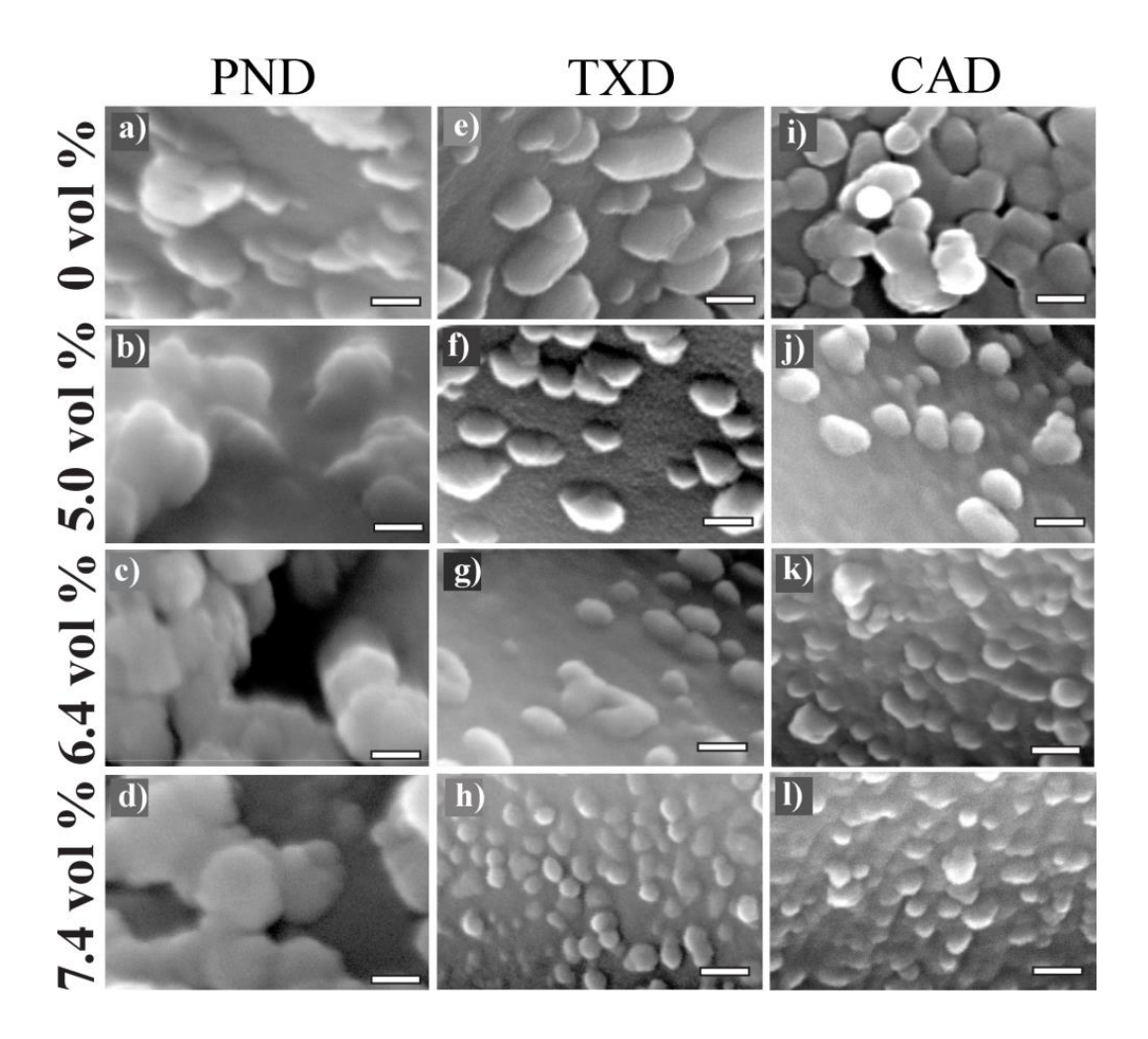


Figure 6.4: Scanning Electron Micrographs for Pre-Infiltrated LSCF Nano-Particles Produced using Different Solution Additives. 0.50 molar CAD LSCF pre-infiltrated nano-GDC and LSCF precursor gel decomposition (a-e) and after 1.50 molar TXD LSCF pre-infiltrated nano-GDC and LSCF precursor gel decomposition (f-j) a GDC scaffold. Scale bars indicate a length of 50 nm.

Figure 6.5 shows the raw data used to calculate the XRD Williamson-Hall particle sizes for PND, TXD and CAD LSCF precursor solutions fired at 600°C, 700°C and 800°C. Due to peak overlap between the nano-GDC and LSCF on the XRD only two peak locations (instead of the standard 3) were used to determine LSCF particle size.

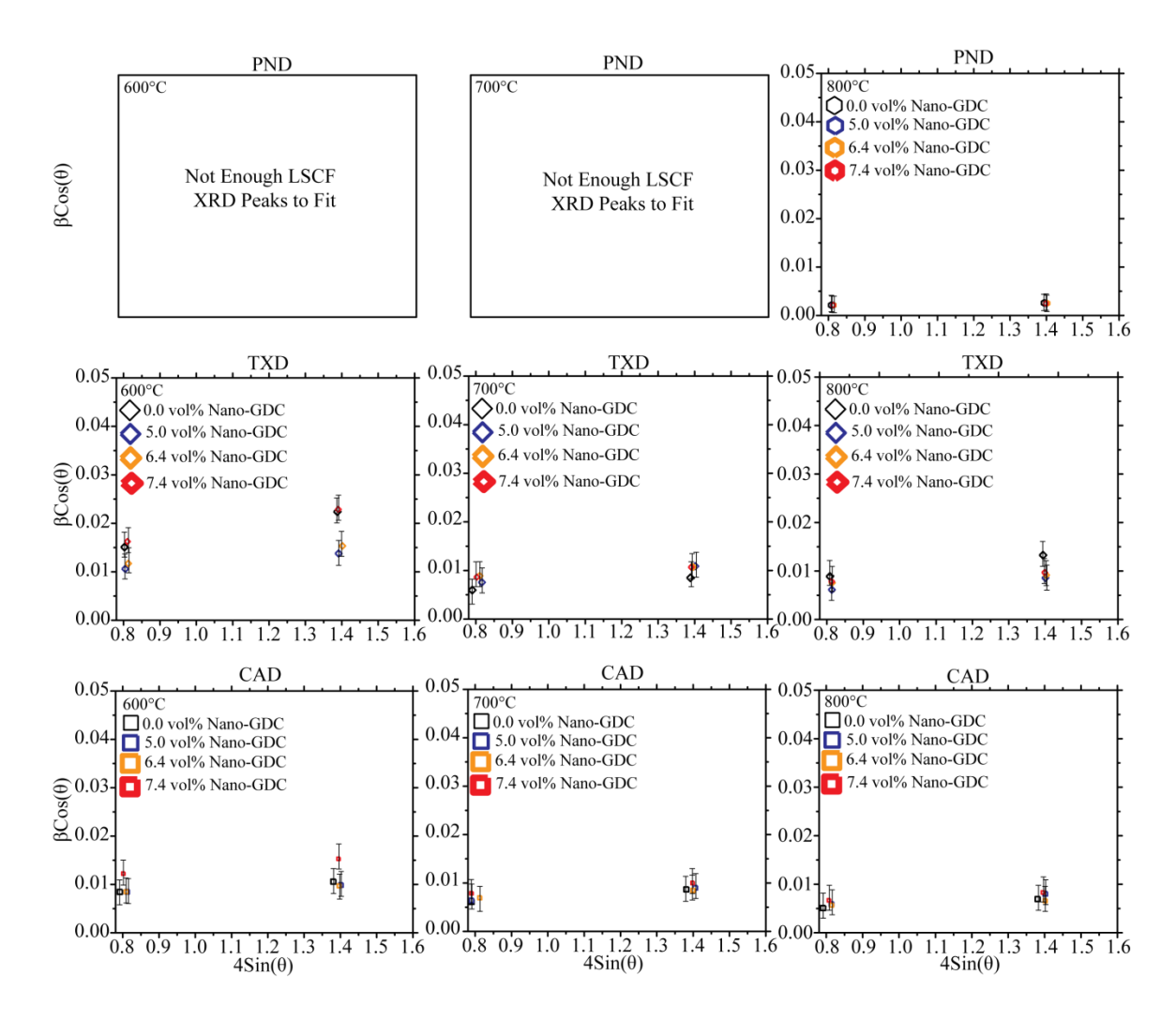


Figure 6.5: Williamson-Hall Raw Data Plots Pre-Infiltrated for PND LSCF, TXD LSCF and CAD LSCF Nano-Particles. Williamson-Hall data was obtained only for two LSCF XRD peaks due to peak overlap between the GDC and LSCF.

Figure 6.6 shows the Williamson-Hall calculated strain % from Figure 6.5 for the pre-infiltrated LSCF nano powders using PND, TXD and CAD solution additives. Strain was calculated directly from the slope of each data set in Figure 6.5.

.

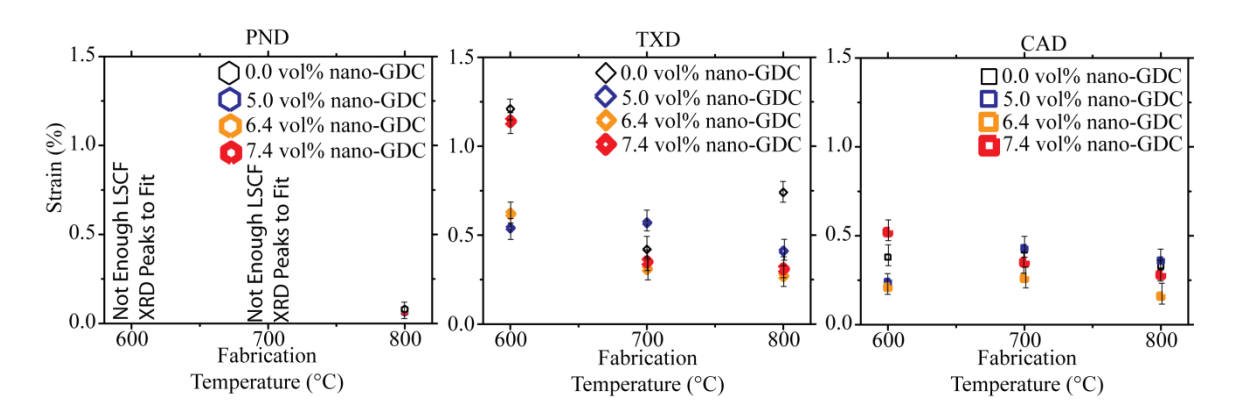


Figure 6.6: Strain Plots Pre-Infiltrated for PND LSCF, TXD LSCF and CAD LSCF Nano-Particles. LSCF nano-particle strain was calculated using 0.0 vol% nano-GDC, 5.0 vol% nano-GDC, 6.4 vol% nano-GDC, and 7.4 vol% nano-GDC fired at 600°C, 700°C and 800°C for 1 hr.

The strain for PND LSCF nano-particles is very large, although is the smallest of any strains reported on Figure 6.6, and has a similar magnitude for each nano-GDC loading level, similar to Section 5.3.1. The PND LSCF nano-particles were again the largest of any precursor solution and have the smallest strain. The TXD LSCF and CAD LSCF nano-particles showed similar trends for the strain displayed in Section 5.3.1, but unlike the strain reported in Figure 5.5 at 600°C, the strain values in Figure 6.6 at 600°C are different enough that the error bars do not completely overlap. The only exceptions are between the: 1) 5.0vol% and 6.4vol%, and 2) 0.0 vol% and 7.4 vol% nano-GDC strain values. Overall strain started at a maximum at 600°C, was reduced at 700°C and then stayed relatively constant at 800°C, compared to the strain calculated at 700°C, which was also observed in Section 5.3.1.

Figure 6.7 shows the raw data used to calculate the nano-GDC (not LSCF) Williamson-Hall particle sizes shown in Figure 6.6 for PND, TXD and CAD LSCF precursor solutions fired at 600°C, 700°C and 800°C. Nano-particle strain was also determined from the slope of each data set, which is shown in the following figure. The

error for the ~28 2-Theta and ~73 2-Theta values used for determining the strain were much larger than previous error values primarily at 600°C and 700°C because there was a much more peak overlap at those 2-Theta values, which made JADE have more difficulty differentiating between the correct values. These error values decreased at 800°C since the peaks were much more defined at higher temperatures. Without the error bars the slope would appear negative in Figure 6.5, but with the error included the slope can be interpreted as 0 or positive in value.

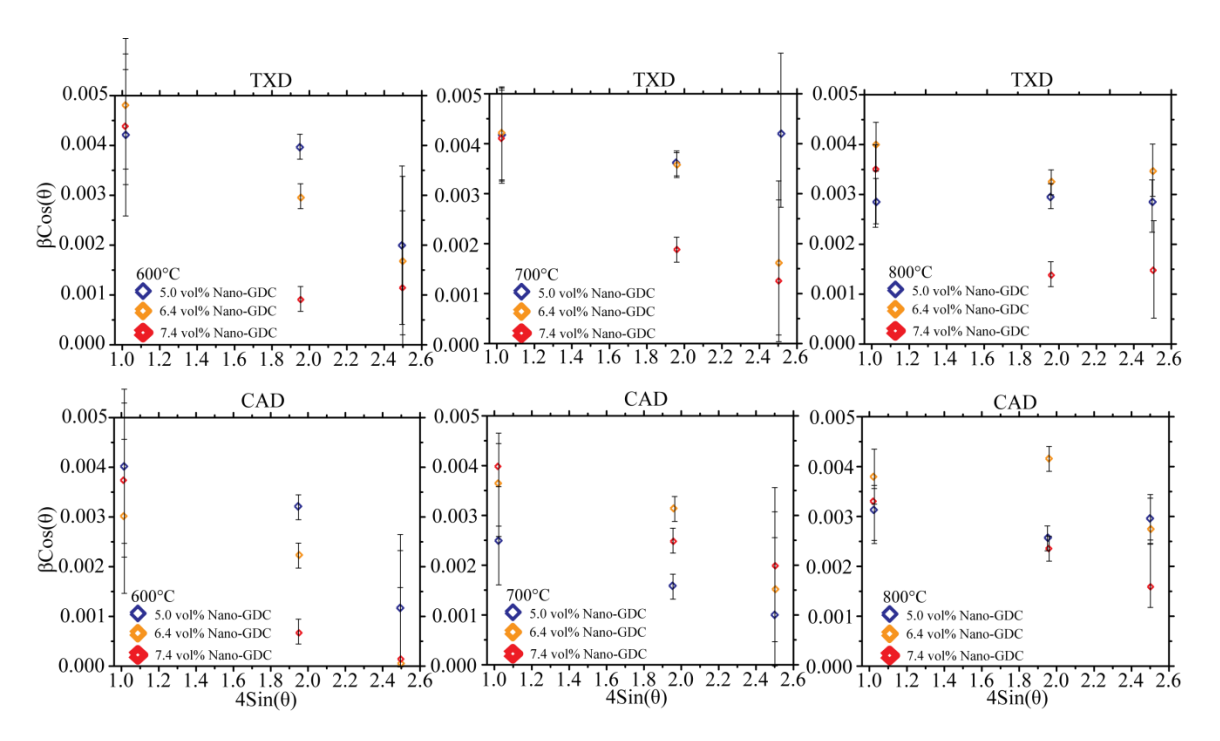


Figure 6.7: Williamson-Hall Raw Data Plots for Pre-Infiltrated Nano-GDC Particle Sizes in TXD LSCF and CAD LSCF Infiltrated Cells. Williamson-Hall data was collected for the ~28 2-Theta, ~56 2-Theta, and the ~76 2-Theta values for nano-GDC.

Figure 6.8 shows the XRD Williamson-Hall calculated strain % from Figure 6.7 for the pre-infiltrated nano-GDC nano powders using PND, TXD and CAD solution additives. Strain was calculated directly from the slope of each data set in Figure 6.7. Since the slope could possibly be 0 or positive, a 0 slope from Figure 6.7 would appear as a horizontal line while a positive slope is similar in appearance to previous Williamson-

Hall plot already shown. The strain for the nano-GDC particles was much smaller than the LSCF nano-particles but still significant (reaching a maximum of 0.08%). The strain

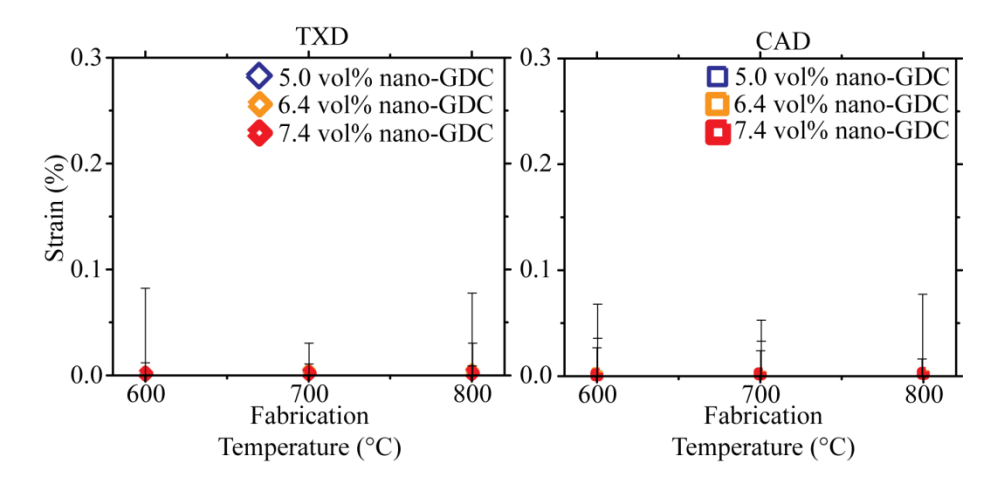


Figure 6.8: Strain Plots for Pre-Infiltrated Nano-GDC Particles in TXD LSCF and CAD LSCF Infiltrated Cells. Strain data was determined from Figure 6.7 for the ~28 2-Theta, ~56 2-Theta, and the ~76 2-Theta values for nano-GDC.

initially starts at a higher values for TXD and CAD cases at 600°C, then decreases at 700°C, and finally increases again at 800°C. This makes sense since the nano-GDC particles were fabricated at 700°C and would be closer to a strain-free state at 700°C. Under a typical LSCF nano-particle atop a GDC nano-particle bilayer situation one would expect the nano-GDC to under significant strain since at 25°C the Thermal Expansion Coefficient (TEC) for LSCF [72] (~21*10⁻⁶ K⁻¹ between 30-1000°C) is larger than that of GDC [151] (~13*10⁻⁶ K⁻¹ between 27-827°C). Bilayer strain measurements (where calculations were based on a 23nm LSCF particle on top a 23 nm nano-GDC particle) were also calculated and ranged in magnitude from 0.001% to 0.02%, which is large but not nearly as large as shown in Figure 6.8. Strain measurements were calculated using the LSCF Young' Modulus [152] (150/GPa at 800°C, 110/GPa at 700°C, and 100/GPa at 600°C), LSCF Poisson's ratio [152] (~0.3 at 600-800°C), LSCF TEC (21.4*10⁻⁶ K⁻¹) [72], GDC Young's Modulus [153] (~200/GPa at 600-800°C), GDC

Poisson's ratio [153] (0.33 at 600-800°C), and GDC TEC [151] (~13*10⁻⁶ K⁻¹). These values considerably are considerably lower than those in Figure 6.8, but additional surface tension described by the Young-LaPlace equation could be an additional source of stress in real-world GDC nano-particles.

Figure 6.9 shows the average oxide nano-particle sizes for PND, TXD and CAD LSCF using various nano-GDC loading levels when fired at 600°C, 700°C or 800°C for 1 hr. The particle sizes and standard deviation values were also calculated from the SEM images shown in Figure 6.2. The LSCF particle sizes stayed relatively constant at nano-GDC loading levels below 5.0 vol%, but were drastically reduced at nano-GDC loading levels above 5.0 vol% for TXD and CAD LSCF nano-particles fabricated at 700°C and 800°C. This is in sharp contrast to the gradual nano-particle reduction shown when using desiccation in Section 5.3.1.

Figure 6.10 shows the average pre-infiltrated nano-GDC and LSCF particle sizes in the PND, TXD and CAD LSCF cells fired at 600°C, 700°C or 800°C for 1 hr. The opaque particle size bars were calculated using the SEM images of Figure 6.2. The columns that are slightly transparent in the back were calculated using the Williamson-Hall technique. Note that the Figure 6.10 SEM particle sizes are the average size for both the GDC and LSCF infiltrate particles (since it is impossible to distinguish between GDC and LSCF infiltrated in the SEM), while the Williamson-Hall particle sizes are the average size of just the LSCF infiltrate. The fact that PND LSCF nano-particle size was not impacted by any nano-GDC loading level, but both TXD and CAD LSCF nano-particle size were, indicates that both a nano-GDC loading level above 5.0 vol% and a

solution additive are required for LSCF nano-particle sizes to be reduced. Possible reasons for this behavior are discussed at the end of this section.

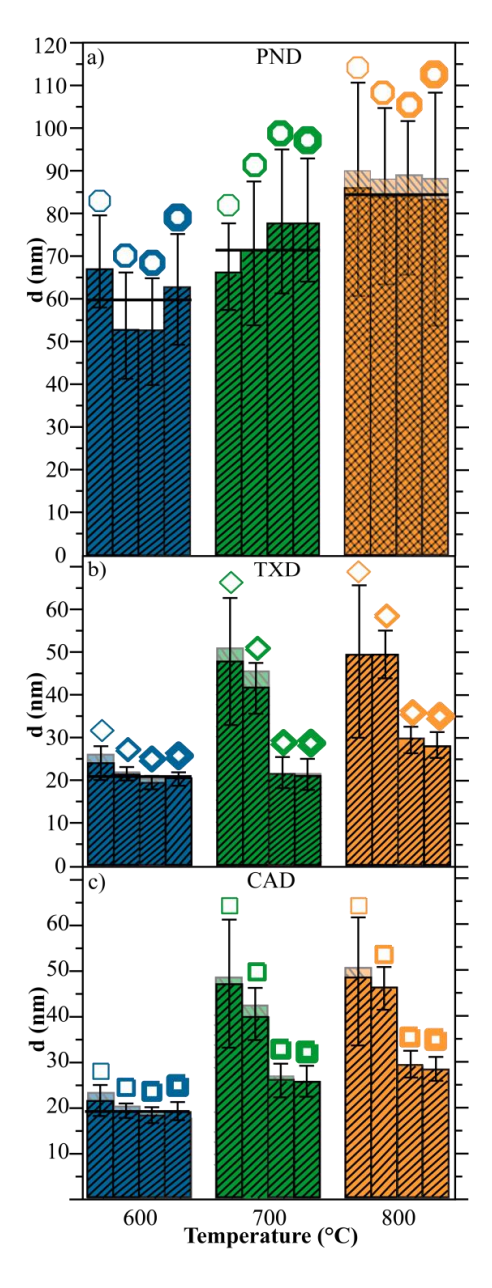


Figure 6.9: Bar-Graph of Average LSCF Infiltrate Particle Size Produced using Pre-Infiltration and Different Solution Additives. a) 1.50 molar PND LSCF, b) 1.50 molar TXD LSCF and c) 0.50 molar CAD LSCF precursor nitrate solutions at various temperatures. PND: \bigcirc =0.0 vol%, \bigcirc =5.0 vol%, \bigcirc =6.4 vol%, and \bigcirc =7.4 vol%. CAD: \square =0.0 vol%, \bigcirc =5.0 vol%, \square =6.4 vol%, and \bigcirc =7.4 vol%. Particle size data collected from SEM images are shown with 100% opacity and are striped pointing to the left, while particle size data collected using the Williamson-Hall method are shown with 50% opacity and are striped pointing to the right. Error bars are +/- a standard deviation calculated using the SEM-measured particle size distribution.

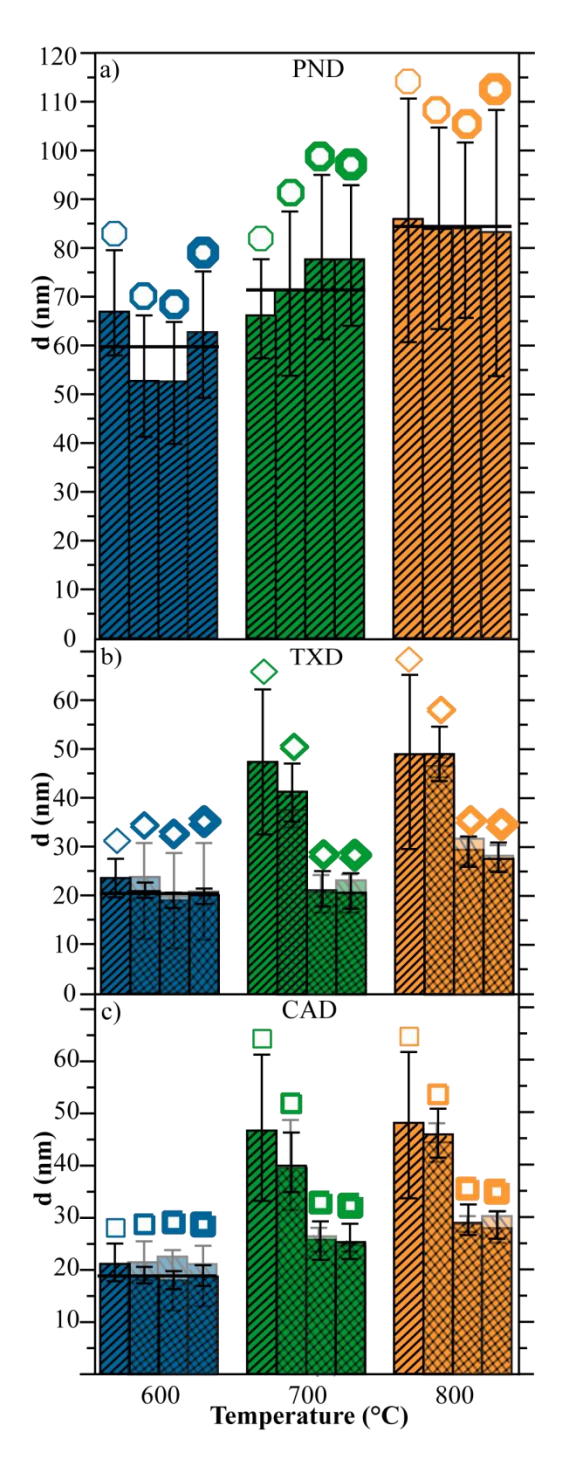


Figure 6.10: Bar-Graph of Average Nano-GDC Infiltrate Particle Size Produced using Pre-Infiltration and Different Solution Additives. a) 1.50 molar PND, b) 1.50 molar TXD LSCF and c) 0.50 molar CAD LSCF precursor nitrate solutions at various temperatures. PND: \bigcirc =0.0 vol%, \bigcirc =5.0 vol%, \bigcirc =6.4 vol%, and \bigcirc =7.4 vol%. CAD: \square =0.0 vol%, \bigcirc =5.0 vol%, \bigcirc =6.4 vol% and \bigcirc =7.4 vol%. Particle size data collected from SEM images are shown with 100% opacity and are striped pointing to the left, while particle size data collected using the Williamson-Hall method are shown with 50% opacity and are striped pointing to the right. Error bars are +/- a standard deviation calculated using the SEM-measured particle size distribution.

Figure 6.11 shows the raw EIS data for the pre-infiltrated CAD and TXD LSCF symmetrical cells tested at 500°C, 600°C and 700°C operating temperatures. Consistent with the LSCF particle size trends, the EIS data shows that the cathode resistance decreases with both increasing temperature and nano-GDC loading levels above 5.0 vol%. The raw EIS impedance data for CAD LSCF and TXD LSCF have both shown that pre-infiltration improves performance but the performance increase is larger when using TXD LSCF, which corresponds to the larger particle size reduction shown in Figure 6.2. The TXD LSCF performance using desiccation was also shown to be better than its CAD LSCF counterpart as well, which was previously shown to be the result of reduced infiltrate LSCF nano-particle size.

Figure 6.12 shows the R_P data for desiccated PND, CAD and TXD LSCF-GDC symmetrical cells determined from the raw impedance data. The R_P for CAD and TXD LSCF both decreased with increasing nano-GDC amount, while that for the PND LSCF did not change in response to pre-infiltrated nano-GDC. Since the LSCF particle size did not change either with PND LSCF, (just like desiccation), having the R_P not change is unsurprising. The 0.1 Ω cm² operating temperature decreased from ~650°C to ~545°C when using TXD LSCF and from ~700°C to ~600°C when using CAD LSCF. The operating temperature was not affected when using PND LSCF.

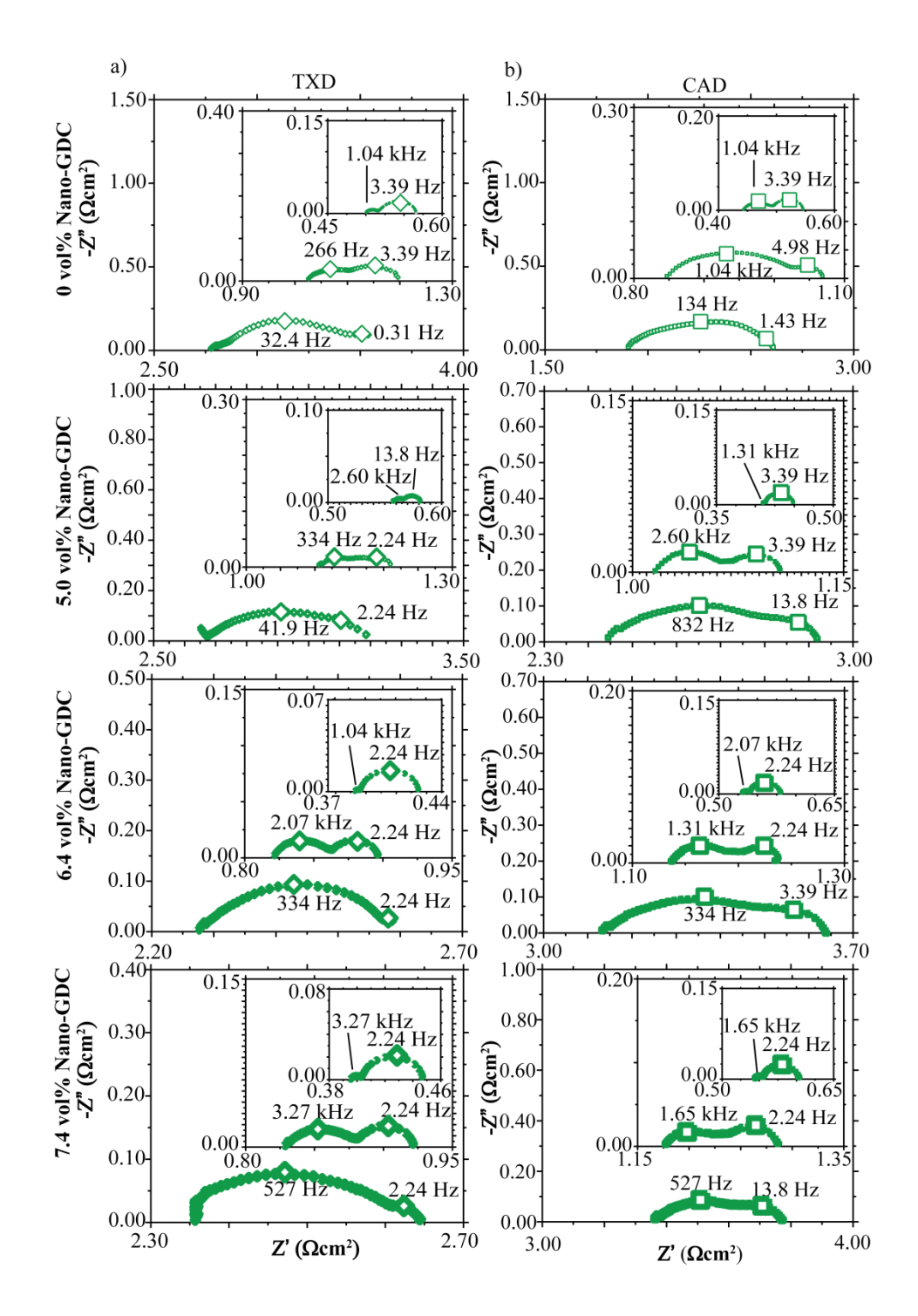


Figure 6.11: Raw Impedance Data Plots of Pre-Infiltrated LSCF-GDC NMCCs Produced using Citric Acid and Triton X-100. The outermost data was taken at 500° C, the nested data was taken at 600° C and the double nested data was taken at 700° C. TXD: $\lozenge=0.0$ vol%, $\bullet=5.0$ vol%, $\bullet=6.4$ vol% and $\bullet=7.4$ vol%. CAD: $\square=0.0$ vol%, $\bullet=5.0$ vol%, $\bullet=6.4$ vol%, and $\bullet=7.4$ vol%. All cathodes used 12.0 vol% LSCF. Differences in ohmic offset are due to thickness variations in the electrolyte between cells and not the result of electronic losses from GDC resistivity changes.

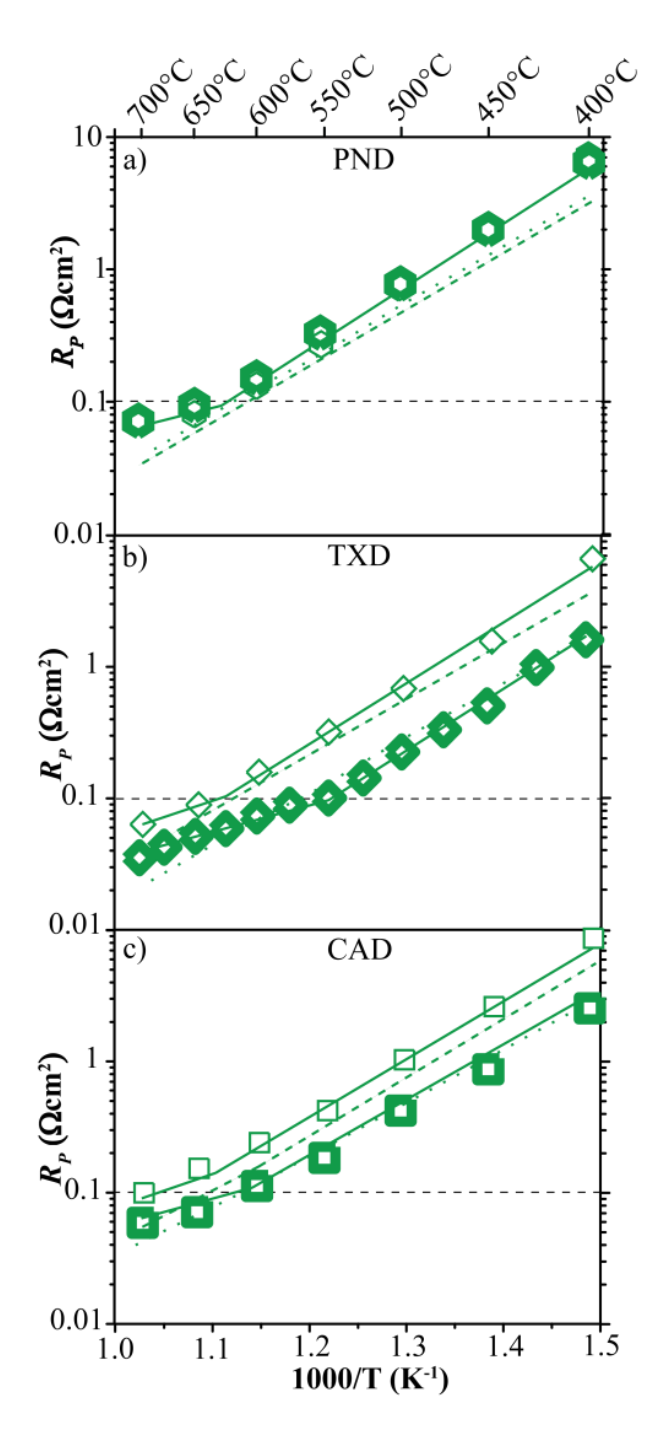


Figure 6.12: LSCF-GDC R_P Arrhenius Plots for NMCCs Produced using Pre-Infiltration and Different Solution Additives. a) 1.50 molar pure nitrate, b) 0.50 molar Citric Acid-contain and c) 1.50 molar TXD LSCF precursor nitrate solutions at 700°C fpr 1 hour. PND: \bigcirc =0.0 vol% and \bigcirc =7.4 vol%. CAD: \square =0.0 vol% and \bigcirc =7.4 vol%. All cathodes used 12.0 vol% LSCF. Differences in ohmic offset are due to thickness variations in the electrolyte between cells and not the result of electronic losses from GDC resistivity changes.

SIMPLE model R_P predictions were also made using nano-particle sizes from Figure 6.2. The SIMPLE model predicts similar performance changes compared to the experimental results. This suggests that LSCF nano-particle size reductions alone were responsible for the observed cathode performance gains. Similar behavior was observed for the desiccated LSCF of Section 5.3.1, which makes these results unsurprising.

Figure 6.13 [7] shows the ohmic resistivity of the GDC IC scaffold for the different operating temperatures. All the ohmic resistivity data for PND, CAD and TXD LSCF symmetrical cells match the resistivity of pure GDC, which indicate that differences in performance shown in Figure 6.12 were not caused by electronic losses in the scaffold.

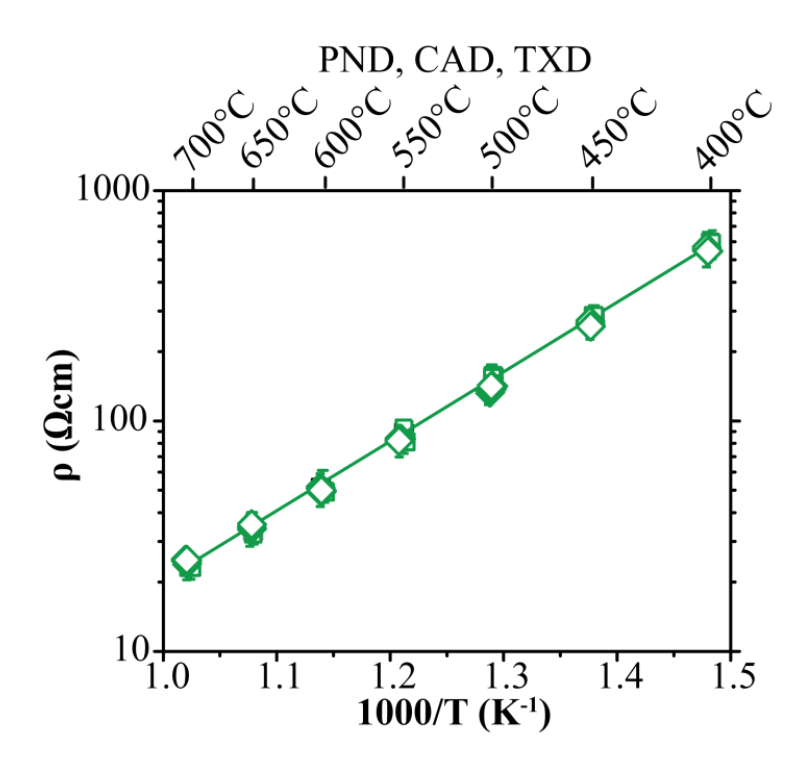


Figure 6.13: Arrhenius Ohmic Resistivity Plots for Pre-Infiltrated LSCF -GDC NMCCs Tested in Air using Different Solution Additives. PND: \bigcirc =0.0 vol%, \bigcirc =5.0 vol%, \bigcirc =6.4 vol%, and =7.4 vol%. CAD: \square =0.0 vol%, \bigcirc =5.0 vol%, \bigcirc =6.4 vol%, and \bigcirc =7.4 vol% and TXD: \bigcirc =0.0 vol%, \bigcirc =5.0 vol%, \bigcirc =6.4 vol% and \bigcirc =7.4 vol%. The inclined solid line is the resistivity of pure GDC from literature [7].

6.3.2 Pre-Infiltration and Solution Additive Impact on Infiltrate Phase Purity

Figure 6.14 [117, 118, 134-137, 141] shows ex-situ XRD data for PND, TXD and CAD-containing LSCF oxide powder fired at 700°C for 1 hr using different loading levels of nano-GDC. Just like the desiccated LSCF results of Section 5.3.2, in Figure 6.14 the phase purity of the powder increased as the solution changed from PND (left column) to CAD (right column) without the use of nano-GDC. After nano-GDC was added the phase purity could not be determined accurately due to peak overlap between the GDC and LSCF phase.

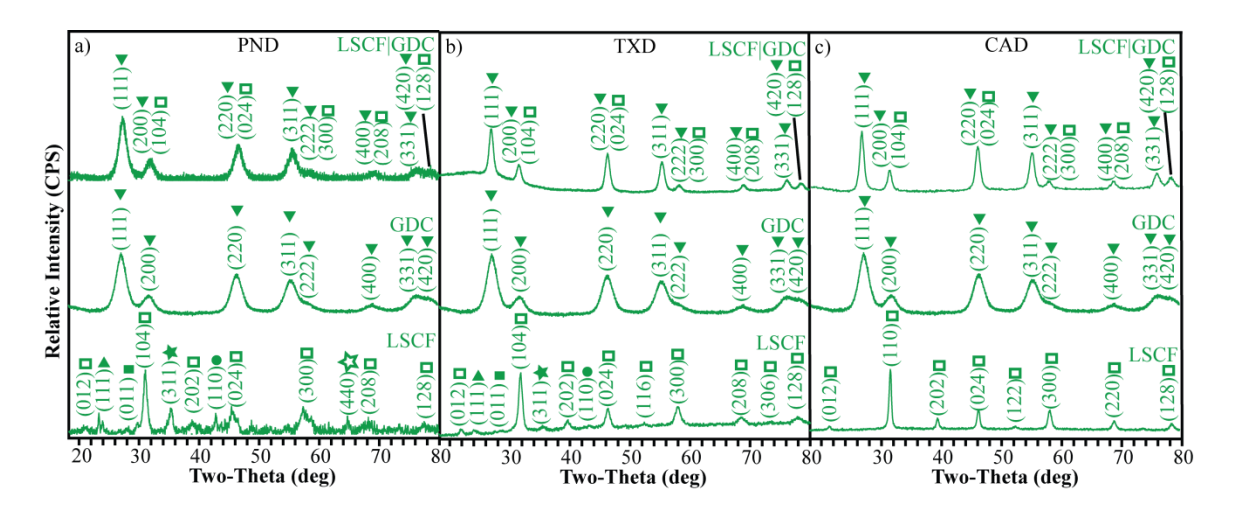


Figure 6.14: XRD Scans for Pre-Infiltrated LSCF and GDC Nano-Particles with Different Solution Additives. a) 0.50 molar Citric Acid-containing pre-infiltrated nano-GDC precursor gels and b) 1.50 molar Triton X-100-containing pre-infiltrated nano-GDC precursor gels (b) outside GDC scaffolds at 700°C. The pre-infiltrated nano-GDC\LSCF vol% ratio for all samples is 50:12. \blacktriangledown = $Ce_{0.9}Gd_{0.1}O_{1.95}$ (JCPDS # 01-075-0161) [118]. \Box = $La_{0.6}Sr_{0.4}Co_{0.8}Fe_{0.2}O_3$ (JCPDS # 00-048-0124) [117], \bigstar = $Co_{0.0}O_4$ (JCPDS # 01-074-2120) [141], \bigstar = $Co_{0.0}O_4$ (JCPDS # 01-080-1537) [134], \bullet = La_2O_3 (JCPDS # 01-071-4953) [135], \blacktriangle = La_2O_3 (JCPDS # 01-071-4953) [137].

Figure 6.15 [117, 118] shows 0.0 vol% nano-GDC and 7.4 vol% nano-GDC XRD data for LSCF 1.50 molar PND oxide powder fired at various temperatures between 80°C and 800°C. This data suggests that the addition of 7.4 vol% nano-GDC made the 0.0 vol% LSCF powder, at all fabrication temperatures (except at 80°C), phase pure. Exact

conclusions whether small impurity oxide phases are present are difficult to make due to the strong overlapping XRD signal of the nano-GDC.

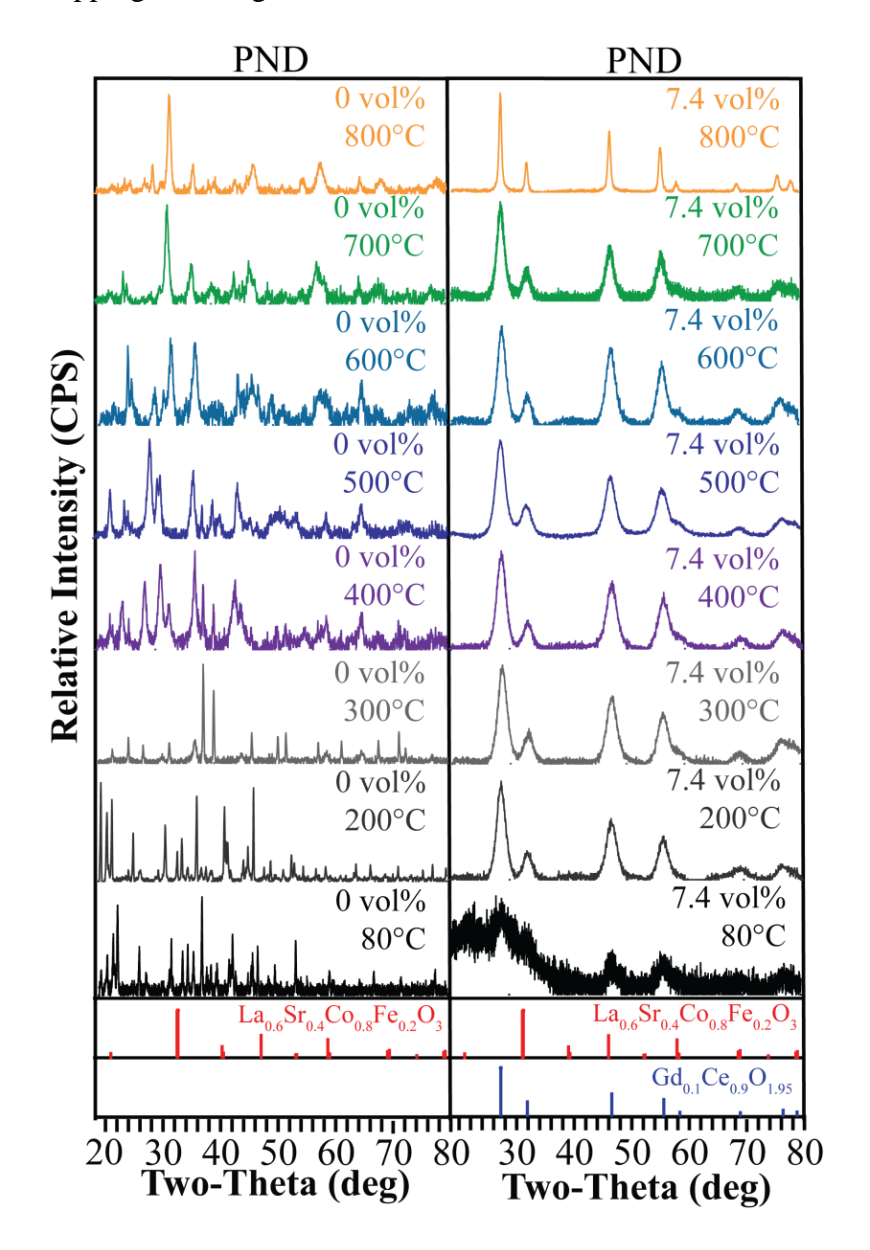


Figure 6.15: XRD Scans for 7.4 vol% Pre-Infiltrated PND LSCF Fired between 80° C and 800° C. The LSCF vol% was held constant at 12.0 vol % in all cases. $Ce_{0.9}Gd_{0.1}O_{1.95}$ (JCPDS # 01-075-0161) [118]. $La_{0.6}Sr_{0.4}Co_{0.8}Fe_{0.2}O_3$ (JCPDS # 00-048-0124) [117].

Figure 6.16 [117, 118] shows 0.0 vol% nano-GDC and 7.4 vol% nano-GDC XRD data for LSCF 1.50 molar TXD-containing oxide powder fired at various temperatures between 80°C and 800°C. The phase purity of the LSCF is phase pure for all fabrication temperatures above 200°C when using 7.4 vol% nano-GDC.

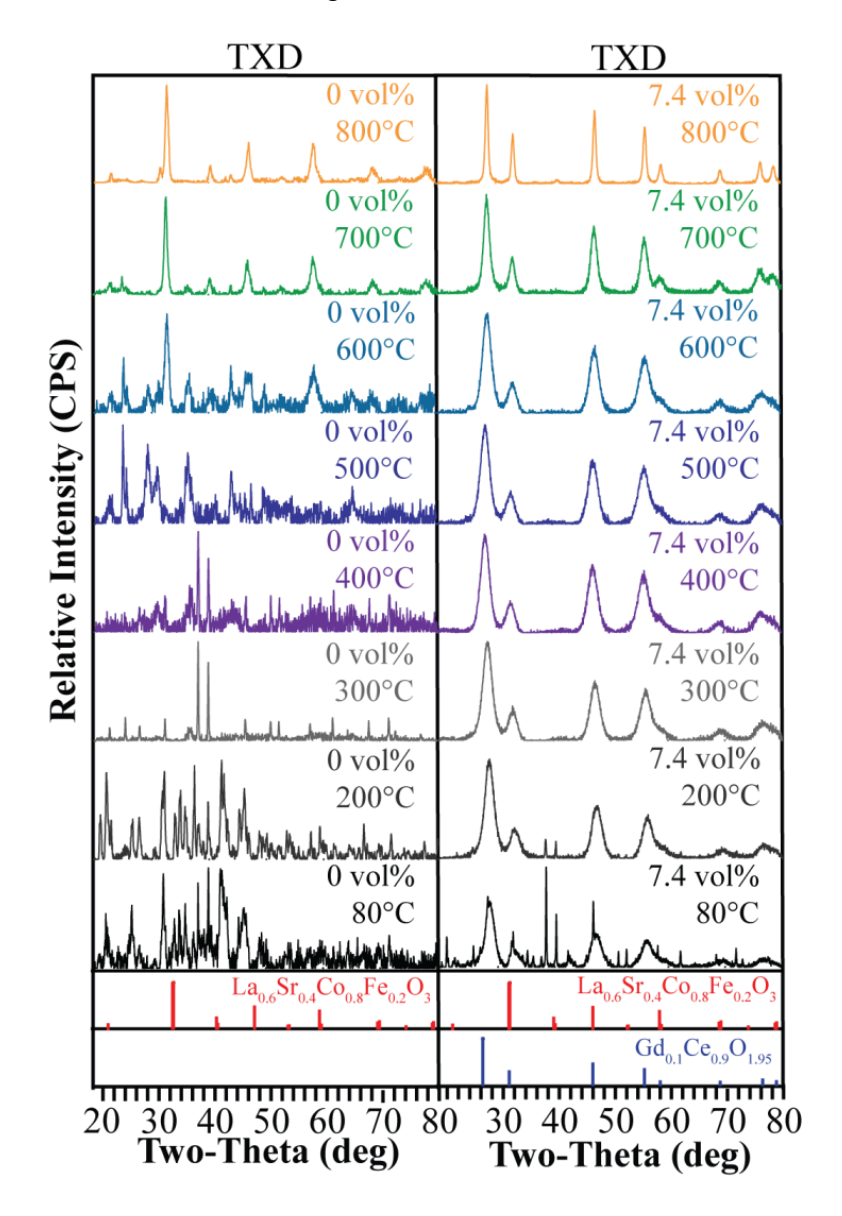


Figure 6.16: XRD Scans for 7.4 vol% Pre-Infiltrated TXD LSCF Fired between 80° C and 800° C. The LSCF vol% was held constant at 12.0 vol % in all cases. $Ce_{0.9}Gd_{0.1}O_{1.95}$ (JCPDS # 01-075-0161) [118]. $La_{0.6}Sr_{0.4}Co_{0.8}Fe_{0.2}O_3$ (JCPDS # 00-048-0124) [117].

Figure 6.17 [117, 118] shows 0.0 vol% nano-GDC and 7.4 vol% nano-GDC XRD data for LSCF 0.50 molar CAD-containing oxide powder fired at various temperatures between 80°C and 800°C. The phase purity of the LSCF is phase pure for all fabrication temperatures when using 7.4 vol% nano-GDC. This is in contrast to the phase purity of CaCl₂-desiccation CAD LSCF which still had phase impurities that formed at lower fabrication temperatures.

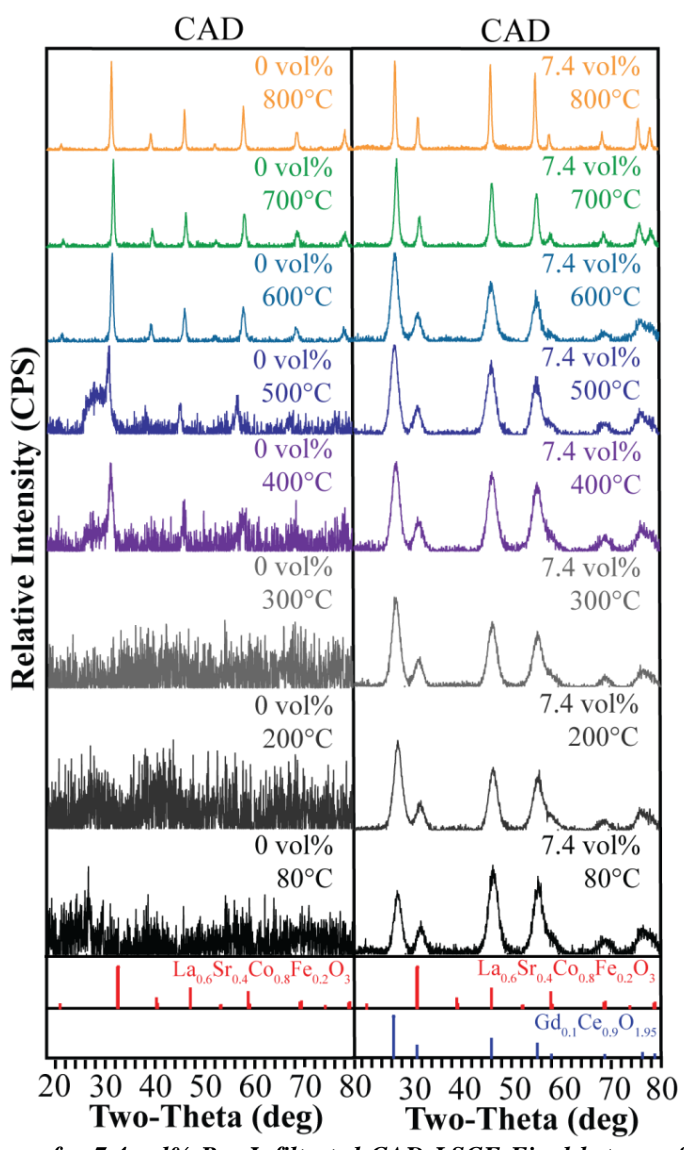


Figure 6.17: XRD Scans for 7.4 vol% Pre-Infiltrated CAD LSCF Fired between 80° C and 800° C. The LSCF vol% was held constant at 12.0 vol % in all cases. $Ce_{0.9}Gd_{0.1}O_{1.95}$ (JCPDS # 01-075-0161) [118]. $La_{0.6}Sr_{0.4}Co_{0.8}Fe_{0.2}O_3$ (JCPDS # 00-048-0124) [117].

The 7.4 vol% nano-GDC TXD LSCF had greater phase purity for all temperatures than the CaCl₂-desiccated TXD LSCF data presented in Section 5.3.2. Phase purity, using desiccation, for temperatures below 600°C still had a noticeable quantity of impurity peaks while the data in Figure 6.17 showed no impurity phases at any fabrication temperature other than 80°C.

Overall, the LSCF oxide phase when using TXD and CAD became the dominant phase around 600°C. However, the addition of nano-GDC was hypothesized to act as a coarsening reducing agent. It is hypothesized that at 600°C the addition of nano-GDC (at any loading level) did not reduce nano-particle size because the LSCF oxide particles have not had time to coarsen. In contrast at 700°C and 800°C coarsening was assumed, based on the results in Figure 6.16-6.17, which is why the TXD LSCF and CAD LSCF nano-particles show reduced particle size at nano-GDC loading levels greater than 5.0 vol%. It is further hypothesized that the PND LSCF nano-particles were not influenced by the nano-GDC because there was no surfactant or chelating agent to limit cation separation, preventing PND LSCF oxide particles from becoming the dominant phase until 700°C, by which time their pre-existing impurity phases had already coarsened.

6.3.3 Pre-Infiltration and Solution Additive Impact on Precursor Solution Decomposition Behavior

Figure 6.18 shows TGA datasets for PND, CAD and TXD LSCF-GDC cells infiltrated with different loading levels of nano-GDC. Since the nano-GDC does not allow for impurity phases to be observed in the XRD plots, TGA was used to observe the effects of nano-GDC. The pre-infiltrated PND LSCF and TXD LSCF TGA data indicates that the LSCF precursor thermal decomposition peaks (at low nano-GDC vol%) shifted to lower temperatures and finally disappeared at higher nano-GDC loading levels.

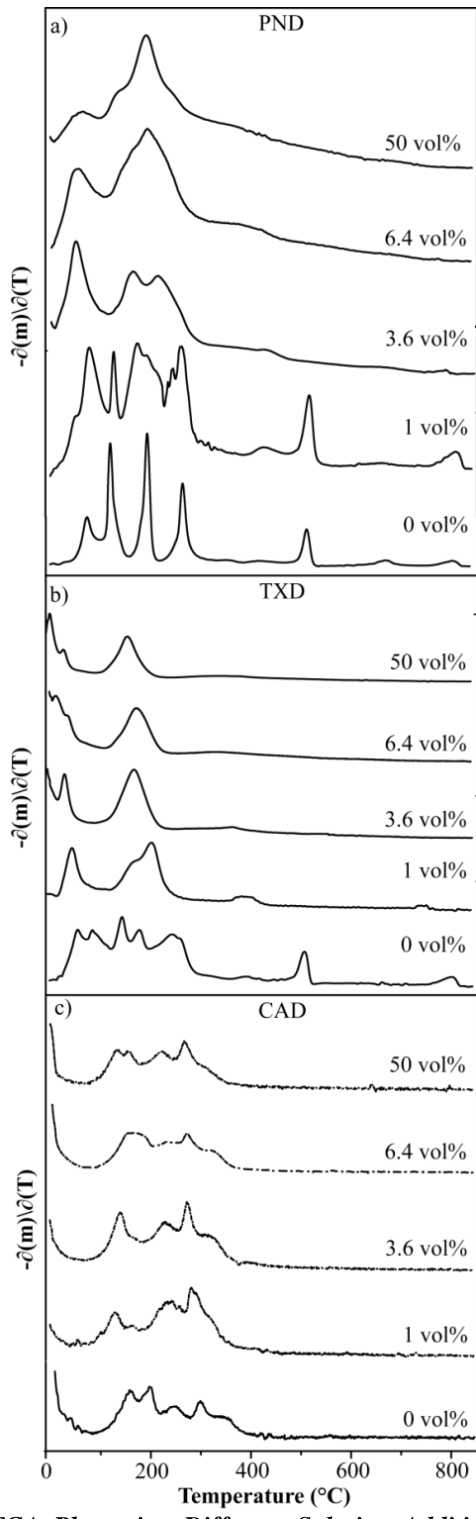


Figure 6.18: **Pre-Infiltrated TGA Plot using Different Solution Additives between 25°C and 850°C**. Samples are for: a) PND LSCF precursor solutions, b) CAD LSCF precursor solutions, and c) TXD LSCF precursor solutions. TGA data was collected up to 850°C.

The CAD LSCF TGA data also shows that a large multistage decomposition event (between 200°C and 400°C) gradually shifted to lower temperatures at higher nano-GDC loading levels. Previous literature studies have shown that ceria catalyzes nitrate decomposition [27], which maybe the reason why nano-GDC reduces the LSCF formation temperature.

6.3.4 Pre-Infiltration and Solution Additive Impacts on Performance and Stability

Figure 6.19 shows 500 hr open-circuit R_P data for 0.0 vol% nano-GDC PND and 7.4 vol% nano-GDC TXD and CAD LSCF-GDC symmetrical cells. As in Chapter 5, the initial performance of TXD LSCF cells were the highest, followed by the CAD LSCF cells, and finally the PND LSCF cells. Figure 6.19 shows that the PND and CAD LSCF-GDC degradation rate appears to be similar in magnitude and much larger than the TXD LSCF-GDC degradation rate. The initial "break-in" rates for all PND, TXD and CAD are much higher that the later, more constant degradation rates, similar to Chapter 5 desiccation. The 100-500 hr break-in degradation rates for PND are 9.8 % / khr while TXD has degradation rates of 6.3 % / khr and CAD degradation rates are 12.0 % / khr. For unknown reasons the degradation break-in rates are clearly larger than desiccation. However, the CAD and TXD LSCF nano-particle sizes required to obtain 500 hr R_P values would need to be between 60-65 nm, which is much larger than the standard deviation shown in Figure 5.6, and the particle sizes shown in Figure 6.20. This suggests that like desiccation, MIEC nano-particle size coarsening was not an active degradation mechanism at 540°C. However, more work beyond the scope of this thesis is needed to understand the active degradation mechanisms in these pre-infiltrated cathodes.

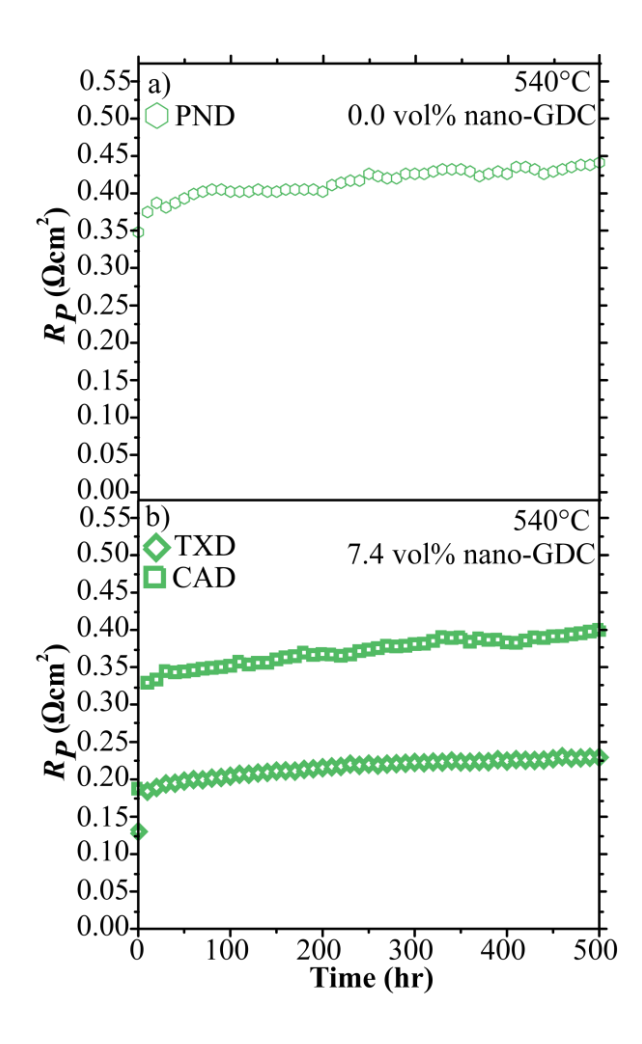


Figure 6.19: LSCF-GDC 500 hour R_P hour Plot for NMCCs Produced using Pre-Infiltration and Different Solution Additives. a) 1.50 molar pure nitrate \bigcirc , and b) 0.50 molar Citric Acid-containing \square and 1.50 molar Triton X-containing \bigcirc precursor nitrate solutions at 700°C for 1 hour.

Figure 6.20 shows SEM images of the CAD and TXD LSCF nano-particle sizes before and after 500 hr at 540°C. The particle sizes remain constant and do not show any signs of coarsening. This can be related back to the low phase impurity fraction seen in the CAD and TXD LSCF XRD data. As mentioned previously, SEM images of the PND LSCF cell were not obtained for this thesis due to time constraints for taking the PND LSCF 500 hr EIS measurement. Particle size coarsening could explain the increased R_P observed with the undesiccated PND LSCF, since particle sizes of ~100 nm were needed to produce the final 500 hr R_P values (calculated using the SIMPLE model), a 100 nm

was well within the standard deviation for PND LSCF nano-particles shown in Figure 6.9. Just like in Section 5.3.4 literature studies [146] support our hypothesis that particle size coarsening was not responsible for the cathode performance degradation observed in Figure 6.19.

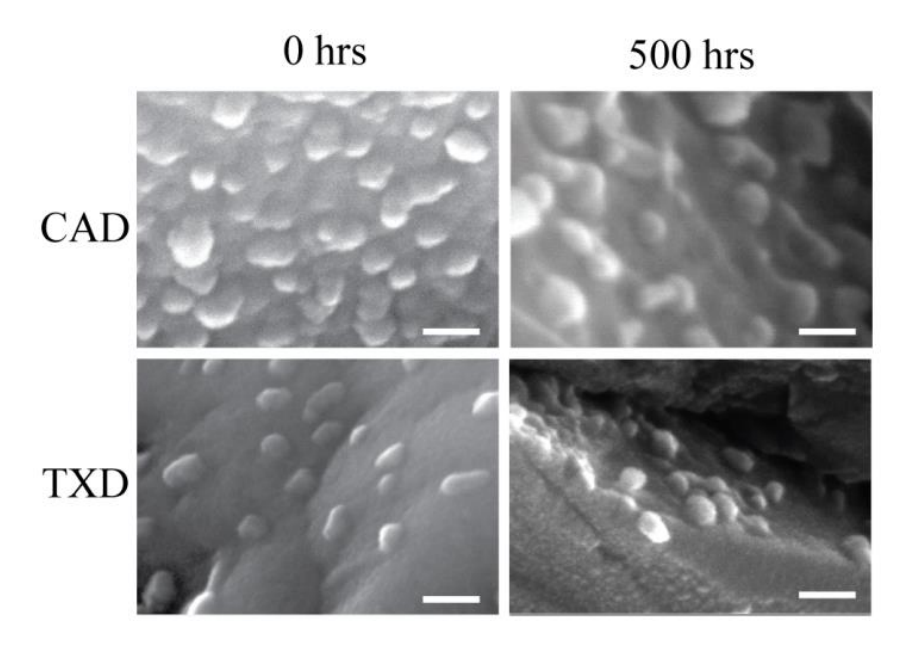


Figure 6.20: Pre-Infiltrated Scanning Electron Micrographs for CAD and TXD LSCF-GDC Symmetric Cells Tested for 500 hrs. Samples held at 540°C were imaged using the SEM for 0.5 molar CAD LSCF symmetric cells: a) 0 hrs and c) 500 hrs, and CaCl₂-Desiccated 1.50 molar TXD LSCF symmetric cells tested at 540°C after b) 0 hrs and d) 500 hrs. Each scale bar is 50 microns in width.

Figure 6.21 shows the raw EIS data before and after 500 hr open-circuit stability testing. The data shows that similar trends to these in Section 5.3.4, with R_P and ohmic offset suggesting that some mechanism other than infiltrate particle size. Further investigation into performance degradation is outside the scope of this thesis but should be investigated in the future.

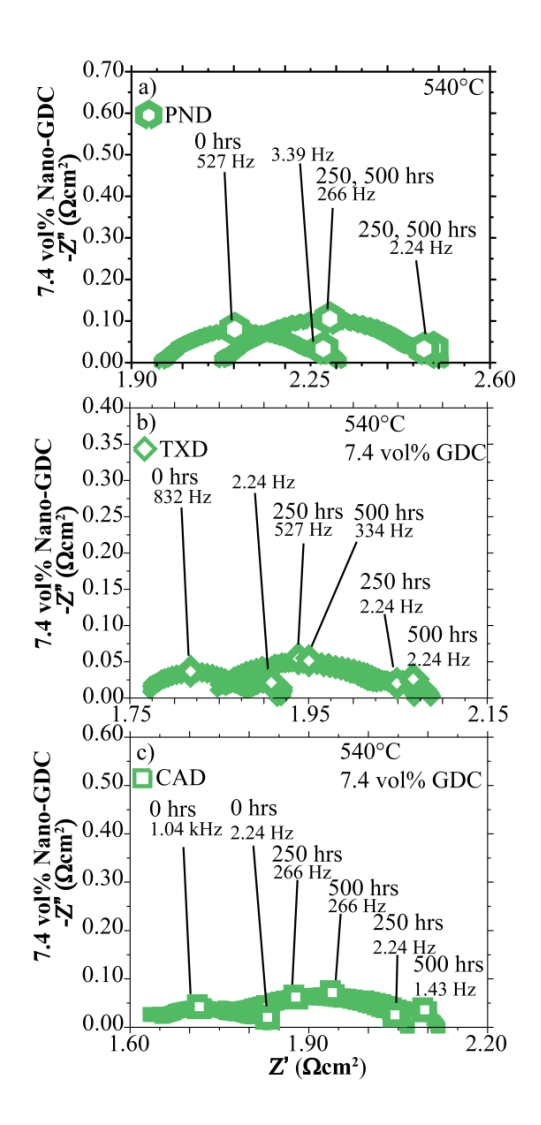


Figure 6.21: Raw Impedance Data Plots of Pre-Infiltrated LSCF-GDC NMCCs Produced using Different Solution Additives. a)1.50 molar Pure Nitrate(\mathbf{O}), b) 0.50 molar Citric Acid-containing (\Box) and c) Triton X-100 containing (\Diamond) precursor nitrate solutions at 700°C. R_P LSCF-GDC NMCC's measurements were taken for 500 hours.

6.4 Summary

In summary, ceria pre-infiltration was shown to reduce infiltrated LSCF nanoparticle size using different precursor solution additives, such as TXD and CAD. Preinfiltration was shown to not have an effect on infiltrated LSCF nano-particle size when a precursor solution additive was not present as with the PND case. Similar behavior was also observed with desiccation. As with desiccation, the magnitude of the TXD and CAD LSCF nano-particle size reduction was dependent on the precursor solution addition choice. With ceria pre-infiltration the average TXD LSCF nano-particle size was reduced from 48 nm to 22 nm, while the average CAD LSCF nano-particle was reduced from 50 nm to 27 nm. In contract to desiccation, the reduction of nano-particle size with ceria pre-infiltration was not gradual, but suddenly decreased once the loading level of nano-GDC was greater than 5.0 vol% for both CAD and TXD LSCF. As with desiccation, ceria pre-infiltration included performance changes were found to be solely the result of infiltrate nano-particle size reductions.

There were differences observed between the trends using pre-infiltration and desiccation. First, the performance degradation rate over 500 hrs was significantly higher using pre-infiltration for both CAD and TXD when compared to desiccation. Second, the XRD data for pre-infiltration was inconclusive due to peak overlap between the GDC and LSCF phases which resulted in TGA data being used to observe changes during decomposition. The TGA data suggests that when the loading level of nano-GDC is increased, the LSCF precursor solution decomposition events are shifted to lower temperatures or completely removed. The decrease in low temperature impurity content this produces may limit particle size growth during manufacturing, resulting in reduced average LSCF particle size.

CHAPTER 7: The Impact of Precursor Solution Desiccation and Nano-Ceria Pre-Infiltration on $La_{0.6}Sr_{0.4}Co_{1-x}Fe_xO_{3-\delta}$ (0 \leq x \leq 1) Infiltrated Cathodes

7.1 Introduction

The previous chapters have shown that the average infiltrated TXD and CAD LSCF nano-particle size can be reduced and NMCC performance can be increased using desiccation and ceria oxide pre-infiltration. In addition, the previous chapters have shown that the performance and average nano-particle size of LSCF-GDC NMCCs both have a strong dependence on surfactant type. The objective of the work in this chapter was to evaluate whether the precursor gel desiccation and ceria oxide pre-infiltration fabrication techniques could also be used to control the average nano-particle size of other CAD MIEC compositions in the $La_{0.6}Sr_{0.4}Co_yFe_{1-y}O_{3-\delta}$ (y= 0 to 1) (LSF-LSC) system.

7.2 Experimental Methods

7.2.1 Cathode-Electrolyte-Cathode Symmetric Cell Production

Symmetrical cathode-supporting electrolytes were fabricated in the same manner that was described in Chapters 4-6. Specifically, porous well-necked GDC IC scaffolds were produced on both sides of these electrolyte pellets. To achieve this, some of the aforementioned Rhodia GDC powder was coarsened at 800°C for 4 hours and then mixed with V-737 electronic vehicle (Heraeus; West Conshohocken, PA) to form a GDC ink with a 34% solids loading. Three layers of GDC ink were then screen printed onto each side of each dense GDC electrolyte pellet using a patterned 80 mesh stainless steel screen with a circular 0.5 cm² open area. Prior to the next ink layer being applied, each ink layer

was allowed to flow across the pellet surface for 5 minutes and then was placed in a bake oven at 120°C for 5 minutes to extract the electronic vehicle solvent and increase the green strength. After screen printing, the samples were heated to 400°C at 3°C/min, held at 400°C for one hour, heated to 600°C at 3°C/min, held at 600°C for one hour, heated to either 1100°C (desiccation) or 1050°C (pre-infiltration) at 5°C/min, held at either 1100°C for 3 hours (desiccation) or at 1050°C for 3 hours (pre-infiltration), and then cooled to room temperature at a nominal cooling rate of 10°C/min. Sintered IC scaffold thickness and roughness measurements were made with a Dektak 3 profilometer (Bruker; Tucson, AZ).

Three different fabrication techniques 1) a standard technique commonly used in the literature [5, 7] that was neither desiccated or pre-infiltrated, 2) the desiccation technique described in Chapter 4, or 3) the ceria pre-infiltration technique described in Chapter 6 were used in conjunction with various precursor solution compositions in the $(La_{0.6}Sr_{0.4}Co_xFe_{1-x}O_{3-\delta})$ (x =0 to 1) system. The standard technique had precursor solutions that were pipetted into the porous GDC cathode scaffolds, allowed to soak into the scaffold for 5 minutes, and gelled at 80°C for 10 min before being fired at 700°C for 1 hr to form nano-sized MIEC oxide particles on the scaffold surface. The desiccation technique is described in Section 4.2.1, and the pre-infiltration technique is described in Section 6.2.1. For all three techniques the MIEC precursor solutions were fabricated in the same manner as described in Sections 4.2.1 and 6.2.1. Desiccated cells used $CaCl_2$ as the desiccant and pre-infiltrated cells used a 7.4 vol% loading level of nano-GDC precursor solution. The cells made by all three techniques used a 12.0 vol% MIEC loading level for each composition. Lastly, symmetric cells were prepared for electrical

measurements by screen printing bilayer LSM-Au current collectors onto each NMCC in exactly the same manner as previous chapters.

7.2.2 Symmetrical Cell Impedance, X-ray Diffraction, and Scanning Electron Microscopy Measurements

NMCC symmetrical cells were characterized using EIS, XRD, and SEM in the same manner as described in Sections 4.2.2, 4.2.3, and 4.2.4 respectively.

7.2.3 Nano-Micro-Composite Cathode Performance Modeling

The NMCC performance was modeled using the SIMPLE model [5, 7, 8] in the manner described in Section 4.2.1.

7.3 Results

7.3.1 Pre-Infiltration, Desiccation and Infiltrated Composition Impacts on Infiltrate Particle Size and Performance

Figure 7.1 shows 600°C raw electrochemical impedance spectroscopy data for symmetrical cells infiltrated with CAD La_{0.6}Sr_{0.4}FeO₃ (LSF), CAD La_{0.6}Sr_{0.4}Co_{0.2}Fe_{0.8}O₃ (LSFC), CAD La_{0.6}Sr_{0.4}Co_{0.5}Fe_{0.5}O₃ (LSCF55), CAD La_{0.6}Sr_{0.4}Co_{0.8}Fe_{0.2}O₃ (LSCF), or CAD La_{0.6}Sr_{0.4}CoO₃ (LSC) using the: a) standard, b) desiccation, or c) pre-infiltration processing techniques. The highest R_P value was observed with CAD LSF using the standard technique while the lowest R_P value was observed using CAD LSC with the pre-infiltration technique. Note the systematic behavior of R_P vs. composition for all three processing methods. Another observation was that desiccation and pre-infiltration both improved performance to a greater extend with cobaltite compositions than ferrite compositions.

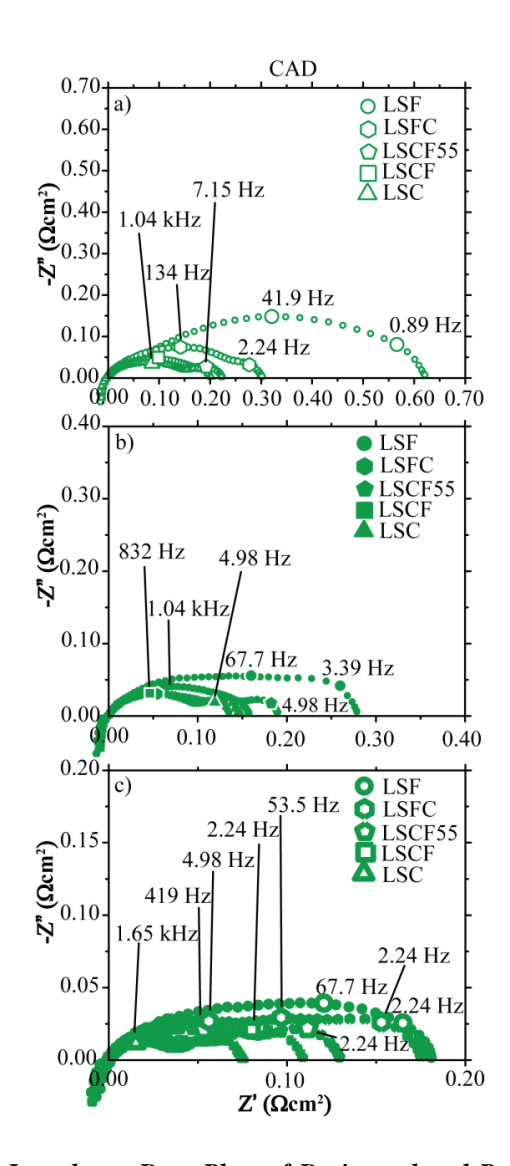


Figure 7.1: Figure 7.1: Raw Impedance Data Plots of Desiccated and Pre-Infiltrated La_{0.6}Sr_{0.4}Co_xFe₁. $_{x}O_{3-\delta}$ (0 \leq x \leq 1) using Citric Acid. Standard: $O=La_{0.6}Sr_{0.4}FeO_{3-\delta}$ (LSF), $O=La_{0.6}Sr_{0.4}Co_{0.2}Fe_{0.8}O_{3-\delta}$ (LSFC), $\triangle = La_{0.6}Sr_{0.4}Co_{0.5}Fe_{0.5}O_{3-\delta}$ (LSCF55), $\Box = La_{0.6}Sr_{0.4}Co_{0.8}Fe_{0.2}O_{3-\delta}$ (LSCF), $\Delta = La_{0.6}Sr_{0.4}CoO_{3-\delta}$ (LSC) ;Desiccated: \bullet = $La_{0.6}Sr_{0.4}FeO_{3-\delta}$ (LSF), $\bullet = La_{0.6}Sr_{0.4}Co_{0.2}Fe_{0.8}O_{3-\delta}$ $=La_{0.6}Sr_{0.4}Co_{0.5}Fe_{0.5}O_{3-\delta}$ (LSCF55), $\blacksquare = La_{0.6}Sr_{0.4}Co_{0.8}Fe_{0.2}O_{3-\delta}$ (LSCF), $\blacktriangle = La_{0.6}Sr_{0.4}CoO_{3-\delta}$ $\mathbf{O} = La_{0.6}Sr_{0.4}Co_{0.2}Fe_{0.8}O_{3-\delta}$ (LSC);Nano-GDC: $O=La_{0.6}Sr_{0.4}FeO_{3-\delta}$ (LSF), $= La_{0.6}Sr_{0.4}Co_{0.5}Fe_{0.5}O_{3-\delta} \ (LSCF55), \ \blacksquare = La_{0.6}Sr_{0.4}Co_{0.8}Fe_{0.2}O_{3-\delta} \ (LSCF), \Delta = La_{0.6}Sr_{0.4}CoO_{3-\delta} \ (LSC). \ All \ data$ was taken at 600°C.

Figure 7.2 shows Arrhenius R_P data for CAD LSF, CAD LSFC, CAD LSCF55, CAD LSCF, and CAD LSC infiltrated cells tested at operating temperatures between 400°C and 700°C for the standard, desiccation and pre-infiltration processing techniques.

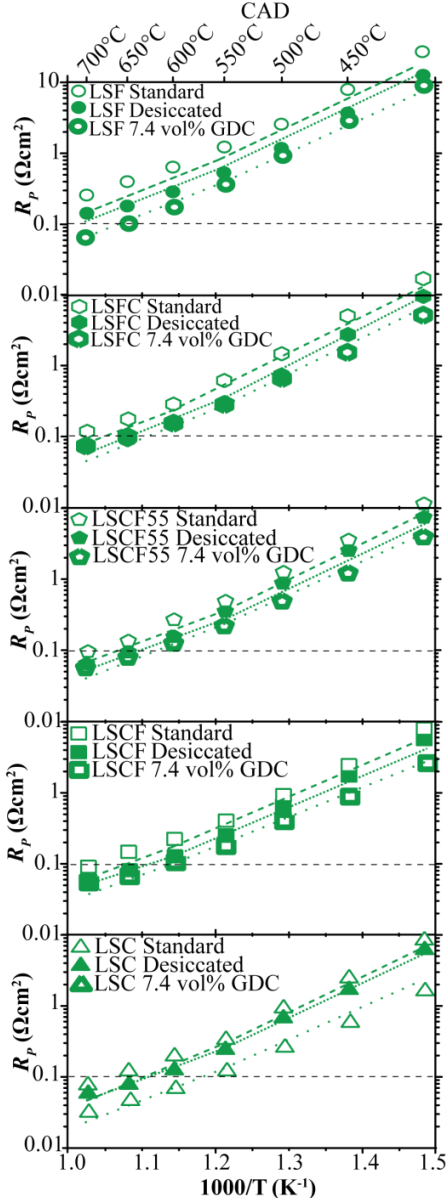


Figure 7.2: Desiccated or Pre-Infiltrated $La_{0,\delta}Sr_{0,4}Co_xFe_{1-x}O_{3-\delta}$ (0 \leq x \leq 1) R_P Arrhenius Plots for NMCCs Produced using Citric Acid. The dashed lines are SIMPLE model predictions, where the top most (for each composition) is for the standard case, the middle most is for the desiccated case and the lowest is for the pre-infiltrated nano-GDC case. Standard: $O=La_{0.6}Sr_{0.4}FeO_{3-\delta}$ (LSF), $\bigcirc=La_{0.6}Sr_{0.4}Co_{0.2}Fe_{0.8}O_{3-\delta}$ $(LSFC), \quad \triangle = La_{0.6}Sr_{0.4}Co_{0.5}Fe_{0.5}O_{3-\delta} \quad (LSCF55), \quad \Box = La_{0.6}Sr_{0.4}Co_{0.8}Fe_{0.2}O_{3-\delta} \quad (LSCF), \quad \Delta = La_{0.6}Sr_{0.4}CoO_{3-\delta}$ \bullet = $La_{0.6}Sr_{0.4}FeO_{3-\delta}$ $=La_{0.6}Sr_{0.4}Co_{0.2}Fe_{0.8}O_{3-\delta}$ (LSC) ;Desiccated: (LSF), $=La_{0.6}Sr_{0.4}Co_{0.5}Fe_{0.5}O_{3-\delta}$ (LSCF55), $\blacksquare = La_{0.6}Sr_{0.4}Co_{0.8}Fe_{0.2}O_{3-\delta}$ (LSCF), $\blacktriangle = La_{0.6}Sr_{0.4}CoO_{3-\delta}$ $\mathbf{O} = La_{0.6}Sr_{0.4}Co_{0.2}Fe_{0.8}O_{3-\delta}$ (LSC);Nano-GDC: $O=La_{0.6}Sr_{0.4}FeO_{3-\delta}$ (LSF), $=La_{0.6}Sr_{0.4}Co_{0.5}Fe_{0.5}O_{3-\delta} \ (LSCF55), \ \blacksquare =La_{0.6}Sr_{0.4}Co_{0.8}Fe_{0.2}O_{3-\delta} \ (LSCF), \Delta = La_{0.6}Sr_{0.4}CoO_{3-\delta} \ (LSC). \ All \ data$ was taken at 600°C.

In Figure 7.2 both desiccation and pre-infiltration are shown to reduce R_P for all material compositions but pre-infiltration reduced R_P to a greater extent than desiccation. The operating temperature for the target R_P values of 0.1 Ω cm² was reduced to a minimum temperature of ~550°C with CAD LSC using pre-infiltration. (Note, the 540°C 0.1 Ω cm² behavior reported in Section 6.3.1 was for pre-infiltrated TXD LSCF, not CAD LSCF). As was observed with Figure 7.1, the cobaltite MIEC materials performed better than the ferrite materials. Based on the R_s values from the literature shown in Figure 2.13, on average the cobaltite materials have a lower R_s (LSC, LSCF, SSC, and BSCF) value than the ferrite compounds (LSF and LSFC), which would tend to lead to improved cathode performance.

Figure 7.3 shows SEM images for: 1) standard (a-e), 2) desiccated (f-j), and 3) pre-infiltrated (k-o) cells fabricated at 700°C. For each processing technique, the average infiltrate particle size decreased slightly as the La_{0.6}Sr_{0.4}Co_xFe_{1-x}O_{3-δ} cobalt content increased; with standard average particle sizes ranging from ~55 nm for CAD LSF to ~50 nm for CAD LSC; desiccated average particle sizes ranging from ~46 nm for LSF to ~39 nm for LSC and pre-infiltrated average particle sizes ranging from ~31 nm for LSF to ~24 nm for LSC.

Figure 7.4 shows the average particle sizes for the various MIEC compositions for the a) standard, b) desiccation and c) pre-infiltration techniques. The nano-particle sizes shown in this figure are taken directly from Figure 7.3. As was stated in Figure 7.3, the nano-particle size decreased within each processing technique, with ferrite materials having larger average nano-particle sizes than cobaltite materials. Overall, desiccation and pre-infiltration both reduced the average nano-particle size with desiccation lowering

particle sizes from 55 nm to 42 nm and pre-infiltration lowering particle sizes from 55 nm to 26 nm. CAD LSC average nano-particle sizes were found to be the smallest of any

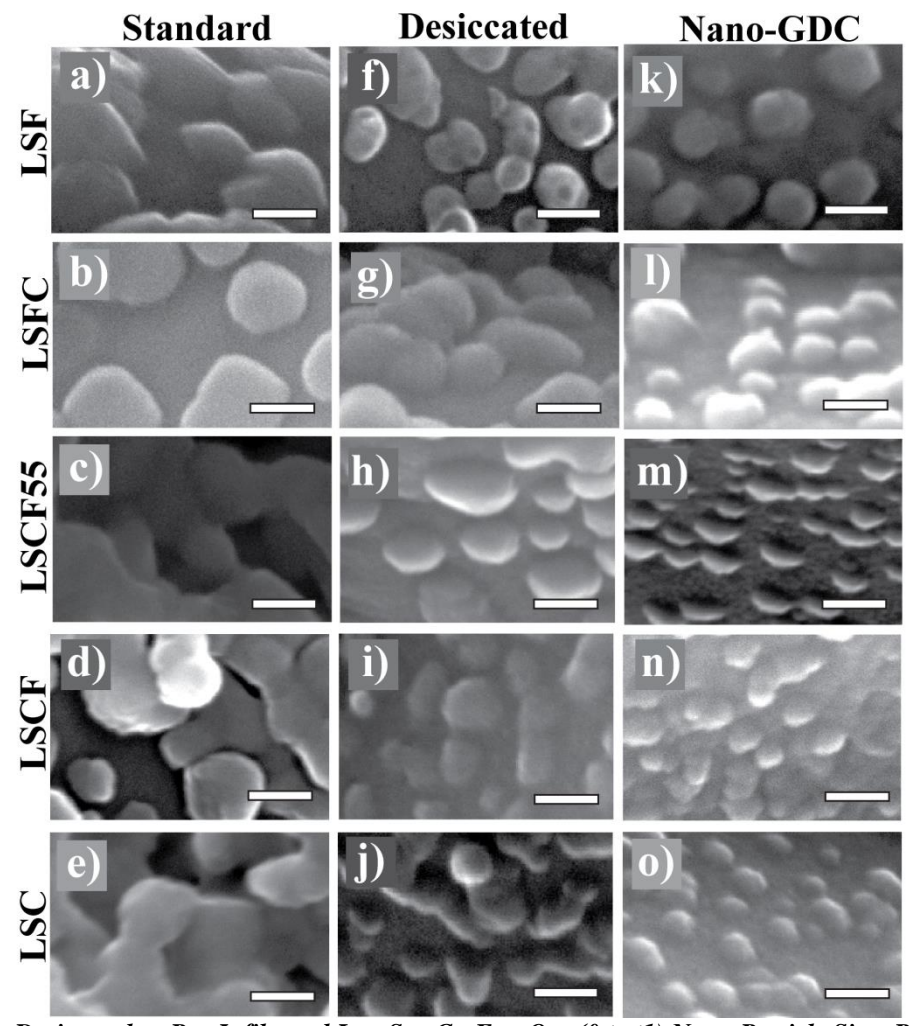


Figure 7.3: Desiccated or Pre-Infiltrated La_{0.6}Sr_{0.4}Co_xFe_{1-x}O_{3- δ} ($0 \le x \le 1$) Nano-Particle Sizes Produced using Citric Acid. Standard (a-e) desiccated (f-j) and pre-infiltrated nano-GDC oxide particles (k-o).

tested composition. This, coupled with the low R_s of LSC om Figure 2.13 which correlates to the CAD LSC cells having the lowest R_P values. The changes in particle size, when input into the SIMPLE model predicted R_P results that were consistent with observed experimental results. Williamson-Hall particle size measurements were not

conducted due to the large number of samples analyzed, and the reliability of the SEMdetermined particle sizes in Chapters 5 and 6.

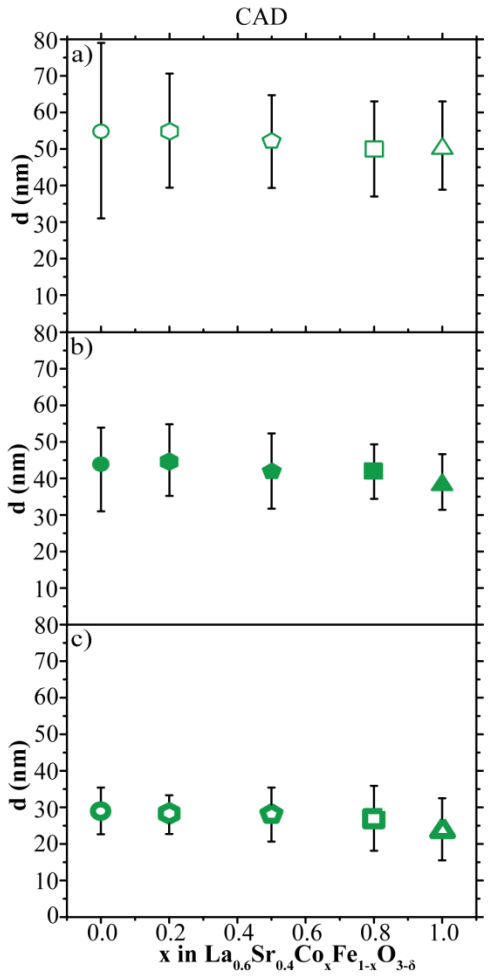


Figure 7.4: $La_{0.6}Sr_{0.4}Co_xFe_{1.x}O_{3.\delta}$ Nano-Particle Sizes Determined from Scanning Electron Microscopy Images. a) Standard, b) desiccated and c) pre-infiltrated nano-GDC nano-particles. Both desiccation and pre-infiltrated nano-GDC cells lower LSCF nano-particle sizes when compared to the standard case. Error bars indicate the standard deviation of LSCF nano-particle sizes calculated from the SEM images. Standard: $O=La_{0.6}Sr_{0.4}FeO_{3.\delta}$ (LSF), $\bigcirc=La_{0.6}Sr_{0.4}Co_{0.2}Fe_{0.8}O_{3.\delta}$ (LSFC), $\bigcirc=La_{0.6}Sr_{0.4}Co_{0.5}Fe_{0.5}O_{3.\delta}$ (LSCF), $\square=La_{0.6}Sr_{0.4}Co_{0.8}Fe_{0.2}O_{3.\delta}$ (LSCF), $\triangle=La_{0.6}Sr_{0.4}Co_{0.5}Fe_{0.5}O_{3.\delta}$ (LSCF), $\square=La_{0.6}Sr_{0.4}Co_{0.8}Fe_{0.2}O_{3.\delta}$ (LSCF), $\square=La_{0.6}Sr_{0.4}Co_{0.8}Fe_{0.2}O_{3.\delta}$ (LSCF), $\square=La_{0.6}Sr_{0.4}Co_{0.8}Fe_{0.2}O_{3.\delta}$ (LSCF), $\square=La_{0.6}Sr_{0.4}Co_{0.8}Fe_{0.2}O_{3.\delta}$ (LSCF), $\square=La_{0.6}Sr_{0.4}Co_{0.5}Fe_{0.5}O_{3.\delta}$ (LSCF), $\square=La_{0.6}Sr_{0.4}Co_{0.5}Fe_{0.5}O_{3.\delta}$ (LSCF), $\square=La_{0.6}Sr_{0.4}Co_{0.8}Fe_{0.2}O_{3.\delta}$ (LSCF), $\square=La_{0.6}Sr_{0.4}Co_{0.5}Fe_{0.5}O_{3.\delta}$ (LSCF), $\square=La_{0.6}Sr_{0.4}Co_{0.8}Fe_{0.2}O_{3.\delta}$ (LSCF), $\square=La_{0.6}Sr_{0.4}Co_{0.8}Fe_{0.2}O_{3.\delta}$ (LSCF), $\square=La_{0.6}Sr_{0.4}Co_{0.5}Fe_{0.5}O_{3.\delta}$ (LSCF), $\square=La_{0.6}Sr_{0.4}Co_{0.8}Fe_{0.2}O_{3.\delta}$ (LSCF), $\square=La_{0.6}Sr_{0.4}Co_{0.8}Fe_{0.2}O_{3.\delta}$ (LSCF). All data was taken at 700°C.

Figure 7.5 shows the ohmic resistivity of the GDC IC scaffold for the various CAD $La_{0.6}Sr_{0.4}Co_xFe_{1-x}O_3$ ($0 \le x \le 1$) EIS measurements in Figure 7.1. All the ohmic resistivity data for tested sample symmetrical cells matched the resistivity of pure GDC,

which indicated that the differences in performance shown in Figure 7.2, were not caused by electronic losses in the IC scaffold.

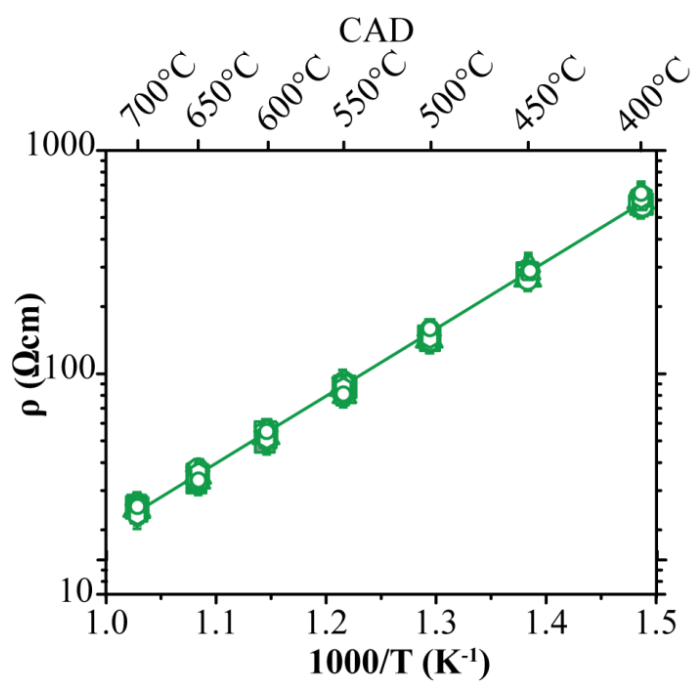


Figure 7.5: Arrhenius Ohmic Resistivity Plots for Desiccated or Pre-Infiltrated $La_{0.6}Sr_{0.4}Co_xFe_{1-x}O_{3.\delta}$ ($0 \le x \le 1$) NMCCs Produced using Citric Acid and Tested in Air. Standard: $O = La_{0.6}Sr_{0.4}FeO_{3.\delta}$ (LSF), $O = La_{0.6}Sr_{0.4}Co_{0.2}Fe_{0.8}O_{3.\delta}$ (LSF), $O = La_{0.6}Sr_{0.4}Co_{0.5}Fe_{0.5}O_{3.\delta}$ (LSF), $O = La_{0.6}Sr_{0.4}Co_{0.8}Fe_{0.2}O_{3.\delta}$ (LSF), $O = La_{0.6}Sr_{0.4}Co_{0.2}Fe_{0.8}O_{3.\delta}$ (LSF), $O = La_{0.6}Sr_{0.4}Co_{0.2}Fe_{0.8}O_{3.\delta}$ (LSF), $O = La_{0.6}Sr_{0.4}Co_{0.5}Fe_{0.5}O_{3.\delta}$ (LSF), $O = La_{0.6}Sr_{0.4}Co_{0.2}Fe_{0.8}O_{3.\delta}$ (LSF). All data was taken at O O O C. The inclined solid line is the resistivity of pure GDC from literature [7].

7.3.2 Pre-Infiltration, Desiccation and Infiltrated Composition Impacts on Infiltrate Phase Purity

Figure 7.6 [117, 154-156] shows standard and desiccated XRD data for the different powder compositions fired at 700°C for 1 hour. The powder produced using the standard method is shown in the upper datasets and the powder produced using the desiccation method is shown in the lower datasets for each material composition. The results in this figure show that desiccation did not affect CAD $La_{0.6}Sr_{0.4}Co_xFe_{1-x}O_3$ $(0 \le x \le 1)$ phase purity.

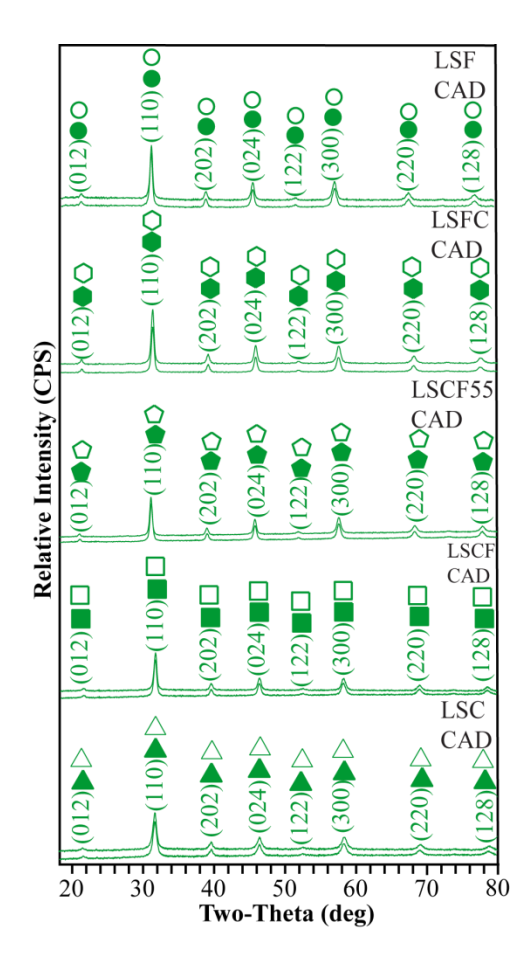


Figure 7.6: XRD Scans for CaCl₂-Desiccated La_{0.6}Sr_{0.4}Co_xFe_{1-x}O_{3-\delta} (0\leq x\leq 1) Produced using Citric Acid. Standard XRD spectra are stacked above the desiccated XRD spectra for each peak. Standard: $O=La_{0.6}Sr_{0.4}FeO_{3-\delta}$ (LSF)(JCPDS # 01-072-8133) [154], $O=La_{0.6}Sr_{0.4}Co_{0.2}Fe_{0.8}O_{3-\delta}$ (LSFC) [155], $O=La_{0.6}Sr_{0.4}Co_{0.5}Fe_{0.5}O_{3-\delta}$ (LSCF55), $O=La_{0.6}Sr_{0.4}Co_{0.8}Fe_{0.2}O_{3-\delta}$ (LSCF) (JCPDS # 00-048-0124) [117], $A=La_{0.6}Sr_{0.4}Co_{0.2}Fe_{0.8}O_{3-\delta}$ (LSFC) [155], $A=La_{0.6}Sr_{0.4}Co_{0.5}Fe_{0.5}O_{3-\delta}$ (LSCF55), $O=La_{0.6}Sr_{0.4}Co_{0.5}Fe_{0.5}O_{3-\delta}$ (LSCF55), $O=La_{0.6}Sr$

Figure 7.7 [118] shows standard and pre-infiltrated XRD data for the different powder CAD $La_{0.6}Sr_{0.4}Co_xFe_{1-x}O_3$ ($0 \le x \le 1$) composition fired at 700°C for 1 hour. As observed previously for CAD LSCF in Figure 6.10 the 7.4 vol% nano-GDC pre-infiltration powder had such a large signal that small impurity oxide phases were not detectable, but large impurity oxide phases were still not observed.

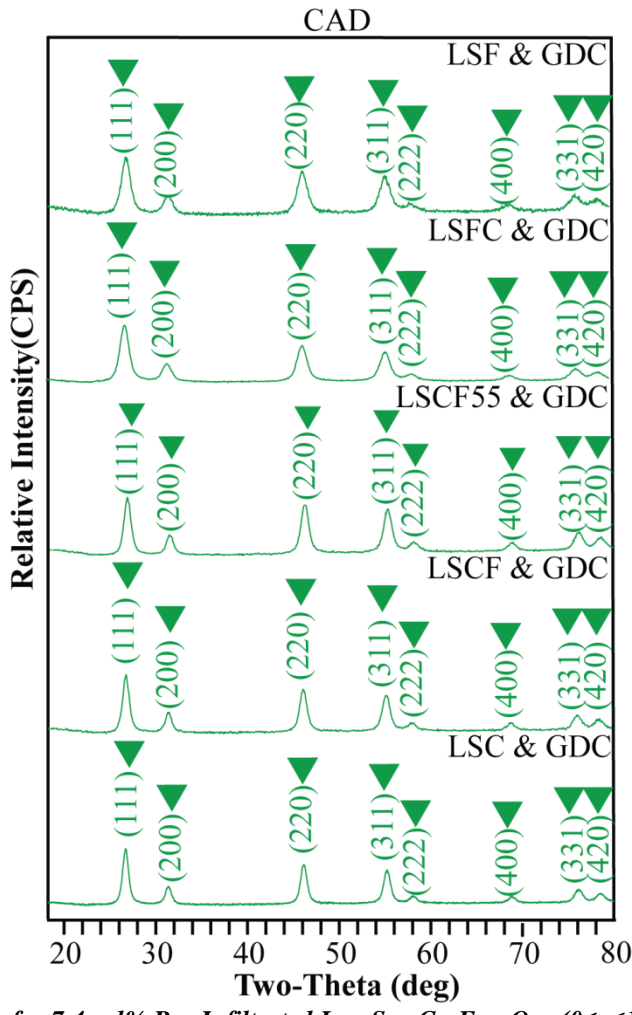


Figure 7.7: XRD Scans for 7.4 vol% Pre-Infiltrated La_{0.6}Sr_{0.4}Co_xFe_{1-x}O_{3- δ} ($0 \le x \le 1$) Produced using Citric Acid. $\nabla = Gd_{0.1}Ce_{0.9}O_{1.95}(JCPDS\ 01-075-0161)\ [118]$.

7.4 Summary

In summary, this chapter was intended to evaluate the impact desiccation and preinfiltration have on infiltrated nano-particle size and NMCC performance when using MIEC compositions other than LSCF. For all tested CAD La_{0.6}Sr_{0.4}Co_xFe_{1-x}O₃ ($0 \le x \le 1$) compositions both nano-particle size and R_P values were shown to be reduced using CaCl₂-desiccation or 7.4 vol% nano-GDC pre-infiltration. The nano-particle size reduction was observed to be the reason for increased performance with all material compositions, just as was seen in Chapters 4-6. Desiccation reduced infiltrated nanoparticle size from 55-50 nm (LSF to LSC) to 45-39 nm (LSF to LSC), while pre-infiltration reduced nano-particle size to 30-24 nm (LSF to LSC). Clearly, pre-infiltration reduced infiltrated nano-particle size for all material compositions to a greater extent than desiccation. Material composition phase purity was not impacted by either desiccation or pre-infiltration, at least at a fabrication temperature of 700°C.

Chapters 4-7 have examined both the desiccation and pre-infiltration techniques and investigated their effects on infiltrated cathode nano-particle size and performance. Based on the results observed, a preliminary recommendation for the desiccation technique would be given as the best technique to use for commercial SOFC production. This recommendation is based on: 1) desiccation having a substantially lower degradation rate at 540°C for both CAD and TXD LSCF cells compared to pre-infiltrated CAD and TXD LSCF cells, 2) desiccation lowering the operating temperature by 75°C (from 650°C to 575°C) compared to the standard technique, and 3) the manufacturing costs for desiccation are low since CaCl₂ is inexpensive and desiccation has a low cost capital expenditure. The main downside of using this technique is an increased manufacturing time due to the desiccation process. However, the desiccation manufacturing time could possibly be expedited through the use of alternative desiccants possessing faster desiccation kinetics.

CHAPTER 8: Determination of Infiltrated Mixed Ionic and Electronic Conducting Nano-Particle Oxygen Surface Exchange Material Properties through Finite Element Modeling of 3D Reconstructed Microstructures

8.1 Introduction

Section 2.8 highlighted that a lack of knowledge regarding the intrinsic oxygen surface exchange resistance, R_s , of infiltrate MIEC materials was one of the greatest obstacles limiting the development and improvement of low temperature NMCCs and SOFCs. Past literature studies have measured thin film R_s values for LSF [52, 54], LSCF [51, 54], LSFC [54, 95], LSC [54, 97], SSC [54, 98], and BSCF [49, 50] compositions. However, no infiltrate R_s values have ever been measured. Further, as stated in Section 1.3, literature studies have shown that large MIEC R_s discrepancies exist between current literature reports of these compositions [10]. Infiltrate R_s measurements are needed because the different stress and surface states of infiltrated MIEC particles could lead to R_s values significantly different than those obtain from thin or bulk films. Further, these R_s values would allow the SOFC community to determine the optimal MIEC infiltrate compositions and correctly model and optimize NMCC performance. Therefore, the objective of the work in this chapter was to: 1) determine R_s values for different infiltrated MIEC materials using FIB-SEM FEM 3D reconstructions, and 2) evaluate the $R\sqrt{1}$ C ratios under which the SR limit and SIMPLE models break down. Both these objectives were achieved through the use of finite element modeling.

8.2 Experimental Methods

8.2.1 Cathode-Electrolyte-Cathode-Symmetric Cell Production

Cathode-supporting symmetrical cells were prepared in the same manner as Section 7.2.

8.2.2 Electrochemical Impedance Spectroscopy Measurements

EIS characterization was performed in the same manner as Section 4.2.

8.2.3 Nano-Micro-Composite Cathode Finite Element Modeling of 3D Reconstructions

As discussed in Section 3.3.3, a set of 2D serial sections were obtained to create a 3D reconstruction using a computer program called MIMICS (Materialise Inc, Leuven Belgium). This 3D reconstruction was then volume meshed using a second computer program called 3-Matic (Materialise Inc, Leuven Belgium), and finally a FEM computer program called COMSOL (COMSOL Inc, Palo Alto California) was used for performance calculations. Section 3.3 outlines the multiple steps involved in: 1) creating the FIB-SEM 3D reconstruction, 2) creating the 3D microstructure volume mesh, and 3) modeling the 3D volume mesh in COMSOL. A step-by-step guide on this procedure is provided in Appendix 2.

Here, the volume mesh of both the cathode and electrolyte was created with a large enough number of tetrahedrons (calculation boxes used in FEM) to provide an accurate determination of the performance. The volume mesh size used in the performance calculations was slightly over 1 million tetrahedrons (using the dimensions provided in Figure 3.11). Performance calculations using a volume mesh size of over 5 million tetrahedrons also conducted using the 3D reconstruction shown in Figure 3.11)

yielded performance values that were only different by ~4%, indicating the adequacy of the FEM mesh size. Next, electrochemical potential lines were generated from the volume mesh using COMSOL. As discussed in Section 3.3.6 and Appendix 2, the potential lines were calculated by applying a scaled R_s value, and a 1V potential to the entire cathode surface mesh, and a 0V potential to the bottom of the electrolyte microstructure. Cathode R_P calculations were then conducted using the calculated electrochemical potential lines to mathematically determine the current crossing the bottom of the electrolyte and the use of Equation 16. R_P values from 3D reconstructions of both 4.1 μ m thick and 8 μ m were compared and R_P predictions from both reconstructions were very close to each other indicating that edge effects had no significant contribution to the final results. Finally, R_P values were calculated using COMSOL for temperatures between 600°C-700°C. These R_P values were then compared against experimentally determined NMCC EIS R_P values from: 1) Chapter 4 for LSCF, 2) Chapter 7 for LSF, LSFC, and LSC, and 3) Nicholas *et al.* [5] for SSC. To calculate R_s, the FEM inputted R_s values were adjusted until the FEM determined and experimentally determined R_P values agreed.

8.3 Results

8.3.1 A Comparison of Finite Element Modeling Mixed Ionic Electronic Conducting Materials Intrinsic Oxygen Surface Exchange Material Properties

Figure 8.1 [51, 54, 95-102] shows the reported literature R_s , k_{chem} , and k_o values from Section 2.7.3 overlaid with R_s values determined from FEM calculations of FIB-SEM 3D reconstructed microstructures. In Figure 8.1, the activation energies of infiltrated CAD LSF (1.01 eV), CAD LSFC (1.18 eV), CAD LSCF (1.04 eV), CAD LSC

(1.08 eV) and CAD SSC (1.38 eV) are lower than or equal to the reported literature data. In contrast, however, the 600-700°C magnitude of these FEM calculated values agree surprisingly well with the literature values (i.e. within 1 order of magnitude).

Figure 8.2 shows all the FEM-determined R_s , k_{chem} and k_o values for LSF, LSFC, LSCF, LSC and SSC on a single plot. The R_s values for the different cathode MIEC materials consistently stay within 2 orders of magnitude of each other, but the k_{chem} and k_o values have a much larger variation. This larger variation in k_{chem} and k_o is caused from a difference in the C_o and γ values shown in Figure 2.12.

From a purely R_s perspective, the best infiltrated MIEC material to use between 600-700°C is SSC because it has the lowest Figure 8.2 R_s value of any MIEC composition and also has k_{chem} and k_o values that are nearly 2 orders of magnitude higher than the other MIEC compositions. These high-temperature results are not surprising since they match closely with what Baumann $et\ al.$ [54] has shown in literature for thin film MIEC materials. However when these results are projected to lower operating temperatures, then LSF becomes a better MIEC material choice since it has the lowest activation energy, and thus (by extension) would have the lowest R_s value. This is surprising since Baumann $et\ al.$ [54] shows thin film LSF to have much higher activation energy (1.8 eV) compared to SSC (1.3 eV) over the 600-700°C temperature range. This disagreement clearly shows that the properties of MIEC infiltrate can be different than MIEC thin films, and justifies the need for FIB-SEM FEM calculations such as those presented here.

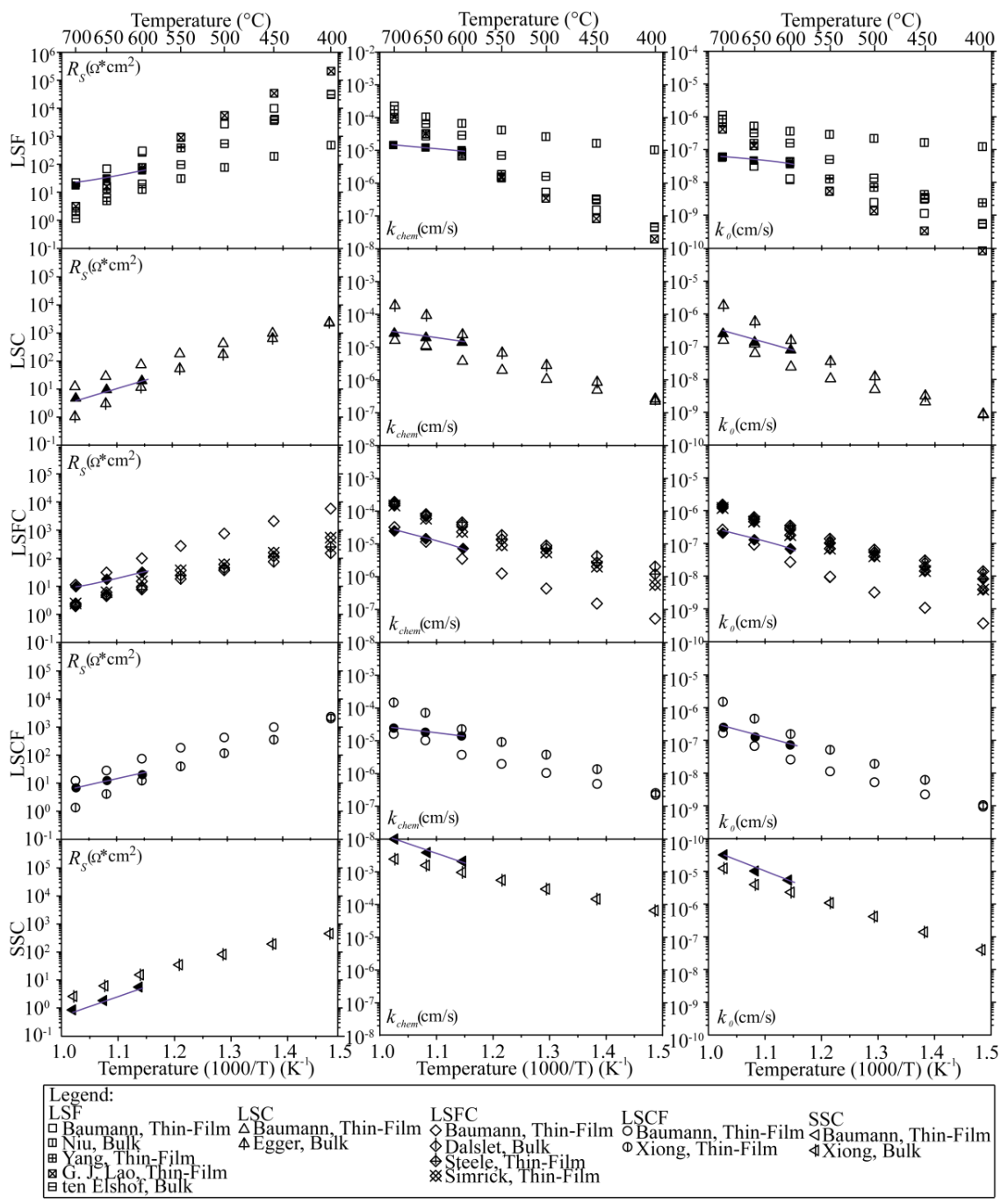


Figure 8.1: R_s , k_{chem} and k_o values Reported in Literature and Calculated using FIB-SEM FEM 3D Reconstructions for the Cathode MIEC Materials LSF, LSFC, LSCF, LSC and SSC. Open symbols are for data from literature studies and closed symbols are for calculated values from FIB-SEM FEM 3D reconstructions [51], [54], [85-92].

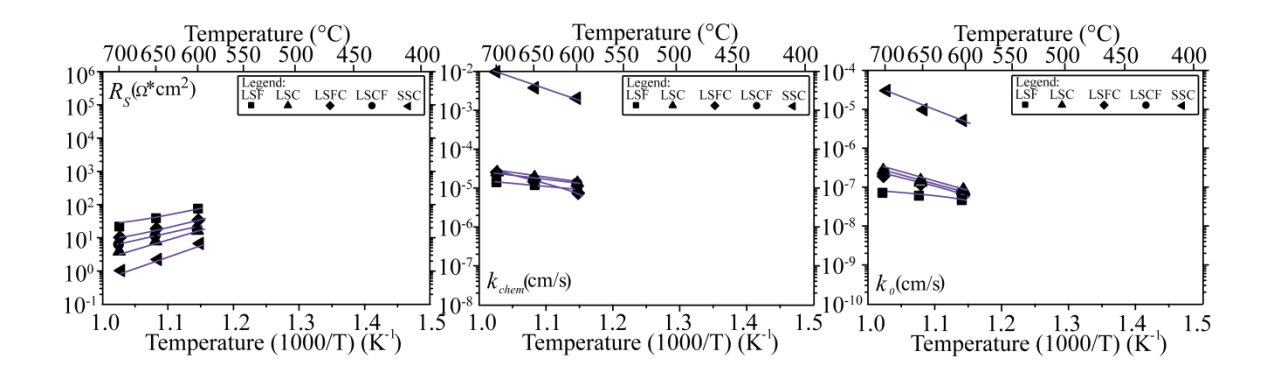


Figure 8.2: R_s , k_{chem} and k_o Values Calculated using the FIB-SEM FEM 3D Reconstruction for Cathode MIEC Materials LSF, LSFC, LSCF, LSC and SSC. The legend in the top-right corner of each subfigure shows the MIEC material for each symbol.

Despite the importance of a low R_s value, determination of the optimal MIEC composition for infiltration should also account for the ability to reduce the size of infiltrate particles made of that composition. In light of this, LSCF (R_{ct} is 5.06 at 600°C, 2.53 at 650°C, and 1.52 at 700°C) and LSC (R_{ct} is 5.46 at 600°C, 2.29 at 650°C, and 1.29 at 700°C) are probably the best MIEC compositions to use at the moment because unlike SSC and LSF both these compositions exhibit large nano-particle size reductions using both desiccation and pre-infiltration shown in Chapters 5-7. Of course, a low MIEC R_s value alone is not enough to guarantee a low MIEC infiltrate cathode R_p . The cathode microstructure also has an effect.

8.3.2 Identifying the Materials Property Combinations Causing the Surface Resistance Limit and the Simple Infiltration Microstructure Polarization Loss Estimation Model to Breakdown

Throughout this thesis three NMCC R_P prediction models have been used: 1) the FIB-SEM FEM, 2) SR Model, and 3) the SIMPLE Model. As mentioned, in Section 2.5.1 and 8.2.4 the FIB-SEM FEM and SIMPLE model calculations take into account the scaled R_s values, scaffold bulk IC and ohmic scaffold effects. The SR model only takes into account the scaled R_s values. The FIB-SEM FEM calculations also are different

from the SIMPLE model in that they use a real scaffold microstructure, while the SIMPLE model uses an idealized scaffold microstructure. These differences between the three models could lead to vastly different R_P values depending on the ratio of the Equation 1 surface scaled R_s value (R_{ct}) to the low scaffold IC (σ) since a low R_{ct}/σ value would produce a high electrochemical potential gradient in the IC scaffold that would raise the impact of the IC scaffold geometry. Therefore, the objective of this section was to determine the full range of the R_{ct}/σ values that could accurately be modeled by the SR model and the SIMPLE model.

Figure 8.3 shows comparisons between the three models, where the calculated R_P value is plotted against the scaled R_s to scaffold IC ratio. The first thing to note is that at high ratio values (where the scaled R_s dominates over the scaffold IC) the three models have very similar R_P values.

In contrast, large differences between the three models start to occur when the scaled oxygen surface exchange resistance is only 100 times larger than the scaffold IC. At this point the scaffold IC and microstructure both start to become a significant component in the R_P calculations. Since the SR model does not account for performance losses in the IC scaffold it continues to predict R_P values using the same activation energy at low and high ratio values. This results in the SR model predicting R_P values that are completely incorrect (i.e. significantly from the FIB-SEM FEM values) at low R_{ct}/σ values. In contrast to the SR model, the SIMPLE model increases its activation energy at ratio values lower than 100 because it does account for IC scaffold contributions. Unfortunately, the SIMPLE model R_P calculations are still significantly different than the actual (i.e. FIB-SEM FEM values) at these low R_{ct}/σ values. In this regime, the FIB-

SEM FEM calculated R_P values are higher than the SIMPLE model R_P values possibly due to increased tortuosity in the real cathode microstructure (something the SIMPLE model assumes is minimal).

For comparison experimentally measured LSCF-GDC R_P and R_{ct}/σ values from 600-700°C and are also shown on Figure 8.3. It is important to note that these experimental values are at or slightly above the 100 ratio mark, and this explains why all 3 models do a reasonably good job describing their performance (SIMPLE model studies in the literature [5, 7, 61] have been able to accurately predict LSCF-GDC NMCC performance to within 33%). However, if improvements are made in lowering the R_s value of future MIEC materials, then R_P values should be predicted using FIB-SEM FEM 3D reconstructions instead of the SR and SIMPLE models.

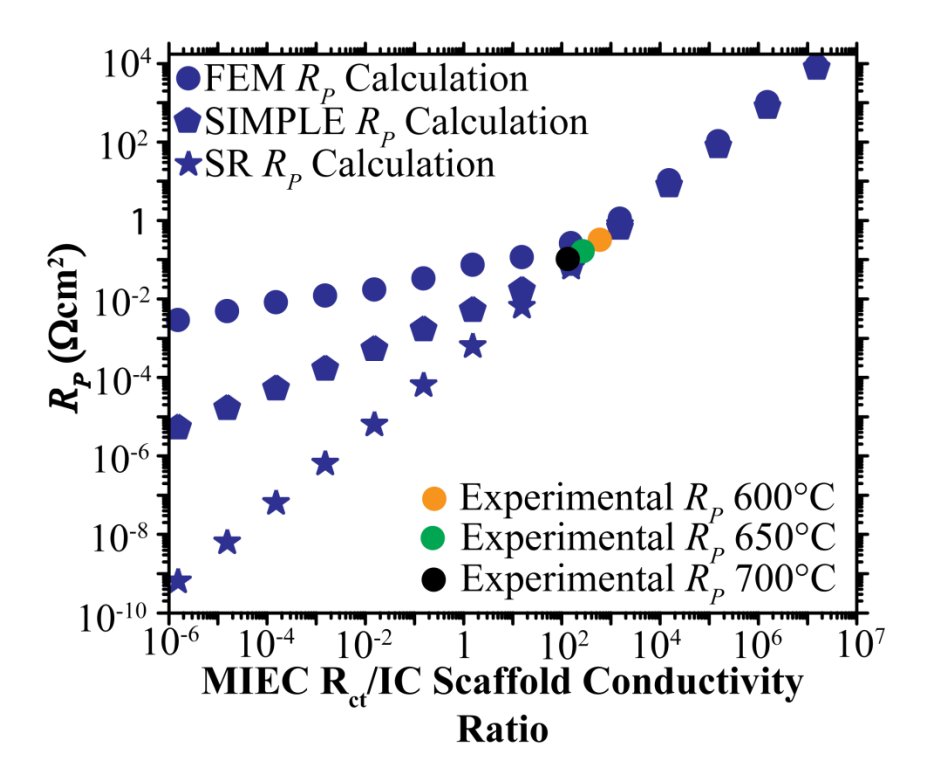


Figure 8.3: Calculated R_P Values from the FIB-SEM FEM 3D Microstructure, SIMPLE Model and Surface Resistance Model Determined for Different R_{ct} / Scaffold GDC Conductivity Ratio Values. $\bullet = FIB$ -SEM FEM R_P values, $\bullet = SIMPLE$ model R_P values, $\star = SR$ R_P values, $\bullet = FIB$ -SEM FEM determined R_P value at 600°C, $\bullet = FIB$ -SEM FEM determined R_P value at 650°C and $\bullet = FIB$ -SEM FEM determined R_P value at 700°C.

8.4 Summary

For the first time NMCC R_s values were determined for various MIEC infiltrate compositions using FIB-SEM FEM 3D reconstructions. The calculated 600-700°C R_s magnitudes were consistent with past literature studies, but had lower or identical activation energies, suggesting that R_s value discrepancies between infiltrated R_s values and literature values may exist at lower temperatures. SIMPLE model and SR limit calculations were compared to the 3D reconstruction values to show the MIEC/IC scaffold ratios required for these models to accurately measure R_P . Knowing accurate R_s values for NMCCs will be useful for future NMCC microstructure optimization studies [31] aimed at improving SOFC performance.

CHAPTER 9: Dissertation Conclusions

In summary, two new methods to systematically control infiltrate MIEC nanoparticle size, and one new method to accurately determine infiltrated MIEC R_s values were developed in this thesis, and the following are conclusions that from this thesis were demonstrated. As shown in Chapters 4-7, precursor solution desiccation and ceria preinfiltration were shown to reduced infiltrated La_{0.6}Sr_{0.4}Fe_xCo_{1-x}O_{3-δ} MIEC nano-particle size when precursor solution additives such as Triton X-100 and Citric Acid were present (these methods were not effective in reducing the size of La_{0.6}Sr_{0.4}Fe_xCo_{1-x}O_{3-δ} MIEC when solution additives were not present). Both desiccation and ceria pre-infiltration lowered the TXD LSCF average nano-particle sizes from 48 to 22 nm. In contrast, desiccation lowered the CAD LSCF average nano-particle size from 50 to 41 nm, while ceria pre-infiltration lowered the CAD LSCF average nano-particle size from 50 to 25 nm. Across the entire LSF-LSC solid solution, pre-infiltration was shown to be more effective than desiccation at reducing the initial cathode polarization resistance. These nano-particle size reductions allowed the cathode operating temperature (the temperature at which the cathode reached a target R_P value of 0.1 Ω cm²) to be reduced, with the largest operating temperature reduction of ~650°C to ~545°C occurring with preinfiltrated TXD LSCF. Figure 9.1 shows that the infiltrated cathodes produced in this thesis were some of the best ever produced [1, 3-5, 27, 28, 71, 76, 77, 157-160].

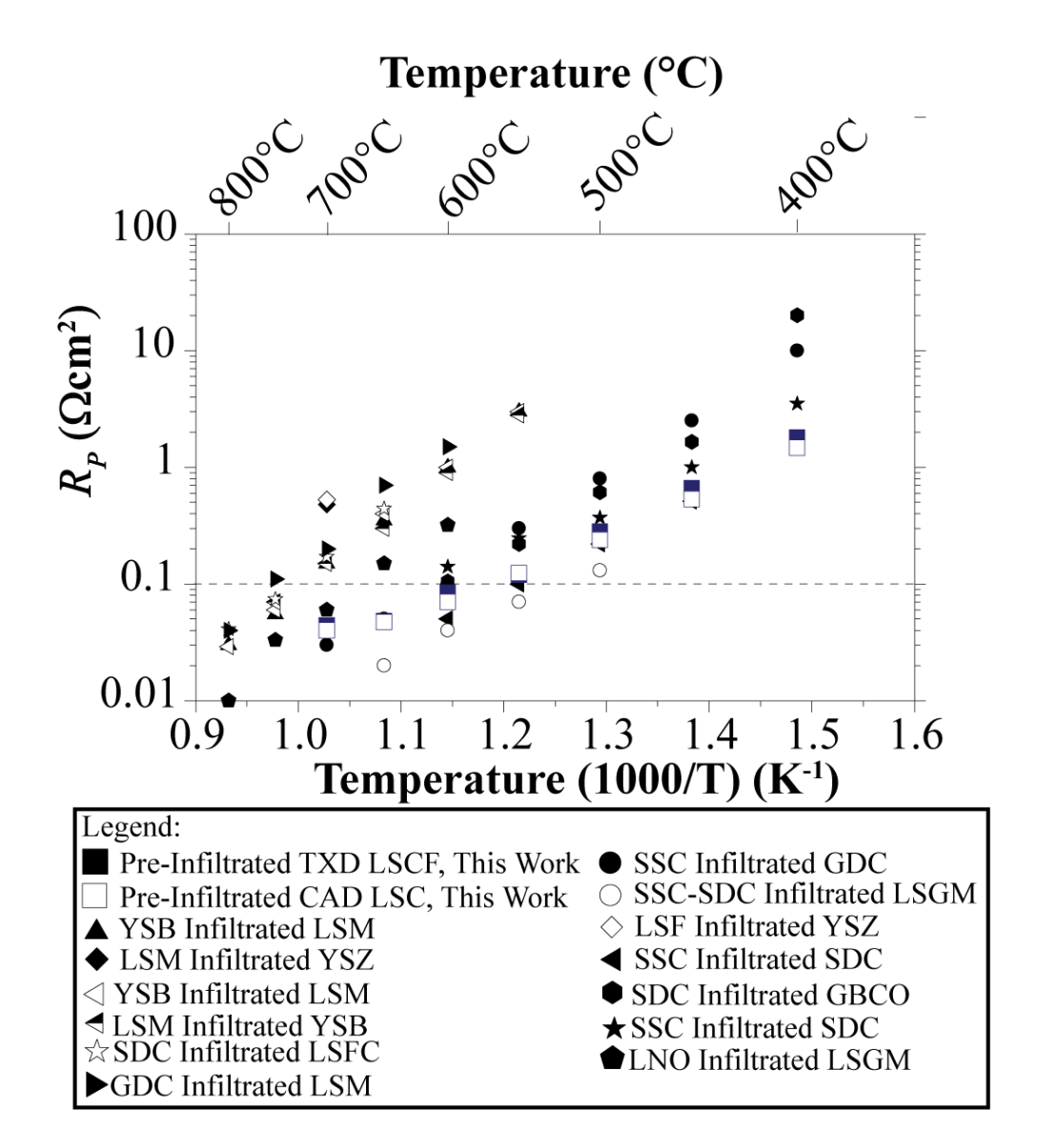


Figure 9.1: Infiltrated Cell Comparison from Different Infiltration Groups. LSCF=La_{0.6}Sr_{0.4}Co_{0.8}Fe_{0.2}O_{3.&}, LSC=La_{0.6}Sr_{0.4}Co_{0.3&}, GDC=Gd_{0.1}Ce_{0.9}O_{1.95}, SSC=Sm_{0.5}Sr_{0.5}CoO_{3.&}, SDC= Sm_{0.2}Ce_{0.8}O_{1.9}, LSGM=(La,Sr)(Ga,Mg)O₃, YSB= Y_{0.25}Bi_{0.75}O_{1.5}, LSM=La_{0.6}Sr_{0.4}MnO_{3.&}, LSF=La_{0.6}Sr_{0.4}FeO_{3.&}, YSZ=(Y₂O₃)_{0.08}(ZrO₂)_{0.92}, GBCO =GdBaCo₂O_{5+&}, LSFC=La_{0.6}Sr_{0.4}Co_{0.2}Fe_{0.8}O_{3.&}, LNO= La₂NiO₄. ■ Pre-infiltrated TXD LSCF, □=Pre-infiltrated CAD LSC, ● [5], ○ [27], ▲ [71], ◆ [76], ◇.[3], ◄ [1], △ [28], ◄ [157], Φ [158], ★ [77], [159], ▶ [4], ♠ [160].

In addition to superior initial performance, the desired TXD and CAD LSCF cathodes produced here were also to have favorable 100-500 hr 540°C degradation rates of 1.7% /khr and 3.3% /kr, respectively, in comparison to the 9.8% /khr 100-500 hr 540°C degradation rates observed for PND LSCF-GDC cells. (Pre-infiltrated TXD and CAD

cells were found to have 100-500 hr 540°C degradation rates of 6.3% /khr and 12.0 % /khr, respectively). In addition, nano-particle size was found to remain constant over 500 hrs at 540°C for all tested cathodes, indicating that nano-structured electrodes can survive intermediate SOFC operating temperatures. Even though pre-infiltrated cells exhibited superior initial performance and took less time to manufacture (6 hours instead of 7 days), desiccated cells are recommended for use in commercial SOFCs because of their superior long-term stability (assuming that faster-acting desiccants can be found and that additional tests performance under bias yield similar results to those open-circuit measurements performed here).

As shown in Chapter 8, infiltrated MIEC R_s measurements for phase pure (i.e. CAD) LSF, LSFC, LSCF, LSC, and SSC were also determined for the first time. These FEM determined R_s values were found to have activation energies equal to or less than reported bulk and thin film R_s values between 600-700°C. This suggests that the low temperature performance of MIEC nano-particles may be considerably better than the same material in bulk or thin film form. From a purely R_s perspective, SSC was shown to be the best-performing MIEC infiltrate at SOFC operating temperatures of 600-700°C while LSF was shown to be the best MIEC infiltrate choice at lower operating temperatures. However, when both R_s and an ability to control the infiltrate particle size were considered, LSC and LSCF were shown to be the best NMCC infiltrate choice.

APPENDICES

Appendix 1: Simple Infiltrated Microstructure Polarization Loss Estimation (SIMPLE) Model Derivation

The following derivation is for the SIMPLE model outlined in Section 2.5.2. This derivation was put together by Dr. Jason D. Nicholas and has been available for electronic download from https://www.egr.msu.edu/nicholasgroup/simple.php since October of 2012.

Motivation

As discussed in Nicholas, J. D., L. Wang, et al. (2012). "Use of the Simple Infiltrated Microstructure Polarization Loss Estimation (SIMPLE) Model to Describe the Performance of Nano-Composite Solid Oxide Fuel Cell Cathodes." Phys. Chem. Chem Phys., the main usefulness of the SIMPLE model is that it provides a quick means of determining the lowest possible R_P for Mixed Ionic Electronic Conductor (MIEC)-Ionic Conductor (IC) composite cathodes when: 1) bulk oxygen transport only happens through the ionic conducting scaffold, and 2) oxygen ion incorporation only occurs at the MIEC particles. These requirements are commonly met for nano-composite cathodes (NCCs) made via the infiltration of a range of MIEC materials (LSCF, SSC, other MIEC cobaltite oxygen surface exchange catalysts, etc.) into a range of ionic conducting scaffolds (ceria, zirconia, lanthanum strontium gallium manganite, etc.). The SIMPLE model can also be used as a SOFC NCC's design tool.

SIMPLE Model Derivation

The SIMPLE model describes the performance of SOFC NCC's made of MIEC nano-composite particles atop an ionic-conductor scaffold. It is based to a large degree on the Tanner Fung Virkar (TFV) model which describes the performance of SOFC cathodes made of electronic conductors atop an ionic conductor scaffold. Therefore, much of the derivation below is an expansion and extension of that found in Tanner, C. W., K.-Z. Fung, et al. (1997). "The effect of porous composite electrode structure on solid oxide fuel cell performance." J. Electrochem. Soc. **144**(1): 21-30.

Modeled Geometry

• Like the TFV model, the SIMPLE model assumes that the ionic conducting scaffold geometry can be represented as a series of columns

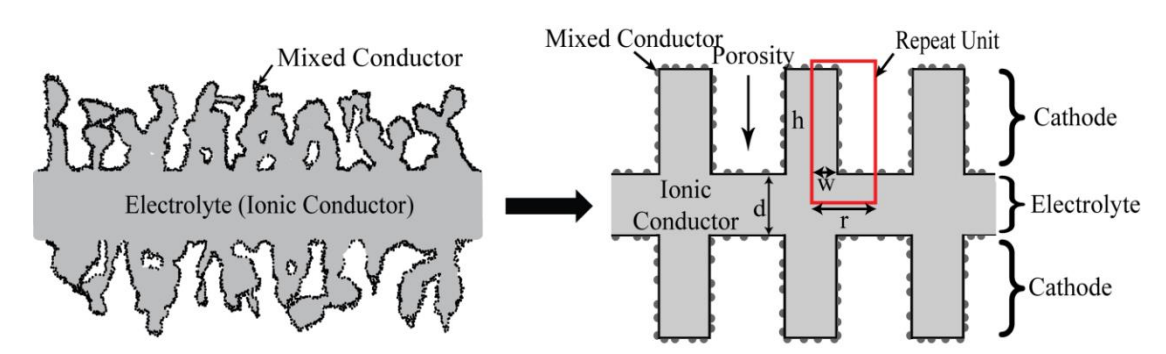


Figure A1.1: An Idealized Representation of a Symmetric SOFC Cathode Cell. (Not Drawn to Scale). Image courtesy of Lin Wang.

- Assuming a columnar cathode microstructure enables an analytical solution for NCC polarization resistance, i.e. the SIMPLE model, to be obtained
- Note that for the idealized geometry in Figure A1.1 W

$$p=1-\frac{w}{r}$$

where p is the volume fraction of pores in the cathode, w is one-half the total scaffold column thickness, and r is the repeat unit thickness

As discussed in Nicholas, J. D., L. Wang, et al. (2012). "Use of the Simple Infiltrated Microstructure Polarization Loss Estimation (SIMPLE) Model to Describe the Performance of Nano-Composite Solid Oxide Fuel Cell Cathodes." Phys. Chem. Chem Phys., the major source of NCC electrical losses is the difficulty of incorporating oxygen into the MIEC, and electrical losses associated with the difficulty of transporting oxygen through the bulk of the ionic conducting scaffold are comparatively small. (This can be observed by comparing the results of the SIMPLE model, which accounts for surface resistance and bulk transport losses, and a Surface Resistance (SR) Model, which only accounts for surface resistance). Because of this, the microstructural details of the scaffolds don't matter that much. The close agreement between the measured and SIMPLE model predicted polarization resistances also speak to this fact.

Model Assumptions: Discussed further in Nicholas, J. D., L. Wang, et al. (2012). "Use of the Simple Infiltrated Microstructure Polarization Loss Estimation (SIMPLE) Model to Describe the Performance of Nano-Composite Solid Oxide Fuel Cell Cathodes." Phys. Chem. Chem Phys.

1. The IC scaffold geometry can be idealized as a series of high aspect-ratio IC columns. Poorly-necked real-world scaffold particles will invalidate this assumption. However, the close agreement between SIMPLE model predictions and real-world measurements of NCC's made of well-necked scaffold particles, suggests this is a reasonable assumption, especially for NCC's where surface exchange resistances dominate the overall polarization resistance, and the microstructural details of the IC scaffold are relatively unimportant.

Corollaries

- a. The equipotential lines within the IC scaffold are horizontal. Finite element modeling results on IC columns in Tanner, C. W., K.-Z. Fung, et al. (1997). "The effect of porous composite electrode structure on solid oxide fuel cell performance." J. Electrochem. Soc. 144(1): 21-30 showed that for large aspect ratio columns such as those in an approximated real-world cathode structure (a 250 nm thick column, 20 microns high), the equipotential lines are horizontal through the majority of the column.
- 2. The only significant resistances are MIEC oxygen surface exchange resistance and IC scaffold bulk oxygen transport.

Corollaries

- a. Bulk oxygen transport only happens through the ionic conducting scaffold (a good assumption since the bulk oxygen conductivities of ionic conductors are many orders larger than that of MIEC materials) and oxygen ion incorporation only occurs at the MIEC particles (a good assumption since MIEC's typically have oxygen surface exchange resistances much lower than IC's).
- b. Losses associated with electron transport through the MIEC can be ignored. Another way to say this is that the electronic conductivity of the infiltrated MIEC is high enough, and the MIEC infiltrate is interconnected enough, that electronic transport losses can be ignored. Analysis on the performance of real cathodes indicated that this is the case for heavily infiltrated cathodes tested near open circuit.

- i. This causes the potential on the surface of the MIEC, ϕ^o , to be the same on all MIECs surfaces throughout the cathode.
- c. Losses associated with oxygen transport through the MIEC can be ignored. Another way to state this assumption is to say that the MIEC nanoparticles are below their characteristic thickness. This is a good assumption since the characteristic thickness values for most MIEC materials are at least several microns from 400-700C, and the infiltrate particle thickness is typically below 25 nm.
- d. Losses associated with gas-phase diffusion can be ignored. Concentration polarization resulting from poor gas-phase diffusion is not expected to contribute to the near open circuit potential R_P predicted by the SIMPLE model since under these conditions the oxygen fluxes are small and the NCC pores are large.
- e. Losses associated with the IC-MIEC interface can be ignored. In the few cases where they have been measured, MIEC-ionic conductor interfacial resistances have been anywhere from 10-100 times less than the ionic surface exchange resistance at sub-700°C temperatures.
- 3. The resistance caused by the movement of charged species is independent of driving force. Another way of saying this is that it is the electrochemical potential, η , which drives charged species, and since $\eta = \mu + zF\phi$, where μ is the chemical potential, zF is the charge on the charged species, and ϕ is the electrical potential, a polarization resistance calculated by assuming an electrical driving

force (as occurs in a symmetric cell impedance test) will be the same as that results from a concentration gradient (as occurs in a working fuel cell).

4. Oxygen transport through the IC scaffold behaves ohmically. This is another way of saying that the ionic conductor behaves as a dilute, ideal solution which has a constant composition and structure throughout.

This proof starts the relationship between the total current, i, and the current density, j.

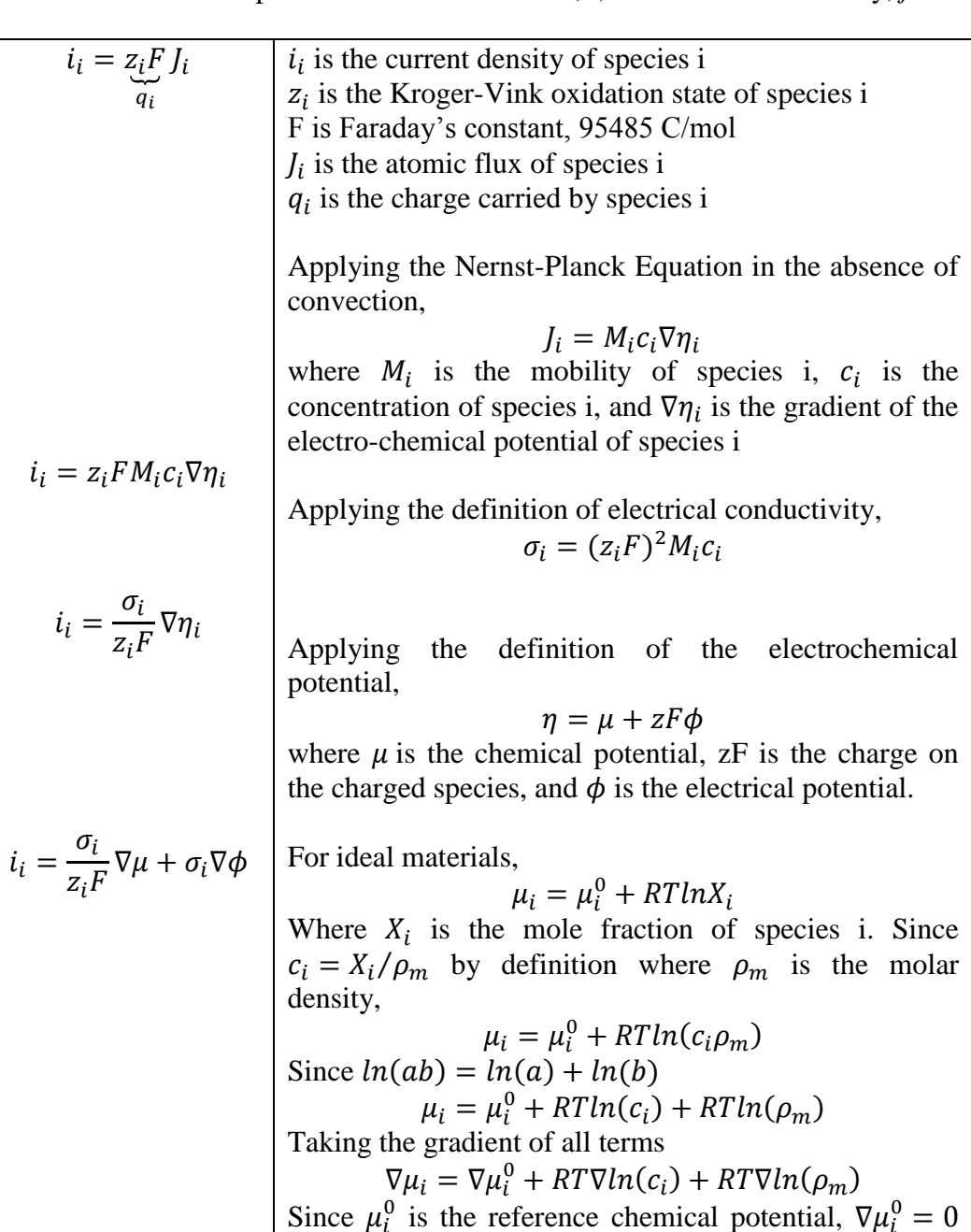


Figure A1.2: Oxygen Transport Proof. Shows IC Scaffold Behaves Ohmically.

Figure A1.2 (cont'd)

and $\nabla \mu_i = RT \nabla ln(c_i) + RT \nabla ln(\rho_m)$ Applying the rule $\frac{dlny}{dx} = \frac{1}{y} \frac{dy}{dx}$ $\nabla \mu_i = RT \frac{\nabla c_i}{c_i} + RT \frac{\nabla \rho_m}{\rho_m}$

Assuming that the composition of the IC is constant, $\nabla c_i = 0$. This is a good assumption for most IC's at intermediate temperatures because they are heavily doped materials where the oxygen vacancy concentration is extrinsically controlled.

Also assuming that the structure of the IC is constant so that the molar density is constant through the ionic conductor, $\nabla \rho_m = 0$, and

$$\nabla \mu_i = 0$$

Plugging this in,

For materials of constant composition and structure that behave ideally, the Nernst-Planck equation says that

 $\begin{bmatrix} i_i = \sigma_i \nabla \phi \end{bmatrix}$ This is a form of Ohm's law.

Proof that this is a form of Ohm's Law

1 1001 that this is a i	term of emil 5 Euv	
$i_i = \sigma_i \nabla \phi$	If angains i is the dominant shares	
	If species i is the dominant charge	
	carrying species we can drop the	
	subscripts	
	subscripts	
$i = \sigma \nabla \phi$		
	Multiplying both sides by the	
	cross-sectional area, A	
	cross-sectional area, A	
$Ai = A\sigma \nabla \phi$		
	The current, <i>I</i> , is related to the	
	current density via	
	-	
	$I = Ai_i$	
$I = A\sigma \nabla \phi$		
, , , , , , , , , , , , , , , , , , ,	The conductivity is defined as	
	The conductivity is defined as	
	$\sigma = \frac{1}{2}$	
	$o = \frac{1}{o}$	
	y hara a is the resistivity	
4	where ρ is the resistivity	
$I = \frac{A}{\rho} \nabla \phi$		
$I = \frac{1}{\rho} \nabla \varphi$		
	The 1D andient is	
	The 1D gradient is	
	$\nabla \phi = \frac{\phi_1 - \phi_2}{I}$	
	$V \varphi = \frac{1}{I}$	
	where lie the noth length	
	where l is the path length	

Figure A1.2 (cont'd)

Figure A1.2 (cont a)		
	$I = \frac{A}{l\rho}\phi_1 - \phi_2$	The voltage is defined as
	$I = \frac{A}{l\rho}V$	$V = \phi_1 - \phi_2$ The resistance of a dense block of material is defined as $R = \frac{\rho * l}{4}$
	$I = \frac{1}{R}V$	where R is the resistance Rearranging
	V = IR This is the forms of Ohm's Law we know and	Rearranging
	love.	

5. Oxygen transport across the MIEC surface behaves ohmically. This is a good assumption because the more-complicated Butler-Volmer Equation predicts ohmic behavior at low overpotentials. Because of this assumption, the SIMPLE model can only be used to predict open-circuit NCC polarization resistances.

Figure A1.1 shows the modeled repeat unit. The resistance across the repeat unit, R_{RU} , is given as:

$$R_{RU} = R_{CA} + \frac{1}{2}R_{EL}$$

where R_{CA} is the resistance of the cathode and R_{EL} is the resistance of the electrolyte

$$AR_{RU} = AR_{CA} + \frac{1}{2}AR_{EL}$$

$$AR_{RU} = R_P + \frac{1}{2}AR_{EL}$$

$$R_P = AR_{RU} - \frac{1}{2}AR_{EL}$$

$$R_P = r\delta R_{RU} - \frac{1}{2}rtR_{EL}$$

$$R_P = r\delta R_{RU} - \frac{d}{2\sigma}$$

Multiplying everything by the geometric cathode area, A, to turn these resistances into Area Specific Resistances

Defining the cathode polarization resistance, R_P , as the area specific resistance of the cathode

Rearranging the expression

Assuming a rectangular geometric cathode area such that $A = r\delta$ and the columns shown in Figure 1 extend into and out of the page by a distance δ , so that Figure 1 shows a portion of the cathode in the r direction.

Since the electrolyte is dense block of material, the definition of resistance can be applied

$$R_{EL} = \frac{\rho_{EL} * l}{A}$$

where ρ_{EL} is the electrolyte resistivity, 1 is the path length, and A is the cross-sectional area.

Since, $\rho = 1/\sigma$, and as shown in Figure 1, for the electrolyte, l = d and $A = r\delta$, this equation becomes:

$$R_{EL} = \frac{d}{\sigma r \delta}$$

where σ is the oxygen ion conductivity of the electrolyte Plugging this in,

Solving for R_{RU}

As stated in in assumptions 3 and 4, the SIMPLE model assumes that current flow across Applying the definition

Figure A1.3: Electrode Polarization Resistance Proof. Depicts the General Equation.

Figure A1.3 (cont'd)

behaves ohmically so $R_{RU} = \frac{V_{RU}}{I_{RU}}$ $R_{RU} = \frac{V_{RU}}{r\delta i_{RU}}$ $R_{RU} = \frac{\phi^0 - \phi _{y=0}}{r\delta i_{RU}}$ If we have a cathode set that depicted and we applicathode and other, be symmetry, ϕ $R_{RU} = \frac{\phi^0}{r\delta i_{RU}}$ The voltage repeat unit g $V_{RU} = \phi$ If we have a cathode and other, be symmetry, ϕ $Symmetry, \phi$ The local cut at one spon bottom of the in Figure 1 origin is in the corner of the and they did the page), of Law accommodation in the page, of Law accommodation in the page of the page of the corner of the symmetry. Since, the density continuity, which				Figure A1.3 (cont a)
$R_{RU} = \frac{V_{RU}}{r\delta i_{RU}}$ $R_{RU} = \frac{\phi^0 - \phi _{y=0}}{r\delta i_{RU}}$ If we have a cathode set that depicted and we apply cathode and other, be symmetry, ϕ $R_{RU} = \frac{\phi^0}{r\delta i_{RU}}$ The local cut at one spond bottom of the in Figure 1 origin is in the corner of the and the y did the page), of Law acce assumption in the corner of the symmetry of the bottom that $i = \sigma^0$. Since, the density control the bottom unit, which	•	*	1 10	
$R_{RU} = \frac{V_{RU}}{r\delta i_{RU}}$ repeat unit g $V_{RU} = \phi^{i}$ $If we have a cathode set that depicted and we apply cathode and other, be symmetry, \phi R_{RU} = \frac{\phi^{0}}{r\delta i_{RU}} The local cut at one spot bottom of the in Figure 1 origin is in corner of the and the y ditter page), or Law acce assumption: i = Since there gradient in direction thin i = \sigma^{-1} Since, the density conthe bottom unit, which$	$=rac{I_{RU}}{r\delta}$	$i_{RU} = rac{I_{RU}}{r\delta}$	$R_{RU} = \frac{V_{RU}}{I_{RU}}$	
$R_{RU} = \frac{\phi^0 - \phi _{y=0}}{r\delta i_{RU}}$ cathode set that depicted and we applicated and other, be symmetry, ϕ . $R_{RU} = \frac{\phi^0}{r\delta i_{RU}}$ The local cut at one spot bottom of the in Figure 1 origin is in tocorner of the and the y did the page), of Law according assumption $i = 0$. Since there gradient in direction thin $i = \sigma^2$. Since, the density conthe bottom unit, which	given as	The voltage across t repeat unit given as $V_{RU} = \phi^0 - \phi _{y=0}$	$R_{RU} = rac{V_{RU}}{r\delta i_{RU}}$	
$R_{RU} = \frac{\varphi}{r\delta i_{RU}}$ at one spond bottom of the in Figure 1 origin is in the corner of the and they did the page), of Law access assumption if $i = 1$. Since there gradient in direction this $i = 1$. Since, the density contained the bottom and the spond bottom of the in Figure 1 origin is in the corner of the and they did the page), of Law access assumption if $i = 1$.	etup, such as ed in Figure 1, ply ϕ^o to one d $-\phi^o$ to the because of	If we have a symmetric cathode setup, such that depicted in Figure and we apply ϕ^o to o cathode and $-\phi^o$ to to other, because symmetry, $\phi _{y=0}=0$	$R_{RU} = \frac{\phi^0 - \phi _{y=0}}{r\delta i_{RU}}$	
$ \dot{i}_{RII} $	the repeat unit 1 (where the the lower left the lower left the repeat unit direction is up obey's Ohm's ecording to a 3 $= \sigma \nabla \phi$ re is only a in the y has reduces to: $\frac{d\phi(x,y)}{dy}$ total current oming out of of the repeat the is equal to a second contact the sequence of the sequen	assumption 3 $i = \sigma \nabla \phi$ Since there is only gradient in the direction this reduces to $i = \sigma \frac{d\phi(x,y)}{dy}$ Since, the total curredensity coming out the bottom of the repounit, which is equal i_{RU} , is given as	$R_{RU} = \frac{\phi^0}{r\delta i_{RU}}$	

Figure A1.3 (cont'd)

$$R_P = \frac{r\phi^0}{\int_0^r \sigma \frac{d\phi(x,y)}{dy} \Big|_{y=0}} dx - \frac{d}{2\sigma}$$

Equation A1.1:

$$R_{P} = \frac{\phi^{0}}{\frac{\sigma}{r} \int_{0}^{r} \frac{d\phi(x, y)}{dy} \Big|_{y=0} dx} - \frac{d}{2\sigma}$$

$$i = \sigma \frac{d\phi(x,y)}{dy}$$
Turns this into
$$i_{RU} = \frac{1}{r} \int_0^r \sigma \frac{d\phi(x,y)}{dy} \Big|_{y=0} dx$$
Plugging in this expression for R_{RU}

Rearranging

This expression shows that the polarization resistance can be determined as long as the potential distribution at the center of the electrolyte is known.

The equation is independent of geometry of the cathode.

- Because of that, it can be used as the basis for Finite Element Modeling studies on crazily complicated cathode geometries aimed at calculating the polarization resistance of those cathodes.
- It can also be solved analytically for idealized geometries.

Regardless of the cathode geometry, the potential distribution within the cathode is solved at steady state by finding solutions to Laplace's Equation.

of many solutions to Eup	THE S E QUINTOIN
Within any material, $\nabla i = -\frac{\partial \rho}{\partial t}$ Where <i>i</i> is the current density, ρ is the charge density, and t is time	This is a form of the charge conservation equation
$\nabla i = 0$	At steady state, $\frac{\partial \rho}{\partial t} = 0$
	Since the electrolyte is assumed to be ohmic,

Figure A1.3 (cont'd)

	$i = \sigma \nabla \phi$
$\nabla(\sigma\nabla\phi)=0$	
	Since the structure and
	composition of the
	electrolyte are assumed
	to be constant as per
	assumption 3, from the
	definition of
	conductivity,
	$\sigma_i = (z_i F)^2 M_i c_i$
$\sigma \nabla (\nabla \phi) = 0$	σ is position independent
Equation A1.2:	
$\nabla^2 \phi = 0$	
This is Laplace's	
Equation.	

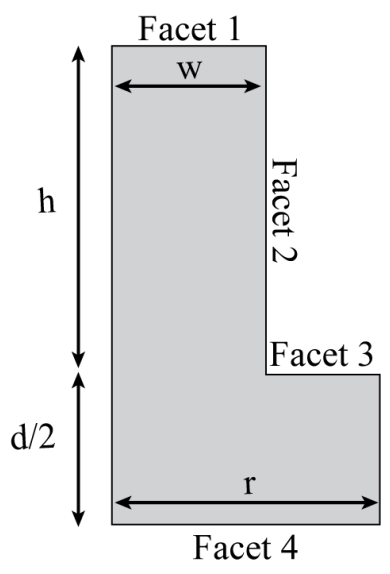


Figure A1.4: Repeat Unit with Numbered Interfaces Across with Current Flows. Due to symmetry, no current flows across the unlabeled leftmost and rightmost interfaces.

By assuming the columnar geometry to the right we can use the boundary conditions below to solve for, first, the potential distribution within the scaffold, and second, for the polarization resistance, Rp.

1st Boundary Condition: At steady state, the current within a volume element of scaffold must sum to zero. (this is the same condition which gave rise to Laplace's Equation)

- 1. This can be applied locally to any volume of material within the scaffold, or
- 2. This can be applied across the entire repeat unit scaffold so that the current across the top 3 facets must equal that across the bottom (i.e 4th) facet

$$I_1 + I_2 + I_3 = I_4$$

2nd Boundary Condition: The current across the surface of Facet 1 is equal to that immediately inside the scaffold

$$I_1 = I|_{y = (h + \frac{d}{2})}$$

Figure A1.5: Solving for Laplace's Equation. Idealized Geometry Boundary Conditions are used.

From assumption 4, we assume ohmic surface reactions so,

$$I_1 = \frac{V_1}{R_1}$$

$$I_1 = \frac{-\left(\phi\left(h + \frac{d}{2}\right) - \phi^o\right)}{R_1}$$

The voltage across the surface is the potential difference on the surface, ϕ^o , minus that on the other side of the surface, i.e. just inside the scaffold. Put mathematically,

$$V_1 = \phi^o - \phi(h + d/2)$$

What is R_1 , the resistance across the surface Facet 1? Well if we were talking about the resistance of a bulk material we would turn to the definition of resistance,

$$R = \frac{\rho l}{A}$$

But what would the path length, l, be across a surface? What would be the resistivity across a surface? Since we don't know either of these terms we multiply both sides by A, and refer the grouped terms as the area specific resistance (ASR), denoted R_s

$$R_S = AR = \rho l$$

Because we can't separate out ρ and l for a surface, we measure area specific resistances of surfaces.

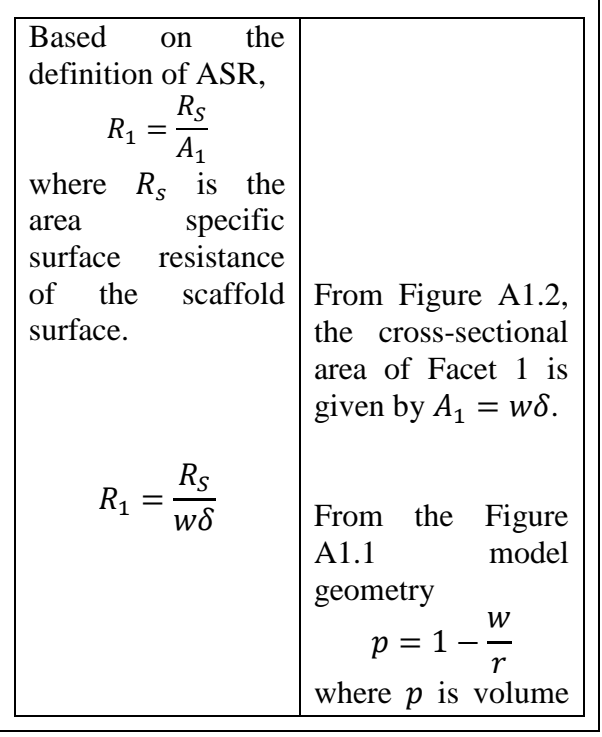


Figure A1.6: **Determining I**₁. Determined for Figure A1.4.

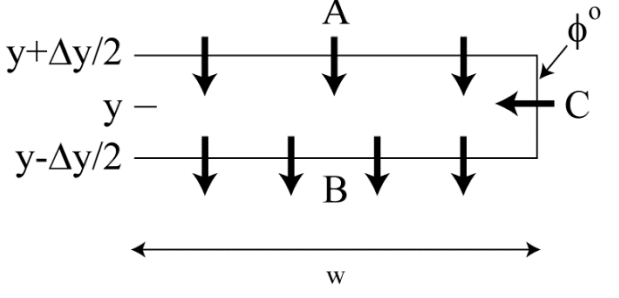
Figure A1.6 (cont'd)

$I_{1} = \frac{-r(1-p)\delta}{R_{c}} \left(\phi \left(h + \frac{d}{2} \right) - \phi^{o} \right)$	$R_1 = \frac{R_S}{r(1-p)\delta}$ Plugging in this expression for R_1 ,	fraction of pores in the cathode, w is one-half the total scaffold column thickness, and r is the repeat unit thickness. Rearranging this, $w = r(1 - p)$
---	--	--

Unlike the case for I_1 and I_3 , the potential along the left side of Facet 2 (i.e. inside the scaffold) changes along the facet. Therefore we must divide the cathode up into infinitesimally small pieces Δy thick, analyze the currents in each of those pieces, and sum the effects together to get the entire current across Facet 2.

$$I_2 = \int_{d/2}^{h+d/2} I_c$$

A small section of the scaffold column:



Since we are assume ohmic surface reactions, $I_C = \frac{V_C}{R_C}$ Assuming horizontal potential lines, $V_c = \phi^0 - \phi(y)$ From the definition of ASR, $R_C = \frac{R_S}{A_C}$ where R_s is the area specific surface resistance of the scaffold surface. $A_C = \delta dy$ $R_C = \frac{R_s}{\delta dy}$ $I_C = \frac{\phi^0 - \phi(y)}{R_S} \delta dy$

$$I_2 = \delta \int_{d/2}^{h+d/2} \frac{\phi^0 - \phi(y)}{R_S} dy$$

 I_2 cannot be evaluated until the potential distribution within the scaffold, $\phi(y)$ is determined. We will have to come back to I_2 later.

Figure A1.7: Determining I₂. Determined for Figure A1.4.

Just as with Facet 1, from assumption 4, we assume ohmic surface reactions so,

$$I_3 = \frac{V_3}{R_3}$$

$$I_3 = \frac{-\left(\phi\left(\frac{d}{2}\right) - \phi^o\right)}{R_3}$$

The voltage across the surface is the potential difference on the surface, ϕ^o , minus that on the other side of the surface, i.e. just inside the scaffold. Put mathematically,

$$V_3 = \phi^o - \phi(d/2)$$

Based on the definition of ASR,
$$R_3 = \frac{R_S}{A_3}$$
 From Figure A1.2, the cross-sectional area of Facet 1 is given by $A_3 = (r - w)\delta$ From the Figure A1.1 model geometry
$$p = 1 - \frac{w}{r}$$
 Multiplying both sides by r.
$$rp = r - w$$
 Plugging in this expression for R_3 ,

 $I_3 = \frac{-rp\delta}{R_S} \left(\phi \left(\frac{d}{2} \right) - \phi^o \right)$

Figure A1.8: **Determining I₃**. Determined for Figure A1.4.

Note that this is not a surface. This facet is located in the middle of the electrolyte. From the definition of current density,

$$I_4 = Ai_4$$

$$I_4 = r\delta i_4$$

$$I_4 = r\delta\sigma\nabla\phi_4$$

$$I_4 = r\delta\sigma \frac{\phi\left(\frac{d}{2}\right) - \phi(0)}{d/2}$$

$$I_4 = \frac{2r\delta\sigma}{d}\phi\left(\frac{d}{2}\right)$$

From Figure A1.2, the cross-sectional area of Facet 4 is given by $A_3 = r\delta$.

Since the scaffold behaves ohmically,

$$i = \sigma \nabla \phi$$

Because of the assumption of horizontal potential lines, from $y=-\frac{d}{2}to\frac{d}{2}$ the electrolyte looks like a dense block of material with a constant gradient in potential across it. Therefore $\nabla \phi$ evaluated at facet 4 is the same as $\nabla \phi$ evaluated between y=0 and $y=\frac{d}{2}$

$$\nabla \phi_4 = \frac{\phi\left(\frac{d}{2}\right) - \phi(0)}{d/2}$$

Tanner, C. W., K.-Z. Fung, et al. (1997). "The effect of porous composite electrode structure on solid oxide fuel cell performance." J. Electrochem. Soc. 144(1): 21-30 do finite difference modeling to show that the assumption of constant potential gradient in the electrolyte is a good one when h<<d, as is the case for the symmetic, electrolyte-supported used to validate the SIMPLE model.

Because of the symmetry in a symmetric cell,

$$\phi(0) = 0$$

Figure A1.9: Determining I₄. Determined for Figure A1.4.

Since charge we must have conservation within an infinitesimally small section of the cathode shown to the right,

$$I_A + I_B + I_C = 0$$

Before we can make use of this relation we need to solve for I_A , I_B , and I_C

Solving for I_A

Since we are in an ohmically behaving scaffold,

$$I_A = \frac{V_A}{R_A}$$

$$I_A = \frac{\phi\left(y + \frac{\Delta y}{2}\right) - \phi(y)}{R_A}$$

$$I_A = \sigma \delta r (1 - p) \frac{\phi \left(y + \frac{\Delta y}{2} \right) - \phi(y)}{\frac{\Delta y}{2}}$$

Table A1.8 (cont'd)
$$I_A = \sigma \delta r (1 - p) \frac{d\phi}{dy} \Big|_{y + \frac{\Delta y}{2}}$$

$$V_A = \phi \left(y + \frac{\Delta y}{2} \right) - \phi(y)$$

Since this is block dense of material with single charge carrier,

$$R_A = \frac{\rho l_A}{A_A}$$

$$R_A = \frac{\Delta y}{2\sigma w \delta}$$

$$R_A = \frac{\Delta y}{2\sigma\delta r(1-p)}$$
 Plugging this in

 l_A , the path length= $\frac{\Delta y}{2}$ $A_A = w\delta$ $\rho = 1/\sigma$

From the Figure A1.1 model geometry

$$w = r(1-p)$$

Applying the definition of derivative,

$$f'(x) = \underbrace{\lim_{h \to 0}}_{h \to 0} \frac{f(x+h) - f(x)}{h}$$

and noting that in the equation to the left,

$$h = \frac{\Delta y}{2}$$

 $h = \frac{\Delta y}{2}$ and noting that this is being evaluate at the position of Facet A, $y + \frac{\Delta y}{2}$

Figure A1.10: **Applying the 1st Boundary Condition Locally**. Applied to Figure A1.4.

Solving for I_B

Similar to the derivation of I_A

Since we are in an ohmically behaving scaffold,

$$I_B = \frac{V_B}{R_B}$$

$$I_B = \frac{\phi\left(y - \frac{\Delta y}{2}\right) - \phi(y)}{R_B}$$

$$I_{B} = -\sigma \delta r (1 - p) \frac{\phi \left(y - \frac{\Delta y}{2}\right) - \phi(y)}{\left(-\frac{\Delta y}{2}\right)}$$

$$I_B = -\sigma \delta r (1 - p) \frac{d\phi}{dy} \bigg|_{y = \frac{\Delta y}{2}}$$

$$V_A = \phi \left(y - \frac{\Delta y}{2} \right) - \phi(y)$$

Since this is a block of dense material with single charge carrier,

$$R_B = \frac{\rho l_B}{A_B}$$

$$R_B = \frac{\Delta y}{2\sigma wt}$$

$$R_B = \frac{\Delta y}{2\sigma t r (1 - p)}$$

$$A_B = wt$$

 $\rho = 1/\sigma$

carrier, $R_B = \frac{\rho l_B}{A_B}$ $l_B, \text{ the path length} = \frac{\Delta y}{2}$ $A_B = wt$ $\rho = 1/\sigma$ From the Figure A1.1 model geometry w = r(1-p) w = r(1-p)

$$w = r(1 - p)$$

Applying the definition of derivative,

$$f'(x) = \lim_{h \to 0} \frac{f(x+h) - f(x)}{h}$$

and noting that in the equation to the left,

$$h = -\frac{\Delta y}{2}$$

and noting that this is being evaluate at the position of Facet A, $y - \frac{\Delta y}{2}$

Solving for I_C

Since we assume ohmic surface reactions

$$I_C = \frac{V_C}{R_C}$$

$$I_C = \frac{\phi^0 - \phi(y)}{R_C}$$

$$I_C = \frac{\phi^0 - \phi(y)}{R_S} A_C$$

$$I_C = \frac{\delta \Delta y}{R_S} \left(\phi^0 - \phi(y) \right)$$

Applying the 1st Boundary Condition locally,

$$I_A + I_B + I_C = 0$$

$$\begin{split} \sigma \delta r (1-p) \left(\frac{d\phi}{dy} \bigg|_{y+\frac{\Delta y}{2}} - \frac{d\phi}{dy} \bigg|_{y-\frac{\Delta y}{2}} \right) \\ + \frac{t\Delta y}{R_s} (\phi^0 - \phi(y)) &= 0 \end{split}$$

$$\sigma r R_s (1-p) \frac{\left(\frac{d\phi}{dy}\Big|_{y+\frac{\Delta y}{2}} - \frac{d\phi}{dy}\Big|_{y-\frac{\Delta y}{2}}\right)}{\Delta y} + (\phi^0 - \phi(y)) = 0$$

Assuming horizontal potential lines,

$$V_c = \dot{\phi}^0 - \phi(y)$$

From the definition of ASR,

$$R_C = \frac{R_S}{A_C}$$

where R_s is the area specific surface resistance of the scaffold surface.

$$A_C = \delta \Delta y$$

Plugging in our expressions for I_A , I_B , and I_C

$$I_{A} = \sigma \delta r (1 - p) \frac{d\phi}{dy} \Big|_{y + \frac{\Delta y}{2}}$$

$$I_{B} = -\sigma \delta r (1 - p) \frac{d\phi}{dy} \Big|_{y - \frac{\Delta y}{2}}$$

$$I_{C} = \frac{\delta \Delta y}{R_{C}} (\phi^{0} - \phi(y))$$

Dividing all terms by $\frac{\delta \Delta y}{R_c}$,

By definition,

Figure A1.10 (cont'd)

$$\sigma r R_s (1-p) \frac{d^2 \phi}{dy^2} - \phi(y) + \phi^0 = 0$$

This is a 2nd order P.D.E which has a solution

Equation 3

$$\phi(y) = \phi^{0} + C_{1}exp\left(\frac{\frac{d}{2} - y}{\alpha}\right) + C_{2}exp\left(\frac{y - \frac{d}{2}}{\alpha}\right)$$

where $\alpha = \sqrt{\sigma r R_s (1-p)}$

All that now prevents us from knowing the potential distribution everywhere is a knowledge of the coefficients C_1 and C_2 .

$$\frac{d^2\phi}{dy^2} = \left(\frac{\frac{d\phi}{dy}\Big|_{y+\frac{\Delta y}{2}} - \frac{d\phi}{dy}\Big|_{y-\frac{\Delta y}{2}}}{\Delta y}\right)$$

The fact that this is indeed a solution can be checked by plugging it into the preceding equation

According to the 2nd Boundary Condition, the current across the surface of Facet 1 must equal that immediately inside the scaffold

$$I_1 = I_A|_{y=(h+\frac{d}{2})}$$

$$\begin{split} \frac{-r(1-p)\delta}{R_{S}} \left(\phi\left(h+\frac{d}{2}\right)-\phi^{o}\right) \\ &= \sigma \delta r (1-p) \frac{d\phi}{dy}\bigg|_{h+\frac{d}{2}} \end{split}$$

$$\frac{-1}{R_S} \left(\phi \left(h + \frac{d}{2} \right) - \phi^o \right) = \sigma \frac{d\phi}{dy} \Big|_{h + \frac{d}{2}}$$

$$\begin{split} \frac{C_1}{R_S} exp\left(\frac{-h}{\alpha}\right) + \frac{C_2}{R_S} exp\left(\frac{h}{\alpha}\right) \\ &= \frac{\sigma C_1}{\alpha} exp\left(\frac{-h}{\alpha}\right) - \frac{\sigma C_2}{\alpha} exp\left(\frac{h}{\alpha}\right) \end{split}$$

$$C_1 exp\left(\frac{-h}{\alpha}\right) \left[\frac{1}{R_S} - \frac{\sigma}{\alpha}\right] = -C_2 exp\left(\frac{h}{\alpha}\right) \left[\frac{1}{R_S} + \frac{\sigma}{\alpha}\right]$$

$$C_{2} = C_{1} exp\left(\frac{-2h}{\alpha}\right) \frac{\left[-\frac{1}{R_{S}} + \frac{\sigma}{\alpha}\right]}{\left[\frac{1}{R_{S}} + \frac{\sigma}{\alpha}\right]}$$

$$C_2 = C_1 exp\left(\frac{-2h}{\alpha}\right) \frac{\left[\frac{-\alpha + R_S \sigma}{\alpha R_S}\right]}{\left[\frac{\alpha + R_S \sigma}{\alpha R_S}\right]}$$
Table A1.9 (cont'd)

From our work above,

$$I_1 = \frac{-r(1-p)\delta}{R_S} \left(\phi \left(h + \frac{d}{2} \right) - \phi^o \right)$$

$$I_A|_{y=(h+\frac{d}{2})} = \sigma \delta r (1-p) \frac{d\phi}{dy}|_{h+\frac{d}{2}}$$

Cancelling like terms

From Equation 3,

$$\phi(y) = \phi^{0} + C_{1}exp\left(\frac{\frac{d}{2} - y}{\alpha}\right) + C_{2}exp\left(\frac{y - \frac{d}{2}}{\alpha}\right)$$

$$\frac{d\phi}{dy}\Big|_{h + \frac{d}{2}} = -\frac{C_{1}}{\alpha}exp\left(\frac{-h}{\alpha}\right) + \frac{C_{2}}{\alpha}exp\left(\frac{h}{\alpha}\right)$$

$$\phi\left(h + \frac{d}{2}\right) = \phi^{0} + C_{1}exp\left(\frac{-h}{\alpha}\right) + C_{2}exp\left(\frac{h}{\alpha}\right)$$

Grouping the $exp\left(\frac{h}{\alpha}\right)$ and $exp\left(\frac{-h}{\alpha}\right)$ terms

Rearranging and making use of the rule Exp(a)/Exp(b)=Exp(a-b)

Combing the fractions

Simplifying

Figure A1.11: Applying the 2nd Boundary Condition to Solve for C₂. Applied to Figure A1.4.

Figure A1.11 (cont'd)

$$C_2 = C_1 exp\left(\frac{-2h}{\alpha}\right) \left[\frac{R_S \sigma - \alpha}{R_S \sigma + \alpha}\right]$$

$$C_2 = C_1 \beta exp\left(\frac{-2h}{\alpha}\right)$$

Plugging this into Equation 3,

$$\phi(y) = \phi^{0} + C_{1}exp\left(\frac{\frac{d}{2} - y}{\alpha}\right) + C_{2}exp\left(\frac{y - \frac{d}{2}}{\alpha}\right)$$

We get Equation 4,

$$\phi(y) = \phi^{0} + C_{1}exp\left(\frac{\frac{d}{2} - y}{\alpha}\right) + C_{1}\beta exp\left(\frac{y - 2h - \frac{d}{2}}{\alpha}\right)$$

Defining
$$\beta = \left[\frac{R_S \sigma - \alpha}{R_S \sigma + \alpha}\right]$$

Before we can apply the steady-state charge conservation boundary condition,

$$I_1 + I_2 + I_3 = I_4$$

We need to simplify each of these terms by making use of Equation 4.

Simplifying I_1

$$I_1 = \frac{-r(1-p)\delta}{R_S} \left(\phi \left(h + \frac{d}{2} \right) - \phi^o \right)$$

$$I_{1} = \frac{-r(1-p)\delta C_{1}}{R_{S}} \left(exp\left(\frac{-h}{\alpha}\right) + \beta exp\left(\frac{-h}{\alpha}\right) \right)$$

Simplifying
$$I_2$$

$$I_2 = \delta \int_{d/2}^{h+d/2} \frac{\phi^0 - \phi(y)}{R_S} dy$$

$$\begin{split} I_2 &= -\frac{C_1 \delta}{R_S} \int_{d/2}^{h+d/2} exp \left(\frac{\frac{d}{2} - y}{\alpha} \right) \\ &+ \beta exp \left(\frac{y - 2h - \frac{d}{2}}{\alpha} \right) dy \end{split}$$

$$I_{2} = -\frac{C_{1} \exp\left(\frac{-2h}{\alpha}\right) \left(-1 + exp\left(\frac{h}{\alpha}\right)\right) \delta \alpha \left(exp\left(\frac{h}{\alpha}\right) + \beta\right)}{R_{S}}$$

Table A1.10 (cont'd)

Equation 4,

$$\phi(y) = \phi^{0} + C_{1}exp\left(\frac{\frac{d}{2} - y}{\alpha}\right) + C_{1}\beta exp\left(\frac{y - 2h - \frac{d}{2}}{\alpha}\right)$$

Equation 4,

$$\phi(y) = \phi^{0} + C_{1}exp\left(\frac{\frac{d}{2} - y}{\alpha}\right) + C_{1}\beta exp\left(\frac{y - 2h - \frac{d}{2}}{\alpha}\right)$$

Evaluating this integral in Mathematica

Distributing the – sign into the $\left(-1 + \right)$ $exp\left(\frac{h}{\alpha}\right)$, breaking the $exp\left(\frac{-2h}{\alpha}\right)$ into Figure A1.12 (cont'd)

$$I_{2} = \frac{\alpha C_{1} \delta}{R_{S}} \left(exp\left(\frac{h}{\alpha}\right) - 1 \right) \left(1 + \beta exp\left(\frac{-h}{\alpha}\right) \right)$$

Simplifying I_3

$$I_3 = \frac{-rp\delta}{R_S} \left(\phi \left(\frac{d}{2} \right) - \phi^o \right)$$

Equation

$$I_{3} = \frac{-rp\delta C_{1}}{R_{S}} \left(1 + \beta exp\left(\frac{-2h}{\alpha}\right) \right)$$

 $\phi(y) = \phi^{0} + C_{1}exp\left(\frac{\frac{d}{2} - y}{\alpha}\right) + C_{1}\beta exp\left(\frac{y - 2h - \frac{d}{2}}{\alpha}\right)$

two $exp\left(\frac{-h}{\alpha}\right)$ terms and multiplying each of these by one of the parentheses

Simplifying I_4

$$I_4 = \frac{2r\delta\sigma}{d}\phi\left(\frac{d}{2}\right)$$

$$I_{4} = \frac{2r\delta\sigma}{d} \left(\phi^{0} + C_{1} + C_{1}\beta exp\left(\frac{-2h}{\alpha}\right)\right)$$

Equation 4,

$$\phi(y) = \phi^{0} + C_{1}exp\left(\frac{\frac{d}{2} - y}{\alpha}\right) + C_{1}\beta exp\left(\frac{y - 2h - \frac{d}{2}}{\alpha}\right)$$

Substituting the terms in purple into

$$I_1 + I_2 + I_3 - I_4 = 0$$

And solving for C_1 in Mathematica,

$$C_1$$

$$= \frac{-2\frac{\sigma r}{d}\phi^{0}}{\frac{(1-p)(1+\beta)}{R_{S}}exp\left(\frac{-h}{\alpha}\right) + \frac{\alpha}{R_{S}}\left(1-exp\left(\frac{-h}{\alpha}\right)\right)\left(1+\beta exp\left(\frac{-h}{\alpha}\right)\right) + \left(\frac{pr}{R_{S}} + 2\frac{\sigma r}{d}\right)\left(1+\beta exp\left(\frac{-2h}{\alpha}\right)\right)}$$

Equation 1 says,
$$R_P = \frac{\phi^0}{\frac{\sigma}{r} \int_0^r \frac{d\phi(x, y)}{dy} \Big|_{y=0} dx}$$

$$R_P = \frac{\phi^0}{\sigma \frac{d\phi(y)}{dy}\Big|_{y=0}} - \frac{d}{2\sigma}$$

Since the potential lines are assumed to be flat,

By plugging the expression for C_1 above into Equation 4,

$$\phi(y) = \phi^{0} + C_{1}exp\left(\frac{\frac{d}{2} - y}{\alpha}\right) + C_{1}\beta exp\left(\frac{y - 2h - \frac{d}{2}}{\alpha}\right)$$

the potential throughout the entire cathode will be known. Taking the derivative of that analytical expression with respect to y and then substituting in for y=0 (in Mathematica)

$$\frac{d\phi(y)}{dy}\Big|_{y=0}$$
 can be determined.

Equation 5, the TFV Equation:

$$R_{P} = \frac{rR_{S}}{\left(\frac{1+\beta}{1+\beta exp\left(\frac{-2h}{\alpha}\right)}\right)(1-p)rexp\left(\frac{-h}{\alpha}\right) + \left(\frac{1+\beta exp\left(\frac{-h}{\alpha}\right)}{1+\beta exp\left(\frac{-2h}{\alpha}\right)}\right)\alpha\left(1-exp\left(\frac{-h}{\alpha}\right)\right) + rp}$$

where

$$\alpha = \sqrt{\sigma r R_s (1-p)}$$
 and $\beta = \left[\frac{R_s \sigma - \alpha}{R_s \sigma + \alpha}\right]$

Figure A1.13: Solving for the Cathode Polarization Resistance. This is the SIMPLE model expression shown in Chapter 2.

In this formulation R_S is the effective resistance on the cathode surface. To a first order approximation, one can think of oxygen incorporation occurring on the surface of the MIEC nano-particles as occurring in parallel with oxygen incorporation occurring on the bare, exposed surface of the IC scaffold

$$\frac{1}{\left(\frac{R_s}{A_{sc}}\right)} = \frac{1}{\left(\frac{R_{S,MIEC}}{A_{MIEC}}\right)} + \frac{1}{\left(\frac{R_{S,IC}}{A_{IC}}\right)}$$

where $R_{S,MIEC}$ is the intrinsic area specific surface resistance of the MIEC infiltrate phase, $R_{S,IC}$ is the intrinsic area specific surface resistance of the MIEC infiltrate phase, A_{SC} is the surface area of the scaffold before infiltration, A_{MIEC} is the exposed surface area of the MIEC infiltrate phase, and A_{IC} is the exposed surface area of the IC scaffold after infiltration

$$\frac{A_{sc}}{R_s} = \frac{A_{MIEC}}{R_{SMIEC}} + \frac{A_{IC}}{R_{SIC}}$$

$$\frac{A_{sc}}{R_s} = \frac{A_{MIEC}}{R_{S,MIEC}} + \frac{A_{sc} - A_{MIEC}}{R_{S,IC}}$$

$$\frac{A_{sc}}{R_s} = \frac{A_{MIEC}}{R_{s\,MIEC}}$$

$$R_{s} = \frac{A_{sc}R_{S,MIEC}}{A_{MIEC}}$$

The area specific resistances have been divided by their corresponding areas so the formula for resistors in parallel could be applied

Reducing the complex fraction

$$A_{IC} = A_{sc} - A_{MIEC}$$

In a typical MIEC infiltration, A_{MIEC} is at most 2-3 times that of A_{sc} . However, because of assumption 2, $R_{S,IC} \gg R_{S,MIEC}$. This causes the second term to drop out

Rearranging for the effective resistance on the scaffold surface

Plugging this into Equation 5

Figure A1.14 (cont'd)

Yields Equation 6, the SIMPLE Model Equation

$$R_{P} = \frac{r\left(\frac{A_{SC}R_{S,MIEC}}{A_{MIEC}}\right)}{\left(\frac{1+\beta}{1+\beta exp\left(\frac{-2h}{\alpha}\right)}\right)(1-p)rexp\left(\frac{-h}{\alpha}\right) + \left(\frac{1+\beta exp\left(\frac{-h}{\alpha}\right)}{1+\beta exp\left(\frac{-2h}{\alpha}\right)}\right)\alpha\left(1-exp\left(\frac{-h}{\alpha}\right)\right) + rp\left(\frac{-h}{\alpha}\right)}$$

where

$$\alpha = \sqrt{\sigma r R_s (1 - p)} \text{ and } \beta = \left[\frac{R_S \sigma - \alpha}{R_S \sigma + \alpha}\right]$$

Appendix 2: Focused Ion Beam – Scanning Electron Microscopy (FIB-SEM) 3D Reconstruction and Modeling Instructions

3-Matic Volume Mesh Creation

Figure A2.1 shows a group of 2D FIB-SEM serial section images used to construct a 3D microstructure. These images were taken using the SEM backscatter detector, described in Section 3.3.3, and over 200 images were collected using the FIB-SEM. These serial sections were then combined using a 3D reconstruction program named MIMICS (discussed in Section 3.3.4) to generate a 3D reconstruction of the cathode and electrolyte microstructures, shown in Figure 3.11. The 3D microstructures created in MIMICS contained only a surface mesh (a mesh is a set of triangle or tetrahedral elements), but a volume mesh was necessary to perform FEM performance calculations to simulate the cathode volume microstructure.

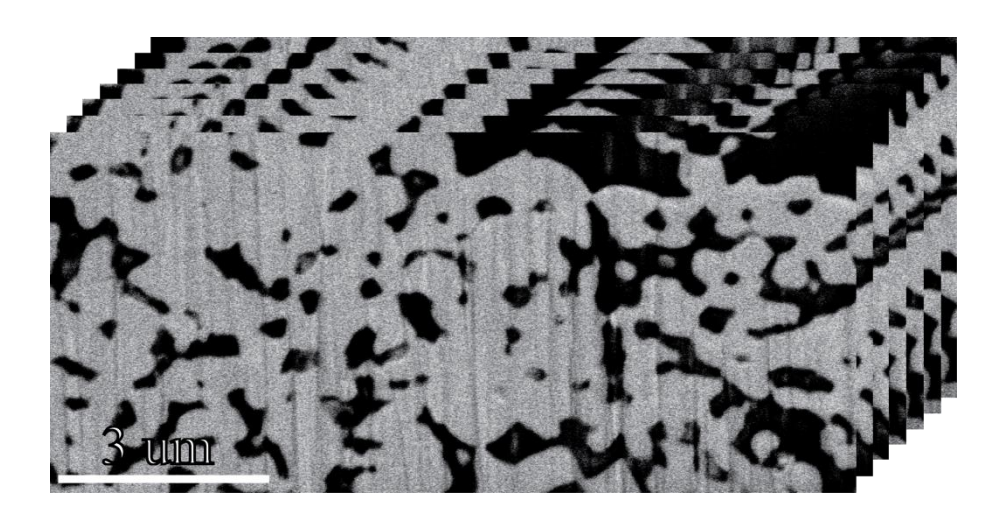


Figure A2.1: Representative 2D FIB-SEM Serial Section Stacked Images used for 3D Reconstruction. These images will be used in the MIMICS computer program to create a 3D reconstruction.

The first task before creating the volume mesh was to merge the electrolyte and cathode 3D microstructures together. This was accomplished by first importing the cathode 3D microstructure into a second 3D reconstruction program named 3-Matic.

Figure A2.2 shows the imported cathode microstructure from MIMICS imported inside 3-Matic. After the cathode microstructure had been imported, then the electrolyte microstructure was imported into the 3-Matic program while the cathode 3D microstructure was on the screen.

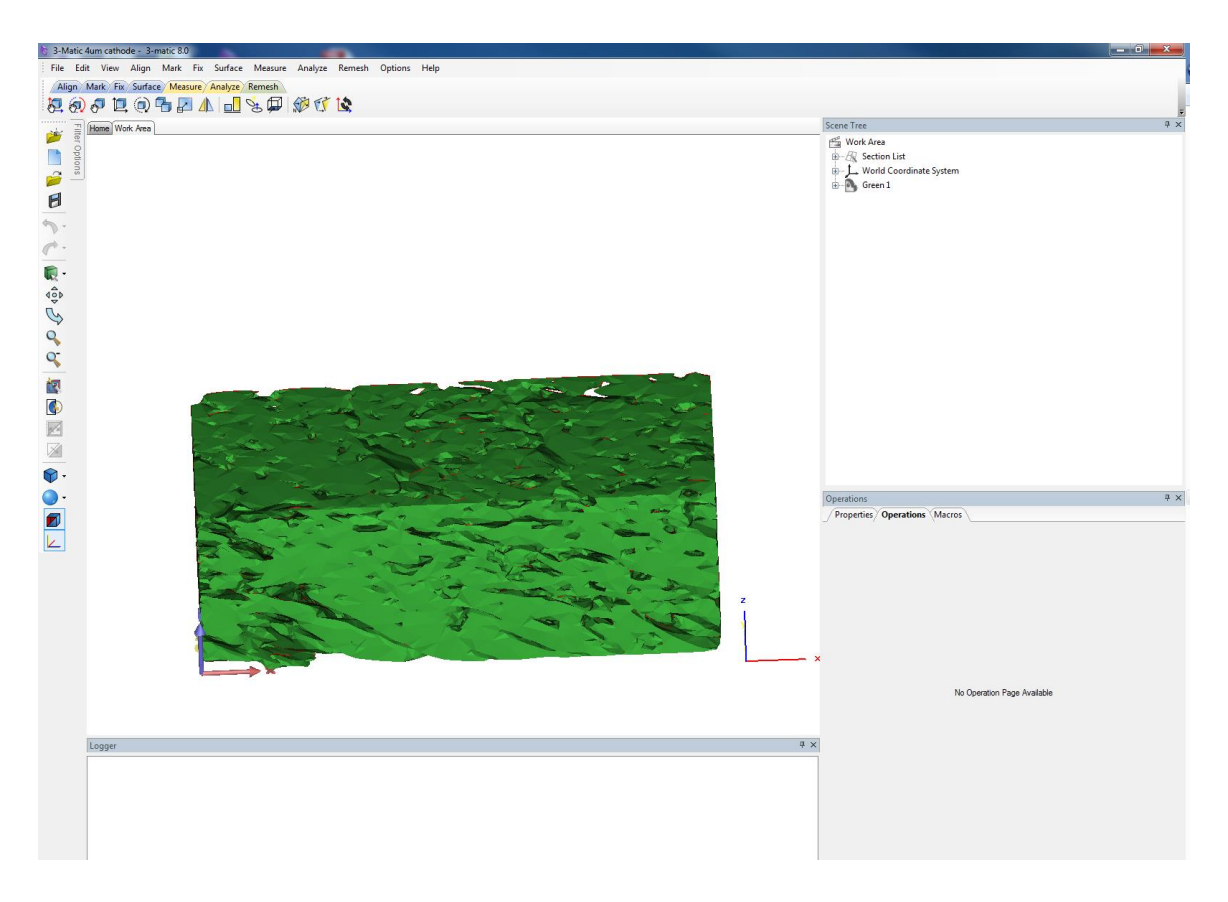


Figure A2.2: **3-Matic Imported 3D Microstructure**. This 3D microstructure was imported from the MIMICS computer program.

To import the electrolyte, while the cathode is on the screen, first left-click on "File", "Import Part", then select the electrolyte file name. Next, the two parts (cathode and electrolyte) will need to be merged together. This was done by first aligning the two parts, because initially they will be overlapped on top of each other after the electrolyte was imported. To align the parts, first left-click on the "Align" option in the top-left of the screen (shown in Figure A2.2), then select the "Interactive Translate" button right below "Align". While left-clicking on the electrolyte microstructure also hold the "Left-Control" key and drag the electrolyte so that it aligns with the bottom of the cathode microstructure.

Figure A2.3 shows the aligned cathode and electrolyte microstructures. After both parts have been aligned they need to be merged. Figure A2.3 also shows in the top-left corner there was an area named "Work Area" where the file names of both the cathode and electrolyte microstructures (both files are called "Green1" for this thesis) are listed. Hold "Control" and left-click on both file names, then right-click and select "Merge". This creates a single, merged microstructure between the cathode and electrolyte. The merged microstructure then needs to have its surface mesh turned into a volume mesh for use with the COMSOL program.

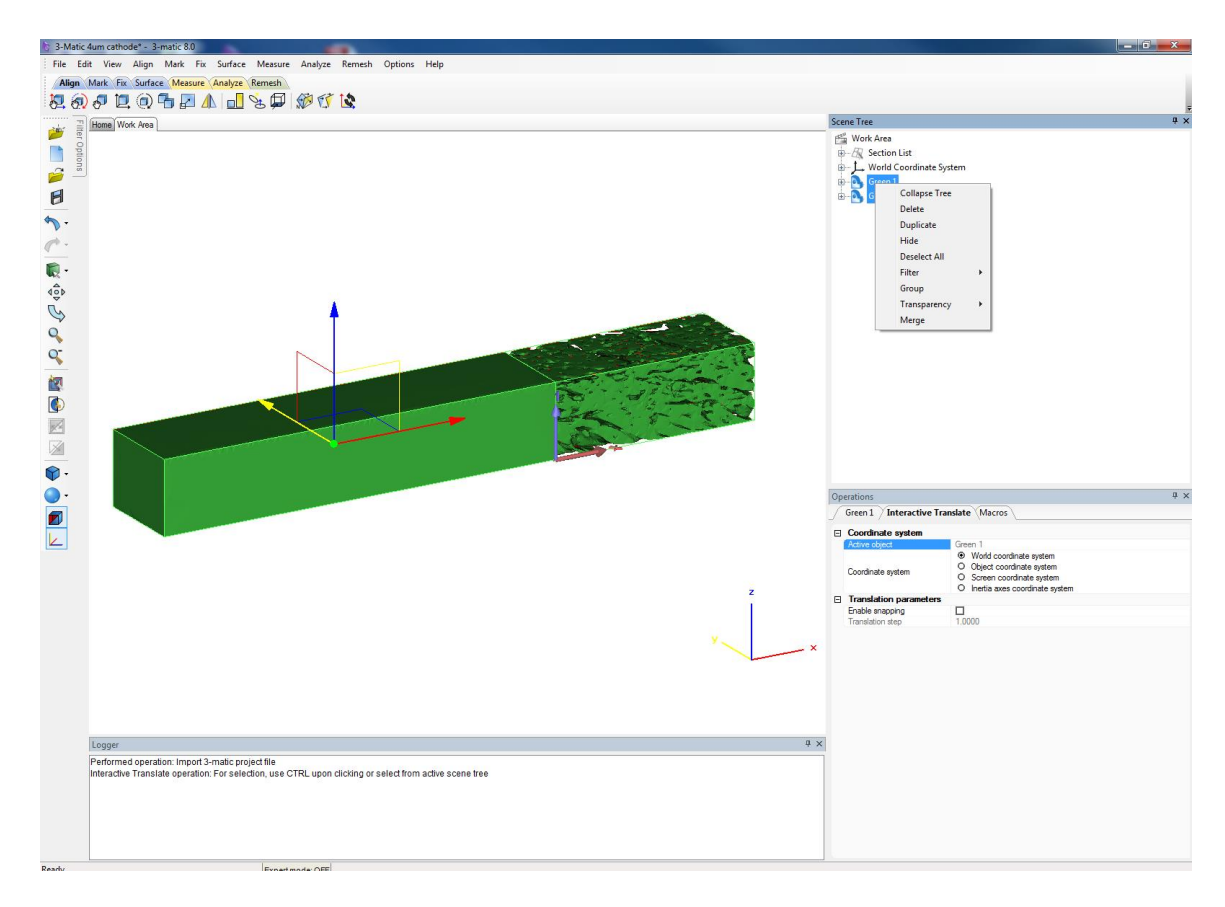


Figure A2.3: **3-Matic Cathode and Electrolyte Merged Microstructures**. The cathode and electrolyte microstructures were both created, before being merged, in the MIMICS computer program.

The process of obtaining a working volume mesh involves multiple steps. First, the 3D reconstruction from MIMICS is a surface mesh and when exported into 3-matic, needs to have the triangles on the surface "cleaned". The surface mesh will typically have meshing errors such as: 1) intersecting triangles, 2) inverted normals, 3) noisy shells, 4) planer holes, 5) overlapping triangles and 6) bad edges. The 3-Matic program allows the user to fix these errors prior to volume meshing the sample. If these errors are not resolved then 3-Matic will be unable to create a volume mesh. The volume mesh size and number of tetrahedrons that are generated can all be influenced during the volume meshing process. The same concerns apply with the tetrahedral number as with the number of triangles mentioned above, so a compromise needs to be found. Due to the

sample size, this thesis used over 1 million tetrahedrons, and was found to be acceptable as the final R_P value did not change when the same sample was analyzed using over 5 million tetrahedrons.

COMSOL 3D Volume Mesh Performance Calculations

After the volume mesh was created, it needed to be imported into an FEM program. As mentioned in Section 3.3.5 the FEM program used in this thesis was COMSOL. To import the 3D cathode microstructure volume mesh the following steps were taken. First, a new file was created with a 3D spatial dimension. Next, the "Electric Current (ec)" physics model was selected for COMSOL to use for calculations. The electric current model was used because electrochemical potential lines were calculated by COMSOL, which the electric current model is designed for. Finally, the "Stationary" study type was selected and "Finish" checked. A stationary study was used because the calculated electrochemical potential lines were assumed to be determined at steady-state, and were not changing with respect to time.

Figure A2.4 shows the standard instruction screen for COMSOL. To import the volume mesh, first right-click on the "Mesh" option on the left menu and select "Import", then load the volume mesh file exported from 3-Matic. Communicating the correct unit scale for COMSOL to use was also very important, and should be completed before any other actions are taken. To change the unit scale, first left-click on "Geometry" in the left menu and set the "Length Unit" to "um" in the drop-down box. Keep the "Angular Unit" as "Degrees" and select the "Scale values when changing units" check-box. If these options were not selected then the calculated R_P value could be larger or smaller than what it realistically should be.

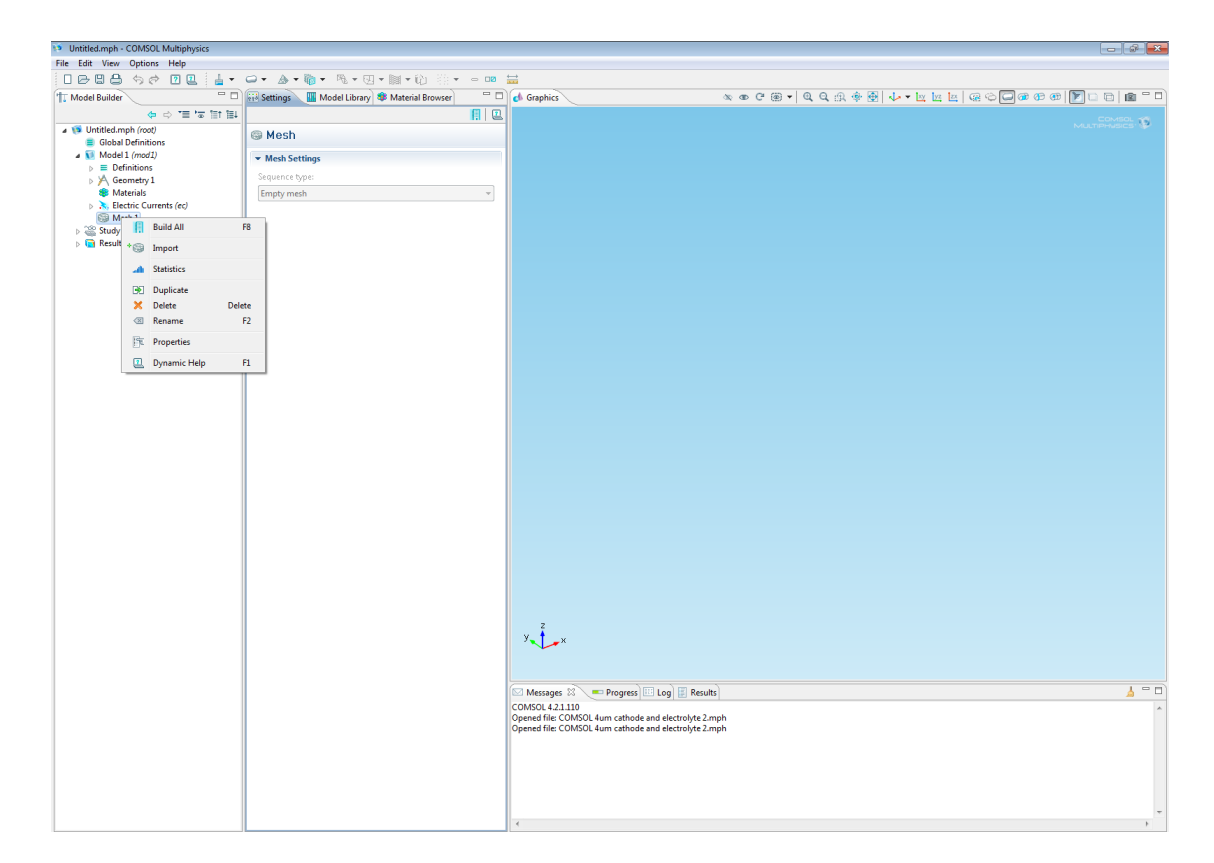


Figure A2.4: **COMSOL Volume Mesh Import Screen**. This is the primary screen used in the COMSOL computer program to perform calculations on imported microstructures.

After importing the volume mesh, the material properties of the cathode and electrolyte microstructures needed to be defined and assigned to the volume mesh. There were two material properties which were used in COMSOL for this thesis, which were:

1) the GDC IC in the electrolyte and cathode scaffold and 2) the infiltrated MIEC material R_s value for the surface layer of the cathode scaffold microstructure. The following procedure was used to assign these material properties.

Figure A2.5 shows the imported volume mesh created in 3-Matic. First, right-click on "Materials" in the left menu, and create a new material named "GDC". Select all the domains (the entire volume mesh) and assign an electrical conductivity and relative permittivity value to the entire volume mesh. Sections of the microstructure shown in

blue were selected. Next the infiltrated NMCC R_s value was assigned to the surface of the cathode microstructure.

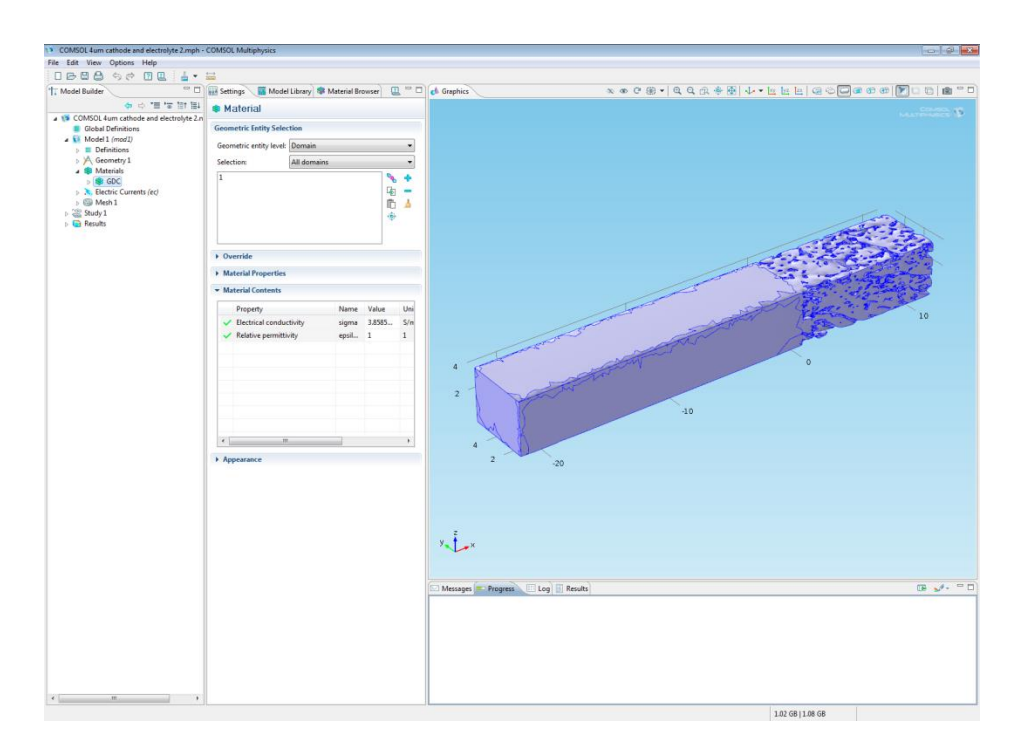


Figure A2.5: GDC Conductivity Assigned to Cathode and Electrolyte Microstructure Volume Mesh. Selected areas to be assigned GDC conductivity values are blue.

Figure A2.6 shows the volume mesh with the GDC conductivity from Figure A2.5 but with an R_s surface impedance layer applied to the entire surface of the cathode microstructure. This surface impedance layer was applied to all surfaces of the cathode microstructure (such as the viewable surface and interior pore surfaces). The surface impedance layer was applied by right-clicking on "Electric Current (ec)" on the left menu and selecting "Distributed Impedance". All domains were selected as was done in Figure A2.5, and electrolyte material domains were manually removed (volume and surface mesh) until only the cathode surface mesh remained on all five sides of the cathode. Finally, the "Surface Impedance" from the "Layer Specification" dropdown box was

selected, and surface resistance and capacitance values were inputted for the infiltrated MIEC material.

This surface impedance layer was assumed to be an interconnected layer of infiltrated MIEC nano-particles that had minimal electronic conductivity losses, and the only source of resistance was the oxygen surface exchange resistance (named surface resistance). The surface resistance value was a scaled R_s value, shown in Equation 1 that took into account the infiltrated nano-particle size. In real life applying a potential to the edges of the microstructure is unnecessary because the edges of the microstructure would be connected to other GDC in the next repeating unit and would not have infiltrate. However, if the reconstruction is large enough these incorrect edge polarizations will not affect the final result. A 3D reconstruction which was 8 um thick (instead of 4.1 um) was constructed which predicted an R_P value very close to the values reported for this microstructure, which indicates that these edge effects have minimal contribution to the final result.

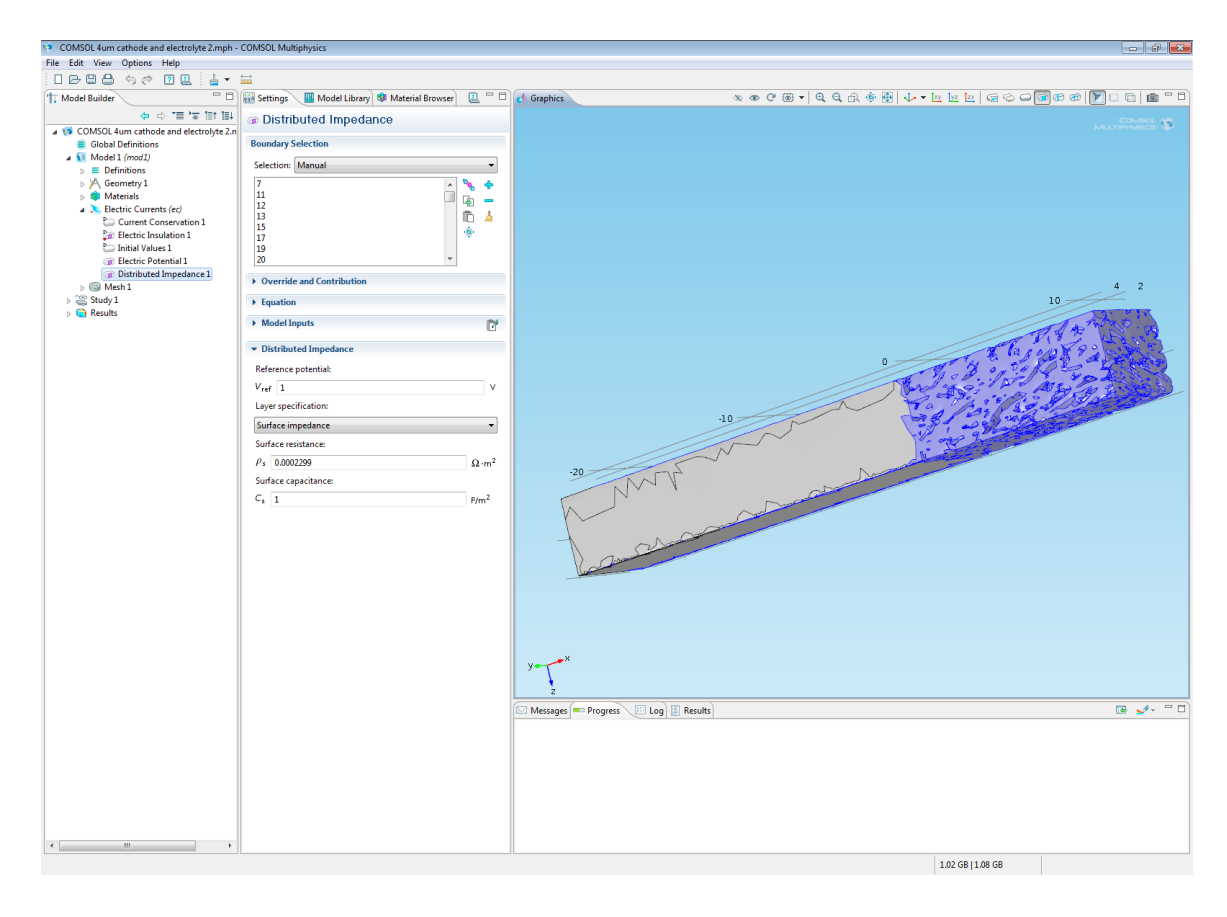


Figure A2.6: Scaled R_s Surface Impedance Assigned to the Cathode Surface Layer Mesh. Selected areas to be assigned R_s surface impedance values are blue.

Once the GDC conductivity and R_s values were assigned to the 3D microstructure, then electrochemical potential values were assigned so COMSOL was able to determine an electrochemical potential gradient through the entire electrolyte and cathode microstructure. First, a 1V potential was applied to the cathode surface mesh in exactly the same location as the surface resistance. This 1V potential was applied to the surface resistance in Figure A2.6 in the reference potential (V_{ref}) box. Next, a 0V reference potential was applied to the bottom surface of the electrolyte surface mesh. The magnitude of the 1V applied potential was shown to not influence R_P predictions in preliminary calculations.

Figure A2.7 shows the 3D microstructure with a 0V potential applied to the bottom surface of the electrolyte. The 0V electric potential is applied by right-clicking on "Electric Currents (ec)" on the left menu and selecting "Electric Potential". Manually select the bottom surface mesh of the electrolyte in the same way as mentioned previously and input a 0V reference potential, (V_o) .

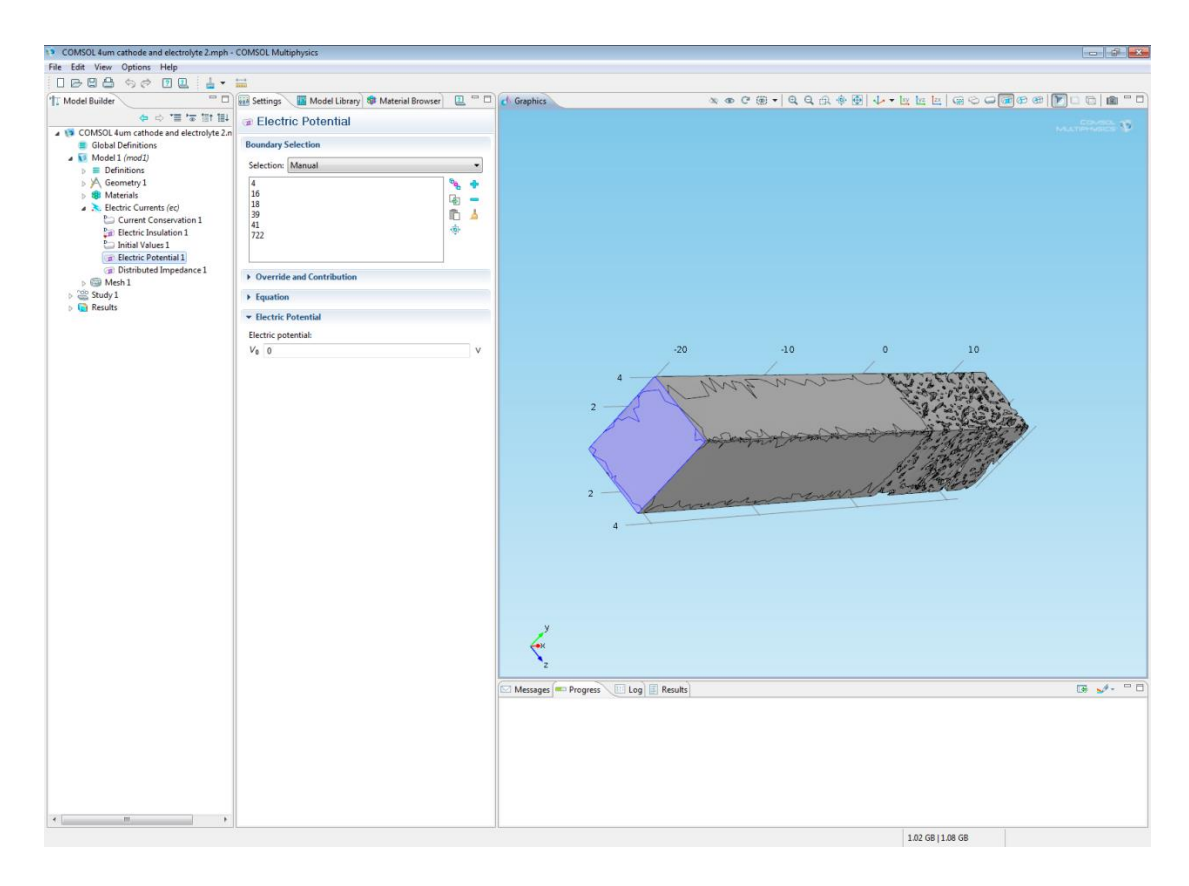


Figure A2.7: **0V Reference Potential Applied to the Electrolyte Surface Layer Mesh**. Selected area to be assigned 0V value is blue.

Applying a 1V potential difference was a mathematical approach to simulate an oxygen partial pressure gradient in the SOFC. This is commonly done in the SOFC modeling community [33] Since the COMSOL program does account for oxygen partial pressure differences (which normally would be the driving force for oxygen vacancy transport) an electrochemical difference is applied as the driving force. The

electrochemical potential gradient lines can now be calculated. Right-click on "Study" in the left menu, and select "Compute" to run the calculation.

Figure A2.8 shows the 3D reconstruction volume mesh with calculated electrochemical potential line gradients through the cathode and electrolyte material. The electrochemical potential starts at the highest value on the cathode side, and gradually becomes lower towards the electrolyte which correlates with the potential gradient specified. The electrochemical potential can be shown for the surface mesh, but also

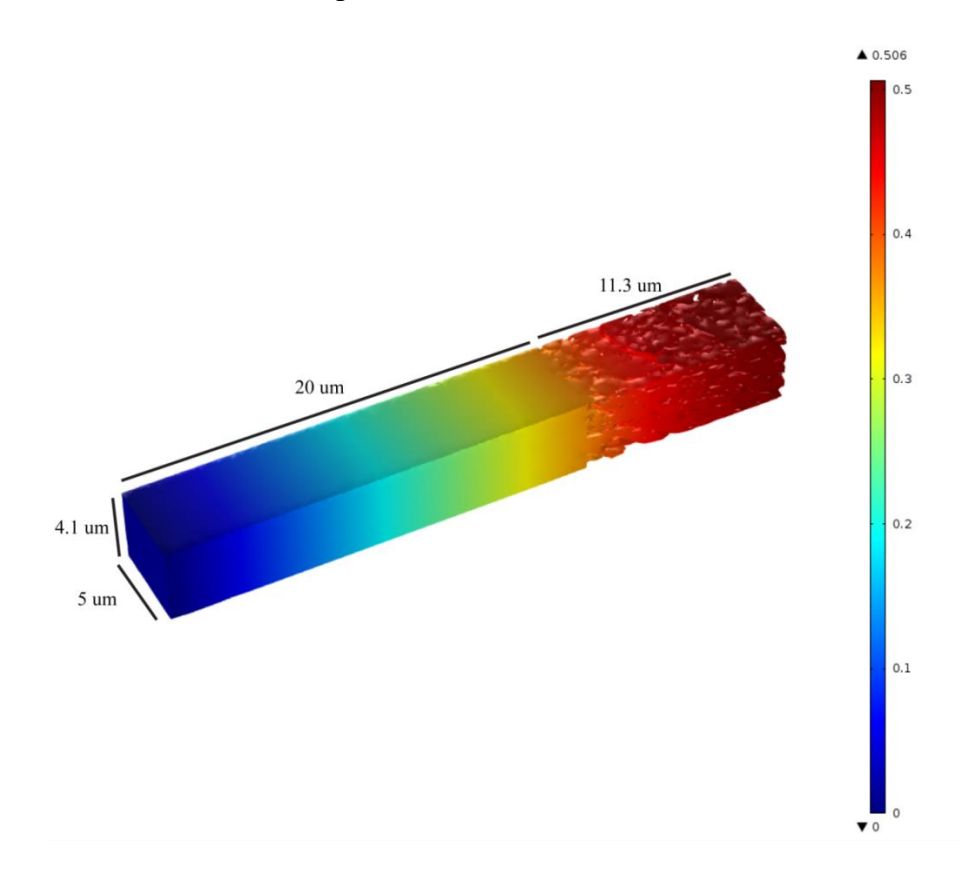


Figure A2.8: **FIB-SEM 3D Reconstruction Electrochemical Potential Gradient**. Electrochemical Potential Gradient was determined using the COMSOL computer program.

for the entire volume mesh using a multislice plot.

Figure A2.9 shows the same electrochemical potential distribution in Figure A2.8 but using a multislice plot instead, which depicts the electrochemical potential through the volume of the microstructure at different x, y, and z coordinate positions. The

electrochemical potential lines appear to: 1) uniformly decrease in magnitude from the cathode to electrolyte through the entire volume, and 2) the surface has greater electrochemical potential values then the center of the microstructure.

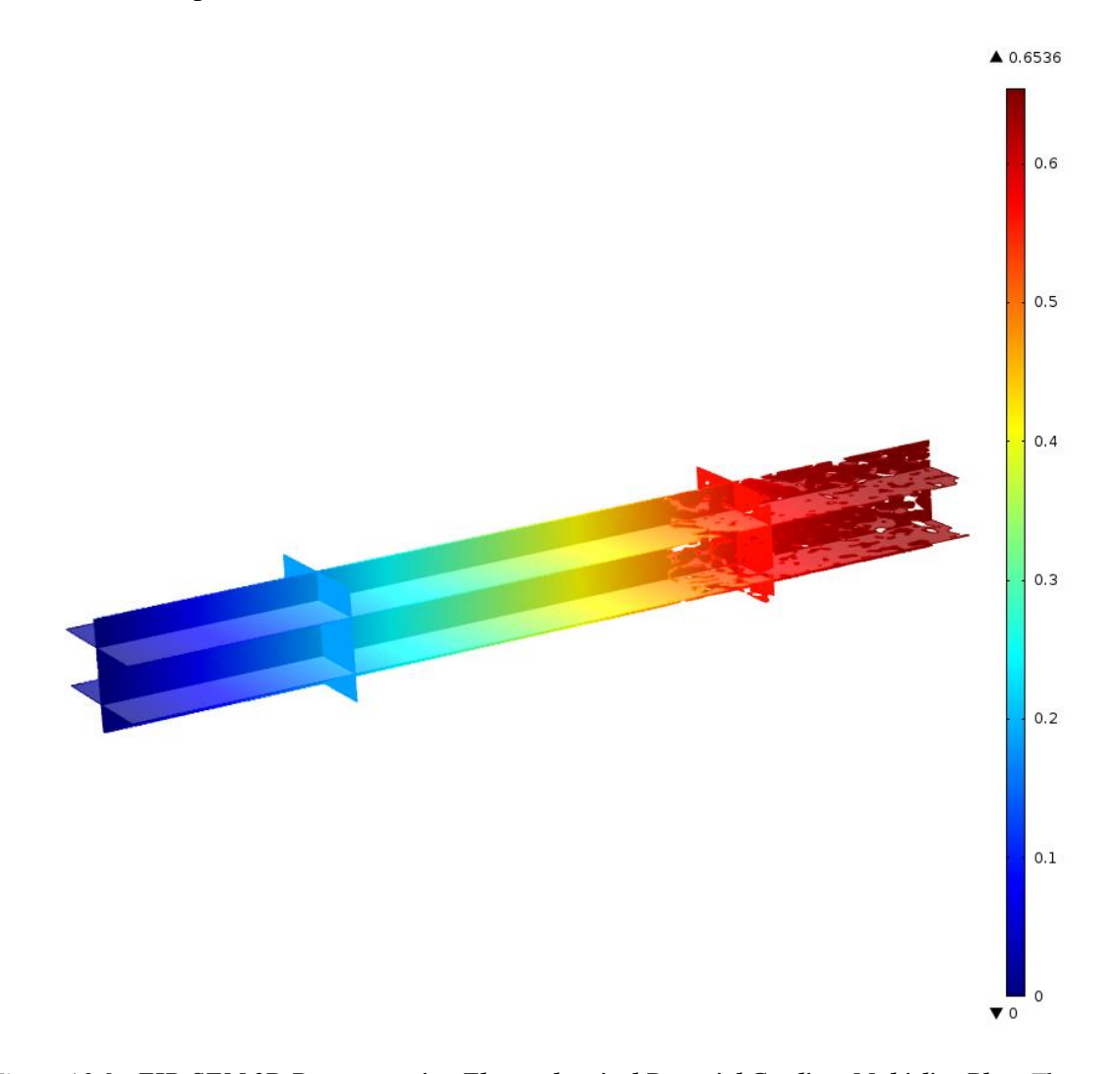


Figure A2.9: FIB-SEM 3D Reconstruction Electrochemical Potential Gradient Multislice Plot. The multislice electrochemical potential gradient plot was determined using the COMSOL computer program.

The first step to calculate an R_P value is to integrate the current density across the surface with a 0V potential applied to it. An integration area near the 0V potential (at the bottom of the electrolyte) needs to be created using a "Cutplane".

Figure A2.10 shows a "Cutplane" created near the bottom of the electrolyte material. This can be achieved by first left-clicking on "Results" on the left menu, right-

click on "Data Sets" and selecting "Cutplanes". Set the "Dataset" to whatever solution you used to calculate the potential lines (solution1 used in this thesis), select the "Plane" that is perpendicular to the oxygen vacancy transport in your microstructure (in this thesis the vacancy flow is in the x-direction), and set the coordinate value for your plane. Next, right-click on "Derived Solutions" on the left menu and select "Integration", then "Surface Integration". Set the "Data Set" as your cutplane and change the "Expression" to current density flux in the direction your vacancies are traveling (again it's in the x-direction for this thesis). Right-click "Surface Integration" on the left menu and select "Evaluate" to produce an integrated current value across the bottom surface of the electrolyte. The integrated current can then be used in Equation A1 to produce an R_P value.

$$R_P = \left(\frac{V}{I} * A\right) - \left(\frac{d}{2*\sigma_{IC}}\right)$$
 [A1]

V is the applied voltage on the cathode surface mesh (V), I is the integrated current (A), A is the area of integration for the integrated current (m²), d is the electrolyte thickness (m), and σ_{IC} is the IC scaffold conductivity (S/m). A derivation for Equation A1 was provided in Section 3.3.2. The integrated area, A, also needs to be calculated, so the calculated R_P is correct for the microstructure geometry that was used.

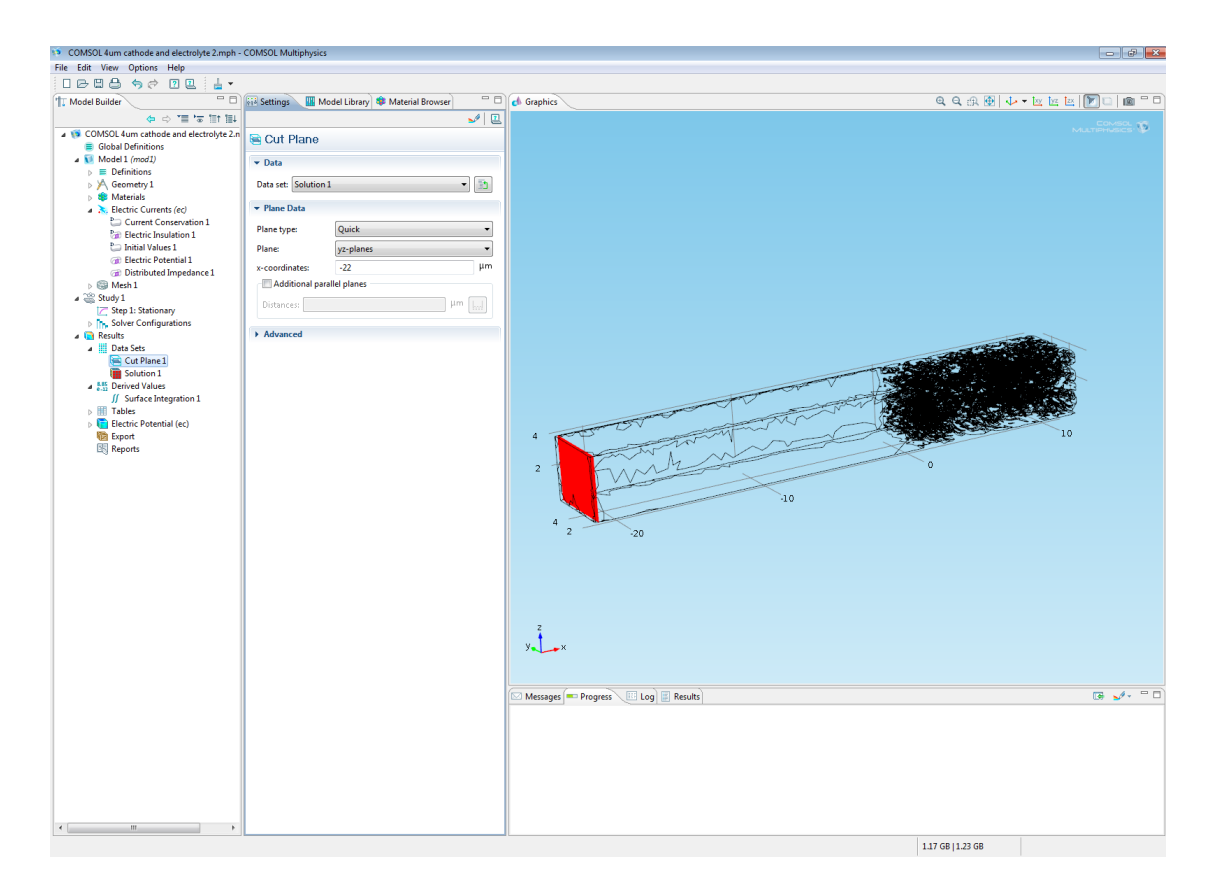


Figure A2.10: Cutplane used to Integrate Current Density Across Electrolyte Surface Mesh. The cutplane was applied to the 3D reconstruction using the COMSOL computer program.

To calculate the integration area the actual dimensions of the microstructure can be measured from COMSOL. Right-click on "Geometry" in the left menu and select "Measurements".

Figure A2.11 shows the geometry measurements screen. First select the "Finalized Geometry" in the "Type of Geometry" drop-down box. Next, select "Edge" in the "Geometric Entity Level" drop-down box and "Manual" in the "Selection" drop-down box. Select the entire edge that you wish to measure, and add those sections with the plus button underneath the manual selection. The length will be updated and displayed underneath "Measurements". The blue line is just an example of two sides that were selected for this demonstration.

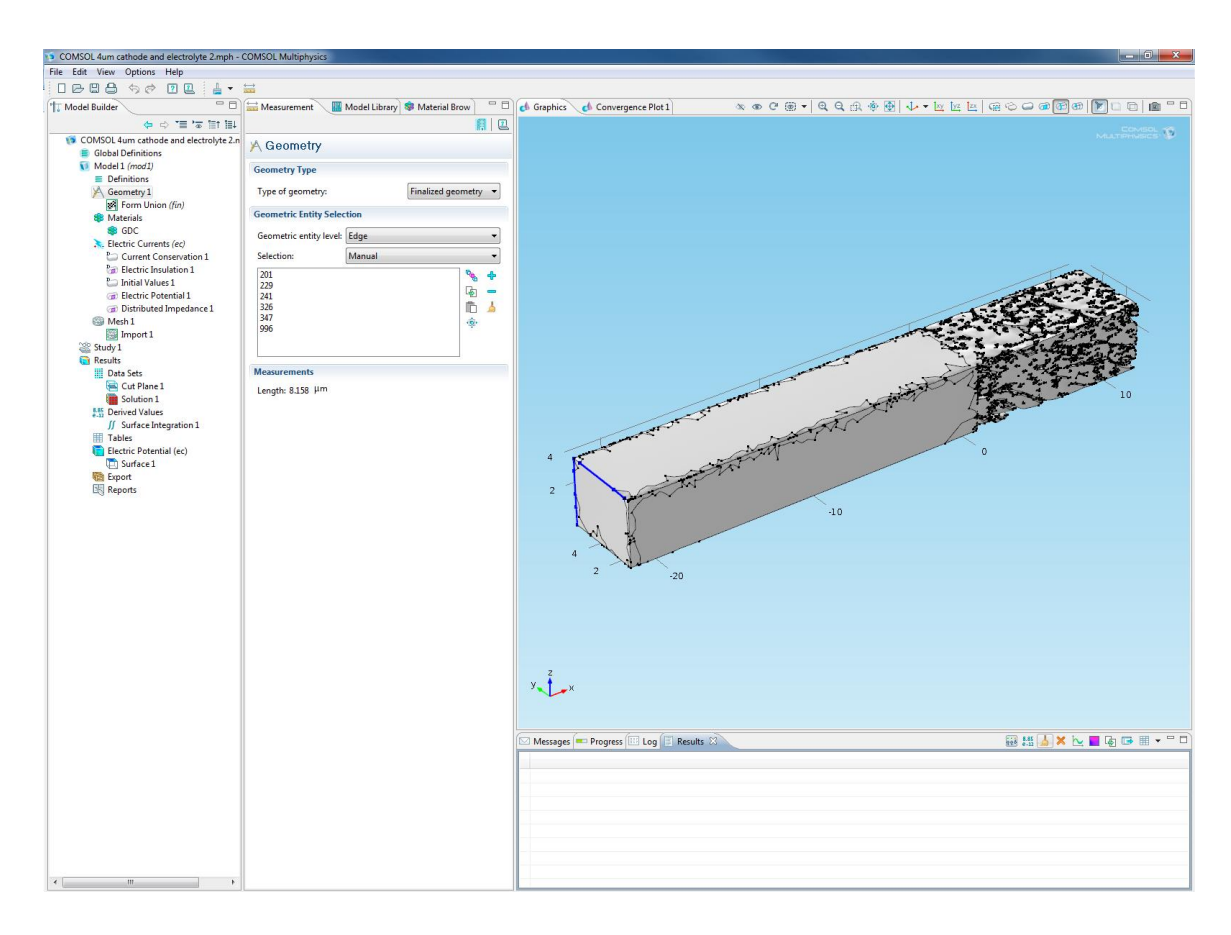


Figure A2.11: **COMSOL Integration Area Calculation**. The blue lines indicate the selected area to be measured. Additional lines can be selected to determine other microstructure lengths.

BIBLIOGRAPHY

BIBLIOGRAPHY

- [1] F. Zhao, Z. Wang, M. Liu, L. Zhang, C. Xia and F. Chen, *J. Power Sources*, "Novel Nano-Network Cathodes for Solid Oxide Fuel Cells" **185**, (2008)
- [2] T. Z. Sholklapper, H. Kurokawa, C. P. Jacobson, S. J. Visco and L. C. De Jonghe, *Nano Lett.*, "Nanostructured Solid Oxide Fuel Cell Electrodes" **7**, (2007)
- [3] J. M. Vohs and R. J. Gorte, *Adv. Mater.*, "High-Performance SOFC Cathodes Prepared by Infiltration" **21**, (2009)
- [4] S. P. Jiang, *Mat. Sci. Eng. A-Struct.*,"A Review of Wet Impregnation An Alternative Method for the Fabrication of High Performance and Nano-Structured Electrodes of Solid Oxide Fuel Cells" **418**, (2006)
- [5] J. D. Nicholas and S. A. Barnett, *J. Electrochem. Soc.*, "Measurements and Modeling of Sm_{0.5}Sr_{0.5}CoO_{3-x}-Ce_{0.9}Gd_{0.1}O_{1.95} SOFC Cathodes Produced Using Infiltrate Solution Additives" **157**, (2010)
- [6] M. Shah and S. A. Barnett, *Solid State Ionics*, "Solid Oxide Fuel Cell Cathodes by Infiltration of La_{0.6}Sr_{0.4}Co_{0.2}Fe_{0.8}O_{3-x} into Gd-Doped Ceria" **179**, (2008)
- [7] J. D. Nicholas, L. Wang, A. V. Call and S. A. Barnett, *Phys. Chem. Chem. Phys.*, "Use of the Simple Infiltration Microstructure Polarization Loss Estimation (SIMPLE) Model to Predict the Measured Polarization Resistance of Infiltrated Nano-Composite Solid Oxide Fuel Cell Cathodes" **14**, (2012)
- [8] M. Shah, J. D. Nicholas and S. A. Barnett, *Electrochem. Commun.*, "Prediction of Infiltrated Solid Oxide Fuel Cell Cathode Polarization Resistance using Simple Models" **11**, (2009)
- [9] M. Shah, P. W. Voorhees and S. A. Barnett, *Solid State Ionics*, "Time-Dependent Performance Changes in LSCF-Infiltrated SOFC Cathodes: The Role of Nano-Particle Coarsening" **187**, (2011)
- [10] Q. Yang, "Development and use of a New Curvature Relaxation Technique to Measure the In Situ Oxygen Surface Exchange Coefficients and Stress of Lanthanum Strontium Ferrite Films". Michigan State University, Ph.D Dissertation, 162, (2014)
- [11] U.S. Census Bureau, http://www.census.gov/popclock/, Population Clock, (2015)
- [12] U.S. Energy Information Administration, http://www.eia.gov/forecasts/ieo/, International Energy Outlook 2014, (2014)
- [13] J. D. Nicholas, *Electrochem. Soc. Interface*, "Highlights from the 2013 National Science Foundation Solid Oxide Fuel Cell Promise, Progress, and Priorities (SOFC-PPP) Workshop" **22**, (2013)

- [14] K.-T. Shiu, J. Zimmerman, H. Wang and S. R. Forrest, *Appl. Phys. Lett.*, "Ultrathin Film, High Specific Power InP Solar Cells on Flexible Plastic Substrates" **95**, (2009)
- [15] E. D. Wachsman and K. T. Lee, *Science*, "Lowering the Temperature of Solid Oxide Fuel Cells" **334**, (2011)
- [16] B.C.H. Steele and A. Heinzel, *Nature*, "Materials for Fuel-Cell Technologies" **414**, (2001)
- [17] C. Schlitzberger, N. O. Brinkmeier and R. Leithner, *Chem. Eng. Technol.*, "CO₂ Capture in SOFC by Vapor Condensation and CH₄ Production in SOEC Storing Excess Electricity" **35**, (2012)
- [18] M. A. Laguna-Bercero, S. J. Skinner and J. A. Kilner, *J. Power Sources*, "Performance of Solid Oxide Electrolysis Cells Based on Scandia Stabilised Zirconia" **192**, (2009)
- [19] A. Hauch, S. D. Ebbesen, S. H. Jensen and M. Mogensen, *J. Mater. Chem.*, "Highly Efficient High Temperature Electrolysis" **18**, (2008)
- [20] General Electric, http://www.ge-energy.com/prod_serv/products/gas_turbines_cc/en/h_system/index.htm, General Electric Website, (2015)
- [21] K. W. Bedringås, I. S. Ertesvåg, S. Byggstøyl and B. F. Magnussen, *Energy*, "Exergy Analysis of Solid-Oxide Fuel-Cell (SOFC) Systems" **22**, (1997)
- [22] S. H. Chan, C. F. Low and O. L. Ding, *J. Power Sources*, "Energy and Exergy Analysis of Simple Solid-Oxide Fuel-Cell Power Systems" **103**, (2002)
- [23] Ceres Power Holdings PLC, http://www.cerespower.com/store /files/218-Ceres%20Power%202010_interactive-V2.pdf, SOFC Efficiency, (2015)
- [24] Hexis Inc.,
- http://www.hexis.com/sites/default/files/media/publikationen/130524_hexis_broschuere_galileo_e_web.pdf, Gaileo Product Brochure, (2015)
- [25] F. J. Gardner, M. J. Day, N. P. Brandon, M. N. Pashley and M. Cassidy, *J. Power Sources*, "SOFC Technology Development at Rolls-Royce" **86**, (2000)
- [26] D. Stöver, H. P. Buchkremer and S. Uhlenbruck, *Ceram. Int.*, "Processing and Properties of the Ceramic Conductive Multilayer Device Solid Oxide Fuel Cell (SOFC)" **30**, (2004)
- [27] Z. L. Zhan, D. Han, T. Z. Wu, X. F. Ye, S. R. Wang, T. L. Wen, S. Cho and S. A. Barnett, *RSC Adv.*, "A Solid Oxide Cell Yielding High Power Density below 600°C" **2**, (2012)

- [28] Z. Y. Jiang, C. R. Xia and F. L. Chen, *Electrochim. Acta,* "Nano-Structured Composite Cathodes for Intermediate-Temperature Solid Oxide Fuel Cells via an Infiltration/Impregnation Technique" **55**, (2010)
- [29] Y. Zhang, Q. Sun, C. Xia and M. Ni, *J. Electrochem. Soc.*, "Geometric Properties of Nanostructured Solid Oxide Fuel Cell Electrodes" **160**, (2013)
- [30] H. Zhang, F. Zhao, F. L. Chen and C. R. Xia, *Solid State Ionics*, "Nano-Structured Sm_{0.5}Sr_{0.5}CoO_{3-δ} Electrodes for Intermediate-Temperature SOFCs with Zirconia Electrolytes" **192**, (2011)
- [31] X. Song, A. R. Diaz, A. Benard and J. D. Nicholas, *Struct. Multidiscip. O.*, "A 2D Model for Shape Optimization of Solid Oxide Fuel Cell Cathodes" **47**, (2013)
- [32] E. D. Wachsman and S. C. Singhal, *Am. Ceram. Soc. Bull.*, "Solid Oxide Fuel Cell Commercialization, Research and Challenges" **89**, (2010)
- [33] C. W. Tanner, K.-Z. Fung and A. V. Virkar, *J. Electrochem. Soc.*, "The Effect of Porous Composite Electrode Structure on Solid Oxide Fuel Cell Performance" **144**, (1997)
- [34] C. Sun and U. Stimming, *J. Power Sources*, "Recent Anode Advances in Solid Oxide Fuel Cells" **171**, (2007)
- [35] L. Rose, O. Kesler, Z. Tang and A. Burgess, *J. Power Sources*, "Application of Sol Gel Spin Coated Yttria-Stabilized Zirconia Layers for the Improvement of Solid Oxide Fuel Cell Electrolytes Produced by Atmospheric Plasma Spraying" **167**, (2007)
- [36] J. Otomo, K. Waki and K. Yamada, *J. Fuel Cell Sci. Tech.*, "Multicriteria Assessment of the Performance of Solid Oxide Fuel Cells by Cell Design and Materials Development: Design and Modeling Approach" **10**, (2013)
- [37] ETH Zurich University, http://www.nonmet.mat.ethz.ch/research/Functional_Ceramics/Single_Chamber_Solid_Oxide_Fuel_Cells, Single Chamber Solid Oxide Fuel Cells, (2015)
- [38] L. Fan, C. Wang and B. Zhu, *Nano Energy*, "Low Temperature Ceramic Fuel Cells using all Nano Composite Materials" **1**, (2012)
- [39] A. F. Jankowski and J. P. Hayes, *J. Vac. Sci. Technol. A*, "Sputter Deposition of Yttria-Stabilized Zirconia onto a Porous Au Substrate" **13**, (1995)
- [40] N. Nakagawa, H. Yoshioka, C. Kuroda and M. Ishida, *Solid State Ionics*, "Electrode Performance of a Thin-Film YSZ Cell Set on a Porous Ceramic Substrate by RF Sputtering Technique" **35**, (1989)
- [41] A. Negishi, K. Nozaki and T. Ozawa, *Solid State Ionics*, "Thin-Film Technology for Solid Electrolyte Fuel-Cells by the RF Sputtering Technique" **3-4**, (1981)

- [42] A. F. Jankowski and J. P. Hayes, *Surf. Coat. Tech.*, "Reactive Sputter Deposition of Yttria-Stabilized Zirconia" **76–77**, (1995)
- [43] L. Wang, *Manuscripta Math.*, "Compactness Methods for Certain Degenerate Elliptic Systems" **78**, (1993)
- [44] T. Tsai and S. A. Barnett, *J. Electrochem. Soc.*, "Bias Sputter Deposition of Dense Yttria-Stabilized Zirconia Films on Porous Substrates" **142**, (1995)
- [45] L. S. Wang, E. S. Thiele and S. A. Barnett, *Solid State Ionics*, "Sputter Deposition of Yttria-Stabilzied Zirconia and Silver Cermet Electrodes for SOFC Applications" **52**, (1992)
- [46] J. Pena-Martinez, D. Marrero-Lopez, D. Perez-Coll, J. C. Ruiz-Morales and P. Nunez, *Electrochim. Acta*, "Performance of XSCoF (X = Ba, La and Sm) and LSCrX' (X' = Mn, Fe and Al) Perovskite-Structure Materials on LSGM Electrolyte for IT-SOFC" **52**, (2007)
- [47] F. S. Baumann, J. Fleig, H.-U. Habermeier and J. Maier, *Solid State Ionics*, "Impedance Spectroscopic Study on Well-Defined (La,Sr)(Co,Fe)O_{3-δ} Model Electrodes" **177**, (2006)
- [48] E. Bucher, A. Egger, P. Ried, W. Sitte and P. Holtappels, *Solid State Ionics*, "Oxygen Nonstoichiometry and Exchange Kinetics of Ba_{0.5}Sr_{0.5}Co_{0.8}Fe_{0.2}O_{3-x}" **179**, (2008)
- [49] M. Burriel, C. Niedrig, W. Menesklou, S. F. Wagner, J. Santiso and E. Ivers-Tiffee, *Solid State Ionics*, "BSCF Epitaxial Thin Films: Electrical Transport and Oxygen Surface Exchange" **181**, (2010)
- [50] E. Girdauskaite, H. Ullmann, V. V. Vashook, U. Guth, G. B. Caraman, E. Bucher and W. Sitte, *Solid State Ionics*, "Oxygen Transport Properties of $Ba_{0.5}Sr_{0.5}Co_{0.8}Fe_{0.2}O_{3-x}$ and $Ca_{0.5}Sr_{0.5}Mn_{0.8}Fe_{0.2}O_{3-x}$ Obtained from Permeation and Conductivity Relaxation Experiments" **179**, (2008)
- [51] H. Xiong, B. K. Lai, A. C. Johnson and S. Ramanathan, *J. Power Sources*, "Low-Temperature Electrochemical Characterization of Dense Ultra-Thin Lanthanum Strontium Cobalt Ferrite (La_{0.6}Sr_{0.4}Co_{0.8}Fe_{0.2}O₃) Cathodes Synthesized by RF-Sputtering on Nanoporous Alumina-Supported Y-Doped Zirconia Membranes" **193**, (2009)
- [52] Q. Yang, T. E. Burye, R. R. Lunt and J. D. Nicholas, *Solid State Ionics*, "In situ Oxygen Surface Exchange Coefficient Measurements on Lanthanum Strontium Ferrite Thin Films via the Curvature Relaxation Method" **249–250**, (2013)
- [53] F. S. Baumann, J. Fleig, H. U. Habermeier and J. Maier, *Solid State Ionics*, "Ba_{0.5}Sr_{0.5}Co_{0.8}Fe_{0.2}O_{3-δ} Thin Film Microelectrodes Investigated by Impedance Spectroscopy" **177**, (2006)

- [54] F. S. Baumann, J. Fleig, G. Cristiani, B. Stuhlhofer, H. U. Habermeier and J. Maier, *J. Electrochem. Soc.*, "Quantitative Comparison of Mixed Conducting SOFC Cathode Materials by Means of Thin Film Model Electrodes" **154**, (2007)
- [55] T. Yamaguchi, S. Shimizu, T. Suzuki, Y. Fujishiro and M. Awano, *Electrochem. Commun.*, "Fabrication and Characterization of High Performance Cathode Supported Small-Scale SOFC for Intermediate Temperature Operation" **10**, (2008)
- [56] T. Suzuki, Y. Funahashi, Z. Hasan, T. Yamaguchi, Y. Fujishiro and M. Awano, *Electrochem. Commun.*, "Fabrication of Needle-Type Micro SOFCs for Micro Power Devices" **10**, (2008)
- [57] C. Yang, W. Li, S. Zhang, L. Bi, R. Peng, C. Chen and W. Liu, *J. Power Sources*, "Fabrication and Characterization of an Anode-Supported Hollow Fiber SOFC" **187**, (2009)
- [58] N. Droushiotis, U. Doraswami, D. Ivey, M. H. D. Othman, K. Li and G. Kelsall, *Electrochem. Commun.*, "Fabrication by Co-Extrusion and Electrochemical Characterization of Micro-Tubular Hollow Fibre Solid Oxide Fuel Cells" **12**, (2010)
- [59] R.H.F. Verhoeven, "Characterization of La_{0.75}Sr_{0.25}Cr_{0.5}Mn_{0.5}O_{3-δ} (LSCM) Redox-Stable Perovskite Anodes for Solid Oxide Fuel Cells.". University of Twente Ph.D Dissertation, 63, (2006)
- [60] E. S. Raj, J. A. Kilner and J. T. S. Irvine, *Solid State Ionics*, "Oxygen Diffusion and Surface Exchange Studies on (La_{0.75}Sr_{0.25})_{0.95}Cr_{0.51}Mn_{0.5}O_{3-δ}" **177**, (2006)
- [61] T. E. Burye and J. D. Nicholas, *J. Power Sources*, "Improving La_{0.6}Sr_{0.4}Co_{0.8}Fe_{0.2}O_{3-δ} Infiltrated Solid Oxide Fuel Cell Cathode Performance through Precursor Solution Desiccation" **276**, (2015)
- [62] A. A. Yaremchenko, V. V. Kharton, E. N. Naumovich and F. M. B. Marques, *J. Electroceram.*, "Physicochemical and Transport Properties of Bicuvox-Based Ceramics" **4**, (2000)
- [63] J. B. Goodenough, *Solid State Ionics*, "Ceramic Solid Electrolytes" **94**, (1997)
- [64] O. Yamamoto, Y. Arati, Y. Takeda, N. Imanishi, Y. Mizutani, M. Kawai and Y. Nakamura, *Solid State Ionics*, "Electrical Conductivity of Stabilized Zirconia with Ytterbia and Scandia" **79**, (1995)
- [65] X. Guo, E. Vasco, S. Mi, K. Szot, E. Wachsman and R. Waser, *Acta Mater.*, "Ionic Conduction in Zirconia Films of Nanometer Thickness" **53**, (2005)
- [66] M. A. F. Öksüzömer, G. Dönmez, V. Sariboğa and T. G. Altinçekiç, *Ceram. Int.*, "Microstructure and Ionic Conductivity Properties of Gadolinia doped Ceria (Gd_xCe_{1-x}O_{2-x/2}) Electrolytes for Intermediate Temperature SOFCs Prepared by the Polyol Method" **39**, (2013)

- [67] C. D. Savaniu and J. T. S. Irvine, *Solid State Ionics*, "La-Doped SrTiO3 as Anode Material for IT-SOFC" **192**, (2011)
- [68] M. D. Gross, J. M. Vohs and R. J. Gorte, *Electrochem. Solid-State Lett.*, "A Strategy for Achieving High Performance with SOFC Ceramic Anodes" **10**, (2007)
- [69] L. Zhang, F. Zhao, R. Peng and C. Xia, *Solid State Ionics*, "Effect of Firing Temperature on the Performance of LSM–SDC Cathodes Prepared with an Ion-Impregnation Method" **179**, (2008)
- [70] Z. Jiang, L. Zhang, K. Feng and C. Xia, *J. Power Sources*, "Nanoscale Bismuth Oxide Impregnated (La,Sr)MnO₃ Cathodes for Intermediate-Temperature Solid Oxide Fuel Cells" **185**, (2008)
- [71] Z. Y. Jiang, L. Zhang, L. L. Cai and C. R. Xia, *Electrochim. Acta*, "Bismuth Oxide-Coated (La,Sr)MnO₃ Cathodes for Intermediate Temperature Solid Oxide Fuel Cells with Yttria-Stabilized Zirconia Electrolytes" **54**, (2009)
- [72] H. Ullmann, N. Trofimenko, F. Tietz, D. Stöver and A. Ahmad-Khanlou, *Solid State Ionics*, "Correlation between Thermal Expansion and Oxide Ion Transport in Mixed Conducting Perovskite-Type Oxides for SOFC Cathodes" **138**, (2000)
- [73] H. Uchida, S. Arisaka and M. Watanabe, *Solid State Ionics*, "High Performance Electrodes for Medium-Temperature Solid Oxide Fuel Cells: Activation of La(Sr)CoO₃ Cathode with Highly Dispersed Pt Metal Electrocatalysts" **135**, (2000)
- [74] H. Uchida, S.-i. Arisaka and M. Watanabe, *J. Electrochem. Soc.*, "High Performance Electrode for Medium-Temperature Solid Oxide Fuel Cells: Control of Microstructure of La(Sr)CoO₃ Cathodes with Highly Dispersed Pt Electrocatalysts" **149**, (2002)
- [75] H. Hayashi, M. Kanoh, C. J. Quan, H. Inaba, S. R. Wang, M. Dokiya and H. Tagawa, *Solid State Ionics*, "Thermal Expansion of Gd-Doped Ceria and Reduced Ceria" **132**, (2000)
- [76] Y. Y. Huang, J. M. Vohs and R. J. Gorte, *J. Electrochem. Soc.*, "Characterization of LSM-YSZ Composites Prepared by Impregnation Methods" **152**, (2005)
- [77] C. R. Xia, W. Rauch, F. L. Chen and M. L. Liu, *Solid State Ionics*, "Sm_{0.5}Sr_{0.5}CoO₃ Cathodes for Low-Temperature SOFCs" **149**, (2002)
- [78] J. D. Nicholas and S. A. Barnett, 217th Meeting of the Electrochemical Society, 39-58, (2010)
- [79] N. P. Bansal and B. Wise, *Ceram. Int.*, "Sol-Gel Synthesis of La_{0.6}Sr_{0.4}CoO_{3-x} and Sm_{0.5}Sr_{0.5}CoO_{3-x} Cathode Nanopowders for Solid Oxide Fuel Cells" **38**, (2012)

- [80] Y. Chen, Y. Lin, Y. X. Zhang, S. W. Wang, D. Su, Z. B. Yang, M. F. Han and F. L. Chen, *Nano Energy*, "Low Temperature Solid Oxide Fuel Cells with Hierarchically Porous Cathode Nano-Network" **8**, (2014)
- [81] X. Huang, T. H. Shin, J. Zhou and J. T. S. Irvine, *J. Mater. Chem. A*, "Hierarchically Nanoporous La_{1.7}Ca_{0.3}CuO₄₋₈ and La_{1.7}Ca_{0.3}NixCu_{1-x}O₄₋₈ (0.25 \leq x \leq 0.75) as Potential Cathode Materials for IT-SOFCs" **3**, (2015)
- [82] I. M. Hung, K.-Z. Fung, D.-T. Hung and M.-H. Hon, *J. Eur. Ceram. Soc.*, "Thermal Stability of Ordered Mesoporous Yttria-Stabilized Zirconia" **28**, (2008)
- [83] Q. Liu and F. Chen, *Mater. Res. Bull.*, "Self-Rising Approach to Synthesize Hierarchically Porous Metal Oxides" **44**, (2009)
- [84] R. Chao, R. Munprom, R. Petrova, K. Gerdes, J. R. Kitchin and P. A. Salvador, *J. Am. Ceram. Soc.*, "Structure and Relative Thermal Stability of Mesoporous (La,Sr)MnO₃ Powders Prepared Using Evaporation-Induced Self-Assembly Methods" **95**, (2012)
- [85] D. Grosso, C. Boissiere, B. Smarsly, T. Brezesinski, N. Pinna, P. A. Albouy, H. Amenitsch, M. Antonietti and C. Sanchez, *Nat. Mater.*, "Periodically Ordered Nanoscale Islands and Mesoporous Films Composed of Nanocrystalline Multimetallic Oxides" **3**, (2004)
- [86] J. M. Serra, S. Uhlenbruck, W. A. Meulenberg, H. P. Buchkremer and D. Stöver, *Top. Catal.*, "Nano-Structuring of Solid Oxide Fuel Cells Cathodes" **40**, (2006)
- [87] J. S. Beck, J. C. Vartuli, W. J. Roth, M. E. Leonowicz, C. T. Kresge, K. D. Schmitt, C. T. W. Chu, D. H. Olson and E. W. Sheppard, *J. Am. Chem. Soc.*, "A New Family of Mesoporous Molecular Sieves Prepared with Liquid Crystal Templates" **114**, (1992)
- [88] D. Grosso, C. Boissière, L. Nicole and C. Sanchez, *J. Sol-Gel Sci. Technol.*, "Preparation, Treatment and Characterisation of Nanocrystalline Mesoporous Ordered Layers" **40**, (2006)
- [89] C. J. Brinker, Y. Lu, A. Sellinger and H. Fan, *Adv. Mater.*, "Evaporation-Induced Self-Assembly: Nanostructures Made Easy" **11**, (1999)
- [90] F. Cagnol, D. Grosso, G. J. d. A. A. Soler-Illia, E. L. Crepaldi, F. Babonneau, H. Amenitsch and C. Sanchez, *J. Mater. Chem.*, "Humidity-Controlled Mesostructuration in CTAB-Templated Silica Thin Film Processing. The Existence of a Modulable Steady State" **13**, (2003)
- [91] H. Gu, H. Chen, L. Gao, Y. Zheng, X. Zhu and L. Guo, *Electrochim*. *Acta*, "Electrochemical Characterization of Co-Doped Sr_{0.8}Ce_{0.2}MnO_{3-δ} Cathodes on Sm_{0.2}Ce_{0.8}O_{1.9}-Electrolyte for Intermediate-Temperature Solid Oxide Fuel Cells" **54**, (2009)

- [92] N. Ortiz-Vitoriano, C. Bernuy-López, A. Hauch, I. Ruiz de Larramendi and T. Rojo, *Int. J. Hydrogen Energy.*, "Electrochemical Characterization of La_{0.6}Ca_{0.4}Fe_{0.8}Ni_{0.2}O₃ Cathode on Ce_{0.8}Gd_{0.2}O_{1.9} Electrolyte for IT-SOFC" **39**, (2014)
- [93] X. G. Cao and S. P. Jiang, *Int. J. Hydrogen Energy.*, "Identification of Oxygen Reduction Processes at (La,Sr)MnO₃ Electrode/La_{9.5}Si₆O_{26.25} Apatite Electrolyte Interface of Solid Oxide Fuel Cells" **38**, (2013)
- [94] D. W. Yun, H. S. Seo, J. H. Jun and K. Y. Kim, *Int. J. Hydrogen Energy.*, "Evaluation of Nb- or Mo-Alloyed Ferritic Stainless Steel as SOFC Interconnect by using Button Cells" **38**, (2013)
- [95] B. T. Dalslet, M. Søgaard and P. V. Hendriksen, *J. Electrochem. Soc.*, "Determination of Oxygen Transport Properties from Flux and Driving Force Measurements" **154**, (2007)
- [96] Y. Niu, W. Zhou, J. Sunarso, L. Ge, Z. Zhu and Z. Shao, *J. Mater. Chem.*, "High Performance Cobalt-Free Perovskite Cathode for Intermediate Temperature Solid Oxide Fuel Cells" **20**, (2010)
- [97] A. Egger, E. Bucher, M. Yang and W. Sitte, *Solid State Ionics*, "Comparison of Oxygen Exchange Kinetics of the IT-SOFC Cathode Materials $La_{0.5}Sr_{0.5}CoO_{3-\delta}$ and $La_{0.6}Sr_{0.4}CoO_{3-\delta}$ " **225**, (2012)
- [98] T. C. Yeh, "Electronic and Ionic Properties of Solid Oxide Fuel Cell Materials". Northwestern University, Ph.D Dissertation, 190, (2012)
- [99] G. J. la O' and Y. Shao-Horn, *J. Electrochem. Soc.*, "Oxygen Surface Exchange Kinetics on Sr-Substituted Lanthanum Manganite and Ferrite Thin-Film Microelectrodes" **156**, (2009)
- [100] J. E. ten Elshof, M. H. R. Lankhorst and H. J. M. Bouwmeester, *J. Electrochem. Soc.*, "Oxygen Exchange and Diffusion Coefficients of Strontium-Doped Lanthanum Ferrites by Electrical Conductivity Relaxation" **144**, (1997)
- [101] B. C. H. Steele and J. M. Bae, *Solid State Ionics*, "Properties of La_{0.6}Sr_{0.4}Co_{0.2}Fe_{0.8}O_{3-x} (LSCF) Double Layer Cathodes on Gadolinium-doped Cerium Oxide (CGO) Electrolytes II. Role of Oxygen Exchange and Diffusion" **106**, (1998)
- [102] N. J. Simrick, A. Bieberle-Hütter, T. M. Ryll, J. A. Kilner, A. Atkinson and J. L. M. Rupp, *Solid State Ionics*, "An Investigation of the Oxygen Reduction Reaction Mechanism of La_{0.6}Sr_{0.4}Co_{0.2}Fe_{0.8}O₃ using Patterned Thin Films" **206**, (2012)
- [103] C. Xia and M. Liu, *Solid State Ionics*, "Low-Temperature SOFCs Based on $Gd_{0.1}Ce_{0.9}O_{1.95}$ Fabricated by Dry Pressing" **144**, (2001)

- [104] C. Xia and M. Liu, *Solid State Ionics*, "Microstructures, Conductivities, and Electrochemical Properties of Ce_{0.9}Gd_{0.1}O₂ and GDC–Ni Anodes for Low-Temperature SOFCs" **152–153**, (2002)
- [105] Y. Liu, S. Zha and M. Liu, *Adv. Mater.*, "Novel Nanostructured Electrodes for Solid Oxide Fuel Cells Fabricated by Combustion Chemical Vapor Deposition (CVD)" **16**, (2004)
- [106] G. Y. Meng, H. Z. Song, H. B. Wang, C. R. Xia and D. K. Peng, *Thin Solid Films*, "Progress in Ion-Transport Inorganic Membranes by Novel Chemical Vapor Deposition (CVD) Techniques" **409**, (2002)
- [107] J. Schoonman, J. P. Dekker, J. W. Broers and N. J. Kiwiet, *Solid State Ionics*, "Electrochemical Vapor Deposition of Stabilized Zirconia and Interconnection Materials for Solid Oxide Fuel Cells" **46**, (1991)
- [108] A. Mineshige, K. Fukushima, K. Tsukada, M. Kobune, T. Yazawa, K. Kikuchi, M. Inaba and Z. Ogumi, *Solid State Ionics*, "Preparation of Dense Electrolyte Layer using Dissociated Oxygen Electrochemical Vapor Deposition Technique" **175**, (2004)
- [109] D. Perednis and L. J. Gauckler, *Solid State Ionics*, "Solid Oxide Fuel Cells with Electrolytes Prepared via Spray Pyrolysis" **166**, (2004)
- [110] S. Suda, M. Itagaki, E. Node, S. Takahashi, M. Kawano, H. Yoshida and T. Inagaki, *J. Eur. Ceram. Soc.*, "Preparation of SOFC Anode Composites by Spray Pyrolysis" **26**, (2006)
- [111] E. Koep, C. M. Jin, M. Haluska, R. Das, R. Narayan, K. Sandhage, R. Snyder and M. L. Liu, *J. Power Sources*, "Microstructure and Electrochemical Properties of Cathode Materials for SOFCs Prepared via Pulsed Laser Deposition" **161**, (2006)
- [112] H.-S. Noh, J.-W. Son, H. Lee, H.-S. Song, H.-W. Lee and J.-H. Lee, *J. Electrochem. Soc.*, "Low Temperature Performance Improvement of SOFC with Thin Film Electrolyte and Electrodes Fabricated by Pulsed Laser Deposition" **156**, (2009)
- [113] C. Brahim, A. Ringuedé, E. Gourba, M. Cassir, A. Billard and P. Briois, *J. Power Sources*, "Electrical Properties of Thin Bilayered YSZ/GDC SOFC Electrolyte Elaborated by Sputtering" **156**, (2006)
- [114] G. La O', J. Hertz, H. Tuller and Y. Shao-Horn, *J. Electroceram.*, "Microstructural Features of RF-sputtered SOFC Anode and Electrolyte Materials" **13**, (2004)
- [115] San Diego State University, http://www.ptl.sdsu.edu/index.html, Powder Technology Laboratory, (2015)
- [116] Louisiana State University, http://www.ece.lsu.edu/emdl/facilities/screen%20printer.html, Electronic Material and Device Laboratory, (2015)

- [117] J. E. ten Elshof and J. Boeijsma, *J. Powder Diffr.*, "Powder Diffraction of La_{1-x}A_xCo_{0.8}Fe_{0.2}O₃ (A=Sr,Ba)" **11**, (1996)
- [118] G. Brauer and H. Gradinger, Z. Anorg. Allg. Chem., "Über Heterotype Mischphasen bei Seltenerdoxyden. I" **276**, (1954)
- [119] S. P. Jiang and W. Wang, *Solid State Ionics*, "Novel Structured Mixed Ionic and Electronic Conducting Cathodes of Solid Oxide Fuel Cells" **176**, (2005)
- [120] Science Education Research Center at Carleton College, http://serc.carleton.edu/research_education/geochemsheets/techniques/SEM.html, Scanning Electron Microscopy, (2015)
- [121] Georgia State University, http://hyperphysics.phy-astr.gsu.edu/hbase/quantum/bragg.html, X-ray Diffraction Characterization Internal Schematic, (2015)
- [122] V. Mote, Y. Purushotham and B. Dole, *J. Theor. Appl. Phys.*, "Williamson-Hall Analysis in Estimation of Lattice Strain in Nanometer-Sized ZnO Particles" **6**, (2012)
- [123] Direct Industry, http://www.directindustry.com/prod/ta-instruments/thermogravimetric-analyzer-38477-517952.html, TA Thermogravimetric Analysis Device, (2015)
- [124] D.-H. Lee and N.-G. Cho, *Meas. Sci. Technol.*, "Assessment of Surface Profile Data Acquired by a Stylus Profilometer" **23**, (2012)
- [125]Zeiss, http://www.zeiss.com/microscopy/en_us/downloads/brochure-downloads.html, "Zeiss Scanning Electron Microscope Instruction Manual", (2015)
- [126] K. Huang and J. B. Goodenough, "Solid Oxide Fuel Cell Technology: Principles, Performance and Operations", Woodhead Publishing, (2009)
- [127] J. D. Nicholas and S. A. Barnett, *J. Electrochem. Soc.*, "Finite-Element Modeling of Idealized Infiltrated Composite Solid Oxide Fuel Cell Cathodes" **156**, (2009)
- [128] J. B. Goodenough, Annu. Rev. Mater. Res., "Oxide-Ion Electrolytes" 33, (2003)
- [129] H. Iwai, N. Shikazono, T. Matsui, H. Teshima, M. Kishimoto, R. Kishida, D. Hayashi, K. Matsuzaki, D. Kanno, M. Saito, H. Muroyama, K. Eguchi, N. Kasagi and H. Yoshida, *J. Power Sources*, "Quantification of SOFC Anode Microstructure Based on Dual Beam FIB-SEM Technique" **195**, (2010)
- [130] Materialize, http://biomedical.materialise.com/mimics, Software and Services for Biomedical Engineering, (2015)

- [131] D. R. Burfield, K. H. Lee and R. H. Smithers, *J. Org. Chem.*, "Desiccant Efficiency in Solvent Drying Reappraisal by Application of a Novel Method for Solvent Water Assay" **42**, (1977)
- [132] ASTM International, "E112-96: Standard Test Methods for Determining Average Grain Size", (2004)
- [133] K. S. Pitzer and Y. W. Shi, *J. Solution Chem.*, "Thermodynamics of Calcium-Chloride in Highly Concentrated Aqueous Solution and in Hydrated Crystals" **22**, (1993)
- [134] X. Liu and C. Prewitt, *Phys. Chem. Miner.*, "High-Temperature X-ray Diffraction Study of Co₃O₄: Transition from Normal to Disordered Spinel" **17**, (1990)
- [135] P. Aldebert and J. P. Traverse, *Mater. Res. Bull.*, "Etude par Diffraction Neutronique des Structures de Haute Temperature de La₂O₃ et Nd₂O₃" **14**, (1979)
- [136] D.V. Karpinsky, I.O. Troyanchuk, K. Barner, H. Szymczak and M. Tovar, *J. Phys-Condens. Matter*, "Crystal Stucture and Magnetic Ordering of the LaCo_{1-x}Fe_xO₃ System." **17**, (2005)
- [137] L. Pauling, Z. Kristall., "The Crystal Structure of the A-Modification of the Rare Earth Sesquioxides" **69**, (1929)
- [138] Y. Leng, S. H. Chan and Q. Liu, *Int. J. Hydrogen Energ.*, "Development of LSCF-GDC Composite Cathodes for Low-Temperature Solid Oxide Fuel Cells with Thin Film GDC Electrolyte" **33**, (2008)
- [139] Y. Shen, V. A. B. Almeida and F. Gitzhofer, *J. Therm. Spray Technol.*, "Preparation of Nanocomposite GDC/LSCF Cathode Material for IT-SOFC by Induction Plasma Spraying" **20**, (2011)
- [140] H. Scher and R. Zallen, *J. Chem. Phys.*, "Critical Density in Percolation Processes" **53**, (1970)
- [141] W. L. Smith and A. D. Hobson, *Acta Crystallogr.*, *Sect. B: Struct. Sci,* "The Structure of Cobalt Oxide, Co₃O₄" **29**, (1973)
- [142] A. J. Jennings, S. J. Skinner and Ö. Helgason, *J. Solid State Chem.*, "Structural Properties of La_xSr_{2-x}FeO_{4± δ} at High Temperature and Under Reducing Conditions" **175**, (2003)
- [143] A. Buyukaksoy, V. Petrovsky and F. Dogan, *J. Electrochem. Soc.*, "Efficient Cathodes for Solid Oxide Fuel Cells Prepared by Polymeric Precursor Infiltration" **159**, (2011)
- [144] A. J. Samson, M. Søgaard, P. Hjalmarsson, J. Hjelm, N. Bonanos, S. P. V. Foghmoes and T. Ramos, Durability and Performance of High Performance Infiltration Cathodes" **13**, (2013)

- [145] M. Shah, G. Hughes, P. W. Voorhees and S. A. Barnett, *ECS Trans.*, "Stability and Performance of LSCF-Infiltrated SOFC Cathodes: Effect of Nano-Particle Coarsening" **35**, (2011)
- [146] A. Call, "Performance and Structural Evolution of Nano-Scale Infiltrated Solid Oxide Fuel Cell Cathodes". Northwestern University, Ph.D Dissertation, 104, (2015)
- [147] T. E. Burye and J. D. Nicholas, Ionic and Mixed Conducting Ceramics 9, 85-91, (2014)
- [148] M. R. Afshar, N. Yan, B. Zahiri, D. Mitlin, K. T. Chuang and J.-L. Luo, *J. Power Sources*, "Impregnation of La_{0.4}Ce_{0.6}O_{1.8}–La_{0.4}Sr_{0.6}TiO₃ as Solid Oxide Fuel Cell Anode in H₂S-Containing Fuels" **274**, (2015)
- [149] F. Bidrawn, G. Kim, N. Aramrueang, J. M. Vohs and R. J. Gorte, *J. Power Sources*, "Dopants to Enhance SOFC Cathodes based on Sr-Doped LaFeO₃ and LaMnO₃" **195**, (2010)
- [150] M. Mogensen, M. Sogarrd, P. Blennow and K. K. Hansen, 8th European SOFC Forum, (2008)
- [151] V. V. Kharton, F. M. Figueiredo, L. Navarro, E. N. Naumovich, A. V. Kovalevsky, A. A. Yaremchenko, A. P. Viskup, A. Carneiro, F. M. B. Marques and J. R. Frade, *J. Mater. Sci.*, "Ceria-Based Materials for Solid Oxide Fuel Cells" **36**, (2001)
- [152] Y. Kimura, T. Kushi, S.-i. Hashimoto, K. Amezawa and T. Kawada, *J. Am. Cer. Soc.*, "Influences of Temperature and Oxygen Partial Pressure on Mechanical Properties of La_{0.6}Sr_{0.4}Co_{1-y}Fe_yO_{3-δ}" **95**, (2012)
- [153] U. Stimming, S.C. Singhal, H. Tagawa and W. Lehnert, Journal of the Electrochemical Society Conference Procedings V, 1370, (1997)
- [154] J. B. Yang, W. B. Yelon, W. J. James, Z. Chu, M. Kornecki, Y. X. Xie, X. D. Zhou, H. U. Anderson, A. G. Joshi and S. K. Malik, *Phys. Rev. B: Condens. Matter* "Crystal Structure, Magnetic Properties, and Mossbauer Studies of La_{0.6}Sr_{0.4}FeO_{3-δ} Prepared by Quenching in Different Atmospheres" **66**, (2002)
- [155] Y. Li, K. Gerdes, T. Horita and X. Liu, *J. Electrochem. Soc.*, "Surface Exchange and Bulk Diffusivity of LSCF as SOFC Cathode: Electrical Conductivity Relaxation and Isotope Exchange Characterizations" **160**, (2013)
- [156] R. Sonntag, S. Neov, V. Kozhukharov, D. Neov and J. E. ten Elshof, *Physica B*, "Crystal and Magnetic Structure of Substituted Lanthanum Cobalitites" **241–243**, (1997)
- [157] Z. Y. Jiang, Z. W. Lei, B. Ding, C. R. Xia, F. Zhao and F. L. Chen, *Int. J. Hydrogen Energ.*, "Electrochemical Characteristics of Solid Oxide Fuel Cell Cathodes

Prepared by Infiltrating (La,Sr)MnO₃ Nanoparticles into Yttria-Stabilized Bismuth Oxide Backbones" **35**, (2010)

[158] B. Wei, Z. Lu, T. S. Wei, D. C. Jia, X. Q. Huang, Y. H. Zhang, J. P. Miao and W. H. Su, *Int. J. Hydrogen Energ.*, "Nanosized Ce_{0.8}Sm_{0.2}O_{1.9} Infiltrated GdBaCo₂O_{5+δ} Cathodes for Intermediate-Temperature Solid Oxide Fuel Cells" **36**, (2011)

[159] L. F. Nie, M. F. Liu, Y. J. Zhang and M. L. Liu, *J. Power Sources*, "La_{0.6}Sr_{0.4}Co_{0.2}Fe_{0.8}O_{3-\delta} Cathodes Infiltrated with Samarium-doped Cerium Oxide for Solid Oxide Fuel Cells" **195**, (2010)

[160] G. M. Yang, C. Su, R. Ran, M. O. Tade and Z. P. Shao, *Energ. Fuel.*, "Advanced Symmetric Solid Oxide Fuel Cell with an Infiltrated K₂NiF₄-Type La₂NiO₄ Electrode" **28**, (2014)